

Surface adhesion of the pathogens
Leishmania mexicana and
Streptococcus pneumoniae



Amy Rebecca Hall
Department of Physics and Astronomy
University of Sheffield

Thesis submitted for the degree of
Doctor of Philosophy
June 2015

I would like to dedicate this thesis to my parents,
Val and Terry,
and to my loving boyfriend, Danny.

Acknowledgements

Firstly, I would like to thank my supervisors Prof. Mark Geoghegan and Prof. David Dockrell for their guidance and support throughout my PhD studies, and Dr Adrian Eley for his supervision of my initial research on *Chlamydia trachomatis*. This work would also not have been possible without the considerable support of my collaborators: Dr Matthew Rogers in the London School of Hygiene and Tropical Medicine, and Prof. Neil Cameron in Durham University. I would also like to thank Dr Ahmed Eissa, who synthesized the sugar-amines used in this work and helped to characterize the initial glycopolymer samples, and the Nanobiophysics Group at the Université catholique de Louvain; specifically Prof. Yves Dufrière, Dr David Alsteens, Dr Audrey Beaussart, Dr Sofiane El Kirat and Prachi Tripathi, who willingly shared their expertise in biological force spectroscopy with me. I would also like to thank EPSRC for funding my studies.

In the University of Sheffield, I have many people to thank for their advice and assistance with various aspects of the work, not least Ana Lorena Morales García, who performed the FMM analysis, was my sounding board for experimental ideas and was a willing assistant on synthesis days. For their assistance with AFM: Prof. Jamie Hobbs, Nic Mullin, Ross Carter, Jacob Albon, Rik Bailey and Rebecca Savage. For their assistance with various aspects of the polymerization work: Paul Chapman, Andrew Parnell, Rita La Spina, Maryam Raftari, Andrew Pryke and Sarah Canning. To Polymer Physics Group members that I shared an office and cup of tea with during my studies: Matt Mears, Latifah Alfahid, Tom Kennelly, Fabio Pontecchiani, Ellie Dougherty, Ateyyah Al-Baradi, Youmna Mouhamad, Masaharu Ibaragi, Warren Taylor, Tao Wang, Jason Zhang and Mike Weir, and also to my colleagues in the Medical School, including Martin Bewley, Joe Ford, Helen Marriott, Lucy Morris, Richard Budd, Rohit Bazaz, Jamil Jubrail, Paul Collini, Jody Aberdeen and Joby Cole.

I am very grateful to the technical staff in the Department of Physics and Astronomy, including Simon Dixon, Paul Kemp-Russell, Chris Vickers, and Pete Robinson, for their help with fixing or adapting various items; the departmental administrative staff, particularly Catherine Annabel, Julie Milner and Bec Raynor for dealing effectively with my various orders and queries; and technical staff in the Department of Infection and Immunity, particularly Ian Geary and Ben Harvey. Special thanks also go to my dad for taking the time to proof-read the various drafts of this manuscript.

I would also like to thank friends that I did not work with directly, but who supported me in this endeavour, often through discussions over a cup of tea in the Austin Room or in the pub after work, and made the last few years very enjoyable, including John, Matt L and Sam, Chris, Emile, Patricia, Saida, Liam, Darren, Lloyd, Stefan, James, Woody, Sam, Markez, Lee, Nicola, Raveen, Jonny, Rachel, Nusrat, Ed and Kim, Dine, Alessandra,

Drew, Jen, Emma and Dan; and my friends from outside Sheffield: Kate, Ben, Joe, Matt T, Matt S, Steve, Tim, Callum, Sarah J, Sarah MD, Anne, Bethany, Harriet, Hannah and Vincent.

Finally, I thank Danny, for his love, patience and support; Danny's parents and nana, who have looked after me like one of their own; and my family: Mum, Dad, Gary, Natalie, Ralph, Molly, Emily and Nigel, for their support, love and encouragement.

Abstract

In this work, two pathogenic microorganisms, *Streptococcus pneumoniae* and *Leishmania* parasites, are studied using AFM force spectroscopy with chemically modified tips in order to characterize their adhesive properties. In the work on *S. pneumoniae*, neutral hydrophobic and negatively-charged hydrophilic probes are used to detect non-specific forces on capsulated and unencapsulated type 2 bacteria. This work confirms the role of capsular polysaccharide in masking binding sites through a combination of steric hindrance and electrostatic repulsion, and shows that under the capsular surface there are pneumococcal molecules capable of hydrophobic binding. These results provide evidence that capsular reduction is important for achieving binding to the extracellular matrix of mucosal cells, and a good capsule coverage is essential to prevent binding of opsonins and detection by the immune system. It also supports the proposal that weak non-specific interactions act to reinforce and stabilize stronger, specific binding interactions when *S. pneumoniae* colonizes the nasopharynx. In the work on *Leishmania* parasites, specific sugar-binding interactions are investigated using galactose- and glucose-glycopolymer probes and *Leishmania mexicana* (two morphological forms of wild type parasites, an LPG-deficient mutant and its add-back), as well as one form of *Leishmania major*. The glycopolymer probes are developed and characterized using surface analysis techniques including FTIR-ATR, ellipsometry and optical tensiometry, and are shown to bind successfully and specifically to appropriate lectin-coated surfaces in an AFM assay. The experiments on the parasites show that sand fly midgut-adhesive forms of *Leishmania mexicana* interact strongly with both types of glycopolymer, having an effective areal force (considering all events > 20 pN) of 16 ± 2 nN μm^{-2} for galactose and 14 ± 2 nN μm^{-2} for glucose. It also shows that this adhesion is lifecycle-stage specific, with infectious parasites having an effective areal force of 5 ± 2 nN μm^{-2} for galactose and 6 ± 1 nN μm^{-2} for glucose. Glycopolymer-parasite binding is also found to be LPG-dependent, with the LPG-deficient *L. mexicana* mutant and midgut-adhesive *L. major* (which has different, bulkier LPG) showing interaction levels comparable to the infectious lifecycle form. These results support the proposal that sugar moieties on the midgut epithelium of permissive sand flies are important for disease transmission. This work therefore confirms that AFM is a useful tool to quantitatively evaluate the interaction strength between selected biomolecules and different microorganisms, and can be tailored to a specific biological question: in this case providing valuable information about host colonization by *S. pneumoniae* and transmission of *Leishmania* parasites.

Conference presentations

Atomic force microscopy study of the adhesion of *Leishmania* parasites to glycopolymer surfaces

A. R. Hall, M. Rogers, A. Eissa, N. Cameron, D. Dockrell, M. Geoghegan

Oral presentation. BAMN2013, Jeju, South Korea (2013).

Scanning force microscopy study of the adhesion of *Leishmania* parasites to glycopolymer surfaces

A. R. Hall, M. Rogers, N. Cameron, D. Dockrell, M. Geoghegan

Oral presentation. AFM User Meeting, Louvain-la-Neuve, Belgium (2012).

Scanning force microscopy study of the adhesion of *Leishmania* parasites to glycopolymer surfaces

A. R. Hall, M. Rogers, A. Eissa, N. Cameron, D. Dockrell, M. Geoghegan

Poster presentation. PhysCell2012, Hyères, France (2012).

The study of cells using scanning force microscopy

A. R. Hall, A. Eley, M. Geoghegan

Poster presentation. 8th European Biophysics Congress, Budapest, Hungary (2011).

Contents

List of Abbreviations	x
List of Figures	xiii
List of Tables	xviii
1 Introduction	1
1.1 Application of atomic force microscopy (AFM) in biological systems . . .	2
1.1.1 Types of tip-surface interactions	3
1.1.2 Force spectroscopy (FS) on cells	6
1.1.3 FS using cell probes	8
1.1.4 FS using chemically coated tips	11
Measuring hydrophobic and hydrophilic interactions . . .	11
Measuring typical ligand-receptor bond strengths . . .	12
1.2 <i>Streptococcus pneumoniae</i>	14
1.2.1 Virulence factors, the complement system and opsonization . . .	14
1.2.2 Pneumococcal cell structure	18
The cell wall	18
The capsule	20
1.2.3 The impact of pneumococcal surface charge on interactions with different self-assembled monolayers	22
1.3 <i>Leishmania major</i> and <i>Leishmania mexicana</i>	24
1.3.1 Leishmaniasis: disease characteristics and transmission	25
1.3.2 <i>Leishmania</i> parasite lifecycle	27
1.3.3 <i>Leishmania</i> -sand fly binding mechanisms	29
1.4 Glycopolymers	34
1.5 Summary of project objectives	38
2 Methodology	42
2.1 AFM	42
2.1.1 Imaging modes	44
Contact mode	44
Tapping mode	46
2.1.2 Force spectroscopy	46
2.1.3 Force mapping	49

2.2	Fitting force spectroscopy data	50
	The freely jointed chain model	51
	The worm-like chain model	52
	Other considerations for fitting FS data	53
2.3	Statistical methods	54
2.3.1	Finite mixture models	54
2.3.2	Histogram bin generation for unimodal force distributions	56
2.3.3	Applying thresholds to adhesion data	57
	Effective force per unit area (areal force)	57
2.3.4	Determining statistical significance	58
2.4	AFM details	60
2.4.1	Cantilever calibration for AFM	61
2.4.2	Different methods of cell immobilization	64
2.5	Preparation of hydrophobic and hydrophilic AFM tips	66
2.6	Preparation of lectin-coated mica surfaces	67
2.7	<i>Streptococcus pneumoniae</i> methodology	71
2.7.1	<i>S. pneumoniae</i> growth	71
2.7.2	Harvesting and washing of <i>S. pneumoniae</i>	75
2.8	<i>Leishmania</i> parasite methodology	75
2.8.1	<i>Leishmania</i> parasite culture	75
	Culture and passaging	75
	Counting	77
	Parasites used for final measurements	78
2.8.2	<i>Leishmania</i> parasite sample preparation	78
3	Development of methodology	80
3.1	<i>S. pneumoniae</i> sample preparation for AFM under liquid	80
3.1.1	Optimization of mechanical trapping of <i>S. pneumoniae</i>	80
	AFM of <i>S. pneumoniae</i> in air: cell sizes and morphology	80
	Estimating cell size from the dry AFM images	83
	Polycarbonate membrane hole size as a function of etching time	85
	Matching cell size with membrane etching time	90
3.1.2	Bacterial filtration	90
	Initial method	90
	Final method	91
3.1.3	Sample assembly	93
3.1.4	Successful trapping: AFM images of <i>S. pneumoniae</i> D39 in a polycarbonate membrane under PBS	94
3.1.5	Live/dead staining	96
3.2	Glassware and substrate cleaning protocol	98
3.3	PMAA brush synthesis	100
3.3.1	Original synthesis method: ATRP of <i>t</i> BMA and subsequent hydrolysis to PMAA	102

	Initiation of substrates	102
	Polymerization of <i>tert</i> -butyl methacrylate brushes . . .	103
	Hydrolysis to poly(methacrylic acid) brushes	104
3.3.2	Improved PMAA brush synthesis route	104
	APTES layer formation	106
	Initiation	106
	Growth of the poly(methacrylic acid) brush	107
3.3.3	Conversion of poly(methacrylic acid) brushes to glycopolymer brushes	108
3.3.4	PMAA and glycopolymer brush characterization	110
	Ellipsometry	110
	Contact angle	112
	Changes associated with glycosylation	112
3.4	Overcoming AFM issues	117
3.4.1	Vibration and noise	117
3.4.2	Evaporation	117
3.4.3	Drift in AFM force maps	118
3.4.4	Tip contamination	119
3.5	Selection of AFM parameters	120
3.6	AFM data processing	122
3.6.1	Calculating height maps using force data	122
3.6.2	Force curve baseline correction	124
3.7	DDT and MUA AFM control experiments	124
4	<i>Streptococcus pneumoniae</i> results	130
4.1	Introduction	130
4.1.1	Comparative bacterial hydrophobicity studies: context for ad- hesion properties of <i>S. pneumoniae</i>	131
	Genus <i>Streptococcus</i> bacteria	131
	Other bacteria	132
4.1.2	A detailed look at the properties of selected pneumococcal surface molecules	135
4.2	Sample experiment: D39 <i>Streptococcus pneumoniae</i> and MUA	137
4.2.1	Locating a cell pair and testing their tolerance of repeated mapping	138
4.2.2	Location-dependent force curve features	141
4.2.3	Where to draw the line: selection of mask boundaries	144
4.2.4	Can data from different maps of the same cell be combined? .	146
4.2.5	The effect of different forces and dwell times on the measured peak adhesive force	151
4.2.6	Can a single Gaussian fit be compared with the first Gaussian component of a finite mixture model?	154

4.3	Results: comparison of interactions between capsulated and unencapsulated <i>Streptococcus pneumoniae</i> and tips coated with hydrophilic or hydrophobic surfaces	154
4.3.1	Does the bacterial adhesion vary between capsulated and unencapsulated bacteria, and hydrophobic and hydrophilic surfaces?	155
4.3.2	How do the forces measured on the bacteria compare to those measured as part of the control experiments?	161
4.3.3	Does the shape of the Gaussian distribution vary between the two FMM components?	162
4.3.4	Is there a difference between the relative proportion of force points attributed to the first and second Gaussian distributions?	164
4.3.5	Is there a difference in the number of cells showing a bimodal distribution between the different tip-cell combinations?	167
4.3.6	Are the larger forces, i.e. those associated with the secondary peak, distributed randomly or in a pattern on the bacterium surface?	169
4.4	Conclusions and interpretation of results	169
4.5	Summary	172
5	<i>Leishmania</i> results	174
5.1	Introduction	174
5.2	Glycopolymer-lectin binding experiments	177
5.3	Dry <i>Leishmania mexicana</i> AFM images	186
5.4	<i>Leishmania mexicana</i> AFM images in PBS: cell damage	188
5.5	Systematic mapping approach: maps of the whole parasite and maps of the centre of the parasite	190
5.5.1	Optical images of parasites with a motile flagellum but attached body	193
5.6	Parasite morphologies	196
5.7	<i>Leishmania mexicana</i>	203
5.7.1	Finite-mixture model analysis	203
	Comparison of mean forces of the Gaussian components	203
	Distribution of fit parameters according to the weight of the component	206
5.8	Do any parasites show an uneven distribution of high forces across their surface?	211
5.9	Multiple binding events within a single force-distance curve	214
	A closer look at force curves from a single parasite.	215
5.10	Analysis of <i>Leishmania</i> parasite adhesion using the mean adhesive force of FS curves containing binding events	221
5.10.1	How do forces measured on <i>L. mexicana</i> compare to the lectin-binding control experiments?	224
5.10.2	Effective force per unit area	225

5.11 Discussion and interpretation of results	231
5.12 Summary	237
6 Conclusions	238
A Force curve contact point calculation code	242
B Chemical structures of molecules required for ATRP initiation	243
C <i>P</i>-values for the <i>Leishmania</i> parasite comparisons	245
Bibliography	250

List of Abbreviations

α -BiBB	α -bromoisobutyryl bromide
AFM	atomic force microscope
ANOVA	analysis of variance
APTES	(3-aminopropyl)triethoxysilane
ATRP	atom transfer radical polymerization
BHI	brain heart infusion
C3	complement component 3
CBP	choline-binding protein
CbpA	choline-binding protein A
CDF	cumulative distribution function
CFU	colony forming unit
conA	concanavalin A
CRP	C-reactive protein
CuAAC	copper catalysed azide-alkyne cycloaddition
D39	<i>Streptococcus pneumoniae</i> strain D39
DDT	1-dodecane thiol
DI	deionized
DLVO	Derjaguin, Landau, Verwey, and Overbeek
DMSO	dimethyl sulfoxide
DNA	deoxyribonucleic acid
EDC	<i>N</i> -(3-dimethylaminopropyl)- <i>N</i> '-ethylcarbodiimide hydrochloride
ELISA	enzyme-linked immunosorbent assay
EM	expectation-maximization algorithm & electron microscope
fH	human complement factor H
FJC	freely jointed chain
FMM	Finite mixture model
FP22	<i>Streptococcus pneumoniae</i> strain FP22
FS	force spectroscopy
FTIR-ATR	Fourier-transform infrared spectroscopy with attenuated total reflectance
G_s	the mean of a single Gaussian model
G_i	the mean of the i^{th} Gaussian component of a finite mixture model
Gal	galactose
GalNAc	<i>N</i> -acetyl-galactosamine
Glu/Glc	glucose

gp63	glycoprotein 63
GPI	glycosylphosphatidylinositol
HFN	human fibronectin
HIFBS	heat-inactivated fetal bovine serum
HPA	<i>Helix pomatia</i> lectin
LPG1 ⁻ AB	add-back: a previously lipophosphoglycan-deficient mutant which has been returned to its wild type form
l/n	leptomonad/nectomonad
lept	leptomonad
<i>L. maj</i>	<i>Leishmania major</i>
<i>L. mex</i>	<i>Leishmania mexicana</i>
LPG	lipophosphoglycan
LPG1 ⁻	lipophosphoglycan-deficient mutant
LSHTM	London School of Hygiene and Tropical Medicine
LTA	lipoteichoic acid
LVDT	linear variable differential transformer
LytA	major autolysin
MAA	methacrylic acid
Man	mannose
meta	metacyclic
MFP-3D	The Asylum MFP-3D atomic force microscope
MUA	11-mercaptoundecanoic acid
nect	nectomonad
NHS	<i>N</i> -hydroxysuccinimide
NLR	Nod-like receptor
NMP	nitroxide-mediated polymerization
NPS	nano positioning system
OD	optical density
ODT	1-octadecane thiol
OLS	optical lever sensitivity
OTS	octadecyltrichlorosilane
PtBMA	poly(<i>tert</i> -butyl methacrylate)
PAFr	platelet-activating-factor receptors
PavB	pneumococcal adherence and virulence factor
PBS	phosphate-buffered saline
PEI	poly(ethyleneimine)
PI	propidium iodide
Ply	pneumolysin
PMAA	poly(methacrylic acid)
pro	procyclic
PSD	power spectral density
PSG	promastigote secretory gel
PspA	pneumococcal surface protein A
PspC	pneumococcal surface protein C

RAFT	reversible addition-fragmentation chain-transfer polymerization
RB	reticulate body
RCA	Radio Corporation of America
RNA	ribonucleic acid
SAM	self-assembled monolayer
SBA	soybean agglutinin
SFM	scanning force microscopy
SIMS	secondary ion mass spectrometry
SLD	super luminescent laser diode
SMFS	single molecule force spectroscopy
TA	teichoic acid
<i>t</i> BMA	<i>tert</i> -butyl methacrylate
TEM	transmission electron microscope
v/v	volume/volume
w/v	weight/volume
WLC	worm-like chain
WT	wild type
ζ-potential	zeta-potential

List of Figures

1.1	Heterogeneity in force curves obtained with Si ₃ N ₄ AFM tips on two separate bacterial cells in water.	7
1.2	Different force curves obtained using <i>Lactococcus lactis</i> cell probes on a pig gastric mucin-based surface.	9
1.3	Diagrams of cell walls in (a) Gram positive and (b) Gram negative bacteria.	11
1.4	Schematic illustration of the structural cell wall components of <i>Streptococcus pneumoniae</i>	19
1.5	A cartoon of the proposed arrangement of different biomolecules on the surface of <i>Streptococcus pneumoniae</i>	19
1.6	Left and middle: EM and TEM images of D39 <i>S. pneumoniae</i> . Right: medians and interquartile ranges of capsule thickness as measured for D39 and an unencapsulated derivative.	21
1.7	Chemical structures of 1-dodecane thiol and 11-mercaptoundecanoic acid.	22
1.8	Phlebotomine sand fly and cutaneous leishmaniasis ulcers.	25
1.9	Different morphological forms of <i>Leishmania mexicana</i> (these forms are common to all <i>Leishmania</i> species) from different stages of the parasite lifecycle.	28
1.10	An illustration of the lifecycle of <i>Leishmania</i> in a compatible vector, demonstrating the time-dependency and position of the observed morphological forms.	28
1.11	SEM image of <i>Leishmania</i> promastigotes attached to the microvillar epithelial cells that line the midgut of a female <i>Phlebotomus papatasi</i> sand fly.	29
1.12	Polymorphic structures of LPG molecules from different species/morphological stages of <i>Leishmania</i> parasites.	31
1.13	Schematic diagram representing the reversible attachment between <i>Leishmania</i> promastigotes and the PpGalec receptor in the sand fly midgut.	32
1.14	Fluorescent image showing binding of midgut lysate from a permissive sand fly to <i>L. major</i> parasites and its inhibition by pre-incubation of parasites with GalNAc.	33
1.15	Example force curves between soybean agglutinin and porcine submaxillary mucin containing galactosamine residues.	37

2.1	Schematic diagram of an Atomic Force Microscope (AFM).	43
2.2	Example AFM height and deflection images: a <i>Chlamydia trachomatis</i> reticulate body.	45
2.3	Example force-distance curves showing the different sample characteristics which can be probed using AFM.	47
2.4	Model force-distance curves, showing idealized adhesion events.	48
2.5	Thermal power spectral density curves taken in air and liquid, showing the fit used to calculate the AFM cantilever spring constant, k	63
2.6	D39 <i>Streptococcus pneumoniae</i> growth curves.	73
2.7	FP22 <i>Streptococcus pneumoniae</i> growth curves.	73
3.1	AFM images of D39 <i>S. pneumoniae</i> in air.	82
3.2	D39 <i>Streptococcus pneumoniae</i> capsule visualisation.	83
3.3	AFM images of FP22 <i>S. pneumoniae</i> in air.	84
3.4	Example of the image processing used to determine average hole size for NaOH etching experiments.	87
3.5	Change in membrane hole diameter over etching time in 4M NaOH.	88
3.6	The increase in the ratio of merged holes containing more than two holes to joined pairs with increased etching time.	89
3.7	Schematic diagram showing two pneumococcal filtration methods.	92
3.8	AFM images of D39 <i>S. pneumoniae</i> in PBS.	95
3.9	Selected live/dead fluorescence images showing <i>S. pneumoniae</i> on a glass slide under a cover slip (with and without prior treatment with ethanol) and <i>in situ</i> in a polycarbonate membrane.	97
3.10	The reaction cells used for polymer brush synthesis on cantilever chips and silicon wafers.	103
3.11	Chemical structures of sugar amines and a reaction scheme showing PMAA glycosylation via EDC/NHS and subsequent exposure to sugar amine.	109
3.12	Photos showing galactose-coating: in progress, and the different hydrophilicity levels of an area of PMAA brush coated with galactose-ethyl-amine compared to EDC/NHS functionalized brush.	113
3.13	Galactose glycopolymer-coated cantilever chip in position in the AFM cantilever holder.	113
3.14	FTIR-ATR and Raman data showing the different absorbance spectra and intensity profiles of control wafers at different points during the glycopolymer brush fabrication process.	116
3.15	Comparison of AFM drift in a force map and subsequent image.	119
3.16	Two force curves showing different indentations for the same applied force on glass and a <i>Leishmania</i> parasite.	123
3.17	DDT and MUA control experiments in water.	125
3.18	DDT and MUA control experiments in PBS.	128
4.1	A more detailed look at the location of various virulence factors in relation to the pneumococcal cell wall and capsule.	136

4.2	Consecutive height maps of a pair of D39 pneumococci obtained with various applied forces and dwell times on the surface.	139
4.3	Force-distance curves showing different characteristic features associated with the substrate, a cell on the substrate and a cell trapped in a hole. From a <i>Streptococcus pneumoniae</i> D39-MUA experiment.	142
4.4	Height and force maps of a pair of D39 pneumococci showing different mask thresholds.	145
4.5	Graphs comparing different force measures including Gaussian fits and the median of all the masked force map data for two force maps, and the combined data from the two maps.	148
4.6	Comparison of finite mixture model Gaussian fits of data from two force maps of the same cell, and the fit of the combined data from both maps.	150
4.7	Force maps of a pair of D39 pneumococci obtained with various applied forces and dwell times on the surface.	152
4.8	Graphs showing adhesive force measures for the same pair of bacteria when measured using different forces (top) and different dwell times (bottom).	153
4.9	Graph showing the difference between average force measures for the capsulated and unencapsulated <i>S. pneumoniae</i> strains and the hydrophobic and hydrophilic tip coatings.	156
4.10	Graphs showing comparative indentation depths for capsulated and unencapsulated <i>S. pneumoniae</i> strains, using a hydrophobic AFM tip.	158
4.11	Graph showing the comparative widths of the first and second Gaussian components fitted to the \log_{10} force data of the capsulated and unencapsulated <i>S. pneumoniae</i> strains and the hydrophobic and hydrophilic tip coatings.	163
4.12	Graph showing the likelihood of a force curve being attributed to the first or second distribution in the histogram of the \log_{10} force data, for the capsulated and unencapsulated <i>S. pneumoniae</i> strains and the hydrophobic and hydrophilic tip coatings.	166
4.13	Graphs generated from the two component Gaussian finite mixture model of the \log_{10} force histogram for the D39 <i>S. pneumoniae</i> cell that showed a stable bimodal distribution when probed using MUA.	166
4.14	Graph showing the likelihood of the histogram of the \log_{10} force data having a bimodal distribution, for the capsulated and unencapsulated <i>S. pneumoniae</i> strains and the hydrophobic and hydrophilic tip coatings.	168

5.1	Representative force maps from the glucose and galactose lectin control experiments, showing strong binding events between glycopolymer-coated tips and lectin-coated samples and a decrease in adhesion to levels similar to that measured on bare mica when a blocking agent was added to the buffer for experiments with a glycopolymer tip and lectin-coated surface.	180
5.2	Graphs showing the average adhesive force for different force maps taken as part of the glycopolymer-lectin experiments.	182
5.3	Graphs showing the proportion of force curves in individual glycopolymer control experiment force maps which measured adhesive forces > 30 pN.	185
5.4	Contact mode AFM images of <i>Leishmania mexicana</i> paramastigotes on a glass substrate taken in air.	187
5.5	Tapping mode AFM images of a wild type <i>Leishmania mexicana</i> nectomonad on a PEI-coated substrate taken in PBS.	189
5.6	Image taken from the video feed from the MFP-3D in-built microscope at 40× magnification of a <i>Leishmania mexicana</i> metacyclic-rich parasite sample on a PEI-coated glass substrate in PBS.	191
5.7	AFM height and force maps of a <i>Leishmania mexicana</i> metacyclic parasite taken in PBS using a glucose-glycopolymer-coated AFM tip.	192
5.8	Still images from the MFP-3D in-built microscope at 40× magnification showing two separate <i>Leishmania</i> parasites with active flagella, even while a force map is being taken. Parasites are attached to a PEI-coated glass substrate in PBS.	194
5.9	Height maps showing wild type <i>Leishmania mexicana</i> procyclic parasite morphologies.	198
5.10	Height maps showing wild type <i>Leishmania major</i> nectomonad parasite morphologies.	199
5.11	Height maps showing LPG1 ⁻ mutant <i>Leishmania mexicana</i> leptomonad parasite morphologies.	200
5.12	Height maps showing LPG1 ⁻ add-back <i>Leishmania mexicana</i> nectomonad/leptomonad parasite morphologies.	201
5.13	Height maps showing wild type <i>Leishmania mexicana</i> metacyclic parasite morphologies.	202
5.14	Graph comparing the mean forces of finite mixture model components used to fit <i>Leishmania mexicana</i> - glycopolymer force data.	204
5.15	Graphs showing the mean forces of the components of the finite mixture model and their associated weights (λ) for different <i>Leishmania mexicana</i> - glycopolymer combinations.	207
5.16	Graphs showing the widths (σ) of the components of the finite mixture model and their associated weights (λ) for different <i>Leishmania mexicana</i> - glycopolymer combinations.	210
5.17	Patterned forces on wild type <i>Leishmania mexicana</i> procyclic parasites probed with glucose glycopolymers.	212

5.18	Patterned forces on wild type <i>Leishmania mexicana</i> metacyclic parasites probed with galactose glycopolymers.	213
5.19	Different force curves showing different numbers of interaction events, obtained on a single WT <i>Leishmania mexicana</i> procyclic parasite probed with a galactose glycopolymer coated AFM tip.	218
5.20	Schematic diagrams suggesting how multiple adhesion events could be measured in a single retraction curve through interaction of the AFM tip with either a single biomolecule or multiple biomolecules.	220
5.21	Graph comparing the mean forces of the <i>Leishmania</i> parasite-glycopolymer combinations, showing the median force, the mean force and the mean force calculated using forces above minimum thresholds of 20 and 30 pN.	222
5.22	Effective areal force evaluated using force-distance curves with a peak adhesive force > 20 pN, for all parasites.	226
5.23	Effective areal force evaluated using the mean force calculated for peak adhesive forces above a range of thresholds.	228
5.24	Effective areal force evaluated using force-distance curves with a peak adhesive force > 20 pN, excluding parasites with a patterned force distribution.	230
B.1	Chemical structures of reagents required to initiate the silicon wafers and AFM cantilevers ready for ATRP.	244
B.2	Chemical structures of allyl-11-undecane bromoisobutyrate and the initiator molecule (formed over two reactions) used in the revised synthesis method. The molecules are illustrated attached to a silicon substrate (in green).	244

List of Tables

2.1	Significance level notation as used in graphs	60
2.2	Reagents for lectin functionalization of mica.	69
2.3	<i>Leishmania</i> parasite culture medium.	76
3.1	Reagents for original PMAA brush synthesis	102
3.2	Reagents for improved PMAA brush synthesis.	105
3.3	Reagents for conversion of PMAA to glycopolymer brush.	110
3.4	Thickness and water contact angle during glycopolymer conversion.	115
4.1	Force curve parameters for the maps shown in Figure 4.2.	141
5.1	Glycopolymer-lectin binding results: average peak adhesive force.	179
5.2	Average force for the lectin-binding control experiments compared to selected parasite-tip combinations	224
5.3	Differences between the effective force per μm^2 for selected parasite-tip combinations	225
5.4	Differences between the effective force per μm^2 which are different when parasites with patterned regions of high force are excluded from the analysis.	231

Chapter 1

Introduction

The investigation of cell - surface interactions is important for developing our understanding of different organisms, and how they relate to one another. For example, the interaction of pathogens with host cells is intrinsically linked to disease pathogenesis: pathogen characteristics, such as the expression of different virulence factors on the cell surface, can influence processes such as adherence to and penetration through host cell layers, as well as interaction with factors involved in the host immune response. Ultimately, any new information about these interactions can therefore be applied to the development of drugs for disease treatment or vaccines for infection limitation or prevention. It is also possible that any findings could have an impact on decisions regarding the most appropriate path for disease control, affecting health policy. This thesis is focused on two different and taxonomically diverse human pathogens, providing an ideal opportunity to test the chosen methodology in different situations. If successful, the experimental procedures used have the potential to be applied to the study of other pathogenic cells, increasing the relevance of the work to the medical field.

The microorganisms used in the project are *Streptococcus pneumoniae*, a common cause of respiratory infection and invasive disease, and *Leishmania mexicana* and *Leishmania major*, both of which cause the cutaneous form of leishmaniasis. A detailed discussion of the life cycles and characteristics of these two organisms can be found in Sections 1.2 and 1.3 respectively. The adhesion systems which will be

investigated are important in terms of disease spread and infection of human host cells. For *Leishmania* parasites, adhesion is necessary for survival beyond excretion of the blood meal in the sand fly midgut, and for *S. pneumoniae*, attachment of the organism to a new host cell is central to the establishment and spread of an infection.

The experimental methodology is an extension of Scanning Force Microscopy (SFM), combining Atomic Force Microscope (AFM) imaging and force spectroscopy with the use of chemically functionalized tips to study the topographical and adhesion properties of pathogenic cells. This technique is undertaken in liquid conditions, allowing an *in vitro* experiment to recreate some of the environmental characteristics which are experienced by the cells *in vivo*.

1.1 Application of atomic force microscopy (AFM) in biological systems

AFM is becoming increasingly important for recreating biological systems *in vitro*. Following its invention in 1986 by Binnig *et al.* [1], it has been developed and used as a tool for probing biological processes, both for obtaining nanometre-resolution images of surfaces and, when operated in force spectroscopy mode, measuring properties such as elasticity and adhesion. More information about the specifics of the different AFM modes can be found in Section 2.1. The main attraction of the use of AFM for biological samples is that, unlike scanning electron microscopy and other such techniques, extensive and often invasive sample preparation is not required [2,3]. Perhaps most importantly though, microorganisms and other biomaterials can be imaged in ambient and even in liquid conditions [4]. Imaging in aqueous conditions, under growth media for example, simulates the cell/microorganisms' native environment and allows for a more accurate representation of their surface topography and forces [5].

1.1.1 Types of tip-surface interactions

The forces measured by AFM comprise a combination of several different types, generally separated into specific and non-specific categories. At small separations between the tip and the surface (< 1 nm), interactions such as hydrogen bonding, ion bonding and specific receptor-ligand interactions can occur between the molecules on the tip and the surface [6]. The applied force during force spectroscopy ensures both contact and indentation of the surface, the magnitude of which is determined by the user, so interactions due to different types of force, which act over different ranges, can be measured. If a dwell time is used, the tip maintains contact with the surface for a number of milliseconds or more, allowing the molecules in the contact area to diffuse and rearrange, which can be advantageous when probing selective binding interactions such as those involving lectins or antibodies, as it can increase the chance of specific interactions occurring [7, 8]. The main forces which can contribute to the adhesive interaction between an AFM tip and a sample are outlined below.

Between approximately 0.5 nm and 5 nm from the sample, steric repulsion and solvation come into play, affecting polymers on the cell surface and functionalized tip [9, 10]. These interactions are influenced by molecular conformation changes and charge screening at different ionic concentrations, with more screening occurring at higher concentrations [6]. Steric interactions are classed as repulsive osmotic forces, and are due to the compression, and therefore confinement of thermally mobile polymer chains when two surfaces are brought together, causing unfavourable entropy changes due to the reduction in the number of available conformational states [11, 12]. The scale of this steric interaction depends on the length and density of the polymer chains. The range of the force is increased when polymers are already partially confined and entangled, and interact with the approaching surface in bulk, such as in a dense polymer brush. Sparse end-grafted polymer chains of similar character interact with the approaching surface independently, and have a mushroom-like conformation, meaning that they remain closer to the surface, so the effective range and scale of the effect is reduced [13]. In a good solvent, polymer

chains are highly solvated and extend away from the surface, therefore the quality of the solvent can also increase the range of steric forces in the case of both sparse and densely-grafted polymers [14]. Depending on the polymer length, in a good solvent, the range of the force can be of the order of ~ 100 nm.

Entropically-driven steric forces are also experienced between biological molecules and structures such as membranes and lipid bilayers [15,16]. There are three classes of forces here, associated with the protrusion of molecules from the surface, overlap of headgroups in amphiphilic molecules (molecules with both hydrophobic and hydrophilic regions, such as surfactants), and the long range thermal undulation force, which exists between bilayers in solution [17], but is somewhat suppressed when the bilayer is immobilized, and is therefore not of particular interest in relation to this work.

From approximately 0.2 nm up to tens of nanometres from the sample, the tip is likely to be affected by hydrophobic interactions (within the first 5 nm) and the attractive Lifshitz-van der Waals force (effective range of ~ 15 nm in physiological solutions [17]), which is caused by dipoles induced in molecules of the interacting bodies, and is typically characterized by the Hamaker constant of the interacting materials. The Hamaker constant can be estimated for bacteria by assuming the bacterium is a colloidal particle and measuring the contact angle of a bacterial biofilm or layer of bacteria artificially achieved by filtering a suspension through a membrane with holes too small for the bacteria to pass through, resulting in a build up of cells on the suspension-side of the membrane [18]. Note that treatment of the bacterium as a colloidal particle neglects features associated with a dynamic organisms such as excretion of adhesins and other processes, which can vary depending on the environmental conditions surrounding the bacteria. The hydrophobic interaction is governed by the organization of water molecules surrounding a polymer, and is of an entropic nature [10]. It can lead to attraction between hydrophobic molecules or groups, and repulsion between two hydrophilic molecules or groups due to their preference for solvation [19].

At distances > 10 nm, electrostatic forces, which can be both attractive and

repulsive, move to the fore and dominate the tip-sample interaction. The electrostatic field, and therefore force, F , between the sample and tip decays exponentially with separation distance, D , such that $F \propto e^{-\kappa D}$, where κ^{-1} is the Debye screening length. In a strong 0.1 M electrolyte solution, $\kappa^{-1} \approx 1$ nm, and for a 0.001 M solution, $\kappa^{-1} \approx 10$ nm [17]. A weak ionic solution can be taken to have ionic strength of 0.00001 M and in this condition, AFM-measurable electrostatic interactions can occur up to 100 nm from the sample [18].

The magnitude of the electrostatic force is proportional to the charge density of the surface and decreases with increasing ionic strength [20]. This decrease is attributed to the diffusion of ions towards the charged surface of the material, forming a loose double layer of counterions that effectively screens the surface charges from objects in the surrounding media [17]. This is known as the electrostatic double-layer effect, and is very sensitive not only to electrolyte concentration, but also to the pH of the solution and the surface charge on the sample and the AFM tip [10]. The presence of divalent cations in an ionic solution have a dramatic effect on surface potential and counterion distribution at negatively charged surfaces, sometimes referred to as a bridging force, reducing electrostatic repulsion between two negatively charged surfaces and facilitating adhesion between them (e.g. lipid bilayers made up of amphiphilic molecules with anionic or zwitterionic hydrophilic headgroups and hydrophobic tails) [21].

Of particular relevance to force spectroscopy are forces associated with polymers, both synthetic and biological. These forces comprise a mixture of hydrophobic, steric, electrostatic, and van der Waals interactions and their magnitude depends on factors such as the polymer's chemical composition and the degree of ionization of functional groups [22]. Adhesion to ionic polymers decreases with increasing ionic concentration due to charge screening, but neutral polymer adhesion strength is generally unaffected by differing ionic concentrations [6]. Polymers with functional groups along their backbone or terminating the polymer chain are also capable of bridging interactions, where the functional group binds to a suitable group on the opposing surface, forming an initial bond which can then be strengthened by further,

similar bonding or contributions from other factors such as hydrogen or hydrophobic bonding along the length of the polymer. By coating the AFM tip with different molecules, it is possible to investigate this type of selective binding. If the functional groups involved in the bond are at the end of a hydrophilic polymer chain which is solvated in an aqueous solution, the length scale of the interaction is of the order of the contour length of the polymer, which can be as large as ~ 100 nm, and can be greater than this if a long molecule is used to functionalize the AFM tip, as molecules on the tip will also extend into the solution [17].

By probing the same cell types with different AFM tip chemistries (the tip coating should be sufficient that interactions characteristic of the uncoated tips are not observed) and comparing how different types of cells interact with these same chemically coated AFM tips, it is possible to build up a picture of how these different interactions contribute to the adhesion properties of the cell, even though the cell surface chemistries are highly complex. In this work, both the hydrophobic/hydrophilic self-assembled monolayer (SAM) and glycosylated polymer brush AFM tip coatings were sufficiently dense to effectively mask the tip base material and provide a good population of functional groups, which were available for binding interactions, as demonstrated in the control experiments in Sections 3.7 and 5.2 for the SAM and glycopolymer-coated tips, respectively.

1.1.2 Force spectroscopy (FS) on cells

The basic principle of force spectroscopy is that, by moving the AFM tip towards the surface, applying a known force then monitoring cantilever movement as the tip is moved away from the surface (see Section 2.1.2 for a more detailed description of FS), information can be obtained about the strength of the bond between any attached biopolymers and the tip, and the mechanical properties of the surface polymers [23]. It is also possible to investigate some structural characteristics of the biopolymer by observing patterns in unfolding or adhesion events and the corresponding distance between the probe and the sample at which these occur [24, 25]. This technique allows a picture to be built up of how selected binding and folding mechanisms work

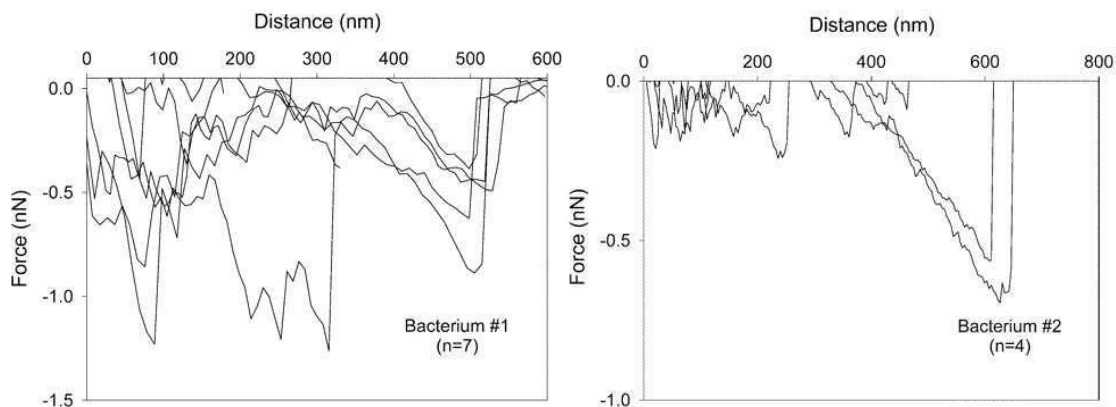


Figure 1.1: Heterogeneity in force curves obtained with Si_3N_4 AFM tips on two separate bacterial cells in water. Reproduced from [27] with permission.

without having to observe them at their characteristic timescale, which can be on a submicroscale level [26].

Force spectroscopy can be used on live cells as a way of probing the levels of heterogeneity of proteins or other molecules on the bacterium surface, as in the work of Camesano *et al.* [27], where the interaction between unmodified Si_3N_4 AFM tips and *Pseudomonas putida* bacterial populations was measured in different conditions. They observed substantial differences in force curves obtained both for the same bacterium and across multiple bacteria on the same sample, as shown in Figure 1.1. In this figure, the depth of the troughs corresponds to the measured force between the Si_3N_4 tip and a cell surface biopolymer, and the variation in distance between the troughs is related to the length of the biopolymer: low levels of force are required to extend a long molecule, but as the polymer is disentangled and stretched out straight, the force appears to increase linearly with distance until the polymer cannot stretch any further and the tip detaches from the end of the polymer. Thus, shallow dips at low probe retraction distances correspond to short, weakly adhered polymers, and large dips at longer distances correspond to longer polymers with higher adhesion forces to the Si_3N_4 probe. Because of the wide variability in adhesion (forces measured ranged from 0.05 nN to > 1 nN), many measurements were considered together and the freely jointed chain (FJC) model (see Section 2.2) was used to interpret them in terms of elastic properties.

1.1.3 FS using cell probes

It is possible to obtain force data on a whole-cell level by functionalizing an AFM probe (e.g. standard cantilever [28], tipless cantilever [29] or colloidal probe [30,31]) with whole bacteria or other cells and measuring the strength of the interaction forces with a defined substrate such as a self assembled monolayer (SAM) or supported lipid bilayer. Whole cell force spectroscopy has been conducted with fungi such as *Aspergillus niger* spores [32], yeasts including *Saccharomyces cerevisiae* [29], and various bacteria to gauge adhesion to metals in different media conditions [7,33], to explore general properties such as hydrophobicity [16], to look for specific interactions against both uncoated surfaces and surfaces which have been functionalized with specific biomolecules [34], and to probe interactions between a probe cell and confluent cell layer [8].

In the case of larger cells such as spores ($> 2 \mu\text{m}$), attachment of a single cell to the cantilever is generally sufficient, but for smaller bacteria with a diameter of $1 \mu\text{m}$ or less, a colloid or microsphere might first be attached to the AFM cantilever before this is then coated with bacteria. The advantage of using a colloid instead of a tipless cantilever as the substrate for bacterial adhesion is that even if the cells form a biofilm when brought into contact with the cantilever, when they are attached to a spherical surface, the interaction area with the test surface will be limited to one or a small number of cells. Additionally, if “fishing” is used to pick up a bacterium which is then used for force spectroscopy measurements, a colloidal probe makes it easier to select a single cell due to the reduced contact area [31]. If a flat surface is used, more cells are likely to contribute to the measured adhesion forces, making the interpretation of the scale of adhesion forces more challenging as it is unclear how many bacteria are involved in the adhesion event.

One example of successful use of bacteria-coated AFM tips to probe specific binding interactions is that of Le *et al.* [35], where *Lactococcus lactis* bacteria were physisorbed onto tips which had been previously treated with a 0.2% w/v solution of polyethyleneimine (PEI), and force curves were obtained on sample surfaces with a pig gastric mucin-based coating. Their results show a mixture of events; either

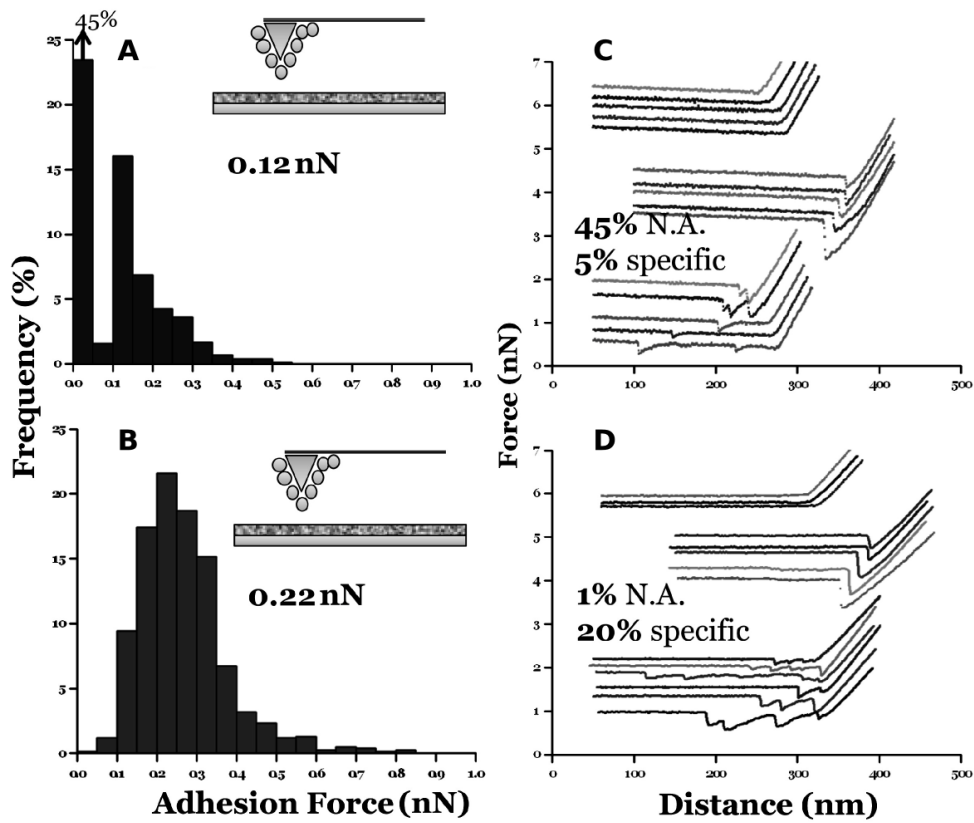


Figure 1.2: Histograms of adhesive force (A and B) and the associated retraction curves (C and D) for two different strains of *Lactococcus lactis* and a pig gastric mucin-based surface. Data are for strains MG1820 (A and C) and IBB477 (B and D). Example curves showing no adhesion, non-specific adhesion and selective binding are presented from top to bottom in E and F, and the relative percentages of events with no adhesion (N.A.) and specific binding are also given. Modified from [35] with permission.

showing no adhesion, non-specific adhesion (no extension before adhesive event) or one or multiple specific binding events (extending a number of nanometres from the sample before the adhesion event), with a different fraction of specific events being found for two different bacterial strains (see Figure 1.2 on page 9).

Despite the success of some whole cell force spectroscopy experiments, results can sometimes be difficult to interpret due to the number of different biomolecules present on the cell surface [36]. Bacteria fall into two main categories, Gram positive and Gram negative, with differing cell wall structure, as shown in Figure 1.3 on page 11 [37]. It is clear from these diagrams that both cell walls have a diverse range of native biomolecules exposed on their surface, protruding through or covalently bound to the peptidoglycan layers or outer membrane for Gram positive and Gram negative cells, respectively. These biomolecules can include teichoic acids, polysaccharides and proteins, the exact combination of which varies between bacterial species. The different biomolecules have diverse hydrophobicities and charge properties and whole cell adhesion measurements will give data from a combination of all of these factors. Work with whole cells is therefore useful to provide a picture of overall interactions between the various components of the cell wall and a given surface, but, as stated above, a single force-distance curve can contain a wide variety of interactions between hundreds if not thousands of different molecules on the cell surface and the test surface, within an area of $\sim 1 \mu\text{m}^2$ for a bacterium slightly larger than $1 \mu\text{m}^2$ in diameter. If the cell is immobilized on the surface instead of on the cantilever or a colloidal probe, a more selective approach can be applied, where data can be obtained for smaller areas of the cell surface ($\sim 0.01 \mu\text{m}^2$ for a cantilever with a tip radius of 20 nm and an indentation depth of just under 100 nm). This configuration also allows the spatial distribution of adhesins to be detected, and multiple different cells can be probed in the same experiment (cell probes can be costly and time consuming to produce so can result in reduced sample sizes). It is for these reasons that experiments for this work were completed using a functionalized tip morphology and the cell on the substrate, such as the experiments outlined in the following section.

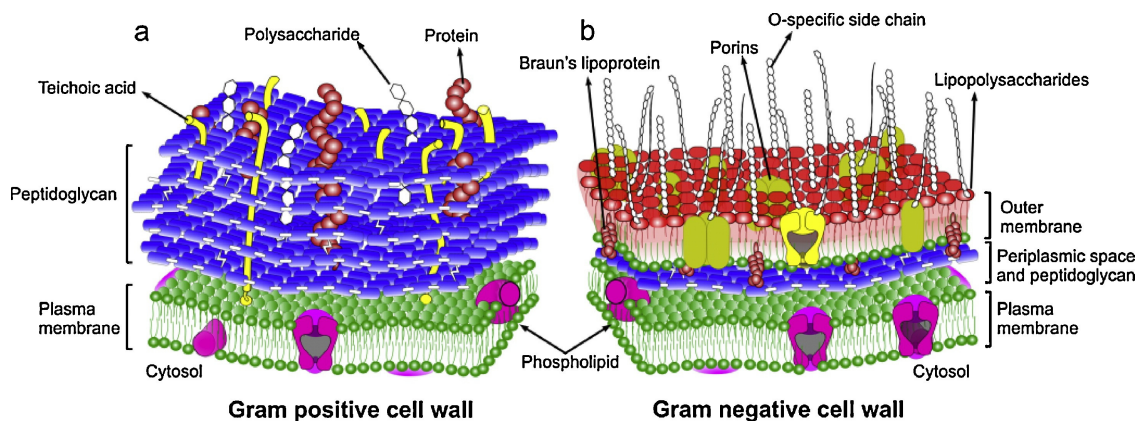


Figure 1.3: Diagrams of cell walls in (a) Gram positive and (b) Gram negative bacteria. From [37] with permission.

1.1.4 FS using chemically coated tips

Measuring hydrophobic and hydrophilic interactions

Hydrophobic/hydrophilic interactions are entropically driven and occur when molecules are in a polar solvent, such as water. The hydrophobic or hydrophilic properties of a molecule depend on the structure of the hydrogen bonds (dipole-dipole interactions) between the solvent and the different chemical groups of the molecule, and are therefore not additive, unlike electrostatic interactions. Hydrophilic groups prefer to form interactions with water rather than each other, meaning that hydrophilic molecules will be solvated in water, which can lead to repulsive intermolecular forces, and the opposite is true for hydrophobic groups [17]. Hydrophilic molecules tend to have a greater charge density, or polarity, however, uncharged and even non-polar molecules can be hydrophilic if they have an appropriate conformation and contain groups capable of hydrogen bonding to water [17]. In biology, charged amino acids tend to be located on the outer surfaces of proteins, and neutral amino acids tend to form a more hydrophobic core, since *in vivo* interactions occur in a water-based system.

As with electrostatic forces, hydrophilic interactions are sensitive to the condition of the solvation medium as the presence of ions in water is thought to affect its structure and therefore the strength of the hydrophobic interaction could be lower when measured in buffer than in pure water [38]. Taresté *et al.* investigated forces

between lipid layers formed of molecules with a headgroup containing two aromatic rings and one carboxyl group [39]. They found that in deionized water (pH 5.5), the interaction was dominated by hydrogen bonding and hydrophobic forces due to the protonation of the carboxyl groups allowing for the formation of hydrogen bonds between the surfaces. Conversely, in 10 mM Tris buffer and at a higher pH of 8.0, the carboxyl groups became ionized and the hydrogen bonding sites were occupied by ammonium cations (from the buffer). In addition to the loss of the hydrogen bonding force contribution, the ionization of the carboxyl groups and presence of ions in the buffer introduced a repulsive electrostatic double-layer force between the two negatively charged surfaces, facilitating their separation and resulting in an adhesion energy almost 5 times lower than at pH 5.5. These double-layer interactions also introduced a repulsive force regime at separation distances of 30 nm, which was not observed in water. Overall, the results suggested that hydrophobic and hydrogen bonding interactions are somewhat additive in nature and that hydrophobic interactions are mostly insensitive to pH and ionic concentration.

Measuring typical ligand-receptor bond strengths

In addition to the generalized interaction forces, molecules tethered to an AFM tip can become involved in specific binding events with molecules on the sample (either artificially attached to a substrate or in situ on a cell). These events range in strength, from tens of piconewtons to hundreds of piconewtons, some even showing adhesion at a nanonewton scale [40]. The measured force is affected by factors such as the trigger force and loading rate; the streptavidin-biotin rupture force was shown to more than double (from 167 ± 20 pN to 442 ± 17 pN) as the loading rate increased from $\sim 40 \mu\text{m s}^{-1}$ to $\sim 6000 \mu\text{m s}^{-1}$ (equivalent to approach/retraction velocities of $1 - 200 \mu\text{m s}^{-1}$), so care must be taken when comparing values obtained in different experiments [35, 41–43].

Specific binding interactions have been measured on a number of different cell types and a brief literature survey yields numerous papers on the subject. A few examples of such work are given in the rest of this section: work on yeast cells by

Touhami *et al.* found 121 ± 53 pN adhesion events between flocculating *Saccharomyces carlsbergensis* yeast cells and an oligoglucose carbohydrate functionalized tip (and 117 ± 41 pN between concanavalin A-functionalized tips and the same cells), but not between the same probes and a similar strain of non-flocculating cells [44].

Regarding mammalian cells, Gunning *et al.* mapped adhesive interactions on living human fibroblasts with wheat germ agglutinin, which binds to part of an epidermal growth factor receptor, where a modal detachment force of 125 pN was recorded [45]. Another example of binding on a fibroblast is that of Osada *et al.* where *N*-acetyl-D-galactosamine was detected on rat cells using a *Vicia villosa* agglutinin lectin-functionalized probe [46]. Lectins are sugar-binding proteins that are found on cell surfaces in all biological systems and which interact with carbohydrates in a highly specific manner, decoding the carbohydrate-encoded information. This interaction is fully reversible and plays a crucial role in many biological processes, including cell adhesion [47, 48]. The adhesive rupture forces measured between the *N*-acetyl-D-galactosamine and the lectin probe were approximately 50 pN, with an applied force of 250 pN. This value is important as a comparative value for selective binding events between *N*-acetyl-galactosamine and *Leishmania* parasites within this work, especially as the trigger value is consistent between the two. It should be noted at this point that it is somewhat easier to probe specific interactions when the lectin involved in the interaction is attached to the cantilever (as in this paper), since with a bulky glycopolymer on the tip it is more likely that specific interactions will be mixed in with general adhesion between the glycopolymer and the sample so might be more difficult to resolve.

Bacteria have also been fairly widely studied, including the Gram negative bacteria *Bradyrhizobium japonicum*. In this case, the specific interaction between soybean agglutinin (SBA) (on the tip) and *N*-acetyl-galactosamine (on the cell) was measured, giving a mean unbinding force of 106 ± 48 pN at a loading rate of 1 nN s^{-1} in phosphate-buffered saline (PBS) [49]. This value varies from that obtained for the lectin-galactosamine interaction measured by Osada, but is of a similar magnitude, so was useful for identifying this type of lectin-binding event within the data for the

Leishmania part of the work.

1.2 *Streptococcus pneumoniae*

Streptococcus pneumoniae, otherwise known as the pneumococcus, is a Gram-positive, α -haemolytic bacterium (i.e. it oxidizes iron in haemoglobin, leading to a greenish colour surrounding bacteria colonies on a blood agar plate) which is pathogenic to humans. It is the leading cause of community-acquired bacterial pneumonia worldwide (with an estimated 14.5 million incidences of severe disease per annum [50]), otitis media (an infection of the middle ear), and the more invasive meningitis and sepsis, particularly in people vulnerable to infection; children, the elderly, immunocompromised individuals and those with medical comorbidity such as chronic heart or lung disease [50, 51] and it continues to cause high mortality and morbidity [52]. Pneumococcal infection is also a frequent complication for patients with visceral leishmaniasis [53, 54]. *S. pneumoniae* is a normal component of the bacterial flora intermittently present on the respiratory epithelium in the nasopharynx, which is part of the upper airway. This asymptomatic colonization can be a precursor to more invasive infections [55, 56]. Colonization can occur at any point in life, but is very common in infancy, with up to 50-70% of 2-3 year olds typically carrying the bacteria for an average period of 60.5 days, depending on the serotype [56]. In the Western world however, this percentage is likely to be reduced to 20-40% of children in day care facilities. Carriage rates are also typically higher in developing countries, where high percentages of adults continue to be colonized by pneumococci, whilst this typically reduces to 20% in developed countries (this percentage is given as a guide as actual percentages vary between countries) [52, 56].

1.2.1 Virulence factors, the complement system and opsonization

The complement system is part of the innate and acquired immune system. It improves the ability of antibodies and immune cells to clear pathogens from the body and consists of more than thirty proteins which are found in blood plasma (at a concentration of $> 3 \text{ g l}^{-1}$) and on cell surfaces [57]. A number of these proteins,

including complement component 3 (C3), are proteases which are activated by proteolytic cleavage (i.e. they become active when broken into smaller peptides). They are activated locally at sites of infection and instigate an inflammatory response via a triggered enzyme cascade [58].

There are three pathways within the complement system; the classical pathway, the mannose-binding lectin pathway and the alternative pathway. The three different routes are triggered by a different initial molecule, but converge to the same molecules further down the enzyme cascade. All pathways produce a C3 convertase, which cleaves the C3 component into C3a and C3b [58]. C3b is deposited covalently on the cell surface and then undergoes one of two processes depending on the carbohydrate environment of the surface. If bound to a bacterium, C3b is likely to bind with factor B, another complement protein, subsequently producing a C3 convertase enzyme which induces more C3 cleavage and therefore C3b deposition. If bound to a host cell with polyanionic surface moieties, C3b is more likely to bind with factor H, the dominant complement-control protein, which prevents inflammation (excessive recruitment of neutrophils and other granulocytes) through overactivation of the complement system [57]. In this case, C3b is further processed to iC3b, which cannot form a C3 convertase enzyme [57]. Deposition of C3b on the bacterium is an example of binding of activated complement proteins to pathogens, and is known as opsonization. Both C3b and iC3b mediate phagocytosis (engulfment of the bacteria by the host cell) through binding to complement receptors CR1 and CR3, respectively, on leukocytes [59], and are considered the most important opsonins in defence against bacterial infection [57].

The small, cleaved parts of some complement proteins recruit and activate additional phagocytes by chemotaxis (e.g. C5a) and, in addition to phagocytosis, the complement system can achieve bacterial clearance via the membrane attack complex (formed by complement proteins C5b - C9). This complex forms transmembrane channels in the bacterial surface and therefore mediates bacterial lysis, but the rigid cell wall of the pneumococcus generally protects it from this form of clearance [58].

Pneumococci have several virulence factors, including pneumococcal surface protein A (PspA), major autolysin (LytA), choline-binding protein A (CbpA), pneumolysin (Ply) and the polysaccharide capsule [60]. Several of these virulence factors (PspA, LytA, CbpA) bind noncovalently to the phosphorylcholine moiety in the pneumococcal cell wall (see Figures 1.4 & 1.5 on page 19) using a conserved choline-binding domain, and are therefore referred to as choline-binding proteins (CBPs) [61]. CbpA is the largest and most abundant of this protein family, and is thought to have a role in colonization of the nasopharynx as a pneumococcal adhesin [62]. The expression rates of the different CBPs varies depending on the location of cells obtained from murine models, with the relative expression of PspA being upregulated in bacteria from the blood stream compared to those found on mucosal surfaces [61].

PspA consists of five domains: at the N-terminus there is a signal peptide, followed by a highly charged antiparallel α -helix, a proline-rich domain, then the choline-binding domain which anchors the molecule in the cell wall, and finally a C-terminal with a tail comprised of seventeen amino acids [63]. The outermost portion of the molecule, which protrudes above the capsular polysaccharide, is highly electronegative (see Figure 1.5 on page 19) and the molecule has a positively charged region towards the C-terminus, rendering it polar [60, 64]. PspA inhibits the classical pathway by hindering C3 activation and reducing C3b binding [65]. PspA-deficient strains have been shown to be more easily phagocytosed by macrophages and neutrophils as an increased amount of C3b is able to bind to the pneumococcal surface [66], and PspA appears to be highly important in pneumococcal meningitis, since increased mouse survival has been observed for infections with PspA-deficient bacteria. [67]

PspA might also help the bacterium evade the host defence molecule C-reactive protein (CRP). CRP is a component of human and mouse serum which binds to pneumococcal cell wall phosphocholine and can initiate the complement cascade via the classical pathway [63]. It is predicted that PspA competes with CRP for suitable binding sites: when already bound to PspA, the phosphocholine is not available for

CRP to bind to, and so the CRP fails to activate the complement cascade, adding to the importance of PspA for pneumococcal virulence. Mutants lacking PspA have been shown to exhibit reduced virulence and higher C3b deposition compared to wild type strains [63] and mice with mutated CRP that is incapable of binding to phosphocholine were incapable of recovering from a severe pneumococcal infection, and generally had a lower survival rate than those with a similar infection but wild type CRP [68]. This illustrates the relationship between decreased rates of CRP-phosphocholine binding and failure of the host immune response to deal effectively with pneumococcal infection, and the importance of PspA in this process.

The N-terminal portion of pneumococcal surface protein C (PspC), another CBP, is believed to have a role in adherence to nasopharyngeal and lung epithelial cells and binds human complement factor H (fH), locally inhibiting components of the alternative and lectin pathways. It has also been shown to have a role in blocking C3b binding [69–71]. However, in the case of experimental murine pneumococcal meningitis, it did not appear to be crucial to successful disease progression, with PspC-deficient mutants not showing significant deviation from their wild type counterparts [67].

Pneumolysin (Ply) is secreted by the bacterium and is a pore-forming thiol-activated cytotoxin that can cause lysis of a variety of cell types [72–74] and inhibit complement activation by inducing C3 conversion externally to the bacteria; inhibiting serum opsonic activity and reducing pneumococcal clearance [75, 76]. In addition to this, it can activate immune responses through pattern recognition receptors such as the Nod-like receptor (NLR) family pyrin protein, domain containing 3 (NLRP3) inflammasome [77] and Toll-like receptor 4, which initiates intracellular signalling cascades and can induce apoptosis of infected macrophages (a host response to infection) [78–80]. Pneumolysin has also been shown to inhibit ciliary beating, enabling bacteria to adhere to the epithelium and avoid elimination along with mucus [81].

1.2.2 Pneumococcal cell structure

Streptococcus pneumoniae, as other Gram positive bacteria, comprises a cell wall with a plasma, or cell membrane innermost (approximately 75 nm thick [82]), then a periplasmic space surrounded by a fairly thick peptidoglycan layer (approximately 160 nm thick [82]). This peptidoglycan layer is augmented by various molecules including teichoic acid and lipoteichoic acid, whose structures can be found in references [83] and [84], respectively. A polysaccharide capsule surrounds the wild type bacteria and is generally believed to be covalently bound to the outer surface of the cell wall [85]. This general structure is shown in Figure 1.4 on page 19.

Although the capsule is the first part of the bacteria to come into contact with an external stimulus, molecules within and anchored to the cell wall can also contribute to interactions once contact is established [82]. The following two subsections will highlight molecules of interest both in the capsule and within the cell wall itself.

The cell wall

The pneumococcal cell wall induces high levels of inflammation in the host [87] and is primarily constructed of peptidoglycan layers and teichoic acid (See Figures 1.3 and 1.4 on pages 11 and 19, respectively). Peptidoglycan is a polymer comprising ‘glycan strands’; alternating β -(1,4) linked *N*-acetyl-D-glucosamine and *N*-acetylmuramic acid [85], the latter of which is joined to a chain of four amino acids: L-alanine – D-isoglutamine – L-lysine – D-alanine [85]. The peptide chains of neighbouring polymers are crosslinked, leading to a strong 3D lattice and therefore providing rigidity and mechanical strength to the bacterium.

The predominant component of teichoic acid is C-polysaccharide [83], which is covalently bound to the peptidoglycan layer on its inner and outer surface (see Figure 1.4), and therefore could be probed by the AFM if large applied forces are used, or when working with unencapsulated mutants [88]. C-polysaccharide contains glucose, 2-acetamido-2,4,6-trideoxygalactose, galactosamine, ribitol phosphate, and phosphorylcholine [88]. The presence of phosphorylcholine is unusual amongst bac-

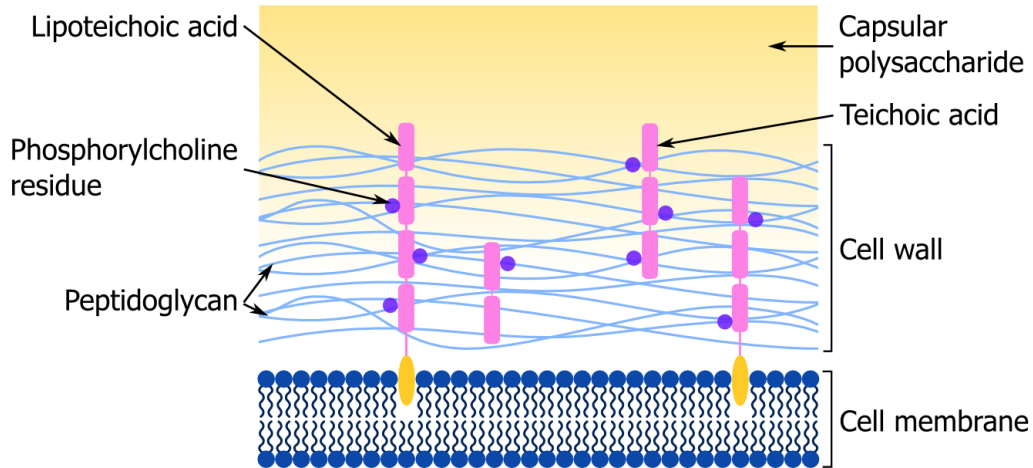


Figure 1.4: Simplified schematic illustration of some of the key structural cell wall components of *Streptococcus pneumoniae*. The peptidoglycan cell wall gives rigidity to the bacterium and anchors the capsule in place. The peptidoglycan is crosslinked and connected to the plasma membrane by teichoic acid (TA) and lipoteichoic acid (LTA), respectively. The peptidoglycan is attached to phosphorylcholine residues which are covalently bound to the TA and LTA. TA and LTA are chemically identical for the main part, but the LTA is terminated with a hydrophobic glycolipid anchor, which mediates binding to the plasma membrane [86].

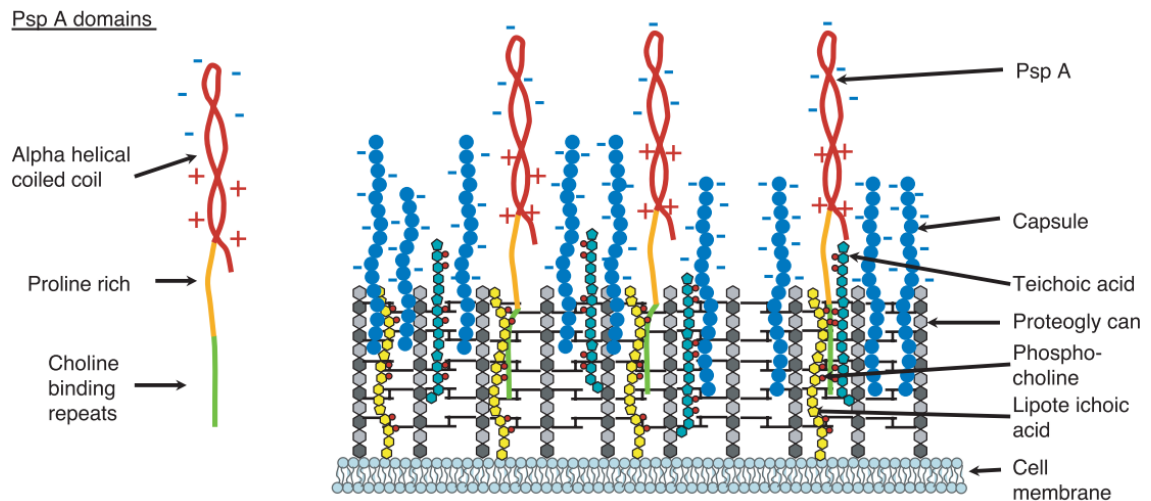


Figure 1.5: A cartoon of the proposed arrangement of different biomolecules on the surface of *Streptococcus pneumoniae*. From [64] with permission.

teria; in *S. pneumoniae*, it is believed to provide a site involved in attachment of bacteria to activated endothelial cells in cases of invasive disease [88]. Additionally, this phosphorylcholine is a partner for non-covalent bonding of CBPs such as PspA, which is attached to the phosphocholine moieties on lipoteichoic acids along its C-terminal portion [64, 68]. This arrangement is illustrated in Figure 1.5 on page 19.

Phosphocholine is involved in binding in the nasopharynx, where it induces cytokine stimulation, leading to upregulation of platelet-activating-factor receptors (PAFr) on the host epithelial cells, which have high binding affinity to bacterial cell wall phosphocholine, and so interactions including phosphocholine are interesting in terms of the colonization of an individual and establishment of infection [55]. Antibody binding assays have suggested that phosphocholine is still partially exposed even on capsulated bacteria, so it is likely that it will come into contact with the AFM tip during force mapping [64].

The capsule

The pneumococcus has a polysaccharide capsule which is made up of repeating oligosaccharide units (see Fig 1.6 on page 21) [88]. Although not toxic in itself, the capsule is commonly considered the bacterium's most important virulence factor [85], since it protects bacteria from uptake by phagocytic cells (the methods used by the immune system to detect pneumococci are summarized in [89]); preventing both complement-mediated opsonophagocytosis by reducing binding of C3b [59, 90, 91] and nonopsonic phagocytosis [92]. A study by Ricci *et al.* found that unencapsulated bacteria were incapable of causing brain inflammation, neuronal damage and death in a murine model of meningitis [67].

Differences in this capsule constitute the basis for more than 90 antigenically distinct serotypes [52, 88] and the exact chemical structure is now known for most of these. Serotypes 1, 2, 3 and 5 have been shown to be more immunogenic than some other strains [88]. The serotype used in this study is serotype 2, strain D39, whose capsular polysaccharide constituents are described in [93, 94], and its unencapsulated

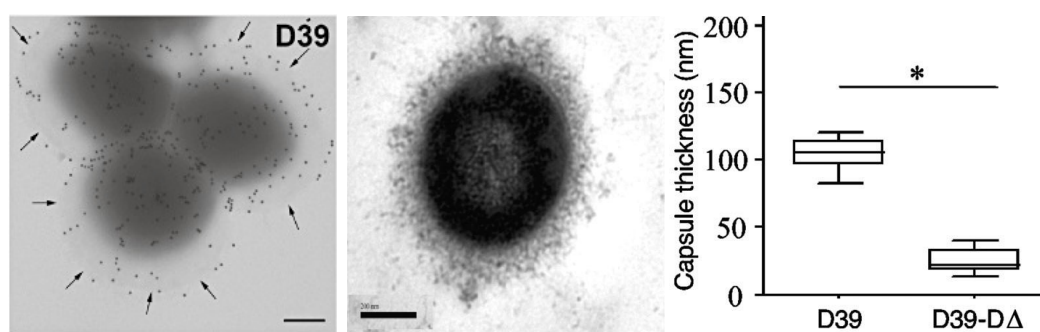


Figure 1.6: Left: capsule visualisation through electron microscopy of *S. pneumoniae* strain D39. Arrows point to the outer edge of the capsule (black dots are gold particles adhered to pneumococcal adherence and virulence factor B) [97]. Middle: TEM image of D39 *S. pneumoniae* and right: corresponding medians and interquartile ranges of capsule thickness as measured for D39 and an unencapsulated derivative. $P < 0.001$ [59]. Scale bars represent 200 nm. Both figures used with permission.

derivative, FP22 [95], from the same source as used in [96].

Because the serotypes of *Streptococcus pneumoniae* are determined due to capsular properties, thickness and composition is not consistent across the species, and increased capsule thickness has been associated with better protection against phagocytosis and clearance by the immune system [92]. This protection is believed to be due to better protection against deposition and function of complement pathway opsonins, targeted at cell surface antigens [90]. The capsule can also help the bacteria to evade neutrophil extracellular traps, which comprise an extracellular matrix of DNA and histones containing anti-pneumococcal serine proteases that contribute to the host's antimicrobial defences against pneumococci [98]. The capsule of strain D39 has been shown to be approximately 100 nm thick [59] (although other work suggests that it is closer to 200 nm thick [97]; see Figure 1.6), and this has implications for the choice of trigger force used, since to get a scientifically valid comparison between the capsulated and unencapsulated types, the indentation by the tip must not be greater than the depth of the capsule. Capsule depth will vary with the ionic strength of the medium: ion concentration affects the steric and electrostatic interactions of the capsule with itself and results in differing thicknesses and adhesion properties [14]. It is therefore important that the imaging medium is kept consistent across the different experiments to prevent ionic strength being a factor in the variability of measured tip-sample interactions.

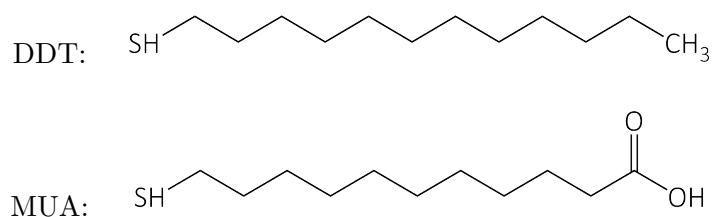


Figure 1.7: Chemical structures of 1-dodecane thiol and 11-mercaptoundecanoic acid.

1.2.3 The impact of pneumococcal surface charge on interactions with different self-assembled monolayers

In this work, hydrophobic forces were mapped across the surface of non-opsonized capsulated and unencapsulated type 2 *Streptococcus pneumoniae*. The surface hydrophobicity of various other cells including yeasts [99, 100], mycobacteria [100, 101] and other bacteria [102–104] has been investigated in other work, generally using a combination of hydrophobic (CH_3 -terminated alkanethiol) or hydrophilic (COOH - or OH -terminated alkanethiol) self-assembled monolayer (SAM)-coated tips. SAMs make fairly stable tip coatings, with a thickness of approximately 5 nm, because the sulfur atoms chemisorb to the gold surface and the monolayer is stabilized by lateral hydrophobic interactions between the alkyl chains [102].

The carbon atom in the CH_3 (methyl) group on the 1-dodecane thiol (DDT) used in these experiments has all of its electrons taken up in bonds (see Figure 1.7), so will remain neutral. DDT is hydrophobic so the interactions with the surface will purely be a gauge of the hydrophobicity of the bacteria and will be unaffected by electrostatic interactions. In contrast, in PBS at pH 7.4, it is likely that the hydrogen of the carboxyl group (COOH) will have dissociated and there will be COO^- groups terminating the 11-mercaptoundecanoic acid (MUA). These negatively charged groups on the MUA will experience electrostatic forces when approaching a charged surface. However, as the PBS contains monopotassium phosphate, disodium phosphate and sodium chloride, when dissociated into counterions, there will be free cations and anions in solution, and the positively charged sodium and potassium ions will diffuse towards the tip, screening some of its negative charge and therefore reducing the impact of the electrostatic component on the measured interaction force between

the cell and the tip.

The charge of the MUA coating is dependent on the pH of the media surrounding it; since the pK_a of an MUA SAM is 4.8 [105], at pHs above 4.8 some of the functional ends will undergo acid dissociation and the net charge of the SAM will increase with increasing pH. This means that in basic conditions it will have a higher proportion of charged end groups than at neutral or more acidic pHs, and below pH 4.8 it will be uncharged. Both pH and pK_a express the negative logarithm of a chemical dissociation, and are effectively ratios. pH represents the dissociation of hydrogen ions, and pK_a is the dissociation of a proton, H^+ , from an acid chemical group to form its conjugate base, A^- , such that $HA \rightleftharpoons H^+ + A^-$ (in the case of MUA, H^+ dissociates to leave COO^-). Therefore, $pK_a = -\log_{10} K_a$, where $K_a = \frac{[H^+][A^-]}{[HA]}$. A lower pK_a means that the molecule is more acidic and will undergo dissociation more readily, in solutions with a wider pH range.

Because the MUA-coated tip will exhibit some negative charge, it is important to consider the charge composition of the bacterial surface, as well as its hydrophobicity. The negative charge of different strains of pneumococci varies, but the level of surface charge can be compared between strains by measuring the zeta- (ζ)-potential, which is the potential at the shear plane (the theoretical surface between layers of compact, strongly attached counterions and diffuse ions surrounding a surface when in liquid [106]). It is a measure of the electrical potential of the interface between the bacterium and an aqueous medium and is a measure of the net charge of the surface [107], since lower ζ -potential corresponds to a higher net negative charge. The ζ -potential of D39 has been reported as -11.3 mV in pH 7.0 PBS [108], making it typical of the ζ -potentials of the capsular variants measured in pH 7.4 PBS [109], thus appearing to class it as having a moderate negative charge. Direct comparison of these two studies should only be taken as a guide since ζ -potentials of *Streptococcus mutans* and *Streptococcus intermedius* have been shown to vary in different strengths of PBS [110].

In addition to the capsule holding a negative charge, as well as measuring the ζ -potential of D39, Swialto *et al.* measured the ζ -potential of an unencapsulated D39

derivative, which was shown to have a ζ -potential of -13.3 mV in pH 7.0 PBS [108], thus having slightly higher negative charge density than its capsulated equivalent. The fact that both the cell wall and the capsule are negatively charged means that the MUA tip and will undergo electrostatic repulsion at pH 7.4, even though charge screening due to the free monovalent ions in the buffer solution might partially reduce this effect. There are no calcium or magnesium salts in the PBS, so the solution is free of divalent cations, which would dramatically reduce the electrostatic repulsion between two anionic surfaces through bridging forces. Although the MUA and pneumococcal surfaces will repel each other electrostatically, because an applied force is used to obtain a force curve, the two surfaces will be brought into contact and some indentation of the bacterium will occur. Therefore, interactions with local positively charged regions or polar molecules on the cell, and other attractive forces such as van der Waals interactions can contribute to the observed adhesion between the tip and the sample.

Discussion of some of the molecules contributing to the charge and hydrophobic characteristics of the pneumococcus were discussed in ‘The cell wall’ on page 18, and are further elucidated in relation to the forces observed in this work in Section 4.3.1.

1.3 *Leishmania major* and *Leishmania mexicana*

The genus *Leishmania* consists of a group of protozoan parasites that present a significant global health challenge. Many species are pathogenic to human beings, causing a variety of forms of leishmaniasis which are found across the tropical and subtropical regions of some 88 countries, with 350 million people at risk of infection [111, 112]. Leishmaniasis has been identified by the World Health Organization as one of the seventeen neglected tropical diseases, and visceral and cutaneous leishmaniasis have a combined incidence upwards of 1 million new cases per year [113, 114]. In recent years, there has been additional interest in leishmaniasis because of the increased incidence of the disease in Western military personnel as a result of the recent conflicts in the Middle East [115].



Figure 1.8: Left: A phlebotomine sand fly taking a blood meal. Reproduced from [119] with permission. Right: A patient with cutaneous leishmaniasis in Peru, from [120] with permission.

1.3.1 Leishmaniasis: disease characteristics and transmission

The leishmaniasis cause three clinical syndromes: cutaneous, mucocutaneous and visceral leishmaniasis. Cutaneous leishmaniasis is the most common form, causing localized lesions and refractory ulcers, which do not readily yield to treatment, on the skin (shown in Figure 1.8) [116]. These ulcers tend to self-heal after many months but leave depigmented, atrophic scars similar to those caused by burns, resulting in lifelong aesthetic stigma [117, 118]. Mucocutaneous leishmaniasis causes extensive destruction of mucous membranes in the pharyngeal and oral-nasal cavities (i.e. in the throat, mouth and nose) [117], resulting in extensive mutilation of the face and acute suffering for those affected. The most severe form of the disease is visceral leishmaniasis, which is a systemic infection that causes immunosuppression, irregular fever, weight loss, fatigue, anemia, hepatomegaly and splenomegaly (swelling or enlargement of liver and spleen respectively) [117, 119]. It is fatal if untreated and is the second largest parasitic killer in the world after malaria, being responsible for more than 50,000 deaths each year [119].

There has been a recent advance towards a multi-species visceral leishmaniasis vaccine [121], and whilst this has a large potential impact on disease control, it is only a single tool and is aimed at protecting against the visceral form of the disease. In order to have a significant impact on the global health burden posed by all forms of leishmaniasis, multiple tools are required, and a transmission-blocking vaccine (which reduces the incidence of a disease by interrupting the infectious

transmission cycle [115,122]) could be a key part of such a multi-faceted approach, particularly since transmission-blocking vaccines are a preferred control measure for malaria, a disease which is also caused by a protozoan parasite and spread by insect vectors [123,124], where the first such vaccines are currently in clinical trials. In this context, it should be noted that “vector” refers to the parasite host responsible for disease transmission between mammals.

Although leishmaniasis is primarily a zoonoses where the majority of vectors obtain their infection from animal reservoirs rather than humans (which are generally believed to be an accidental host [119]), in some areas, the cycle is evolving into a primarily anthroponotic cycle, for example, visceral leishmaniasis due to infection with *Leishmania donovani* transmitted by the permissive vector *Phlebotomus argen-tipes* in the Indian subcontinent. In these cases, an effective transmission-blocking vaccine could be invaluable.

Leishmaniasis is spread via the bite of female haematophagous (blood-feeding) phlebotomine sand flies [125], and a photo of such a sand fly taking a blood meal can be seen in Figure 1.8. The host becomes infected when the feeding sand fly regurgitates the parasites into the wound caused by the bite. Sand flies belong to the family *Psychodidae* in the order *Diptera* and have a body length of 2-3 mm [119]. They fly silently, unlike mosquitoes, and are mostly active between dusk and dawn [117,119]. Only the female flies bite because they require a blood meal for the production of eggs [119], and bites are typically painful since they are pool feeders, inserting their mouthparts into the skin and agitating the saw-like tips so that blood from local superficial capillaries flows into the wound and can then be taken up into the digestive system [125].

The two species of parasite considered in this project are *Leishmania major* and *Leishmania mexicana*, which are associated with causing cutaneous leishmaniasis in the Old World and New World respectively [119]. *L. major* is also suspected of association with Old World mucocutaneous leishmaniasis, but this form of the disease is rarely seen in the Old World and is therefore less well documented [117]. The parasites live as non-flagellated amastigotes in mammalian macrophages [126] and as

extracellular suprapylarian (i.e. they develop in the midgut) flagellated promastigotes in the invertebrate vector [122,127]. The parasites therefore have to cope with different temperatures and pHs amongst other varying environmental characteristics and undergo morphological changes triggered by these differing surroundings [128].

1.3.2 *Leishmania* parasite lifecycle

The transmission and lifecycle of *Leishmania* parasites is very complex, with several distinct morphological forms [129], the nomenclature and shape of which are illustrated in Figure 1.9 on page 28. Each of these forms corresponds to a different stage in the lifecycle, has a different role in the transmission process and is found at different locations within the sand fly (Figure 1.10 on page 28). In brief: upon ingestion by the sand fly, amastigotes change into flagellated procyclics which undergo replication. The next, crucial, stage in the lifecycle is the ability of the parasites to escape from the sac enclosing the blood meal (the peritrophic matrix) and anchor themselves to the microvilli of the abdominal midgut epithelium (Figure 1.11 on page 29) in order to avoid excretion along with the digested blood meal. This is achieved by transformation from the amastigote form into the procyclic form and, subsequently, the nectomonad and leptomonad forms. The parasites are then able to complete further morphological changes dictated by the environmental conditions within the sand fly, migrating into the thoracic midgut and undergoing further replication before creating a plug of promastigote secretory gel (PSG) filled with infectious metacyclic forms, which inhibits sand fly feeding. To alleviate the blockage and be able to swallow the meal, the parasite-loaded PSG plug is partially egested into the new mammalian host [125]. Since the plug is not completely removed during the feed, a sand fly is capable of infecting multiple new mammalian hosts once carrying an established *Leishmania* parasite population [130]. The predominant non-human mammalian reservoir for *Leishmania mexicana* is forest rodents, whereas the most important non-human hosts for *Leishmania major* are the great gerbil and fat sand rat [125]. These processes and the timescales at which morphological changes occur are shown in Figure 1.10 [122,125,128,131].








Morphological category	Criteria	Illustration
Amastigote	Ovoid body form, no flagellum protruding from flagellar pocket.	
Procyclic promastigote	Body length 6.5 - 11.5 μm , flagellum < body length, body width variable.	
Nectomonad promastigote	Body length $\geq 12 \mu\text{m}$, body width and flagellar length variable.	
Leptomonad promastigote	Body length 6.5 - 11.5 μm , flagellum \geq body length, body width variable.	
Haptomonad promastigote	Disc-like expansion of flagellar tip, body form and length variable. Typically found adjacent to sand fly stomodeal valve.	
Metacyclic promastigote	Body length $\leq 8 \mu\text{m}$, body width $\geq 1.0 \mu\text{m}$, flagellum > body length.	
Paramastigote	Kinetoplast adjacent to nucleus (not visible in this illustration), external flagellum present, variable dimensions.	

Figure 1.9: Different morphological forms of *L. mexicana* (these forms are common to all *Leishmania* species) from different stages of the parasite lifecycle. Procyclic, nectomonad, leptomonad and metacyclic promastigotes are of special interest and their text has been coloured to correspond with the colour code in Figure 1.10, below. Optical microscope derived illustrations are all displayed at equivalent magnification. Adapted from [129].

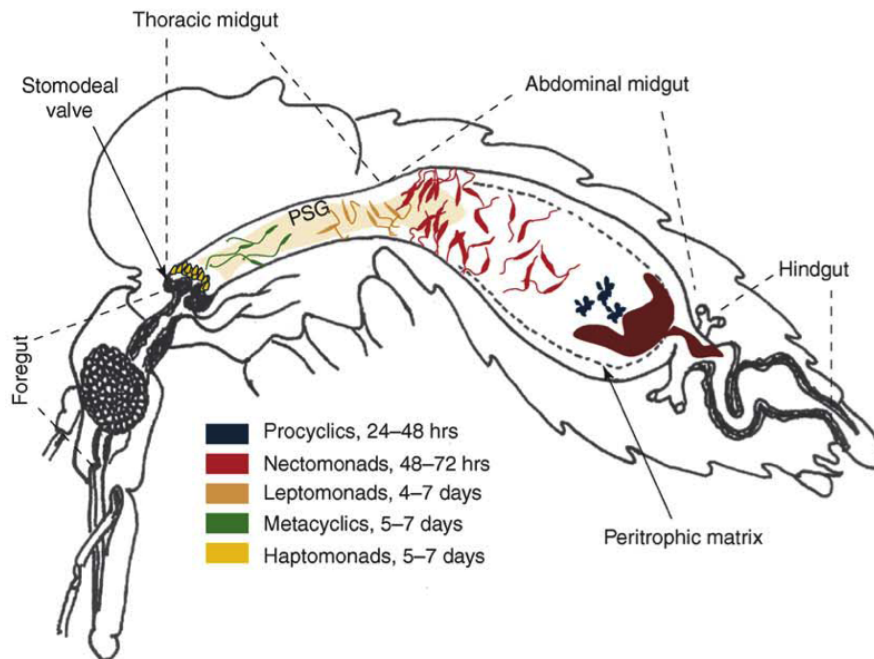


Figure 1.10: An illustration of the lifecycle of *Leishmania* in a compatible vector, demonstrating the time-dependency and position of the observed morphological forms. Reproduced from [122] with permission.

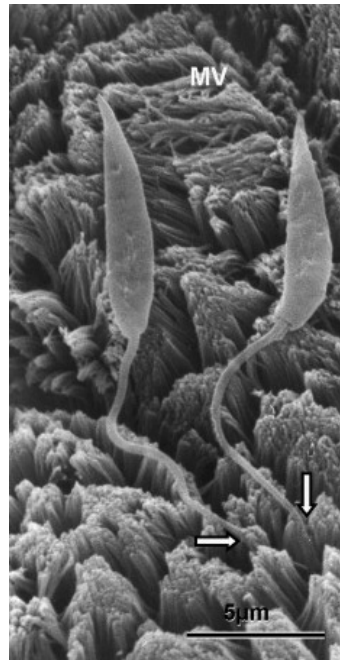


Figure 1.11: SEM image of *Leishmania* promastigotes attached to the microvillar epithelial cells that line the midgut of a female *Phlebotomus papatasi* sand fly. Reproduced from [131] with permission.

The flagellated promastigotes undergo division starting at the anterior end; for a period having two flagella and a thicker or more rounded body before the body itself also splits into two (this is not classed as a morphological category and therefore is not shown in Figure 1.9) [132].

1.3.3 *Leishmania*-sand fly binding mechanisms

The binding mechanism responsible for the persistence of the parasites following defecation has been the subject of much research, and is now generally thought to be a result of a combination of mechanisms which differ for “selective” and “permissive” vectors. Selective vectors are sand flies which have been documented as only being able to carry one species of *Leishmania* for its full developmental cycle i.e. from ingested amastigote through to infectious metacyclic promastigote. An example of a sand fly-parasite combination that exhibits this level of specificity is *Phlebotomus papatasi* and *Leishmania major* [133]. In contrast to this selectivity, permissive vectors are able to support the growth of a range of *Leishmania* parasites and include most of the known vector species, including *Lutzomyia longipalpis* [128].

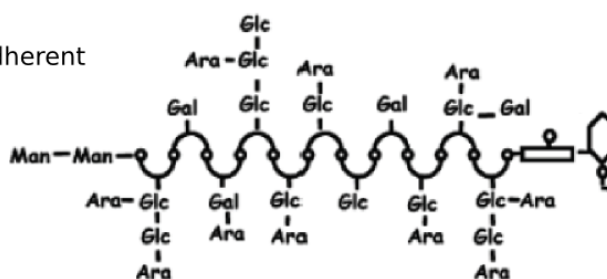
The principal mechanism of adhesion in selective vectors is believed to be due to an interaction between the dominant promastigote surface glycolipid, lipophosphoglycan (LPG), and a sand fly galectin (a beta-galactoside binding lectin) present on the surface of midgut epithelial cells [134]. This proves an elegant attachment mechanism since differences in the length of LPG and modifications in sidechain sugar residues between distinct morphological forms (see *L. major* procyclic and metacyclic LPG in Figure 1.12 on page 31) allow the specific interaction governing adhesion to be switched on and off accordingly, depending on the requirements for that phase in parasite development e.g. procyclics, nectomonads and leptomonads must be able to adhere to the gut in order to persist after defecation, but metacyclics must be detached ready for regurgitation into the next sand fly bite [134, 135]. The lipid synthesis route and uptake pathways used by the parasites to execute such closely controlled chemical changes in their glycosylphosphatidylinositol (GPI)-anchored LPG is explored elsewhere [136].

There is structural heterogeneity in the form of receptors found in different sand fly species midguts, and this is mirrored by the complexity and variety in LPG structure of different *Leishmania* parasite species [122]. Parasites which are transmitted via permissive vectors, e.g. *L. donovani* [137], tend to have a simpler, shorter form of LPG (the full chemical structure of *L. donovani* LPG can be found in reference [138]), whilst parasites which rely on specific vectors, e.g. *L. tropica*/*L. major* [137], tend to have much more complex LPG structures, suggesting evolution driven by the need to survive in invertebrate hosts [122, 137]. This is illustrated in Figure 1.12 on page 31.

One key development in understanding the role of LPG in the transmission of *Leishmania major* via the selective vector *Phlebotomus papatasi* was the identification by Kamhawi *et al.* of a sand fly galectin capable of binding to nectomonad LPG on *L. major* [127]. They found that midgut attachment was mediated by an interaction between the sand fly midgut receptor PpGalec and parasite LPG bearing single galactosyl side-chain residues on the phosphoglycan repeat units. Other research has confirmed that *L. major* promastigotes lacking in the galactosyl side-chain

Leishmania tropica

Uses a selective vector: adherent



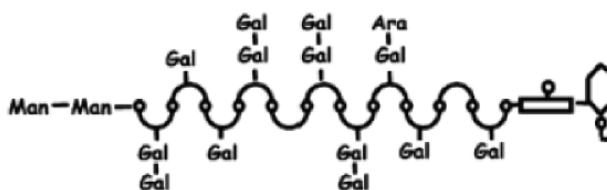
Leishmania donovani

Uses a permissive vector: adherent



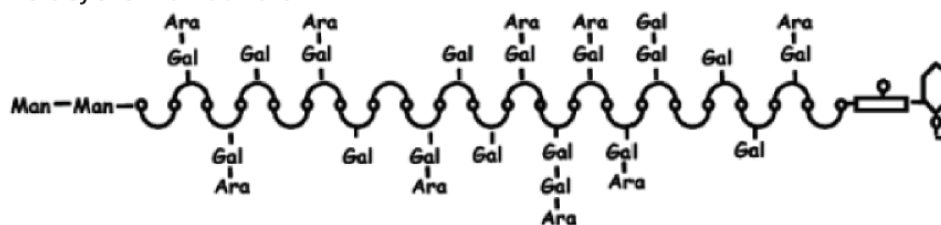
Leishmania major

Procyclic: adherent



Leishmania major

Metacyclic: non-adherent



Leishmania mexicana

Procyclic: adherent

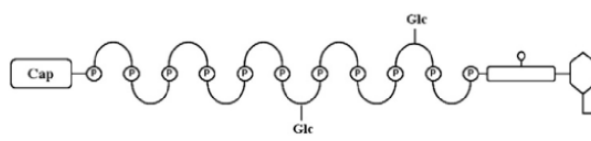


Figure 1.12: Polymorphic structures of LPG molecules from different species/morphological stages of *Leishmania* parasites. “Gal”, “Glc”, “Man” and “Ara” represent galactosyl, glucosyl, mannosyl and arabinosyl side-chain modifications respectively. The cap on *L. mexicana* LPG contains 2 mannose residues and one galactose residue. Modified from [127] and [139] with permission.

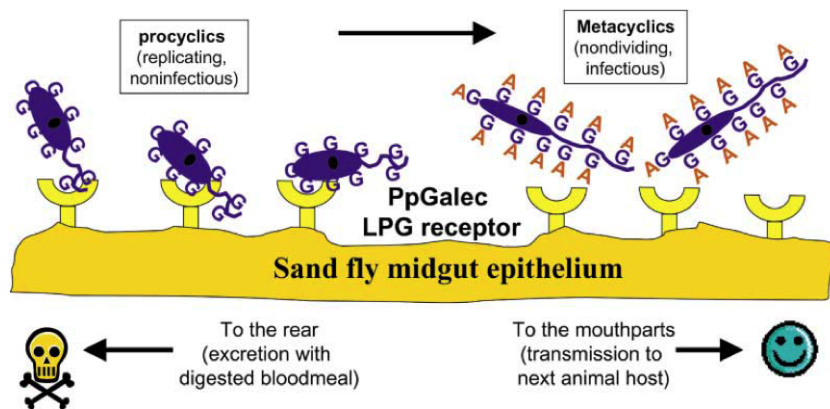


Figure 1.13: Schematic diagram representing the reversible attachment between *Leishmania* promastigotes and the PpGalec receptor in the sand fly midgut (yellow structures). “G” represents galactosyl residues and “A” represents arabinosyl residues (equivalent to “Gal” and “Ara” in Figure 1.12). Modified from [115] with permission.

modifications failed to attach to *P. papatasi* midguts [137,140], and the dissociation of the metacyclic form of the *L. major* parasite from the insect galectin is attributed to LPG modifications which occur during metacyclogenesis (the process of changing into metacyclic form); namely an increase in length of the phosphoglycan backbone and capping of the exposed galactose residues with arabinose [115,135]. This modification and a schematic representation of the change are illustrated in Figures 1.12 and 1.13, respectively (page 32).

It is now, however, becoming apparent that LPG-mediated attachment is not sufficient to dictate species-specific binding; Dobson *et al.* [133] reported that *L. donovani* whose LPG had been engineered to resemble that of the procyclic form of LPG in *L. major* failed to persist in *P. papatasi* following excretion of the blood meal, despite the LPG coat being identical to that of *L. major*. This suggests that, whilst necessary, LPG-PpGalec interactions are not the exclusive cause of specificity, but that additional ligand-based interactions either involving LPG or an alternative surface-expressed molecule are also required. Whichever type of molecule is involved, it must differ between the *L. major* and *L. donovani* species in order to explain these observations.

In permissive vectors, the attachment is believed to be mediated by molecules excluding LPG but as of yet is not clearly understood [128,130,141]. Recent studies have related the attachment of the parasites in different permissive sand fly species

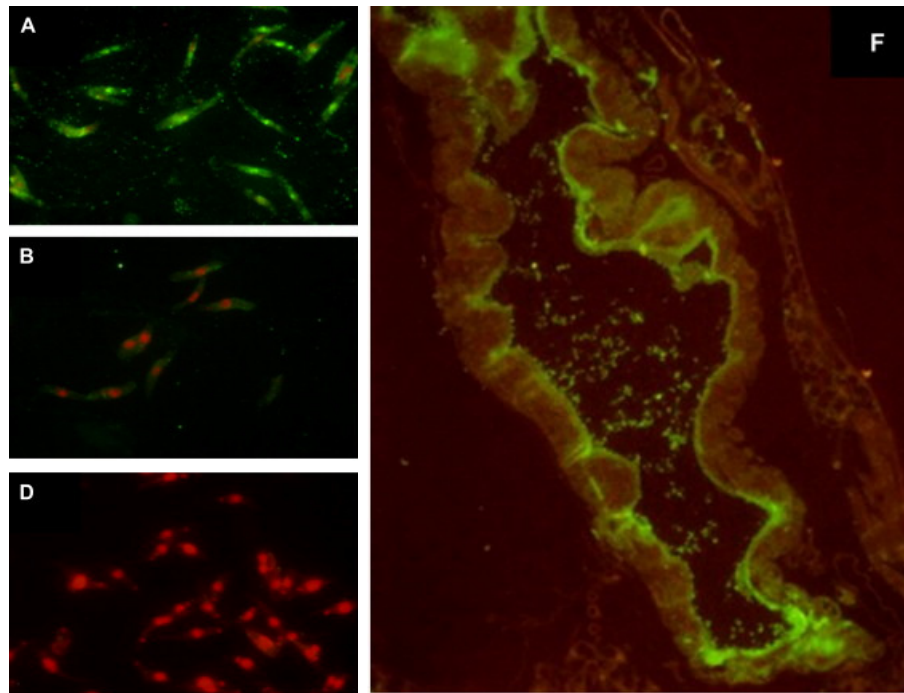


Figure 1.14: (A) GalNAc-containing glycoproteins from midgut lysate of permissive species *P. halepensis* binding to *L. major* visualized by fluorescein-labelled lectin HPA. (B) Preincubation of *L. major* with GalNAc before being incubated with midgut lysate followed by FITC-HPA as in (A) shows a large reduction in fluorescence. (D) Control without midgut lysate. (F) Section of *Lutzomyia longipalpis* midgut, positive reaction of FITC-HPA binding to GalNAc-containing glycoproteins. Figure extracts reproduced with permission [142].

to glycoproteins present on the microvillar border of the midgut surface [53]. These could act as a binding site for lectin-like molecules on the surface of the parasite, in a reversal of the observed galectin-LPG relationship in *L. major*-*P. papatasi* binding [128]. Myskova *et al.* [142] found that *L. major* deficient in LPG was able to undergo a full lifecycle with a high parasite output in two permissive vector species. This was attributed to *N*-acetyl-galactosamine (GalNAc)-containing glycoproteins in sand fly midguts binding to exposed lectin-like receptors or heparin-binding proteins on the surface of *Leishmania* parasites.

GalNAc was shown to be present in the midguts of permissive vectors, but not in specific vectors, using *Helix pomatia* lectin (HPA) blotting [142]. HPA did not bind to the parasites themselves, suggesting that the GalNAc is present solely on the sand-fly epithelium, and separate fluorescent images showed that binding of midgut lysate from permissive vectors to *Leishmania major* is blocked by preincubation with free GalNAc, as shown in Figure 1.14 on page 33. Although there

have been further studies which confirm the presence of an LPG-independent binding mechanism [143,144], the role of GalNAc has not been elucidated further.

1.4 Glycopolymers

In a broad sense, the term “glycopolymer” is appropriate for both synthetic and biological carbohydrate-containing polymers [145], but here the term will be used solely in reference to synthetic polymers with pendant sugar moieties. Glycopolymers are inherently useful because, as analogues of naturally occurring polysaccharides, they can be employed to model biological interactions *in vitro* [146,147]. In addition to this, natural oligosaccharides and polysaccharides are often difficult to extract, making artificially synthesized alternatives that exhibit similar functionality a cost-effective alternative [148]. These factors have led to an extensive library of different glycopolymers and a wide range of fabrication techniques, which have been extensively reviewed [145,146,149,150].

It is predicted that glycopolymers could be used in a variety of medical applications, including targeted drug-delivery systems. For example, liver hepatocytes conjugate strongly to galactose and so could be targeted by galactose-rich micelles containing a drug payload [151]. Alternatively, in certain cases, glycopolymers without a separate drug payload could be used to control disease spread, as in the case of influenza. To establish an infection, the influenza virus first binds to *N*-acetylneuraminic acid residues expressed on bronchial epithelial cells via haemagglutinin on its surface [152]. This lectin has a shallow binding site and so monovalent binding is typically weak, and can be enhanced by multivalent interactions [153], such as would be expected with a suitable glycopolymer. Binding of the glycopolymer to the virus in this way would inhibit its capability to bind to, and therefore invade and replicate inside the host cell, and could prove an effective prophylactic (disease preventing) drug during influenza epidemics [147].

Glycopolymers offer huge variety and flexibility in terms of molecular weight, spacing between the sugar moieties and the polymer backbone (“arm length”), and the choice of sugar. There are two main functionalization routes: by polymeriza-

tion of sugar-containing monomers, or through a post-polymerization glycosylation reaction [151]. Glycomonomers can be used with a wide range of controlled living polymerization techniques, including nitroxide-mediated polymerization (NMP), atom transfer radical polymerization (ATRP) and reversible addition-fragmentation chain-transfer polymerization (RAFT) amongst others [151]. Discussion of these techniques can be found in review articles [145, 146]. Each synthesis route has advantages and disadvantages: the use of functional monomers is the most efficient method in terms of sugar-adding efficiency, but post-polymerization functionalization can generate a large batch of scaffold polymers which can be modified with different sugars or can have varied sugar “density” whilst maintaining identical macromolecular features; a characteristic which is useful for comparative binding studies [148]. For this reason, post-polymerization functionalization was used to prepare the glycopolymers used in this work.

Post-polymerization functionalization has been improved by the use of “click chemistry” reactions [154], which allow sugar moieties to be added to the scaffold polymer in aqueous conditions and at room temperature, in a way that does not require much (if any) purification and has good functional group tolerance [146]. Click chemistry can be used for glycomonomer and glycopolymer synthesis, and sugars containing azide, alkyne and thiol groups have all been shown to result in successful glycopolymers made via click reactions [149]. In particular, the copper catalysed azide-alkyne cycloaddition (CuAAC) reaction has been shown to be a versatile synthesis route, although removal of the copper catalyst is important to eliminate toxicity for biological applications [149, 151]. Thiol-mediated reactions show high reactivity with many compounds and therefore have potential for development of the next generation of glycopolymers [149].

Perhaps the most important function of glycopolymers is their interaction with lectins, which makes them suitable candidates for use in novel biosensors [155]. A key advantage of glycopolymers compared to single sugar molecules is that they take advantage of the “glycoside cluster effect” [156], whereby the combined interaction of multivalent carbohydrates with polyvalent protein receptors [150] leads to

an association constant which is orders of magnitude greater than that of an individual (monovalent) sugar - lectin bond [157]. The mechanism of the effect is thought to be aggregation, whereby multivalent ligands crosslink and bind to multivalent lectins [158]. In biological systems, carbohydrate-binding proteins are typically arranged in complex structures, and linear glycopolymers with multiple sugar moieties available for binding along the length of the polymer chain have demonstrated higher affinity and bond strength compared to individual saccharides, increasing the overall strength of binding to a biologically-relevant binding level [48, 145]. Pendant group functionalized polymers therefore seem to have a more appropriate architecture than end-group functionalized polymers, with respect to bioconjugation applications [159].

Glycopolymer morphology is important for the study of lectin-carbohydrate interactions due to the nature of the lectin binding domains and their accessibility to the sugar moieties. Spacing of the saccharides along the polymer backbone is significant: if the moieties are too far apart, one binding event does not make a second binding event more likely, but too close together and steric hindrance will limit the binding efficiency, especially when bulky or charged groups are used [147, 153]. In addition to this, polymer flexibility and the distance between the sugar moiety and the backbone also affects lectin-binding success: if the polymer is too stiff, or the saccharides too close to the backbone, the accessibility of the recognition domains can be reduced due to inability to adapt to lectin geometry, inhibiting binding [48]. This has been demonstrated by several groups who found that the addition of a spacer molecule between the sugar moieties and the polymer backbone enhanced binding efficiency [48, 160].

Successful binding of glycopolymers to animal-derived lectins has been observed in many studies [47, 148, 151, 160] (a more extensive list can be found elsewhere [48]), but most of the binding events have been confirmed using techniques such as surface plasmon resonance [161], enzyme-linked immunosorbent assays (ELISA) [148] and turbidimetric assays [162].

One key example of the use of AFM to characterize this binding is the work of

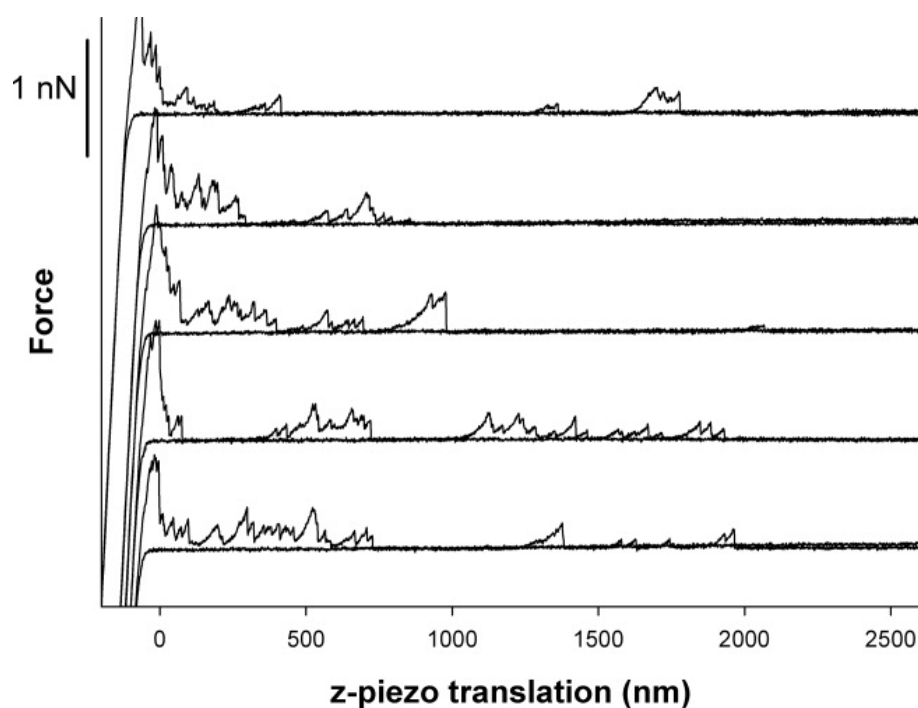


Figure 1.15: Examples of force– z -piezo retraction curves (equivalent to force-distance curves) between porcine submaxillary mucin-functionalized AFM tips and soybean agglutinin immobilized on mica. The observed unbinding forces are characteristic of individual lectin-galactose binding events occurring at increasing tip-sample distances as the mucin is extended and different bound galactose moieties along the length of the mucin experience force up to a point of rupture. The force-distance curves were obtained at room temperature in aqueous 100 mM Hepes buffer at pH 7.2. Reproduced with permission [163].

Sletmoen *et al.* [163], where porcine submaxillary mucin containing GalNAc residues was attached to an AFM tip and introduced to galactose-binding lectins immobilized on a surface. Rupture forces of approximately 250 – 300 pN were observed for a similar loading rate to that used in this PhD (albeit in a different buffer; Hepes instead of PBS). A selection of force curves obtained as part of their study is shown in Figure 1.15. Although these experiments were carried out in more controlled conditions than on a cell surface (i.e. using only the molecules of interest), they give a useful guide to the scale of the forces which can be expected for the magnitude of interactions associated with galactose-lectin interactions. Because of this, the same sugar-specific ligands as used by Sletmoen *et al.* [163]; soybean agglutinin (SBA) for galactose and concanavalin A (conA) for glucose; were used for control experiments to confirm the measurability and specificity of binding between AFM tips functionalized with synthetic galactose, glucose and mannose glycopolymers and different galectin-functionalized surfaces.

1.5 Summary of project objectives

In this work, AFM force spectroscopy (FS) is applied to two new, taxonomically diverse, pathogenic organisms, adding to the range of different cells which have previously been subjected to this method of analysis. This experimental technique offers a way to probe binding interactions on live cells, in a buffered aqueous solution, without the additional complications of working *in vivo* or in complex culture-based models. This enables the adhesive forces between the pathogen and an AFM tip coating of choice to be measured and compared, building up a picture of the binding properties of the cells and the impact that different cellular characteristics have on this adhesion, e.g. the presence or absence of polysaccharides on the outer cell surface. The technique also allows the location and patterning of adhesive areas to be illustrated, which can be used to determine whether the cells have an adhesive polarity.

In order to probe non-specific cell-surface interactions, well established hydrophobic/hydrophilic SAM-coating methods are used to create the FS probes, and

for the specific binding experiments, novel glycopolymer-coated FS probes are fabricated. Development of these probes requires refinement of polymer brush growth methodology, development and characterization of two types of glycopolymer brush (described in Chapter 3), and use of an AFM lectin-binding assay to test the specificity of the glycopolymer-coated AFM tips (described in Chapter 5). These developments are necessary in order to investigate the adhesive properties of the two organisms, giving a unique insight into the role of different molecules in the attachment of the microorganisms to different surfaces and providing information useful for prevention of colonization or transmission.

Both of the organisms used in this work have a widely varied outer layer (the polysaccharide capsule of the pneumococcus and the LPG coat of the *Leishmania* parasite) which has caused limitations in treatment and prevention schemes, which are usually limited to a few species at best [116]. By working in partnership with researchers investigating pathogen - host cell attachment using more traditional methods (such as *in vivo* or fluorescence-based assays), it is possible to confirm or reject molecules that have been proposed to be involved in adhesive interactions. Probe molecules with positive adhesion characteristics can then be ranked based on quantitative information obtained using the AFM, and compared for different probes or sample types. AFM also has the additional benefit of allowing the user to determine whether there is any adhesive polarity on a cell, by assessing the distribution of adhesive elements. This evaluation of a given range of possible target molecules can then be translated back into the medical field, increasing the efficiency of research into possible drug targets. The specific adhesive qualities evaluated in this work for each of the two microorganisms are discussed below.

Streptococcus pneumoniae

In Chapter 4 it is shown that the specific use of hydrophobic and hydrophilic AFM tips enables the non-specific interactions involved in *S. pneumoniae* adhesion to be characterised and compared between capsulated and unencapsulated bacteria. The use of mechanical trapping means that the bacterial surface is not affected by harsh

chemical treatments, and therefore the measured interactions are a suitable representation of the bacterial surface which binds to mucosal cells in the nasopharynx. Hydrophobic and hydrophilic AFM tips are characterized on similarly-coated gold surfaces (see Chapter 3), then applied to both capsulated and unencapsulated type 2 pneumococci to determine whether there is any difference in the adhesive properties of the wild type and unencapsulated mutant.

To evaluate differences between the two strains used in this work, the force map adhesion data are analysed using finite mixture model analysis and Gaussian models of the \log_{10} force data. This reveals that the pneumococcal capsule is effective at blocking access to positively charged and hydrophobic moieties of pneumococcal surface proteins and other adhesins via electrostatic repulsion and steric hindrance, with fewer force-distance curves containing binding events on capsulated bacteria than on unencapsulated bacteria. The positive binding interactions are also shown to be weak for both the hydrophobic and hydrophilic tips, highlighting that specific binding interactions are important in host colonization, and predicting a role for multiple, weak hydrophobic bonding in initiation or stabilization of interactions with mammalian cells. The interaction is not found to be orientational, with no clear pattern of high force areas found on either capsulated or unencapsulated bacteria.

***Leishmania* parasites**

In Chapter 5 it is shown that the newly-developed galactose and glucose glycopolymer-coated AFM tips are capable of detecting specific binding events with rupture forces similar to those in the literature. These experiments also illustrate that the level of non-specific binding measured using the glycopolymer tips is very low, with adhesion to mica surfaces, and lectin- or sugar-amine-blocked experiments on lectin-coated samples, resulting in adhesion forces close to the noise threshold of the force curve data.

Parasites are immobilized by physisorption on a positively charged surface, requiring no cell processing beyond harvesting via centrifugation and dropping onto pre-coated glass slides. During AFM experiments, several parasites are observed to

have a moving flagellum, indicating that they are still alive while being mapped, and the different morphological characteristics of parasites from the different lifecycle stage-rich samples are illustrated.

The glycopolymer tips are used to map wild type sand fly midgut-adhesive and infectious, non-adhesive promastigote lifecycle forms of *Leishmania mexicana*, LPG-deficient midgut-adhesive forms and their add-back, and wild type midgut-adhesive *Leishmania major*. This enables the adhesion levels to the two sugars to be measured and compared between different lifecycle stages, and to evaluate the effect of LPG removal and more complex LPG (of *L. major* relative to *L. mexicana*) on binding to galactose. In order to quantify the adhesion, force map adhesion data are analysed using finite mixture models, and additional analysis using force curves containing binding events larger than the noise threshold of the data are used, generating mean forces above a given threshold, and also an “effective areal force”. These measures are then combined, illustrating several patterns within the parasite data. Midgut adhesive wild type *L. mexicana* parasites are shown to bind to both glycopolymers, and this adhesion is shown to be lifecycle-stage specific, with infectious forms showing significantly less interaction with the glycopolymers. The work also suggests a role for *L. mexicana* LPG in binding to galactose-containing moieties, as removal of LPG significantly reduces the adhesive interactions between the parasite and the tip. These results indicate that sugar residues expressed on the midguts of permissive sand flies could be involved in parasite-sand fly binding, and therefore could be important in terms of understanding leishmanial disease transmission.

Chapter 2

Methodology

This chapter details the various standard methods used in the project, including AFM operation, specifications and calibration (Section 2.1), growth conditions and sample preparation for the bacteria and parasites (Sections 2.7 and 2.8, respectively), and the methods used to coat AFM cantilevers with hydrophilic and hydrophobic monolayers (Section 2.5). Aspects of the methodology which required substantial development are not included here, but are instead covered in Chapter 3, where any relevant steps are discussed, alongside the key data used to refine the protocols.

2.1 AFM

In its simplest form, AFM consists of a sharp tip (generally tens of nanometres across: the resolution of topographical images is limited by the sharpness of the scanning tip) at the end of a flexible cantilever that is raster scanned across a sample surface in the x - y plane by a three dimensional piezoelectric scanner system (piezoelectric materials are able to respond mechanically to an applied voltage, changing their size in either one or a number of dimensions) whilst the interaction force between the tip and the sample is monitored, allowing an image of the sample to be built up line by line (see Figure 2.1 on page 43). Typically, the x -direction is referred to as the ‘fast scan’ axis, since this is the direction the tip moves along whilst in contact with the surface (assuming the scan is set to 0° or 180°), and the y -direction is known as the slow scan axis [164]. The response of the cantilever to surface

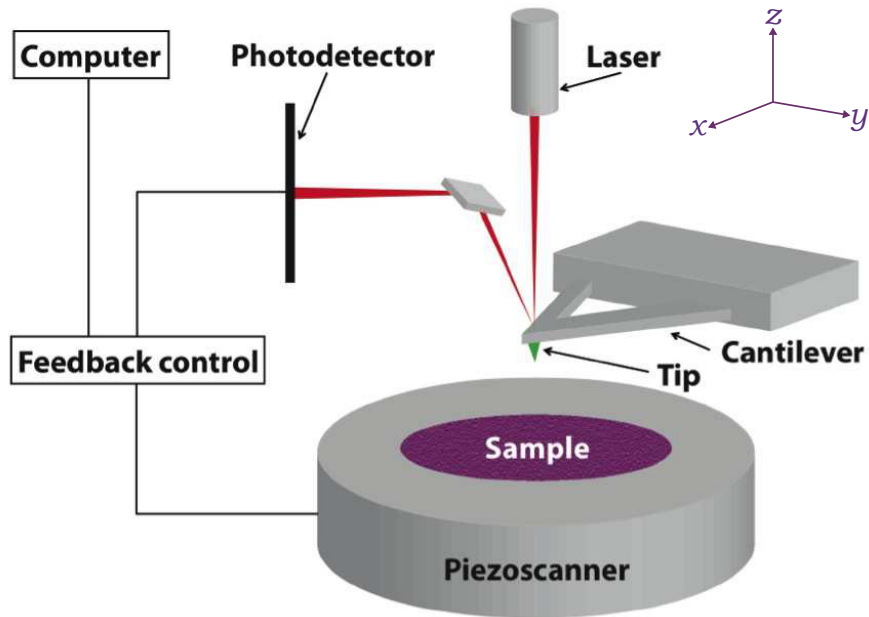


Figure 2.1: Schematic diagram of an Atomic Force Microscope (AFM). Not to scale.

forces is measured optically, using a laser, which is aligned on the upper side of the cantilever (generally as close to the tip edge as possible without losing intensity in the detector) and then reflected onto a segmented photodiode [11]. The photodiode is capable of tracking how far the reflected laser spot has been displaced from its neutral position at a user-determined set point near the centre of the photodetector; the higher the set point, the higher the force between the tip and the sample (0.5 V was used as a standard engage set point for images obtained in this work). As the cantilever bends either towards (attractive force) or away from (repulsive force) the sample, the position of the laser beam on the segmented photodiode will move down or up, accordingly [4]. The signal noise in the photodiode sets the lower limit of measurable interaction forces and so low coherence light sources are desirable because they reduce the optical interference and produce a clearer signal [164]. An example of an AFM set up with x , y and z piezos integrated into the sample stage is illustrated in Figure 2.1. When imaging, the tip would be lowered relative to the sample so that it is able to interact with the surface.

During imaging, feedback gains are used to alter the size of voltage modulation applied for a given amount of ‘error’ (δ), which is the difference between the pho-

to detector feedback signal and the set point in the z direction. The higher the gains of the feedback loop are, the larger the response of the piezo to the same size error. If the gains are too low, the cantilever will not move far enough to map effectively, but if they are too high, the image will be prone to ‘ringing’, where the piezo moves too far up and down trying to correct itself, leading to oscillation about the ‘correct’ z piezo height. There are two types of gain used to correct the height feedback loop: proportional and integral (G_p and G_i , respectively), where

$$\text{Feedback output} = G_p \delta + G_i \int \delta dt. \quad (2.1)$$

The proportional gain has less effect on the image quality so has usually been left at zero in this work. However, image quality can sometimes be improved by setting the proportional gain to a value of around or below one tenth of the value of the integral gain. Integral gain is increased until ringing is observed due to overshooting the required piezo adjustment, before being reduced to the point just before ringing starts, since this is the point at which the z piezo is mapping the surface topography most effectively (typically this is a value of 10 or more) [164].

2.1.1 Imaging modes

Contact mode

Contact mode maintains constant force and therefore constant cantilever deflection and distance between the back end of the cantilever and the sample, which is achieved by modulating the z piezo voltage using a feedback loop [4]. For example, if the deflection increases above the set point, the piezo voltage is reduced by the feedback loop, shrinking the piezo and retracting the tip from the sample. Calibrated z piezo position is the output from the ‘height’ channel in the software.

Another type of image that is commonly used is a deflection image. Deflection images are useful because details on the surface of raised features are more clearly visualized than in height images, where the range of the scale often makes these details difficult to resolve. The deflection data channel gives the error signal of the

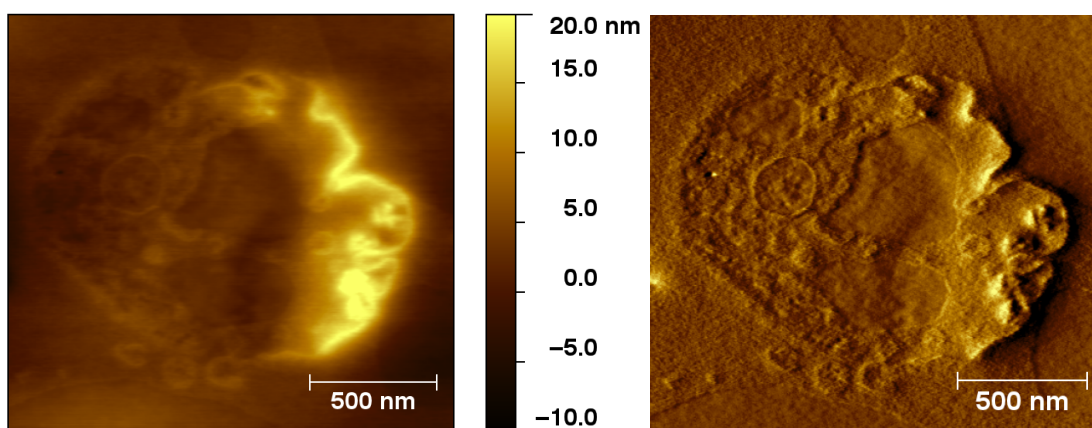


Figure 2.2: Example height (left) and deflection (right) images of a *Chlamydia trachomatis* reticulate body, taken using contact mode with an Si_2N_3 tip in air.

feedback from the segmented photodiode; the z -distance between the set point and the actual deflection of the cantilever [164]. For most colour scales, a positive distance, i.e. higher actual deflection than set point, produces a lighter pixel colour; and a negative distance, a darker pixel. This gives a 3D-type appearance to the images. Deflection images can highlight poor topography tracking, and, if the feedback loop were perfect, would be completely flat.

Figure 2.2 shows example height and deflection images of a *Chlamydia trachomatis* reticulate body (RB) on a glass microscope slide, taken using an Si_2N_3 cantilever with spring constant of approximately 60 pN nm^{-1} . Before use, the slide was soaked overnight in a surface-cleaning decontaminating decon90 solution (Decon Laboratories Ltd., UK), then sonicated (2510 ultrasonic cleaner, Branson, UK) in methanol, acetone and pure water then air-dried. A suspension of serovar E *Chlamydia trachomatis* harvested from 3 day growth in a murine epithelial cell line (McCoy cells) in filtered water ($0.2 \mu\text{m}$ pore size) was dropped onto the slide and left to dry for one hour before being imaged in air. Because the fragile RB cell has dehydrated and flattened to a few tens of nm thick, cell structure is observable in the height image, but even at this small z range, the deflection image is a useful visualization tool as surface textures are more clear.

Tapping mode

Tapping mode is a dynamic mode where the cantilever is oscillated by a small piezo in the cantilever holder, at a selected drive amplitude and frequency (close to its resonance frequency), and the changes in cantilever amplitude and phase are monitored. The tip touches the sample at the lowest point in its oscillation and, because of this, tapping mode is sometimes referred to as intermittent-contact mode [165]. The reduced sample contact in this mode means that lateral forces applied by the tip on the sample are also reduced, which is advantageous for imaging many soft polymeric or biological samples [5]. Tapping mode, like contact mode, is typically undertaken using the feedback loop to modulate the height of the cantilever so that oscillation amplitude is kept constant at a selected set point, typically at around 80 % of the free amplitude (the free amplitude is the amplitude of cantilever oscillations in the imaging media; air, water etc., due to the applied piezo drive voltage). Again, the amplitude is measured using the photodetector. Smaller amplitudes indicate that the sample has a higher feature at (x,y) , so voltage to the z -piezo is reduced, retracting the cantilever from the sample [164].

2.1.2 Force spectroscopy

Another mode used in much biological study is force spectroscopy (FS), where the tip is moved in the z direction towards and then away from the sample surface, and the cantilever deflection is monitored [45]. A plot of deflection against z distance can then be obtained and converted into a force-distance curve using the deflection sensitivity and spring constant of the cantilever (see Section 2.4.1 on page 61 for an explanation of this) [166]. The different parts of the force-distance curve contain information about a number of sample properties including surface forces, mechanical properties, viscoelasticity and adhesion for the (x,y) coordinate where the curve was taken [165]. The parts of the force curve that correspond to these different characteristics are demonstrated in Figure 2.3. Experimental parameters such as applied force and cantilever stiffness can be optimized for the desired application, for example, nano-indentation studies generally require cantilevers with a higher spring

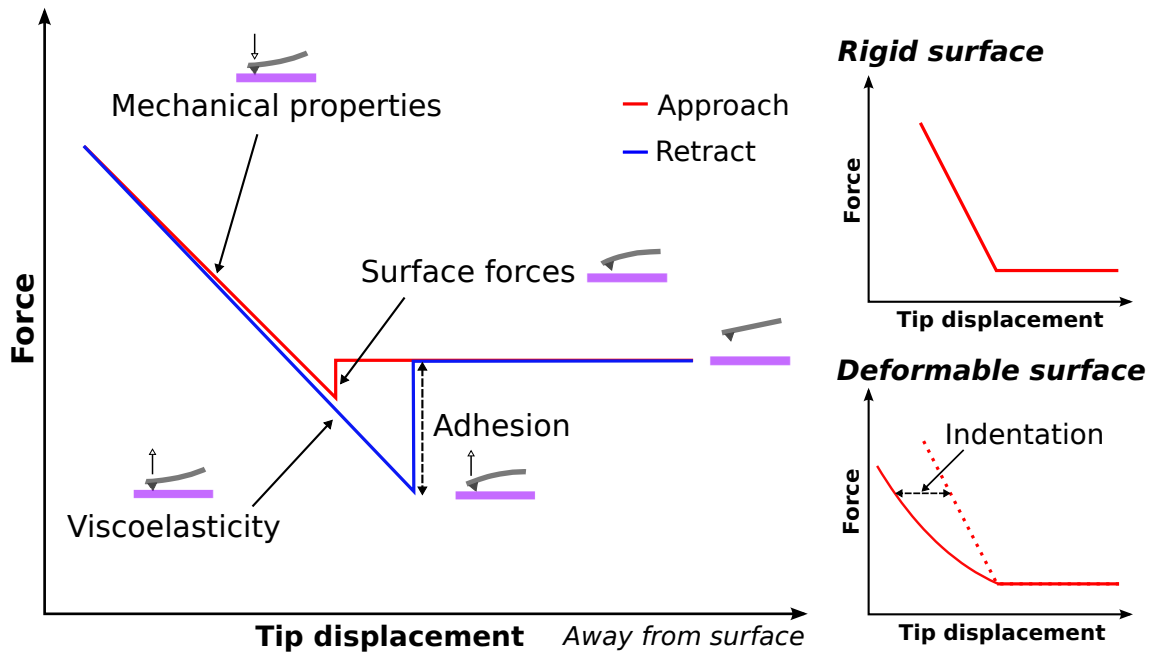


Figure 2.3: Left: An example force-distance curve for a non-deformable surface with attractive forces between the AFM probe and the sample. Right: the difference in approach force curves for non-deformable (top) and deformable (bottom) samples in the absence of surface forces. Based on a figure from [165].

constant in order that the relatively large force applied on the sample by the tip during indentation does not bend the cantilever so much that the deflection becomes saturated (i.e. the laser spot moves to the farthest point on the photodetector so further increase in deflection is not registered by the system) [164].

Figure 2.4 on page 48 shows a schematic illustration of a force curve, as might be obtained in good, low noise imaging conditions on a non-deformable sample (see Figure 2.3 on page 47 for an example of the curvature which can be expected for a soft, deformable surface). The red line represents the cantilever approaching the surface (i.e. the data collected move from right to left with increasing time), and the blue line, the cantilever moving away from the surface (data collected from left to right with increasing time). In this plot (Figure 2.4), there is a mildly repulsive interaction between the surface and the tip on approach, shown by the upwards curve at distances just above the surface on the red portion of the curve. If the interaction were attractive, this portion would dip below the straight approach line before increasing linearly as force is applied to the sample (as in Figure 2.3) [164].

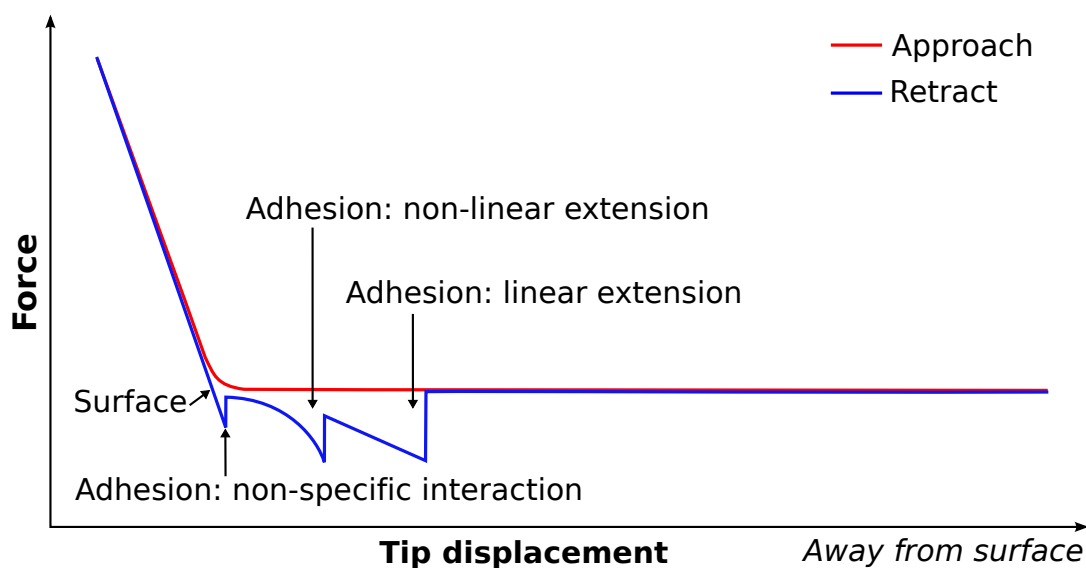


Figure 2.4: Model force curves. The red line is the approach curve, and the blue line is the retract curve. In addition to a non-specific interaction, two further adhesion events are shown on the retraction curve; one with non-linear sample stretching and the other with a linear extension.

The low ‘peak’ at small distances from the surface on the blue portion of the curve in Figure 2.4 indicates that there is some non-specific adhesion between the tip and the sample, but the two further adhesion peaks are due to interactions between the tip and a molecule(s) on the surface, and could be characteristic of a specific interaction [37]. They also show two different types of event; one rupture preceded by a linear extension, and the other by a non-linear extension of the sample. This, coupled with the distance moved by the tip before rupture and the peak force (adhesive force), provides information about molecular characteristics at the (x,y) coordinate of the force curve, which is of interest to those studying selective binding mechanisms, such as for the *Leishmania* part of this project.

The adhesion force can be evaluated using an algorithm in the software; in the case of the Asylum Research MFP-3D™ software running in Igor Pro (WaveMetrics Inc., USA), as used for all force curves in this project, adhesive force is calculated by subtracting the minimum in the force data from the average of the ten force data points obtained when the cantilever has reached the maximum retraction value. It is therefore important that the baseline is as flat as possible, since any slope will skew the measured force data. The chance of sloping baselines can be reduced by

lowering the speed at which the tip moves through the imaging media, but a slight slope can be corrected for by line subtraction on an initial force curve on a hard sample which is then applied to all force curves in the experiment. This baseline-minimum point force value is used for the force map, and whilst it gives the maximum adhesion observed at that (x,y) coordinate, it does not provide information about the type of extension, or whether there are multiple adhesion peaks observed in a single retraction curve. Because of this, it does not distinguish between non-specific and specific adhesion, so if that information is required, further analysis and more detailed curve fitting is required.

When a number of force curves are obtained, the results are generally combined into a histogram of frequency against adhesive force. These histograms typically have a non-normal distribution and are compared using non-parametric statistics such as the median and range of the distribution [167]. It is also not unusual to find a bimodal [41, 168–170] or trimodal [167, 170, 171] distribution over a large range of forces, due to the different strengths of characteristic binding interactions between the tip-sample combination.

FS data can be obtained using different chemically modified tips in place of standard silicon nitride (Si_3N_4) ones, as is the case for many of the examples in Chapter 1. This allows for specific binding interactions to be modelled *in vitro*, providing information about the strength of individual binding interactions between ligand and receptor molecules [34, 44] or in other similar molecular recognition systems [45, 102, 165].

2.1.3 Force mapping

Force mapping allows the user to select a grid, typically 32×32 or 64×64 pixels, over a chosen area of the sample, and take a force curve at each of these (x,y) coordinates [172]. Once complete, the data forms a “force volume map” [173], as it records both sample height and the adhesion force at a central point within each pixel (the contact area for a standard cantilever tip is ≤ 50 nm in diameter), calculated by an algorithm within the AFM software. Typically, the dimensions of a

cell according to the height map are comparable to those obtained from a standard AFM image taken of the same cell [174]. Force maps can either be obtained via force spectroscopy, when the tip is coated with numerous active molecules, or single molecule force spectroscopy (SMFS), when there is only one active molecule (or at most a few molecules) attached to the AFM tip.

One limitation of force mapping is the time required to obtain a single map. Typically, a rate of 1 Hz is used, meaning that one force curve is obtained per second, however, for very soft samples which require an increased force distance (the range in height included in a single approach and retract curve), or those using a stiffer cantilever, in order to maintain a reasonable loading rate (loading rate = tip velocity \times cantilever spring constant), a lower scan rate might be required [11]. Additionally, if a dwell time is used, the scan time will increase further. Dwell times are a user-determined period, typically 250 – 500 ms, for which the tip continues to apply the trigger force to the sample in order to allow rearrangement of molecules and formation of bonds before the tip is withdrawn. This means that for a 32×32 pixel map, the scan time is a minimum of 18 min, and for a 64×64 map, that time is increased to a minimum of 1 h 8 min (compared to ~ 8 min for a typical 512×512 pixel image). This is acceptable for some experiments, particularly those using inorganic materials, but a long scan time is not ideal for biological systems, particularly where live cells are concerned, because they can change during that time. It is therefore important to select a scan time which allows enough detail to be obtained whilst the systems being observed in the sample are stable.

2.2 Fitting force spectroscopy data

Derjaguin, Landau, Verwey, and Overbeek (DLVO) theory is often used to describe the interactions probed by AFM force curves [175], but in its basic form it does not account for the interplay between all of the different types of force, being solely based on a combination of attractive van der Waals interactions and repulsive double-layer forces [17], and discretion must be used when selecting it for analysis [16, 104]. The extended form does include some extra features, and can be a better

model for the forces in a more complex system [176]. However, there is currently no comprehensive theory for bacterial or cell interactions at a colloidal level, as adhesion in these systems involves such a wide range of surface molecules and polymers with different physio-chemical natures as well as contributions from cell elasticity and hydrodynamics [22].

Instead of considering adhesion for the cell as a whole, in some cases, physical properties of polymers can be elucidated. There are two principal methods for this, which are outlined in the following two subsections.

The freely jointed chain model

The FJC model considers the polymer as consisting of n rigid elements with a length l_k (the Kuhn length) that are connected through flexible joints which can rotate freely in any direction. At low forces, the polymer formation is that of a Gaussian chain, but as force is increased, orientation becomes less random, with preferential alignment oriented along the direction of the external force. Smaller Kuhn lengths correspond to a more flexible polymer [14, 27]. In the FJC model, the force required to stretch a polymer to a length x is given by

$$F_{\text{chain}} = \frac{-k_B T}{l_k} \mathbf{L}^{-1} \left(\frac{x}{l_c} \right), \quad (2.2)$$

where k_B is the Boltzmann constant, T is the absolute temperature, l_c is the contour length of the portion of the chain that was stretched, and \mathbf{L}^{-1} is the inverse Langevin function, approximated by the first four terms of its series,

$$\mathbf{L}^{-1} \left(\frac{x}{l_c} \right) = 3 \left(\frac{x}{l_c} \right) + \frac{9}{5} \left(\frac{x}{l_c} \right)^3 + \frac{297}{175} \left(\frac{x}{l_c} \right)^5 + \frac{1539}{875} \left(\frac{x}{l_c} \right)^7. \quad (2.3)$$

When Camesano *et al.* [27] applied the FJC model to their data, they found that the polymers had segment lengths between 0.154 nm and 0.45 nm, but that 65 % of measurements gave a segment length of 0.154 – 0.20 nm, suggesting that many of the polymers present on the cell surface were highly flexible.

The worm-like chain model

An alternative model that is also widely used to fit force curve data is the worm-like chain (WLC) model, which has been applied to data obtained when probing bacteria with hydrophobic tips [103], and is generally thought more appropriate in the case of less flexible polymers such as double-stranded DNA and proteins. In contrast to the FJC model, the polymer is considered as a continuous flexible chain of length L_c with a bending stiffness, κ , that can be used to evaluate the persistence length, L_p

$$L_p = \frac{\kappa}{k_B T}, \quad (2.4)$$

where k_B is the Boltzmann constant and T is the absolute temperature [177].

There is no analytical solution to the WLC model, but the most common approximation is the interpolated WLC derived by Bustamante *et al.* [178], given by

$$F = \frac{k_B T}{L_p} \left[\frac{1}{4} \left(1 - \frac{x}{L_c} \right)^{-2} - \frac{1}{4} + \frac{x}{L_c} \right], \quad (2.5)$$

where F is the elastic restoring force of the chain and x is the end-to-end separation distance. In some cases, the persistence length can be obtained from techniques such as small angle X-ray scattering [179]. The suitability of fixing persistence length can be evaluated by comparing experimental data and the WLC model in a force versus normalized distance plot. Such fixing was appropriate in the work by Parnell *et al.* [180] on poly(methacrylic acid) brush swelling, and L_p was taken as 5 Å (it had been previously determined using small angle X-ray scattering for bulk PMAA [179]), which gave a good fit up to high extension levels, and resulted in greater data fitting accuracy for the contour length, L_c , since only one parameter was fitted to the WLC model [180]. A surface modified with dense end-grafted polymer chains is referred to as a polymer brush because steric hindrance between the neighbouring polymer chains causes them to extend away from the surface when in solution, resulting in a brush-like conformation.

Other considerations for fitting FS data

Although adhesion measurements taken using AFM are being used increasingly, care must be taken. Quantitative measurements which require the area of interaction between the tip and the sample for calculations should be undertaken with caution, as tip shape can vary from the parameters given on the pack (although substrates are available which allow the tip geometry to be elucidated by scanning over a grid of thin cylinders or other point-like objects [174, 181]). The contact area can also increase over time due to abrasion during imaging hard samples, which can affect measurement continuity [182].

The mechanical properties of the cell as a whole (e.g. turgor pressure) and the membrane or cell wall tension can also have an impact on adhesion, affecting how the tip interacts with the sample. Calculation of the Young modulus of a cell is not trivial; some work, including that of Sen *et al.* [183], has shown that the relation of indentation depth to membrane tension is not always appropriately modelled when contributions from factors such as adhesion and pre-tension between the surface and the probe are ignored, such as in the Hertz and Hertz-Sneddon models, which describe the indentation of a homogeneous semi-infinite surface using either a spherical or conical probe, respectively [184].

Another possible problem that is more pertinent for biological samples, particularly in the case of force mapping with chemically modified tips, is that of tip contamination with molecules from the sample, and also the longevity of the molecules on the tip (whether they will become detached over time). If chemical attachments have been used to immobilize the sample, there is a chance that they will form stronger bonds with the tip than molecules on the bacterium itself. This can change the chemical properties of the tip and skew the force map results [166, 185]. In order to check for this, a control experiment should be undertaken, measuring forces before and after use with the biological sample to check for any significant changes in measurements or curve characteristics. This could constitute hydrophobic/hydrophilic contrasting experiments or using a surface coated with a specific lectin/molecule as per the tip functionalization.

2.3 Statistical methods

This section outlines the different approaches used to model and compare the force map data obtained in different experiments within this work. The main comparison methods used include finite mixture models (Section 2.3.1), applying minimum force thresholds to the force data (Section 2.3.3), and, for the *Leishmania* parasite work, using this to estimate an effective areal force (Section 2.3.3). The section also discusses how the statistical significance of the resulting data was evaluated (Section 2.3.4), and provides a key for the significance indicators used in graphs in the results chapters.

2.3.1 Finite mixture models

Finite mixture models (FMMs) were used as part of the statistical analysis applied to the data in this work, because, in many cases, histograms of both the peak adhesive force data and the logarithm of the peak adhesive force values appeared to be highly skewed or bimodal. It should be noted that all fitting in this work was done to the peak adhesive force as measured using the adhesion map function in the Asylum Research software, so the models and fits performed are fitting the largest force in a force curve, and do not account for the character of the individual adhesion event(s) within the force curve. Although it would be desirable to extract this additional information, the peak adhesive force in a given force-distance curve is still a useful measure of the types of interactions between the tip and the sample, and gives some indication of the character of the relationship between the two surfaces, with different types of forces having different strengths.

A finite mixture model is generally used when a data set is suspected of having a multimodal distribution, as it is capable of selecting two or more random parameter values, then performing iterations until these parameters are optimized and the model converges with the data [186]. There are two stages to fitting data using an FMM: firstly, the log-likelihood of the number of mixture components is evaluated. This predicts the chance that the data will be well fitted by a given integer number of components, between 1 and 5. Where data follow a normal distribution, they

are likely to be fitted by a single component, but when the probability of accurate fitting using a single component is small (i.e. the data are skewed or otherwise not normally distributed), the number of components selected for use in fitting the data is chosen based on the lowest number of components predicted to be a suitable model for the data (each additional component has an implicit variance which reduces the accuracy of the fit). This also avoids unnecessary over-fitting of the data, which is returned as stable after several runs of the algorithm, since the output varies each time the algorithm is applied. In this work, the number of components for a non-normal \log_{10} force distribution was typically 2, unless the log likelihood of the mixture being stably fitted with 2 components was low compared to 3 components on all runs of the algorithm.

Once a number of components has been selected based on the log-likelihood plots, a second algorithm is used which fits the data using that number of components. One key part of the FMM is the expectation-maximization (EM) algorithm, which iteratively maximizes the log-likelihood values [187]. A first value of the fit parameters (e.g. Gaussian width, height) for the mixture components is randomly generated. Following this, each datum is allocated to one of the components, and the individual component is recalculated using the data solely allocated to it. This is then repeated until convergence occurs. The EM algorithm is stochastic, and therefore can produce different values on repeated runs. For this reason, the EM algorithm is also applied several times to check for repeatability, and the quality of the fit is assessed on how close the theoretical versus empirical cumulative distribution function (CDF) plot is to a straight line: the closer this plot is to giving a straight line, the better the model replicates the data (see Figures 4.6 and 4.13).

This second algorithm generates a histogram which is overlaid with the Gaussian distributions associated with the mixture components. Examples of this can be seen in Figures 4.6 and 4.13 on page 150 and 166, respectively.

A detailed description of the derivation and application of FMMs to data can be found elsewhere [186, 187]. Briefly, the main assumption is that the data are made up of K components, having different characteristics specified by parameter

set θ_k , where $k = 1, 2, \dots, K$. The probability density function of the k^{th} component, $p(x | \theta)$, is given by:

$$p(x | \theta) = \sum_{k=1}^K \lambda_k p_k(x | \theta_k), \quad (2.6)$$

where λ_k is the mixing proportion of the k^{th} component, which describes the likelihood of a datum being associated with that component. The set of parameters is given by $\theta = (\lambda_k, \theta_k)$, where

$$\lambda_k \geq 0 \text{ for } k \in \{1, \dots, K\}, \text{ and } \sum_{k=1}^K \lambda_k = 1. \quad (2.7)$$

In this work, the distributions are fitted with univariate Gaussians and θ_k reduces to (μ_k, σ_k^2) , such that

$$\theta = (\lambda_k, (\mu_k, \sigma_k^2)). \quad (2.8)$$

This means that each fit results in a set of three parameters for each component within the data: λ_k indicates the likelihood that a datum is attributed to the k^{th} component (i.e. $\lambda_1 = 1$ for a unimodal distribution), μ_k gives the mean value of the k^{th} Gaussian component and is therefore a measure of its associated adhesive force, and σ_k^2 , the variance, is a measure of the dispersity of the k^{th} Gaussian component and therefore the range of forces attributed to that component. Combined, these three parameters model and describe the character of the \log_{10} force distribution and are used to compare the different tip-cell combinations in Chapters 4 and 5.

2.3.2 Histogram bin generation for unimodal force distributions

In the cases where a FMM was not appropriate because the data were well modelled by a single Gaussian distribution, the raw adhesion data was converted into a histogram and fitted using Igor Pro. The histogram bin sizes were calculated automatically using Scott's normal reference rule:

$$h = 3.49 \hat{\sigma} n^{-\frac{1}{3}}, \quad (2.9)$$

where h is the bin width, $\hat{\sigma}$ is the standard deviation of the data and n is the number of data points in the sample [188]. The option for bin-centered values was also selected when the histogram was generated to enable accurate fitting. This method generated histograms which appeared similar to those generated during the FMM analysis in the statistical computing environment, R (R Foundation, Vienna, Austria), and so the single Gaussian fit of the data could be considered comparable to the multiple component fit of the same data. A Gaussian curve was fitted to the histogram and the parameters were then extracted and combined with the FMM results for analysis, where appropriate.

2.3.3 Applying thresholds to adhesion data

The FMM analysis considered all of the force curves obtained on the cell, including those with no adhesive events. It is quite common practice to ignore these non-adhesive events when analysing force data from biological samples [25, 167, 168], which is easy to do when individual binding events are being fitted, for example if the WLC model is used, but is not an automatic output when considering the peak adhesive force. However, by applying force thresholds to the data, the characteristics of certain force populations can be examined more closely: the noise in the data was typically 20 pN or lower, and therefore if only force events above 20 pN are included in analysis, these passive curves no longer skew the overall picture of adhesion. This was undertaken in Microsoft Excel (Microsoft Corporation, Redmond, Washington, USA) using the “averageif” and “countif” commands, to involve curves with forces above several different thresholds. This was useful in terms of comparing the average force when different sections of the population were used, and is explored further in Section 5.10.

Effective force per unit area (areal force)

A useful tool to compare relative adhesion strength between different parasite-glycopolymer combinations was to use the calculation of a mean force for data above the threshold, $F_{>t}$, and the number of events above the threshold, $n_{>t}$, to

generate an effective force per unit area, F_{eff} , using the following calculation:

$$F_{\text{eff}} = \frac{n_{>t}}{n} \times n_{1\mu\text{m}} \times F_{>t}, \quad (2.10)$$

where n is the number of events in the map and $n_{1\mu\text{m}}$ is the number of events in $1 \mu\text{m}$, where

$$n_{1\mu\text{m}} = \frac{n}{A}, \quad (2.11)$$

and A is the area of the force map in μm^2 . This approach takes the effective force as being contributed to by an array of points with the area of one pixel in the force map, rather than by an array of points the size of the tip-sample contact area, but since the number of pixels and map size were consistent between experiments, this is a reasonable comparison method, provided that we assume that molecules within the pixel are in an area where they could bind to the AFM tip and contribute to the measured interaction. This is a useful method because it takes account of both the frequency and size of forces between the cell and a probe, and gives a measure of the kind of overall interaction strengths which could be expected if the probe had a large surface area with the same chemical characteristics as the AFM tip and the individual binding interactions added up cumulatively across the contact area between the cell and the probe. This could therefore be a useful tool to view the interactions measured with AFM on a biologically relevant scale, and this approach is used in Section 5.10.

2.3.4 Determining statistical significance

The significance of differences between selected parameters (e.g. median adhesive force) for all cell-tip combinations was determined by firstly running the parameter value of the different cells within a population through a one-way analysis of variance test (one-way ANOVA) [189] to determine whether there was any significant difference within the data sets. The ANOVA test outputs a p -value and an F value, which can either be above or below a critical value, F_{crit} . These outputs are a measure of whether inter-category variation is larger than intra-category variation, and

categories which returned a promising p -value ($p < 0.05$) were selected for further inter-category comparison. In this work, the data have been classed as unpaired because, although the same base stocks were used for the different independent repeats and for measurements of the same cell type using different probes, because the experiments treated single cells rather than a population, and in the case of *S. pneumoniae* the growth rates varied slightly between experiments, the exact same cell was not investigated with different AFM tip chemistries. In addition, the number of data points within a series was not the same for all categories which made paired analysis challenging.

Most force histograms did not show a normal distribution and since < 20 cells were mapped for each condition, it was difficult to tell if the results from the individual cells had a normal distribution, so a non-parametric statistical test was used. The test chosen to determine inter-category significance was the two-tailed Mann-Whitney test [190] with a significance level of 0.05 (sometimes referred to as the Wilcoxon rank sum), which is a non-parametric alternative to the unpaired t -test [191]. The Mann-Whitney test has been suggested as a suitable test for non-parametric single-cell AFM force spectroscopy data [192] and has been used in work involving the organisms used here, for example on *Leishmania amazonensis* migration through a collagen matrix [193] and an investigation of *S. pneumoniae* factor H binding and opsonization [194]. The test was applied using Igor Pro, which calculates an exact critical value (for the size of data set in this work), and the p -values were extracted and tabulated. A non-parametric two-tailed test was chosen because it makes fewer assumptions about the nature of the data being compared, however, fairly similar significance levels were found when comparing the G_s/G_1 mean, median and mean forces for the *S. pneumoniae* data using both the Mann-Whitney test and a two-tailed t -test [190] for unpaired data with unequal variance. In cases where there were only a few cells within a group, such as the G_2 mean of the bimodal force distribution of *S. pneumoniae* data (due to the fact that a number of bacterial cells only expressed a unimodal distribution), there were too few repeat experiments to determine whether there was significant variation between the categories. A larger

data set would be ideal in order to make solid conclusions about differences within this data, although it was still possible to identify and explore the trends within the non-significant data.

Non-significant data is not indicated on the graphs within the results chapters, but significant differences between key categories which are directly comparable are indicated using the following nomenclature:

Table 2.1: Significance level notation as used in graphs

Symbol	p -value	Meaning
*	$0.01 < p \leq 0.05$	significant
**	$0.001 < p \leq 0.01$	very significant
***	$0.0001 < p \leq 0.001$	extremely significant
****	$p \leq 0.0001$	extremely significant

In the work involving *Leishmania* parasites, where there were significant differences between multiple categories and the graphs would have become overcrowded if this data was included, all of the p -values are attached as an Appendix to this work, in the form of a colour-coded comparative table (see Appendix C on page 245).

2.4 AFM details

The AFM used in this work is the MFP-3D-BIO™ by Asylum Research (an Oxford Instruments company, Santa Barbara, USA), which has an integrated optical microscope and AFM, allowing accurate positioning of the cantilever on transparent samples with visible features. In the context of this project, the optical microscope is used for the *Leishmania* parasite work, but not the *Streptococcus pneumoniae* experiments. The MFP-3D™ scanner is set up a little differently to the diagram in Figure 2.1 on page 43, in that although the sample is placed on a piezo-driven xy scanner (flexure type, rather than tube type), the z piezo is not underneath the sample, but instead varies the height of the light source/cantilever assembly inside the scanner head. Another feature of the MFP-3D™ is that it overcomes (or at least lessens) creep and hysteresis associated with typical piezo systems by incorpo-

rating Nano Positioning System (NPSTM) sensors. These sensors calculate the exact distances the component has moved in a given direction as a result of the applied piezo voltage (as opposed to gauging this by the applied voltage, which does not allow for the effects of hysteresis and creep on piezo extension). These inductive NPSTM sensors are a development of traditional Linear Variable Differential Transformers (LVDTs), eliminating Barkhausen noise. The Barkhausen effect exists in ferromagnetic materials, which contain different domains in which all of the spins are aligned and thus share magnetic polarity. The ‘noise’ is caused by sudden changes in magnetic domain size after domain walls are released from pinned points, which are often due to defects in the material, resulting in discrete jumps in the magnetization as external magnetic field increases [195]. Reducing this noise i.e. the size of the jumps in magnetization, makes the sensors sensitive enough for use in accurate nanoscale positioning, and, when used in combination with a feedback control (in closed loop scanning, which is the standard mode of operation for the system), the information from the NPSTM is passed back to the controller and is used to adjust for any drift due to the piezo stack response.

The laser used in the MFP-3DTM is a super luminescent laser diode (SLD), which has both high power and low coherence, and emits at approximately 860 nm wavelength. The light from the SLD is focused onto the cantilever using a lens and is reflected by the cantilever back, which is mounted such that it is tilted at approximately 11° to the horizontal sample plane. The laser beam is then recollimated by a second lens before being reflected onto the segmented photodetector.

The radii of cantilever tips used in this project are 30 nm for the bacteria work (Biolever, Olympus, Japan) and 20 nm for the parasite work (MLCT, Bruker, USA). The actual tip radius will be larger than this because of the additional monolayer or polymer brush coatings used.

2.4.1 Cantilever calibration for AFM

Cantilever deflection is determined using the optical lever sensitivity (OLS), which relates the change in signal voltage coming from the photodiode to the cantilever

deflection causing the voltage change [196]. The OLS varies for each AFM experiment and must be re-calibrated whenever the cantilever or laser spot is repositioned. Inverse OLS calibration measures the slope of the contact region of a deflection- z distance plot in pN nm^{-1} (i.e. when cantilever deflection is increasing due to increasing force while the tip remains in place on the surface) taken on a hard surface (so that the portion of the curve where force is applied to the sample is a straight line, as illustrated in Figure 2.3 on page 47, since this is assumed by the fit) such as mica or glass and, once set, converts all deflection measurements from Volts to nanometres [164]. For the experiments in this thesis, 15 force curves were taken and the OLS measured for all of them. This was then averaged to give the OLS used to calculate the spring constant. If there were any clear outliers, then the highest and lowest values would be discounted and the average taken of the remaining 13, or 15 if two additional curves were taken.

The spring constant of the cantilever is determined using the thermal noise method [197], and all modern AFM software has a built-in package to do this (as well as the deflection sensitivity fitting). Cantilevers come with a general spring constant specification, but the given range is generally very broad and the exact spring constant will vary from cantilever to cantilever and so for accurate force measurements, calibration of spring constant is critical. The thermal noise method involves raising the cantilever off the surface and recording the natural vibrations, referred to as the thermal power spectral density (PSD). In the MFP-3DTM, the deflection data are collected using Fourier transform and are plotted as deflection amplitude ($\text{m Hz}^{-\frac{1}{2}}$) as a function of frequency (Hz) [164]. Example thermal PSD curves obtained in air and in liquid are shown in Figure 2.5 on page 63. There is a clear difference between the thermal PSD taken in air and in liquid for the same cantilever, which is not unexpected due to the different properties of liquid and air in terms of oscillation dampening and other viscosity-related effects, however, the spring constants calculated in the two different media were generally consistent. It was useful to obtain a value both in air and liquid so that the two values could be compared as a check that the fit of the thermal spectra obtained in phosphate

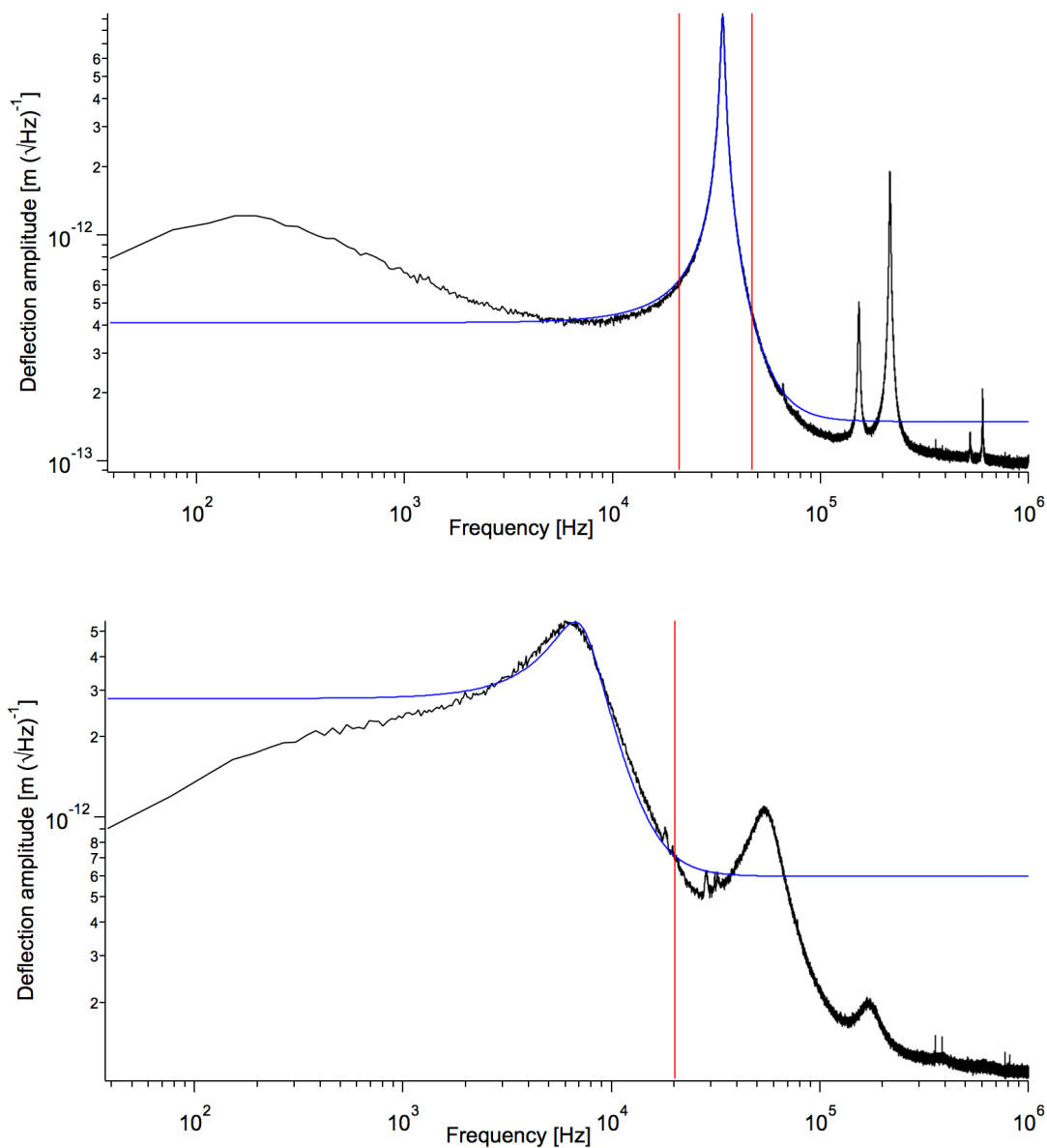


Figure 2.5: Example thermal power spectral density curves taken in air (top) and phosphate buffered saline (bottom) using the same Olympus BioLever cantilever, with an average calculated spring constant of $k = 24 \text{ pN nm}^{-1}$. The black curves are the thermal data (590 and 621 samples for top and bottom, respectively). The blue and red lines are generated by the software while fitting to calculate the spring constant with the OLS set by the user. The thermal curve obtained in liquid has much broader peaks which are shifted to a lower frequency because of the dampening effect of the fluid on the cantilever. Despite the differences between the curves, the spring constants calculated for the two are consistent within a few pN nm^{-1} , with k being slightly higher in liquid.

buffered saline (PBS) was reasonable.

The spring constant is determined by fitting the thermal PSD, specifically the peak associated with the first harmonic of the cantilever (see the blue line in Figure 2.5) and, once set, is used for the rest of the experiment (or until the laser is realigned or the cantilever changed or adjusted) to convert deflection data to force data in the force curves [164]. This conversion is possible because the cantilever can be modelled as a Hookean spring and therefore the force on the cantilever, F , can be derived using Hooke's law,

$$F = -kx, \quad (2.12)$$

where k is the spring constant of the cantilever and x is the cantilever deflection.

2.4.2 Different methods of cell immobilization

As mentioned previously, in order to do AFM successfully on cells, they must be securely attached to the substrate so that they are not disturbed by the movement of the cantilever. There are different methods which can be used to this end, typically divided into chemical or physical adsorption and mechanical trapping, but there is often a trade off between the success of the immobilization, modification of cell surface properties and, in some cases, loss of cell viability (e.g. if the cells are fixed using glutaraldehyde during sample preparation). In addition to loss of viability, cells treated with glutaraldehyde, known to stiffen cell structure, have been found to have lower adhesion forces than untreated cells [198]. Forces measured on the same cell species can vary depending on the method used, so care should be taken when selecting a route for the experiment in question [199]. A reasonably comprehensive comparison of the different methods can be found in the literature [22, 185, 200], but a brief summary of some of the main benefits and drawbacks is presented below.

Use of covalent bonding to attach cells to a substrate can result in crosslinking of the polymers on the cell surface, even on the upper surface of the cell, which affects the extension and conformation of the probed polymers and has the potential to mask binding sites. This is not ideal if the experiment is designed to examine the

surface properties of the microorganism and somewhat negates the benefits of AFM being able to image and map cells in an *in vivo*-type environment. However, covalent bonding can be one of the stronger methods of attachment.

Sample preparation using filtration of the bacterial suspension through a track-etched polycarbonate membrane with a well-defined pore size is the most popular approach for use with spherical cells, and has been applied to yeast and bacterial cells, typically with a pore size slightly below that of the diameter of the cell so that the trapped cell is firmly held in place [25, 170]. It should be noted that the hydrophobicity of the membranes varies for different material batches, so some trial and error can be involved in order to find an ideal match for each species of cell. Although membrane material choice is limited by the options available from the manufacturer, pore size can be tailored by the user; increasing diameter over time by etching with sodium hydroxide (although this also reduces the thickness of the membrane, making it more fragile) [201]. The principal benefit of mechanical trapping is that it uses an inert substrate so the chance of surface modifications such as crosslinking is diminished, and it is for this reason that this method was chosen to immobilize *S. pneumoniae* in this work. There is some evidence, though, that mechanical trapping can apply sufficient stress to cause deformation or cell damage, so cell viability should be tested after filtration, where possible [202].

Physisorption uses electrostatic interactions (and hydrophobic interactions, to a lesser extent) to bond the cell to a surface; pre-coating the substrate with a solution of positively-charged (cationic) polymer before incubation with the bacteria or cell suspension. Here, poly(ethyleneimine) (PEI) was used to immobilize the *Leishmania* parasites, since their irregular shape and ability to “swim” effectively through media limits the potential for mechanical trapping, and adsorption on un-coated glass, silicon and polystyrene surfaces was unsuccessful. PEI should be used with caution since it can permeabilize some gram negative bacteria [203], but in this instance, it proved to be the most effective and repeatable method. Details of the trapping methods used in this project can be found in Sections 2.8.2 and 3.1.2 on pages 78 and 90, respectively.

In addition to the immobilization method, the lifecycle stage of the cell can impact adhesion results because cell surface chemistry can vary with age; Bowen *et al.* saw an increase in *S. cerevisiae* adhesion to mica during the stationary growth phase, where the yeast cell has high hydrophobicity and a decrease in cell ζ -potential [198]. It is also known that imaging media, contact time and applied force can all impact measured adhesion strength, so it is important to carefully consider the experimental parameters [7, 36]. For all of the experiments in this thesis, bacteria were harvested at mid-log phase, and parasites after a few minutes' growth after being defrosted. The same buffer, PBS, was used throughout. All PBS used for cell preparation and AFM was made in bulk: 10 \times PBS (Lonza, Switzerland) was diluted with DI water to 1 \times PBS before it was aliquotted into glass universal vials and autoclaved. The final concentration of PBS had a pH value of 7.3 – 7.5 and contained 144 mg l⁻¹ KH₂PO₄, 9 g l⁻¹ NaCl and 795 mg l⁻¹ Na₂HPO₄. It was free of Ca⁺⁺ and Mg⁺⁺.

2.5 Preparation of hydrophobic and hydrophilic AFM tips

AFM tips were functionalized with self-assembled monolayers for the bacterial work and with glycopolymer brushes for the parasite work. The hydrophobic/hydrophilic SAM-coated tips are described here but the glycopolymer-functionalized tips are considered in Chapter 3.

1-dodecane thiol (DDT) and 11-mercaptoundecanoic acid (MUA) were obtained from Sigma Aldrich Ltd, UK. The probes selected and used for coating were Bi-oLevers (Olympus, Japan), which have two 60 μm long cantilevers and two 100 μm long cantilevers on each chip (both levers are 30 μm wide). The shorter cantilever has a spring constant of approximately 30 pN/nm (generally the spring constant was found to be around 20 pN/nm when coated). The longer cantilever has a smaller spring constant (approximately 6 pN/nm) but did not generally cope well with the strains of force mapping so the shorter cantilever was used. The lever and tip material was silicon nitride with a 20 nm thick gold coating on the tip side and 30 nm coating on the reverse (laser side). Before SAM coating, the typical uncoated tip

height was $> 5 \mu\text{m}$, and the radius was $< 40 \text{ nm}$.

1 mM solutions of DDT and MUA in absolute ethanol (7.1 μl and 0.0055 g respectively in 25 ml of ethanol) were made in clean glass vials under minimal light conditions. The glass vials were then covered with foil and the mixture was sonicated for ~ 5 minutes. Approximately 10 ml of the solution was then added to a clean glass Petri dish containing the cantilevers, again under minimal lighting. The Petri dish was closed and placed in a cardboard box to prevent light affecting the SAM formation and left overnight. The following morning, the cantilevers were rinsed with pure ethanol and transferred to another clean glass Petri dish containing absolute ethanol. The cantilever selected for the experiment was removed from the ethanol and left to dry before being loaded into the AFM cantilever holder. Coated cantilevers were used no more than 48 h after being removed from the thiol solution and were always kept in ethanol until immediately before use, when they were dried under a gentle nitrogen gas flow.

Control experiments were undertaken to check the success of the SAM formation and discussion of these can be found in Section 3.7 on page 124. The SAM-coated surfaces used here were functionalised with DDT or MUA in the same way as the cantilevers, and consisted of a silicon wafer ($425 \pm 25 \mu\text{m}$ thick, Prolog Semicor, Ukraine) which had been cleaned by immersion in piranha solution (see Section 3.2 on page 98 for details of piranha cleaning) and then coated with gold via evaporation of a 1 nm chromium layer (chromium chips, 99.99%, Agar Scientific, UK) followed by a 20 nm gold layer (gold wire, 99.99%, Goodfellow Metals, UK) using an Auto 306 evaporator (BOC-Edwards, UK). The gold-coated substrates were then cut to size and stored in absolute ethanol before use.

2.6 Preparation of lectin-coated mica surfaces

The method used to immobilize lectin on the mica surface is based on that used by Sletmoen *et al.* but, instead of *N*-(3-dimethylaminopropyl)-*N'*-ethylcarbodiimide hydrochloride (EDC) in an acetic acid solution, (3-aminopropyl)triethoxysilane (AP-TES) was used to modify the surface with silanized-amine groups [163]. In addition

to this change, the glutaraldehyde immersion time was reduced from 14 h to < 2 h, and a backfilling agent was used after the lectin stage. This final step was added in order to passivate any unreacted aldehyde groups on the glutaraldehyde, deactivating them by reacting them with the amine group of ethanolamine, effectively replacing the aldehyde end groups with hydroxyl ones. This was to prevent lectin-free sites on the sample binding to amine groups on the glycopolymers and giving false positives due to non-specific interactions. A similar precaution was taken in work by Beaussart *et al.* to prevent non-specific binding to unreacted aldehyde groups on AFM tips which had been functionalized with either an antibody or concanavalin A (con A) [170].

Magnetic stainless steel AFM specimen discs (12 mm diameter, Agar Scientific, UK) were cleaned by sonication in toluene, ethanol and water and were dried under a nitrogen gas flow. A 9.9 mm diameter mica disc (ruby muscovite, Agar Scientific, UK) was attached to a specimen disc using optical adhesive, which was then cured for 15-20 minutes under 254/365 nm UV radiation (UVLS-24 EL lamp, UVP, Cambridge, UK). The mica sample was handled using clean tweezers and kept in a clean polystyrene Petri dish to prevent unnecessary chemical contamination. Samples were used in AFM experiments immediately after the functionalization was complete.

Before coating, the mica disc was repeatedly exfoliated using ScotchTM double-sided adhesive tape until a complete disc was cleaved. Coating was undertaken in clean 20 ml screw-top glass vials, and while the APTES and glutaraldehyde vials were re-used following repeated rinsing with toluene or DI water, respectively, new vials were used for the stages involving lectins in order to minimize the risk of contamination with denatured proteins, which adhere strongly to most surfaces. The reagents (all purchased from Sigma Aldrich Ltd, UK) and quantities used for the mica functionalization are given in Table 2.2.

The toluene was added to a glass vial along with a magnetic stirrer. The APTES was then added and the solution mixed for approximately 30 s. At this point, the stir bar was removed and the freshly-cleaved mica sample was added to the vial,

Table 2.2: Reagents for lectin functionalization of mica.

Amount	Reagent
Formation of APTES layer	
20 ml	toluene \geq 99.5 %
0.2 ml	(3-aminopropyl)triethoxysilane (APTES) 99 %
Formation of aldehyde layer	
6 ml	deionized (DI) water
2 ml	glutaraldehyde 50 wt. % in water
Either addition of glucose-binding lectin	
5 ml	PBS
2.5 mg	concanavalin A, type VI (con A)
Or addition of galactose-binding lectin	
1 ml	PBS
0.5 mg	soybean agglutinin (SBA)
Blocking of unreacted aldehyde groups	
7.5 ml	PBS
0.453 ml	ethanolamine \geq 99.0 % in water

making sure that the mica surface was uppermost. The vial was then closed and left at room temperature (typically 12-15°C in this case) for 30 min. After this time, the mica sample was carefully removed using tweezers and rinsed well with toluene. It was dried under a nitrogen gas flow, placed into a glass Petri dish and transferred to the vacuum oven to anneal for 30 min at 120°C under reduced pressure.

While the APTES layer was annealing, the glutaraldehyde solution was prepared in a new glass vial by adding the glutaraldehyde to the deionized (DI) water and stirring for at least 15 min. After the annealing was complete, the sample was removed from the oven and left to cool for a few minutes. The magnetic stirrer was then removed from the glutaraldehyde solution and the amino-silanized mica sample added, again, making sure that the mica surface was uppermost. The vial lid was loosely closed and it was left at room temperature for 1.5 – 2 h, after which time the sample was removed, rinsed well with DI water and dried under a nitrogen gas flow.

PBS was pre-cooled in the fridge before being used to make the lectin solution in order to reduce the chance of overheating the lectin and denaturing it. The

selected lectin, soybean agglutinin (SBA) for galactose-binding experiments or concanavalin A (con A) for glucose-binding experiments, was then weighed out and added to the required volume of PBS to make a 0.5 mg ml^{-1} solution. This mixture was shaken and sonicated briefly ($\sim 10 \text{ s}$) in order to dissolve any clumps of lectin. If it was felt that the mixture was warming too much (more of an issue for the SBA solution due to its smaller volume), it was returned to the refrigerator for a few minutes before being sonicated for a further few seconds. The mica sample was then added to the vial such that the mica disc was uppermost and the entire active surface was immersed in the lectin solution. The vial was closed tightly and left in the fridge overnight.

The following day, a 1M solution of ethanolamine was made with chilled PBS and mixed well using a magnetic stirrer. The mica sample was then removed from the lectin solution and rinsed well with PBS, using a glass Pasteur pipette and rubber bulb. The stir bar was removed from the ethanolamine solution and the mica sample was transferred into the vial, which was then closed and put in the fridge overnight to allow the aldehyde-passivating reaction to run to completion.

The vial was left in the fridge until the AFM had been calibrated, at which point the sample was removed and rinsed carefully with PBS using a glass Pasteur pipette and rubber bulb. The underside of the sample was then dried with lens tissue and it was attached to a clean glass microscope slide using a small square of ScotchTM double-sided adhesive tape. The upper, mica side of the sample was kept moist throughout and $100 \mu\text{l}$ of PBS was added to the surface once the sample had been attached to the glass slide.

After use, the sample was left under PBS or water overnight, then it was removed from the slide and the tape was peeled off the specimen disc. Any remaining tape residue was removed by scraping it off with a paper towel or a clean blade. The top layer of the mica was removed by cleaving with tape and the sample puck was then sonicated sequentially in ethanol and DI water for 15 min before being dried under a nitrogen gas flow and stored in a clean polystyrene Petri dish before re-use.

A summary of the results of AFM experiments on these lectin samples can be

found in Section 5.2 on page 177.

2.7 *Streptococcus pneumoniae* methodology

Streptococcus pneumoniae was grown in the Medical School at the University of Sheffield and all bacterial work (with the exception of AFM) was undertaken in a microbiological safety cabinet inside a category 2 microbiological laboratory using aseptic techniques. All bacterial stocks were verified by haemolysis pattern, optochin sensitivity and Gram staining. Work focused on the following serotype 2 strains: D39 (capsulated), and its unencapsulated derivative FP22, as used previously by the group [96]. These two strains were chosen in order to assess the impact of the capsule on the hydrophobicity of the bacteria.

2.7.1 *S. pneumoniae* growth

The two pneumococcus strains were grown up from the base stocks in broth, under supervision of Martin Bewley. When required, an aliquot was defrosted in a CO₂ incubator (SANYO, Japan) set at 37°C and then plated out onto a blood agar plate. Blood agar plates contain 4.2 g Columbia agar (VWR International, USA), per 100 ml DI water (> 16MΩ), supplemented with 5% v/v defibrinated horse blood (Fisher Scientific, USA) (100 ml is sufficient for ~ 10 plates). Several 10 µl drops of the suspension were added at one side of the plate using a Gilson pipette and sterile disposable tip. These drops were then streaked across the rest of the plate with a sterile cell loop to enable growth of isolated colonies.

The plate was left to dry, inverted and placed in an incubator at 37°C and 5% CO₂ for between 24 and 48 hours until easily identifiable independent colonies were present on the streaked region. For experiments and to grow stock, 10 – 15 colonies were scraped from the blood agar plate using a sterile cell loop and added to 20 ml of brain heart infusion broth (BHI, Oxoid™) supplemented with 20% v/v heat inactivated fetal bovine serum (FBS, Gibco®) in a 50 ml Falcon tube. BHI broth was made up by adding 18.2 MΩ filtered water (NANOpure Diamond, Barnstead, Triple Red, UK) to the BHI powder, mixing well and autoclaving. FBS complement

was heat inactivated by placing in a water bath at 56°C for 1 h, mixing occasionally. Inactivated FBS was added to the BHI in the Falcon tubes and mixed immediately before the addition of bacteria using a Vortex-Genie 2 (Scientific Industries, USA).

Once the colonies had been added, the caps were loosely placed back on the tubes and secured with autoclave tape. The suspension was then transferred onto a PSU-10i orbital shaker at 250 r.p.m. (Grant-bio, UK) in an incubator at 37°C and 5% CO₂. Bacterial growth was assessed using a Jenway 6300 spectrophotometer (Jenway, UK), at 600 nm to measure the optical density (OD), and this was correlated to the number of colony forming units (CFUs) by performing a Miles Misra Method viability count. Briefly, 1 ml of broth was removed at a given time post-inoculation, the optical density measured, then 8 serial dilutions were carried out by adding 100 µl of the suspension to 900 µl of PBS in a 1.5 ml Eppendorf tube, mixing by vortexing, then adding 100 µl of that suspension to the next 900 µl of PBS and so on until the eighth serial dilution. 3 × 10 µl drops were then added to a quadrant of a blood agar plate numbered according to the dilution. The plates were dried, inverted and left in an incubator at 37°C and 5% CO₂ overnight. The number of individual colonies was counted the next day and the number of CFUs calculated using the following equation:

$$N = \frac{x \times 10^3 \times 10^q}{30}, \quad (2.13)$$

where N is the number of CFUs per millilitre, x is the number of bacterial colonies in a quadrant and q is the quadrant number (such that multiplication by 10^q accounts for the dilution factor of the suspension used to inoculate the quadrant).

Experiments were undertaken using mid-log phase bacteria. To evaluate the optical density at which this typically occurred and obtain a corresponding CFU value at that time, bacterial growth curves were plotted. Representative growth curves for the two species are shown in Figures 2.6 and 2.7 on page 73. Three growth curves were taken for both species, and all showed the characteristic sigmoidal shape, but the exact time at which they started growing varied from suspension to suspension because of uncontrollable variation in the exact number of bacteria used to inoculate

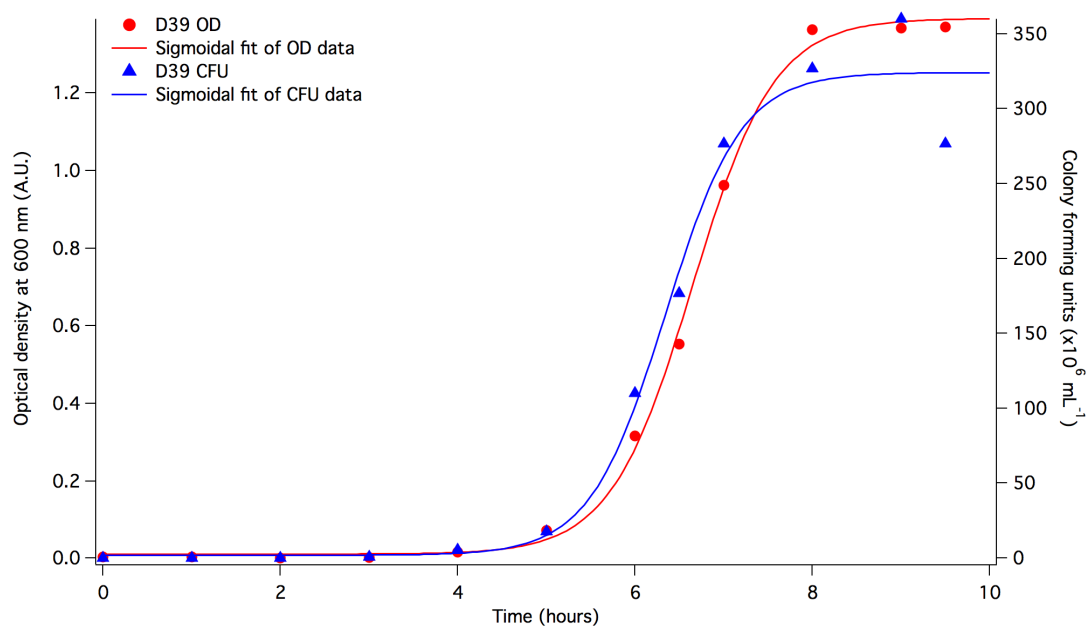


Figure 2.6: Representative D39 *Streptococcus pneumoniae* growth curve with sigmoidal fit of both optical density and number of colony forming units.

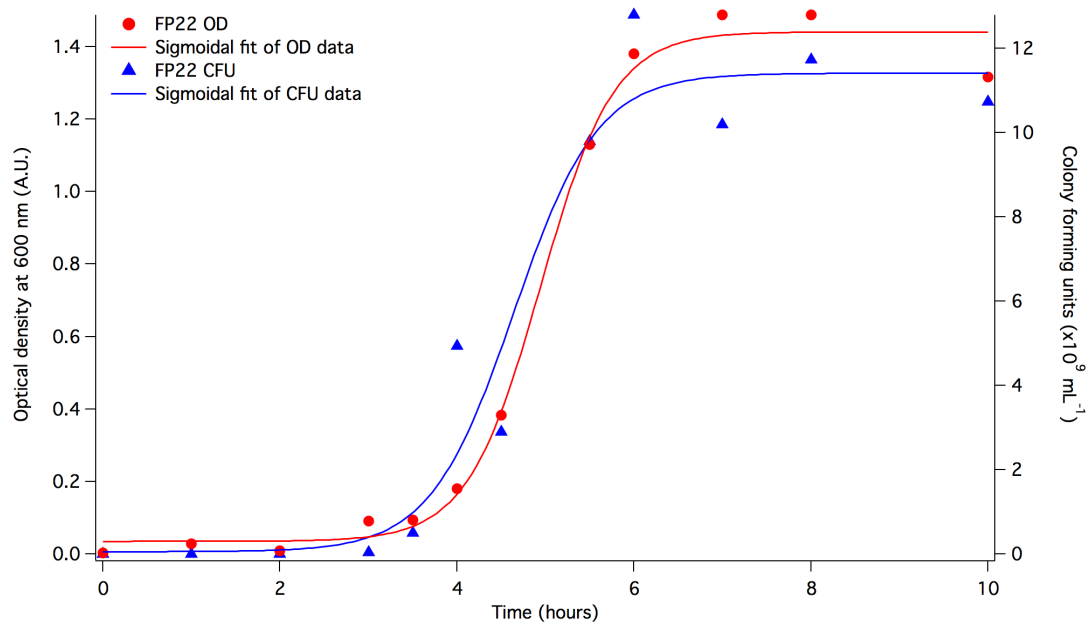


Figure 2.7: Representative FP22 *Streptococcus pneumoniae* growth curve with sigmoidal fit of both optical density and number of colony forming units.

the broth, due to differing numbers of cells in the colonies on the blood agar plates. These curves were therefore used as a guide to the optical density at which cells should be harvested, since measuring the OD using a spectrophotometer could be done easily and quickly, giving an instant result which allowed the harvest time to be varied accordingly for each experiment. For example, a mid-log OD of 0.6 could be reached any time from 4 to 8 hours post inoculation.

It should be noted that the number of colony forming units was higher in the other two D39 curves than the one in Figure 2.6, but the time at which the cells started growing exponentially in the Figure was the median value so it is the one presented here. The maxima for the D39 curves not shown were approximately $12 \times 10^9 \text{ ml}^{-1}$ compared to $0.3 \times 10^9 \text{ ml}^{-1}$. Optical densities were comparable with the Figure. Mid-log CFU values for the non-shown D39 curves were approximately $5 \times 10^9 \text{ ml}^{-1}$, which is comparable to the average FP22 mid-log CFU value of $6 \times 10^9 \text{ ml}^{-1}$.

All of the FP22 growth curves entered the exponential growth phase earlier than the D39 curves. This has been reported previously by Pearce *et al.* [95], where FP22 bacteria had an increased growth rate of 16.9% compared to D39. They proposed that this was due to increased efficiency of cell division as a result of the significant reduction in metabolic efforts typically required for capsule synthesis. The increase in rate in the growth curves described here (between Figure 2.6 and Figure 2.7 on page 73) could also be partly due to a higher number of bacteria in the inoculum: without the capsule, the bacteria can be smaller (see dry AFM images of bacteria in Section 3.1.1) and tend to clump together more, meaning that a colony of equal size and maturity to a D39 colony could contain more bacteria.

Growth curves were also used to determine when to aliquot and freeze down bacteria stocks. Aliquots were taken from a broth inoculated with colonies from an overnight growth of bacteria from the base stock. When the bacteria were in the mid-log phase and at an optical density of 0.6, 1 ml aliquots were transferred into sterile 1.5 ml Eppendorf tubes which were then stored at -80°C .

2.7.2 Harvesting and washing of *S. pneumoniae*

Once at OD 0.6, the Falcon tube containing the bacteria in broth was sealed shut and then centrifuged at 4000 r.p.m. (equivalent to 2880 g_n relative centrifugal force in the Sigma 3K18 model, where g_n is the acceleration due to gravity at the Earth's surface, taken to be 9.81 ms^{-2}) for 5 minutes with refrigeration set to 4°C . The supernatant was the poured off and the pellet resuspended in 2 ml of PBS and split into two 1.5 ml Eppendorf tubes. These suspensions were then centrifuged at 5000 rpm (equivalent to 2300 g_n in the Eppendorf 5415D model) for 3.5 minutes. The supernatant was then removed and each pellet resuspended in 1 ml of PBS before being centrifuged at 2300 g_n for a further 3 minutes. The supernatant was removed once again and each pellet resuspended in 1 ml of PBS, before being taken to the Department of Physics and Astronomy for the next phase of preparation described in Section 3.1 on page 80.

The above method was used for all experiments, with the exception of dry AFM imaging, for which the presence of the salt crystals in the cell suspension leads to crystallization upon drying and therefore makes imaging the bacteria very difficult. For this reason, for the dry AFM images, in the second wash, 18.2 M Ω deionised (DI) water was substituted for the PBS, and following the final centrifugation, the pellet was resuspended in 1 ml DI water.

2.8 *Leishmania* parasite methodology

2.8.1 *Leishmania* parasite culture

Culture and passaging

For initial work, parasites were cultured in the Medical School containment level 2 facilities at the University of Sheffield, following the procedure below. Stocks were maintained under liquid nitrogen in aliquots of approximately 5×10^7 parasites in 1 ml of heat-inactivated fetal bovine serum (HIFBS) (Thermo Scientific HyClone[®]), with 10 % Filter-sterilized dimethyl sulfoxide (DMSO) (Fluka, Switzerland).

To initiate a culture, a vial was removed from liquid nitrogen stores and thawed in hand before being added, dropwise, to 14 ml of unsupplemented buffered M199 medium in a 15 ml Falcon tube. Once the whole vial had been added to the medium, it was mixed using a whirlymixer and then centrifuged at 3000 rpm (equivalent to 1843 g_n relative centrifugal force in the Sigma 3K18 model) for 10 minutes. The supernatant was then poured off and the pellet resuspended in 1 ml of M199 before being added to approximately 10 ml of supplemented M199 medium (pH 7.2) in a non-venting 25 cm flask. The makeup of the supplemented M199 medium is given in Table 2.3.

Table 2.3: *Leishmania* parasite culture medium.

M199 medium (Thermo Scientific HyClone [®]) or Dulbecco's Modified Eagle Medium (DMEM, BioWhittaker [®] , Lonza)	
Amount	Supplement (Gibco [®])
10 % v/v	complement inactivated fetal bovine serum (FBS)
1 % v/v	1:1 penicillin and streptomycin
1 % v/v	Basal Medium Eagles vitamins
292 mg ml ⁻¹	L-glutamine (if not already included in medium)
4.5 mg ml ⁻¹	glucose (already included in DMEM)
(Optional) 1-2 % v/v	filter sterile human urine (not used for these experiments)

In standard *in vitro* culture conditions, at 26°C in sealed 25 cm flasks, the parasites normally reached the log growth phase during day two, continuing for one to two days. This phase corresponded to a high proportion of long (12-20 μm) promastigotes consistent with the nectomonad morphology (see Figure 1.9 for the different parasite morphologies). The stationary phase typically occurred after four or five days. Metacyclic parasites were the final promastigote lifecycle stage and transition to this morphology was typically observed at around 6 days post passage.

When the parasite density was $1 \times 10^7 \text{ ml}^{-1}$ (roughly once a week), the growth cultures were passaged by adding parasites from the current growth to supplemented M199 (pH 7.2) medium at a concentration of $5 \times 10^6 \text{ ml}^{-1}$.

Synchronous population transformation to the infectious metacyclic lifecycle phase (solely performed at the LSHTM) was enhanced by modifying the culture medium, replacing M199 with Graces' Insect Culture Medium (Invitrogen) with the

same supplements as in Table 2.3, excluding glucose and urine, adjusted to pH 5.5. This medium change is designed to mimic the loss of parasites during bloodmeal digestion and defecation by the sand fly. The capacity for infection of mammals with metacyclic-enriched parasites has been shown to be similar to that of sand fly-derived parasites¹.

The metacyclic culture was seeded by mid-log phase promastigotes from a M199 culture, with a predominance of nectomonad lifecycle forms and generally two or three days post passage. Parasites were harvested and washed three times in PBS by centrifugation at 3500 r.p.m. for 10 minutes before being adjusted to 5×10^5 cells ml^{-1} in the supplemented Graces' medium. After culturing in a sealed flask at 26°C for six to seven days, the culture generally contained 85 – 95 % metacyclic promastigotes.

Counting

To homogenize the parasite population and break up any large clumps of parasites before counting, the culture was swirled round in the flask before a sample was taken using a Gilson pipette fitted with a sterile disposable tip. Depending on the concentration of the parasites in the medium, the specimen was diluted with 4 % w/v paraformaldehyde (in PBS) in differing ratios, typically to a dilution of 1:2 or 1:3 parasites to 4 % w/v paraformaldehyde.

After mixing the paraformaldehyde solution with the parasites, approximately 10 μl was injected into the haemocytometer, using the pipette and a new sterile tip. The dilution should be such that there are approximately 100 parasites across the grid on the haemocytometer. Depending on the number observed, either parasites in the 4 corner squares and the central square were counted, or parasites in all 25 squares.

The parasite density, D (ml^{-1}), is given by:

$$D = \frac{25 \times 10^4 \times x \times m}{n} \quad (2.14)$$

¹M. Rogers, private communication.

where x is the number of parasites counted, n is the number of squares counted and m is the dilution factor.

Parasites used for final measurements

After the first few passages (approximately one passage per week), populations of parasites would stop undergoing the transition between distinct morphological stages during culture, instead defaulting into a procyclic-like paramastigote form (See Figure 1.9). This was not ideal, as it meant that comparing the interaction of different morphological stages was not possible.

In medical work, the parasites are regularly put through mammalian (murine) hosts to maintain viability and virility, and to ensure that they continue to undergo the full range of morphological variations after passaging. It was decided that murine passaging was not appropriate at the University of Sheffield due to the logistics of training and obtaining ethical approval without an overarching project based within the University. Therefore, for the final experiments, cryopreserved stocks of each lifecycle stage were obtained directly from the London School of Hygiene and Tropical Medicine. These stocks were stored under liquid nitrogen or in the -80°C freezer in the University of Sheffield Medical School and used directly after defrosting.

2.8.2 *Leishmania* parasite sample preparation

Parasites were immobilized by physisorption onto a pre-coated positively charged surface. To achieve this, glass slides were cleaned by sequential sonication in acetone, ethanol and water and dried under nitrogen gas flow. A freshly made solution of 0.2% w/v poly(ethyleneimine) (PEI, average $M_n \approx 60$ kDa and average $M_w \approx 750$ kDa, Sigma-Aldrich, UK) in 18.2 M Ω filtered water was sonicated for 10 minutes to mix, then added drop-wise to the clean slides. After 1.5 hours, the coated slides were well rinsed with pure water and dried under nitrogen gas flow. The prepared slides were either used immediately or left in a large polystyrene Petri dish at 5°C and used within a few days.

Parasites of a given lifecycle stage were taken out of either liquid nitrogen or -80°C stores and either the whole vial (e.g. if containing 1×10^7 parasites) was defrosted and added drop-wise into approximately 10 ml of room temperature DMEM growth medium, or, if the vial was to be re-used (e.g. if containing 5×10^7 parasites), upon removal from liquid nitrogen (or the -80°C freezer), the vial was kept on dry ice and some cells scraped out of the still-frozen suspension using a sterile cell loop. The scraped cells were transferred into room temperature growth medium with a total volume of 3 – 4 ml. The vial was quickly returned to the liquid nitrogen stores or -80°C freezer to minimize risk of cell damage by defrosting and re-freezing.

Following addition of parasites, the Falcon/Eppendorf tubes were gently shaken and left for a few minutes at room temperature ($\sim 27^{\circ}\text{C}$). After this time, the vial was shaken again to break up any cell clumps and the suspension was centrifuged at 3000 rpm (equivalent to $1620 g_n$ in the Sigma 3K18 model) for 8 minutes with refrigeration set to 4°C . Following this, the pellet was resuspended in 1 ml PBS and centrifuged at 3200 rpm (equivalent to $1000 g_n$ in the Eppendorf 5415D model) for a further 7.5 minutes. Following this, the pellets were resuspended in a total volume of approximately 100 μl PBS. More PBS was added to larger pellets in order to keep a relatively low parasite density so that individual parasites could be located easily for AFM i.e. parasites not in contact with any neighbours.

A small volume of the parasite suspension (no more than 100 μl) was added to the centre of the PEI-coated slide and left for between 1.5 and 2 hours to settle. This time was typically used to calibrate the cantilever on a clean glass slide, both in air and PBS. After the allotted time, the parasite-coated slide was gently rinsed with PBS before being transferred into the AFM for analysis.

Chapter 3

Development of methodology

3.1 *S. pneumoniae* sample preparation for AFM under liquid

Although mechanical trapping is fairly commonly used for bacteria [103, 201, 202, 204], it needs to be tailored to the bacteria in question. Trapping was unsuccessful with the two commercially available sizes of polycarbonate membrane most appropriate for use with *Streptococcus pneumoniae*. It was therefore decided that bacteria size estimation should be undertaken by imaging the bacteria in air, and that this should be used, in conjunction with images of membranes etched for different amounts of time in sodium hydroxide, to gauge the appropriate amount of etching to successfully trap the bacteria. No steps were taken to alter the hydrophobicity of the membrane. In addition to etching membranes, the method of filtration and sample assembly are also discussed below, as these were finalised after some trial and error employing different methods.

3.1.1 Optimization of mechanical trapping of *S. pneumoniae*

AFM of *S. pneumoniae* in air: cell sizes and morphology

To prepare the samples for dry AFM imaging, the cells were harvested as per Section 2.7.2, before approximately 100 μl was added to a glass slide which had been cleaned by sequential sonication (2510 ultrasonic cleaner, Branson, UK) in acetone,

ethanol and 18.2 M Ω DI water (NANOpure Diamond, Barnstead, Triple Red, UK) and dried under nitrogen gas flow. The cells were left to partially dry for 45 minutes to an hour at room temperature before imaging. All images were carried out within 1.5 hours of the start of imaging and were obtained using the D cantilever on a silicon nitride MLCT cantilever chip (Bruker, USA). All images were 512 \times 512 pixels (scan time \sim 8 min). The spring constant of the cantilever used to obtain the images contained within this section was measured as 37 pN nm $^{-1}$ using the thermal noise method (more information about this can be found in Section 2.4.1 on page 61).

Although the D39 bacteria are capsulated, at first look, the bacteria in these dry AFM images do not appear to have an obvious capsule, however, as the capsule is dehydrated, one would expect it to collapse onto the cell wall because the polymers are no longer solvated, and it is therefore feasible that it would not be clearly evident in the dry AFM images shown in Figure 3.1 on page 82. *Streptococcus mitis* is a capsulated [205], α -haemolytic viridans group *Streptococcus* bacteria which shares 99% of its 16S rRNA genes with *Streptococcus pneumoniae*, which is α -haemolytic but not a member of the viridans group [206]. Although the two species have different characteristics, *S. mitis* being primarily a dental biofilm-forming pathogen, topographical AFM images taken in air by Cross *et al.* [207] and more recently by Heim *et al.* [172], show wild-type *S. mitis* bacteria which look similar to the D39 *Streptococcus pneumoniae* bacteria in Figure 3.1, with paired conformation and without a clearly defined thick capsule layer. In their images, septum topology was more exaggerated than here, with raised rings (parallel to the septum) progressing towards the centre of each half of a diplococcus as the cells prepared to divide again. These rings are not visible in the D39 *S. pneumoniae* cells, but some ring-type features are visible on the FP22 mutant bacteria, particularly in the middle and bottom deflection images in Figure 3.3 on page 84, suggesting that there is capsule present on the D39 bacteria which is masking these shallower surface features.

A paper by Gupta *et al.* illustrates the capsule using fluorescently tagged polysaccharides, and in this image the bacteria appear in the form of a chain (Figure 3.2B). This chain formation is consistent with the AFM images of the D39 bacteria ob-

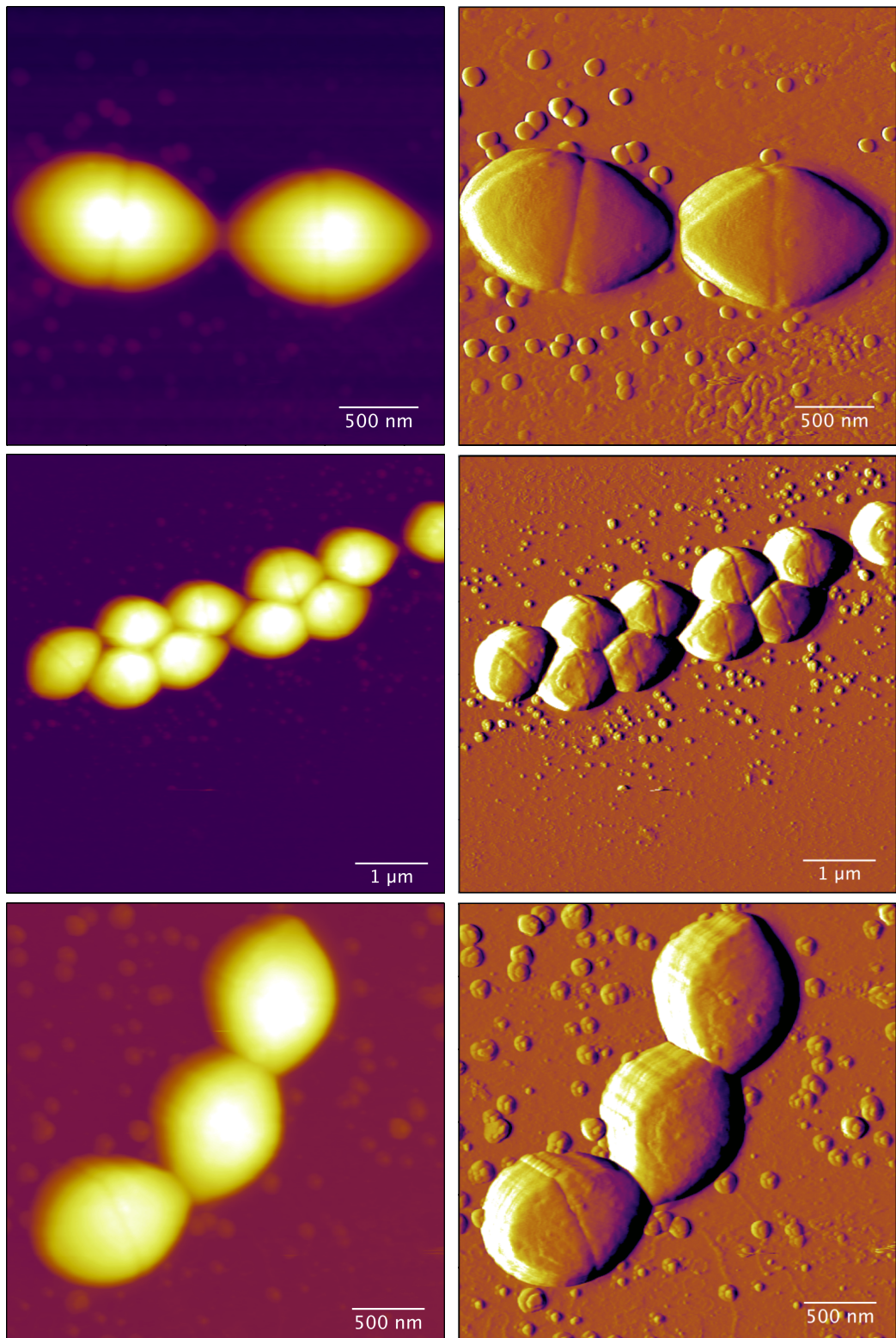


Figure 3.1: Contact (top pair) and tapping (two lower pairs) mode images of D39 *S. pneumoniae* taken in air on a glass slide. Height images on the left, deflection/amplitude images on the right. The bacteria are fairly consistent in shape, being rounded and similarly sized (~ 300 nm tall at the highest point). They tended to be found in pairs or short chains, which is consistent with the fluorescence images in Figure 3.9 on page 97.

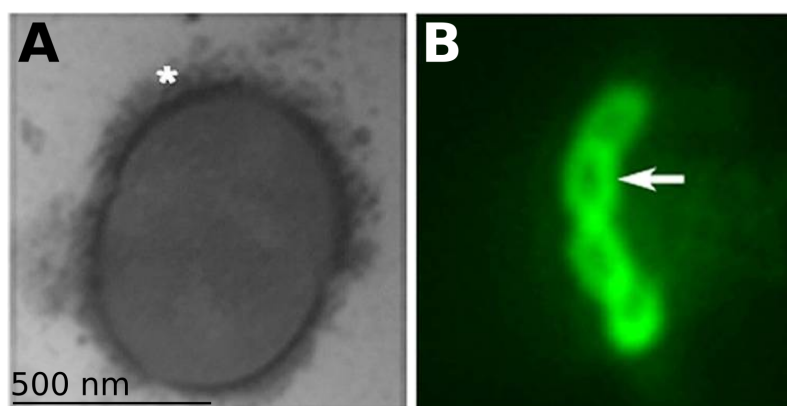


Figure 3.2: D39 *Streptococcus pneumoniae* capsule visualisation. A. Capsule detection by transmission electron microscopy (LRR fixation method). The capsule is indicated by an asterisk. B. Capsule staining using immunofluorescence with staining against pneumococcal type 2 capsule polysaccharides (indicated with an arrow). Reproduced from [208] with permission.

tained in air, shown in Figure 3.1, which contained a mixture of diplococci and small chains, and also with the fluorescent images shown in Figure 3.9 on page 97.

The FP22 bacteria have a different appearance to the D39s in air, having a very low “rim”-type feature around their exposed edges. They also appear flatter across the top, particularly for the larger cells. Both of these features could be due to the lack of a capsule leading to faster dehydration of the cells and less structural rigidity, so that after liquid has escaped from the centre of the cell, the bacterium has a higher tendency to collapse. The FP22s also appear to have a very different typical conformation, tending to prefer irregular clumps to the chain-type morphology of the capsulated bacteria. FP22 pellets were generally more difficult to break up and solvate, which might be partly due to this type of behaviour, with stronger bacterium-bacterium interactions.

Estimating cell size from the dry AFM images

By comparing Figure 3.1 and Figure 3.3 on pages 82 and 84, respectively, it is evident that the capsulated bacteria (D39s) have a much more regular cell size than their unencapsulated derivative (FP22s). The images used in these figures are representative of three separate experiments with bacteria grown from different stock batches.

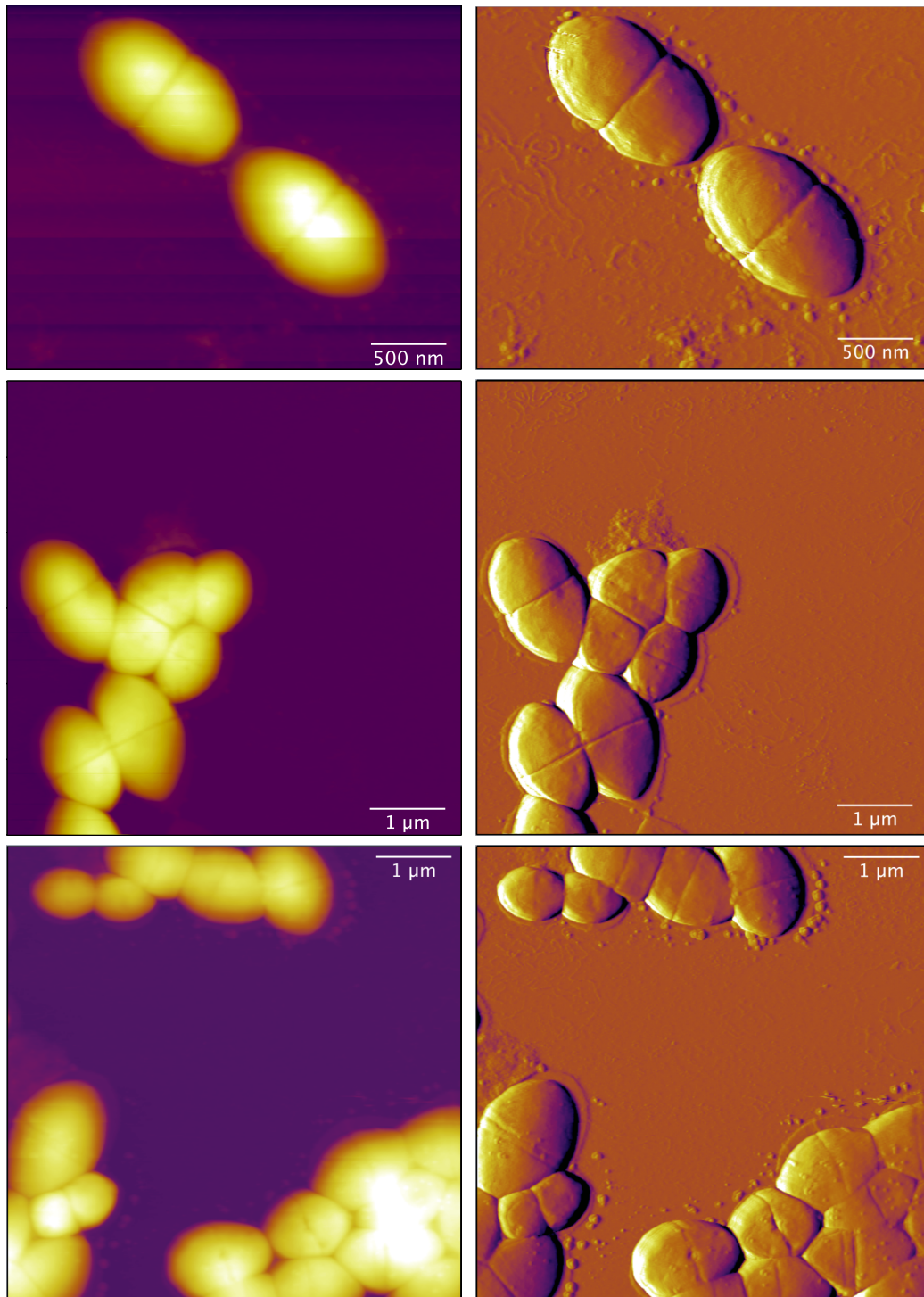


Figure 3.3: Tapping (top two pairs) and contact (bottom pair) mode images of FP22 *S. pneumoniae* taken in air on a glass slide. Height images on the left, deflection/amplitude images on the right. The bacteria here are strikingly different to the D39s, having much more size and shape variation both laterally and in height (200 – 300 nm tall at the highest point). They also generally appeared flatter, suggesting that they dehydrate more rapidly, presumably due to the lack of protective capsule. They tended to be found in larger clumps or in pairs, which is consistent with the fluorescence images in Figure 3.9.

The difficulty in processing the images in order to determine cell size is that the difference between a cell preparing for division and a diplococcus is a fine one, and a cell preparing to divide can be twice the size of a single cell. Automated size analysis was therefore deemed inappropriate in this case. Instead, cell sizes were estimated by taking sections across the widest and longest parts of the cell, and recording the distance between the two cell edges according to the height trace along the section. This only gave a very rough guide as to cell size: the D39 bacteria tended to be approximately 1.0 – 1.1 μm long and mostly between 0.8 μm and 0.9 μm wide, which is consistent with the generally accepted pneumococcal size range of 0.5 - 1.25 μm [209, 210]. The size of the FP22s varied more, but generally the average length was still around 1 μm (while there is no well defined size range for these mutants, other work using similar unencapsulated D39 derivatives shows cells with dimensions consistent with this value [59, 211]). It was therefore decided that the same polycarbonate membrane hole size should be used for both strains.

Polycarbonate membrane hole size as a function of etching time

Mechanical trapping is only successful when the membrane hole size matches the average cell size. The membranes used in this project were 2.5 cm IsoporeTM track-etched polycarbonate membrane filters (Millipore, UK) and the two considered for use with the *S. pneumoniae* bacteria were the 0.6 μm DTTP and the 1.2 μm RTTP options. The size of the holes was then increased from the stock size by etching in sodium hydroxide solution (NaOH) using the method described below, which was established by Dr Robert Turner [201].

To establish how the hole size varied with etching time, five of each membrane type were placed in a 10 cm diameter glass Petri dish. A 4 M solution of sodium hydroxide was made by adding NaOH pellets (Sigma-Aldrich, UK) to 18.2 M Ω DI water in a glass flask and mixing with a magnetic stirrer until the pellets had fully dissolved and the solution appeared clear and homogeneous. The NaOH was then transferred to the Petri dishes so that the membranes were well covered. The dishes were then closed and placed on a hot plate set at 25°C to regulate the temperature

(the ambient temperature of the lab was below standard room temperature, at 10 – 16°C). One membrane was removed every hour and rinsed sequentially in dishes filled with DI water before being placed in separate, semi-closed PS Petri dishes and being allowed to dry. Air-drying was used because the membranes became more fragile with increased etching time and had a tendency to fold and wrinkle if dried under a nitrogen gas flow.

Following etching, the membranes were attached to a glass slide using double-sided sticky tape and imaged dry using the AFM. Tapping mode images were deemed to be more noisy so contact mode was used. All images were 512×512 pixels and three $15 \mu\text{m}$ square images were taken of each membrane in different positions across the sample (note that the example image used in Figure 3.4 is a $10 \mu\text{m}$ square image with the larger pores to show the process more clearly).

Hole sizes were calculated automatically in ImageJ software, version 1.45. To do this, the height images were opened in the Asylum Research AFM software (run in Igor Pro, Wavemetrics, USA) and the scale adjusted so that the entire hole appeared black: at the next stage, the image is converted into a binary colour scale, so if any of the hole is not set to black, the hole size will be underestimated. Examples of incorrect (upper left) and correct (upper right) scaling are given in Figure 3.4 on page 87. Once the colour scales had been adjusted, the image was exported from Igor Pro as an image file and opened in ImageJ, where it was converted to a binary colour scheme (lower left, Figure 3.4) and the scale was calibrated. Most images had cases where two or more of the holes were joined together, and so to include any holes which were only partially joined so they could be included in the statistical analysis, the watershed function was applied (see the three holes in a row in the lower left image in Figure 3.4). At this point, the “Analyze particles” function was used to count the number of holes and provide their area. It was possible to constrain the the range of shapes to be included in the analysis and so to exclude any holes which were conjoined or overly distorted. To achieve this, a circularity range of 0.75-1.00 was applied (bottom right image, Figure 3.4): according to this scale, a value of 1.00 would indicate a perfect circle and 0.00 would correspond to an infinitely elongated

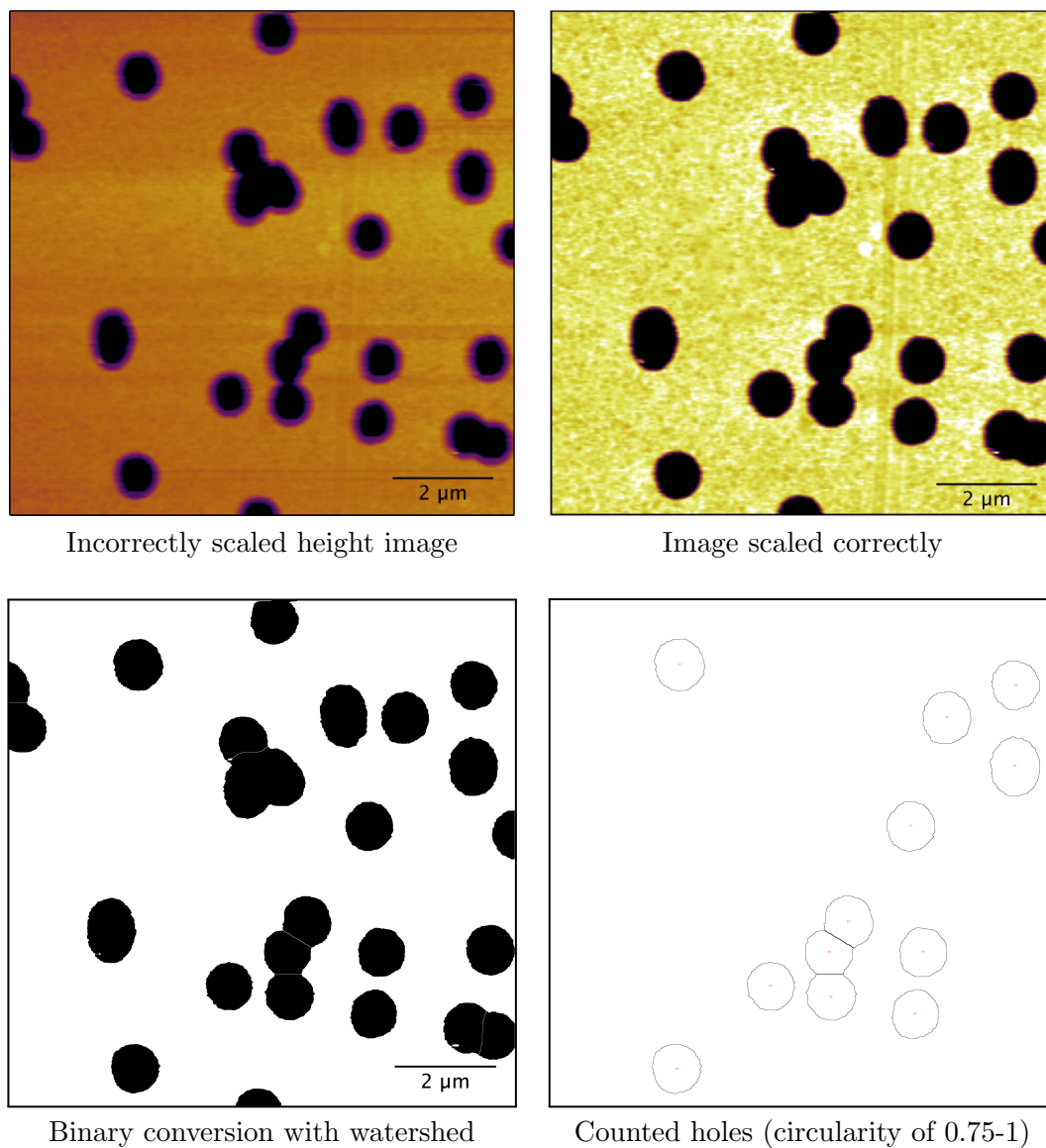


Figure 3.4: Example of the image processing used to determine average hole size for NaOH etching experiments. The chosen example is an unetched 1.2 μm RTTP polycarbonate membrane, top left: height image scaled incorrectly i.e. leading to underestimate of hole size when converted to binary. Top right: image scaled as used for all analysis, with hole size estimated more accurately. Bottom left: image converted to binary with watershed applied to break up joined holes, bottom right: numbered holes as included in the analysis, i.e. with a circularity of 0.75 – 1.

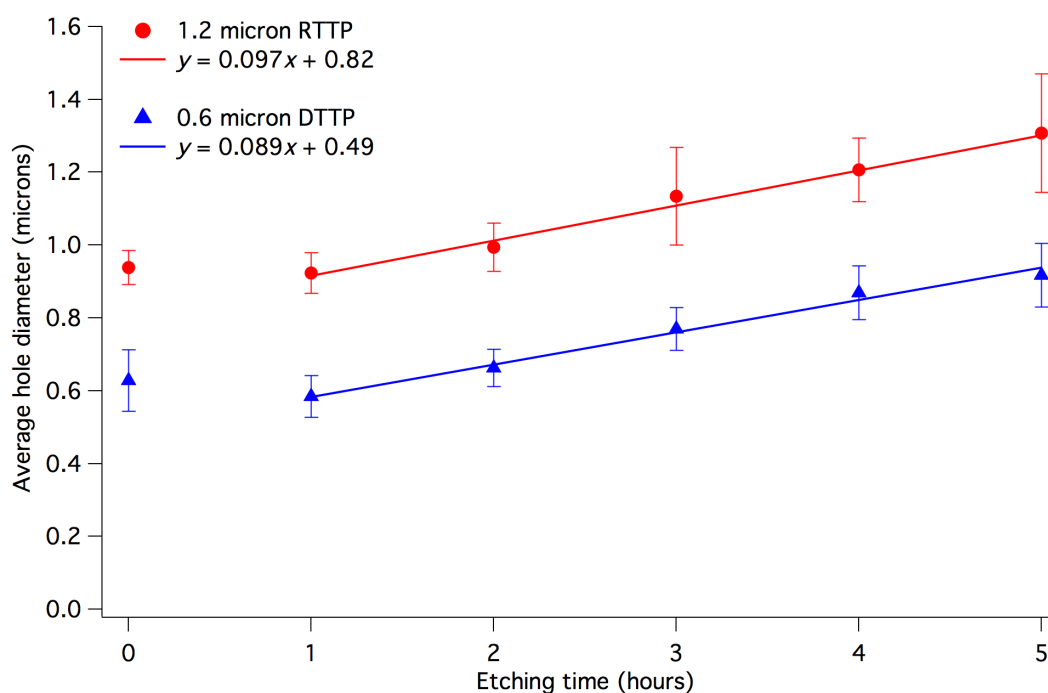


Figure 3.5: A graph showing the change in membrane hole diameter over immersion time in 4M NaOH. The data for the the 0.6 μm DTTP filter is given in blue, and 1.2 μm RTTP filter in red. The error bars show the standard deviation. The data, excluding the zero hour timepoint, was fitted with a weighted least squares fit, and the equations corresponding to the two fits are given in the key.

polygon. This criterion was important because hole diameter was calculated from the area, assuming the holes to be circular, and therefore including anything too distorted would have decreased the accuracy of the calculation. A lower limit was imposed on counted areas of $0.1 \mu\text{m}^2$ to exclude any black specks or small artefacts from being counted in the analysis.

The detailed count information was then exported into Microsoft Excel and the hole diameters were calculated from the hole areas. This value was then averaged and the standard deviation of the data recorded. This information is shown in Figure 3.5. The sample size was between 100 and 170 holes for the 0.6 μm filter and 50 – 100 holes for the 1.2 μm filter. The data were fitted in Igor Pro using a least squares fit weighted to the standard deviation of the datum, and the equations of these fits are shown on the graph. The zero hour timepoint was excluded because it did not fit with the trend in the rest of the data, and there was some slight initial hole shrinkage. This observation was consistent with earlier findings [201].

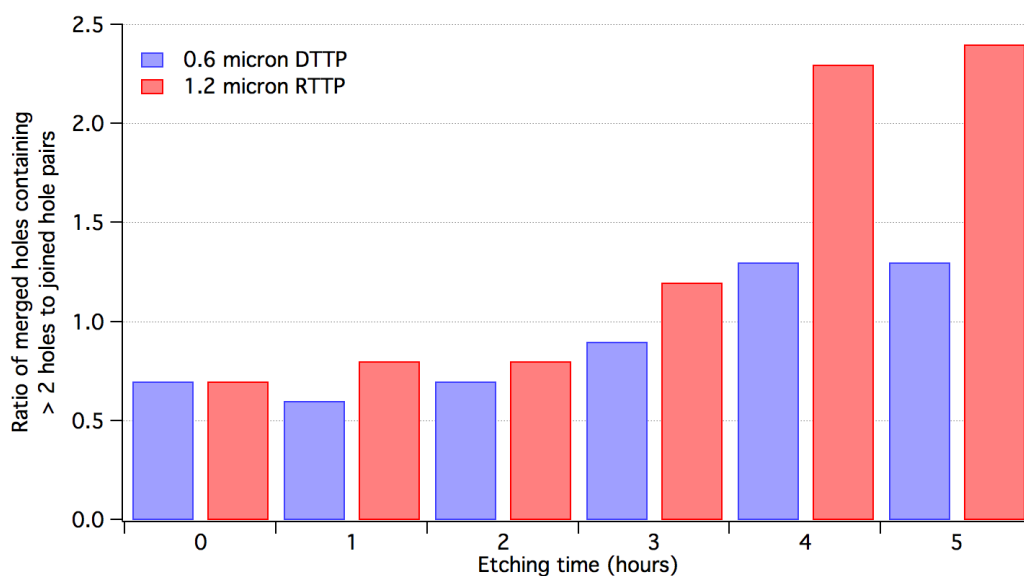


Figure 3.6: A graph showing the increase in the ratio of merged holes containing more than two holes to joined pairs with increased NaOH etching time for both the 0.6 μm DTTP membrane (blue) and the 1.2 μm RTTP membrane (red). The proportion of large joined holes increases more significantly for the 1.2 μm membrane compared to the 0.6 μm membrane, and both increase with longer etching time. The number of joined pairs did not show any significant trend over time for the either membrane.

The increase in hole size with time was fairly similar for both membranes, with the larger initial hole size increasing in diameter slightly more rapidly: a rate of $0.097 \mu\text{m h}^{-1}$ for the 1.2 μm compared with $0.089 \mu\text{m h}^{-1}$ for the 0.6 μm filter. It should be noted that the membranes became more fragile the longer they were immersed in the 4M NaOH, making the samples from the later timepoints more difficult to handle. Therefore, although the same hole diameter could be achieved with a smaller initial hole size as well as a larger initial hole size, in terms of handling practicality, this was not advisable.

In addition to increased hole diameter, with increased etching time, while the number of merged hole pairs did not show any real trend, the ratio of the number of sites containing more than two merged holes and the number of merged pairs did increase, and this is shown in Figure 3.6. This figure shows that the number of merged sites containing > 2 holes became greater than the number of sites with 2 merged holes at 3 h for the 1.2 μm membrane, and 4 h for the 0.6 μm membrane. After this point, the number of sites containing > 2 holes in the 0.6 μm membrane

appeared to stabilize, but continued to increase for the 1.2 μm membrane, so that there were more than double the number of sites with > 2 holes than merged pairs. This increased the membrane instability and would have allowed more cells to pass through the larger holes in the membrane and possibly affect the efficacy of the trapping. Therefore an ideal upper limit of 3 hours etching time was chosen.

Matching cell size with membrane etching time

To select the ideal match of membrane to cells, the diameters of the bacteria and the hole were compared: the *S. pneumoniae* cell size was typically between 1.0 and 1.1 μm , which was only within the ideal 3 hour etching range for the 1.2 μm RTTP filter. The 0.6 μm DTTP filter was therefore discounted. Using the equation of the line of best fit from Figure 3.5, it was predicted that 2.5 hours etching in 25°C 4M NaOH would create an average hole size of 1.06 μm , which was in the middle of the ideal size range. This method was therefore used to prepare all of the membranes for the *S. pneumoniae* experiments. Membranes were typically batch processed in groups of 6-8 filters (3 or 4 per 5 cm Petri dish) and stored in polystyrene Petri dishes before use.

3.1.2 Bacterial filtration

Initial method

Initially, the sample was prepared via filtration of the bacterial suspension through a sterile, disposable syringe (Plastipak, BD, USA) fitted with a 25 mm filter holder (Sartorius Stedim Biotech GmbH, Germany) containing the desired polycarbonate membrane, as described in [212]. Because of the structure of the filter holder, flow was restricted in certain areas of the sample, forming bacteria-free areas in a regular pattern across the polycarbonate membrane and therefore making it more difficult to locate bacteria without simultaneously employing fluorescence imaging to map the bacteria-free areas of the sample.

The poor bacteria location rate for samples made with this filtration method

led to the adoption of the route favoured by the Dufrene research group, at the Université catholique de Louvain, which works on the same principle, but uses a glass filter holder assembly, as shown in Figure 3.7 on page 92. This means that the whole central portion of the polycarbonate membrane is exposed to the cell suspension and also the pressure used to filter the suspension is higher and more regular than when manually depressing a syringe plunger.

Final method

A 15 ml capacity Glass Microanalysis Filter Holder assembly comprising of a fritted glass support, funnel and metal spring clip (Millipore, UK), was fitted onto a conical filter flask that had already been connected to a diaphragm pump (Vacuubrand, Germany). The filter membrane was placed on the fritted glass base, then the funnel was put on top and the assembly was secured using the spring clip. Before use, the membrane was immersed in the PBS solution used to buffer the bacteria (the same as used during cell washing and AFM) to remove any residual dust particles and static charge before sample preparation.

Two methods were used for filtration, as shown in Figure 3.7 on page 92. For the capsulated D39 pneumococcus, 0.4 – 1 ml of bacterial suspension was added to the funnel and the vacuum pump turned on. After 15 – 60 s the liquid was sucked into the filter flask, leaving a visible collection of cells on the membrane surface. The membrane was then removed and rinsed sequentially in PBS-filled polystyrene Petri dishes until the opaque white layer of cells was no longer visible, at which point, the underside was dried on a paper towel and it was transferred to the pre-prepared substrate.

The FP22 bacteria clumped together more easily than the D39 bacteria when suspended in PBS and therefore were harder to dislodge from the membrane when they had formed an artificial biofilm. This led to too many bacteria remaining on the membrane surface even after vigorous rinsing, and a higher number of damaged bacteria. AFM interrogation of single cells was therefore very challenging, and so the filtration method was adapted to reduce the number of bacteria used to make

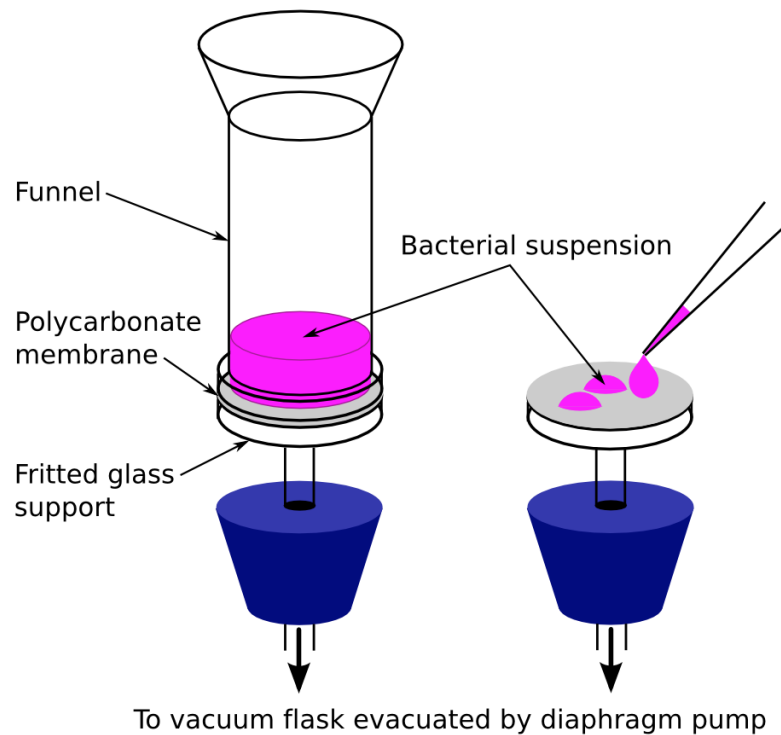


Figure 3.7: Different vacuum filtration methods used for D39 (left) and FP22 (right). The left diagram shows the funnel and fritted glass support, with the membrane in position between the two components. The spring clip securing the glass pieces together has been omitted for clarity. In the right hand image, the upper funnel piece is not used, only the fritted glass support with the membrane placed on top. Individual 50 μ l drops of cell suspension are dropped onto the central area of the membrane using a Gilson pipette and sterile disposable tip.

the sample, ensuring that the layer of bacteria was not too thick to remove during the PBS rinsing steps. The modification employed was simply to remove the funnel, allowing more controlled deposition of the bacteria across the filter surface. This was done by adding approximately $6 \times 50 \mu\text{l}$ drops to the filter using a Gilson pipette and sterile disposable tip (see Figure 3.7 on page 92).

3.1.3 Sample assembly

The final method of sample assembly was reached after several unsuccessful trials. Initially, the polycarbonate membrane was attached using thin magnetic strips in a triangle around the central area, but this did not hold the sample still enough to allow for high resolution images and force maps. Following this, several brands of double-sided pressure sensitive adhesive tape were tested, sticking the polycarbonate membrane to a glass slide. However, most brands failed to attach to the slightly damp sample, with ScotchTM tape (3M, US) being the most successful. Even this tape had a tendency to detach from the glass slide during scanning, leaving the sample floating in the PBS solution and therefore preventing successful scanning. The only test surface that the tape remained stuck to throughout imaging under liquid was a polystyrene Petri dish. However, because of the size of the AFM sample stage, it was still necessary to use a glass slide to support the sample, and the raised ridges around the circumference of the Petri dish led to some vibrational noise as the surface the sample was attached to was not flat on the glass slide.

The final arrangement of the base for the polycarbonate membrane combined all of these features and consisted of a glass microscope slide, onto which a 1×2 cm-sized flat piece of polystyrene Petri dish was attached using ScotchTM double sided tape, with a further strip of double sided tape placed on top of the Petri dish. Care was taken to ensure the tape sat flat on the surface, without any air bubbles or stretched and distorted areas.

Once the membrane had been placed very carefully on the tape to minimise air bubbles beneath the flexible sample, the membrane not directly on the taped area was trimmed off using a clean blade to reduce the chance of it floating and interfering

with the scanner head. The edges of the bacteria-containing area were also marked by scoring with a needle or a blade. At this point, the sample was rehydrated with approximately 300 μl of PBS and transferred into the AFM for analysis.

3.1.4 Successful trapping: AFM images of *S. pneumoniae* D39 in a polycarbonate membrane under PBS

The images shown in Figure 3.8 on page 95 were taken after standard sample preparation, and show some successfully mechanically-trapped bacteria under PBS. There is clear variation in the surface characteristics of the trapped bacteria, and we can assume that this variation is also present in the bacteria considered by the force maps. Any difference in molecule populations on the bacterial surface is likely to translate into different molecules dominating the tip-surface interaction, therefore some variation in adhesive behaviour between individual bacteria should be expected within a given population.

The images presented in Figure 3.8 are either 256×256 or 512×512 pixels and were obtained using tapping mode in PBS. They are a mixture of height and amplitude images (amplitude is equivalent to deflection images in contact mode), and contain trace and retrace images, which are obtained as the tip raster scans from left to right (trace) and right to left (retrace) across the sample to build up the image. This is important because it gives a sense of how loose the polymers are which coat the bacterium: if the image is distorted with material being dragged in the direction of movement, the surface is generally very soft and made up of loose, tethered polymers, consistent with a thick capsular layer. If the image is fairly consistent when scanned in both directions, it suggests a firmer surface consistent with a thinner capsule or where the capsule might have been detached or damaged during sample processing. Typically, it is easier to get clear images of the latter type, because of the movement in the capsular polymers, so although both types are equally represented in this figure, there was a general abundance of the bacteria coated in loose material. These images are not representative of the sample population considered when obtaining force data because, when mapping forces across the sample, no

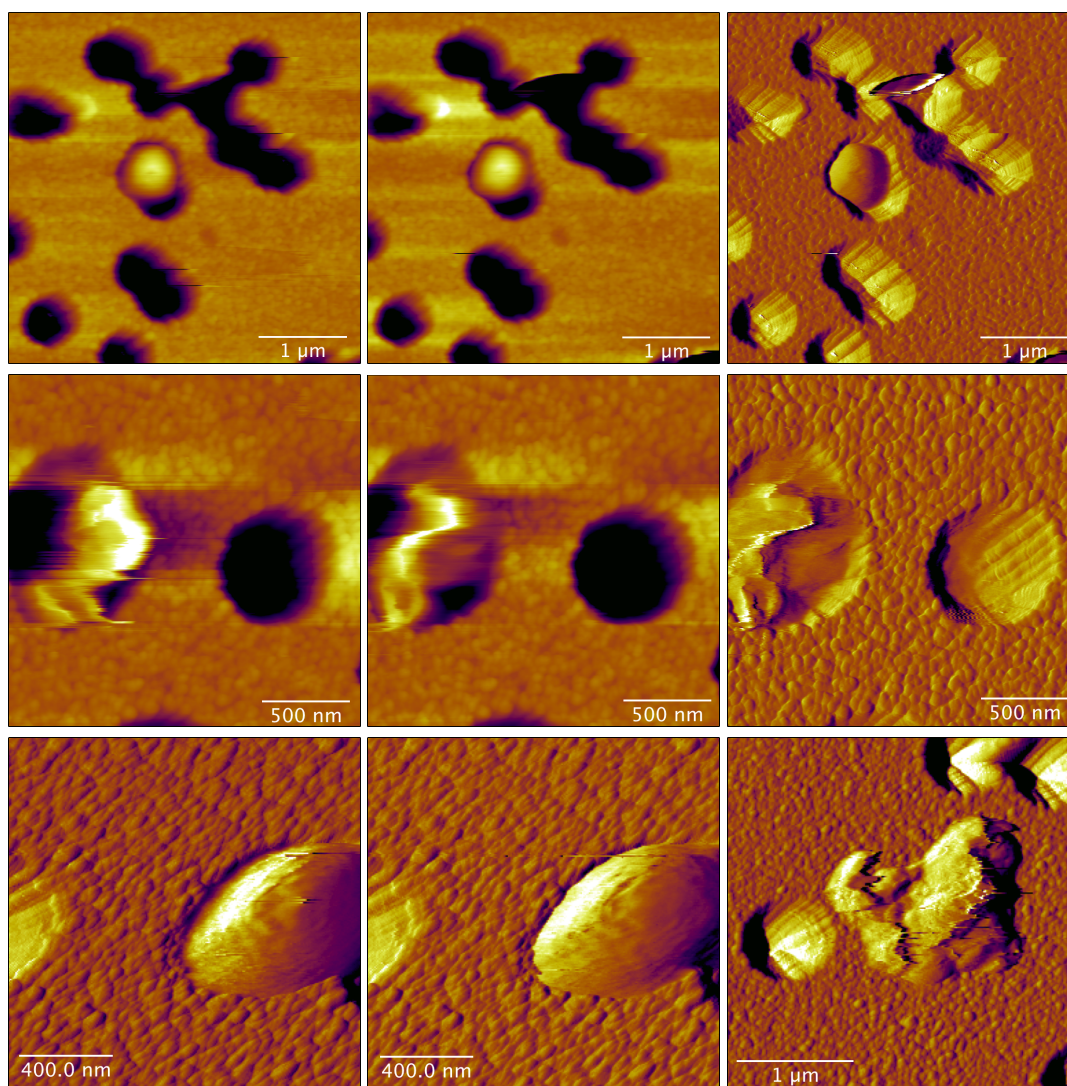


Figure 3.8: Tapping mode images of D39 *S. pneumoniae* taken in PBS after being trapped in etched polycarbonate membranes. The first two rows consist of (from left to right) trace and retrace height images and an amplitude image from the same scan. The bottom row shows two different bacteria: the first two are trace and retrace amplitude images of the same bacterium, and the bottom right image shows a suspected diplococcus on the surface of the membrane. The level of capsule present on the bacteria appears to vary, with some (bottom right, middle row) showing a much looser polymer surface compared to other, much neater-looking bacteria (remaining images).

contact or tapping mode images were obtained and so a higher number of cells with loose surface material are likely to have been probed. Force data experiments are not as dependent on a stable surface because there is little lateral movement when in contact with the sample.

3.1.5 Live/dead staining

Fluorescence imaging was undertaken in the department of Animal and Plant Sciences with the assistance of Dr Ana Lorena Morales García. SYTO[®] 9 and propidium iodide (PI) were added to *S. pneumoniae* cells that had been harvested at an O.D. of approximately 0.6 and resuspended in PBS. The sample was then prepared as normal using the stained cells, but instead of the membrane being placed on a Petri dish fragment, it was placed directly onto a glass microscope slide and not stuck down with double sided tape.

Images were obtained using two different illuminations and could not be obtained simultaneously, with the different channels requiring a manual switch over. The two channels were excited using UV illumination and Olympus WIBA (green) and WIG (red) filter cubes, and images were either taken at 10× or 40× multiplication. Only the excitation wavelength was changed when switching between the two modes such that the two images were co-located. Images were taken of live bacteria in the membrane (Figure 3.9C and D), and of the bacterial suspension dropped onto a microscope slide with a cover slip added on top (Figure 3.9A, B, E and F), and of a scrape performed using a cover slip (images not shown), both for live cells and cells (Figure 3.9A and B) which had been treated for an hour with ethanol before staining (Figure 3.9E and F).

The most surprising result was that although the membrane appeared to have a disc of more opaque material in the centre, consistent with the appearance of the filters used in AFM, only a few bacteria could be discerned when viewed under the fluorescence microscope. This could be in part due to the autofluorescence of the membrane itself making any bacteria harder to distinguish, but low bacteria numbers could explain why locating a bacterium using AFM was often a time consuming

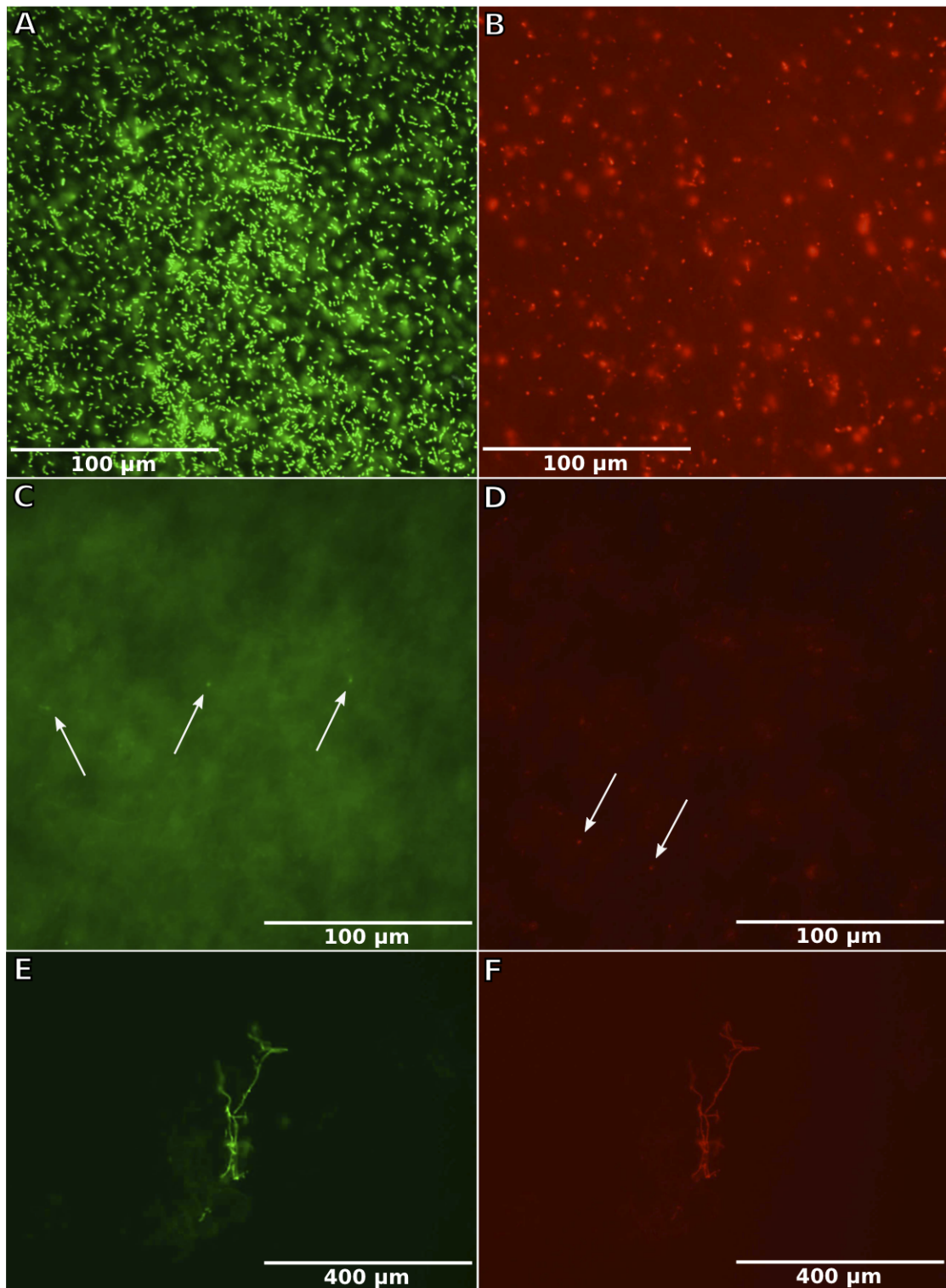


Figure 3.9: Fluorescence images taken under WIBA (green) and WIG (red) filters showing *S. pneumoniae* bacteria co-stained with SYTO[®] 9 (nucleic acid stain: live and dead) and PI (stains damaged/dead bacteria). A & B: live FP22 bacteria on a glass slide under a cover slip. Note the presence of diplococci and small chains. Similar images were obtained for D39 bacteria. C & D: D39 bacteria in situ on a polycarbonate membrane. Note the membrane autofluorescence. 3 live bacteria and 2 suspected dead bacteria (although these do not also appear in in the WIBA-filtered image) are indicated with arrows in C & D, respectively. E & F: inactivated D39 bacteria that show colocalized staining with PI & SYTO[®] 9.

process and was sometimes completely unsuccessful. It is possible that the benefits of mechanical trapping requiring minimal surface modification are outweighed by the need for a higher ratio of successful to unsuccessful experiments, and a covalent attachment method might be more convenient.

Under the WIG filter, only fluorescence emitted by propidium iodide is detected, indicating the presence of bacteria with damaged membranes as PI only penetrates these compromised bacteria, whereas the WIBA filter allows detection of the SYTO[®] 9 nucleic acid stain, which should stain both live and dead Gram-negative and Gram-positive bacteria (i.e. with intact or damaged membranes). Co-staining can reduce SYTO[®] 9 stain fluorescence. This should mean that it is possible to determine the fraction of live cells after sample preparation by comparing the ratio of cells stained both red and green (dead or with damaged membranes), and those which only fluoresce green (live and undamaged).

Cells which fluoresced red did not always co-locate with cells which fluoresced green, suggesting that the focal plane might have been slightly altered for the two conditions, as the SYTO[®] 9 appeared to have good coverage of the cells, as shown in Figure 3.9A and B. Successful co-location of fluorescence is shown in Figure 3.9E and F, where the cells had been exposed to ethanol before imaging in order to inactivate them. The high number of live cells in Figure 3.9A and B suggest that the cells were still live several hours after being harvested and suspended in PBS. Further to this, the presence of live bacteria in the polycarbonate membrane prepared as for the AFM experiments suggests that at least some of the bacteria examined with the hydrophobic and hydrophilic AFM tips were alive, and were therefore undamaged by the process of filtration.

3.2 Glassware and substrate cleaning protocol

Before use in any synthesis or tip coating, glassware was cleaned using one of three methods. Freshly cut silicon substrates were always cleaned in piranha solution comprised of 70 % sulfuric acid (99 % w/v) and 30 % hydrogen peroxide (35 % w/v), in which they were left for 30 minutes to an hour before being rinsed copiously with

18.2 M Ω DI water, then rinsed with acetone and dried under a nitrogen gas flow. The substrates were then placed in a clean glass Petri dish which was sealed by wrapping in foil.

Glassware required for alkanethiol deposition or glycopolymer synthesis was rinsed with the reaction solvent it had been used for, e.g. ethanol for MUA or DDT deposition, toluene for APTES initiation, etc. (typically the same rinsing steps as performed on the samples were also applied to the glassware immediately after use, details of which can be found in the relevant methodology sections). Following rinsing, the glassware was washed using a dilute solution of decon90 (Decon Laboratories Ltd, UK), rinsed well with water and dried, before either being cleaned with piranha solution, methanol-hydrochloric acid solution, or by using the RCA method. A standard rinsing protocol was employed after all methods: items were thoroughly rinsed with copious amounts of 18.2 M Ω DI water, followed by an acetone rinse, after which the items were dried under a nitrogen gas flow and wrapped in foil to prevent recontamination before use within a week.

In the methanol protocol, the glassware was immersed in 1:1 methanol:hydrochloric acid (35 % w/v) for an hour. The RCA method used a 5:1:1 ratio of DI water: ammonia: hydrogen peroxide (35 % w/v). This was mixed in a very large clean beaker and the glassware was added before heating to approximately 80°C on a hot plate inside a fume cupboard. This temperature was maintained for 15 minutes. After this time, the hot plate was turned off and the liquid allowed to cool before the standard rinsing steps were undertaken.

AFM cantilevers are much more delicate than the other materials used and, when cleaned with piranha, seemed to be more susceptible to bending during polymer coating. This bending was so severe that the deflection could not be adjusted enough in the MFP-3D to compensate and reflect the laser fully onto the photodiode. The MFP-3D has a fairly low tolerance to bent cantilevers as the mirror that reflects the laser onto the photodiode is fixed in one position. Piranha-cleaned cantilevers have also been shown to be more at risk of tip damage leading to imaging artefacts [213], and the excessive handling necessary for piranha cleaning also re-

duced the number of viable cantilevers before chemical functionalization. To reduce the chance of over-bending and other issues associated with piranha-cleaned AFM tips, before use, cantilevers from a new box were cleaned for 15 min in an oxygen plasma cleaner which was custom made in-house for use by the Soft Matter group. Plasma cleaning is also an established method for cantilever cleaning before coating or use in experiments where a well characterised tip surface is required [36,214].

3.3 PMAA brush synthesis

Polymethacrylic acid (PMAA) was selected for the polymer backbone of the glycopolymers in the parasite experiments because it is hydrophilic in nature, can be grown into dense polymer brushes via grafting-from ATRP synthesis (where the polymer is grown *in situ* on the sample surface i.e. silicon wafer or AFM tip), and the chemistry required to attach sugar amines to the polymer chain is uncomplicated. All glycopolymer synthesis was performed in the Department of Physics and Astronomy at the University of Sheffield.

Initially, PMAA brushes were synthesized using ATRP of *tert*-butyl methacrylate followed by hydrolysis to PMAA, as described in the following section. However, this method proved unreliable and, although generally successful for silicon wafer substrates, often resulted in unusable AFM cantilevers due to overbending during the polymerization or failure of the polymerization. Various other synthesis routes were tested before the route described in Section 3.3.2 on page 104 was selected for its simpler nature and much higher success rate. This change in synthesis route increased the cantilever survival rate from < 20% to > 80% and was key to the success of the *Leishmania* parasite experiments.

In order to monitor reaction success, each reaction was performed with both AFM cantilever chips and silicon wafer sections in the same environment. Combining the silicon wafer (i.e. planar surface) with the cantilever chips in one cell meant that techniques requiring a relatively large planar surface (e.g. ellipsometry and optical tensiometry) could be employed to check the properties of the finished brush, and therefore quickly determine whether the reaction had been successful. More

in-depth analysis of the chemical bonds and structures present within the brush was completed during the development of the glycosylation protocol while on a collaboration visit to Durham University (see Section 3.3.4 on page 112).

Cantilevers were not characterized directly due to their fragility and small size; even if the cantilever chip body were able to have been tested, the actual coating on the tip of the cantilever could only be examined by techniques such as scanning electron microscopy or perhaps secondary ion mass spectrometry (SIMS), which would be impractical to do either before or after use in the AFM, because of the risk of damage to the tip and the necessity of decontamination after having been in contact with the parasites, which could damage the coating. However, since the cantilever and tip surface is Si_3N_4 , they should be coated similarly to a silicon wafer during the synthesis route, and, to an approximation, the coatings should be comparable, especially because the wafer and cantilever were kept together in the same reaction vessel. Additionally, AFM control experiments were undertaken using glycopolymer-coated tips and lectin-coated surfaces to check that the glycopolymer-coated tips were capable of selectively binding to their specific lectin, and that the levels of non-specific adhesion (to mica or when the lectin-binding was blocked by free lectin or sugar) were negligible. These experiments are discussed further in Section 5.2.

Silicon wafers with a thickness of $425 \pm 25 \mu\text{m}$ and a native oxide layer on the surface (Prolog Semicor, Kiev, Ukraine), were cut to approximately $0.5 - 1 \text{ cm} \times 1 \text{ cm}$ and 3 wafers were included with a batch of 5 MLCT cantilever chips (Bruker AFM Probes, USA) per reaction cell. The silicon wafers were cleaned by immersion in piranha solution, and all glassware was cleaned before use, as described in Section 3.2 on page 98. Cantilevers were from a fresh box and were exposed to oxygen plasma produced by an in-house plasma cleaner for fifteen minutes directly before use.

3.3.1 Original synthesis method: ATRP of *t*BMA and subsequent hydrolysis to PMAA

Both the initiation and polymerization stages of this method required an inert, reduced oxygen environment, so the reaction vessels were degassed by a continuous nitrogen flow for at least 15 min before use (shown in Figure 3.10). The reagents and quantities used in the synthesis are given in Table 3.1. All water used during the synthesis was > 15 M Ω DI filtered water, and all reagents were purchased from Sigma-Aldrich, U.K., unless otherwise stated.

Table 3.1: Reagents for original PMAA brush synthesis

Amount	Reagent
Initiation of substrates	
10 ml	anhydrous toluene $\geq 99.8\%$
25 μ l	allyl-11-undecane bromoisobutyrate (synthesized in-house as per [215])
50 μ l	triethylamine $\geq 99\%$
Polymerization of <i>t</i>BMA	
50 mg	copper(I) chloride 97.0 %
10 ml	<i>t</i> -butyl methacrylate (<i>t</i> BMA) $\geq 98\%$
5 ml	1,4-dioxane $\geq 99.0\%$
100 μ l	<i>N,N,N',N'',N'''</i> -pentamethyldiethylenetriamine $\geq 99\%$
Hydrolysis of P<i>t</i>BMA to PMAA	
0.38 g	<i>p</i> -toluenesulfonic acid $\geq 98.5\%$ (made up to 0.2 M)
10 ml	1,4-dioxane $\geq 99.0\%$

Initiation of substrates

The initiator, allyl-11-undecane bromoisobutyrate (which has a bromine end group and adsorbs to silicon surfaces [216]) was synthesized in the Department of Chemistry with the help of Andrew Pryke, following the route described by Ell *et al.* [215]. The distilled initiator was stored in an ampoule at 5°C, under nitrogen. Small amounts were removed under nitrogen flow using a 12 inch needle and glass syringe when required. The chemical structures of the initiator layers used in this and the improved PMAA brush synthesis routes can be found in Figure B.2 in Appendix B on page 243.

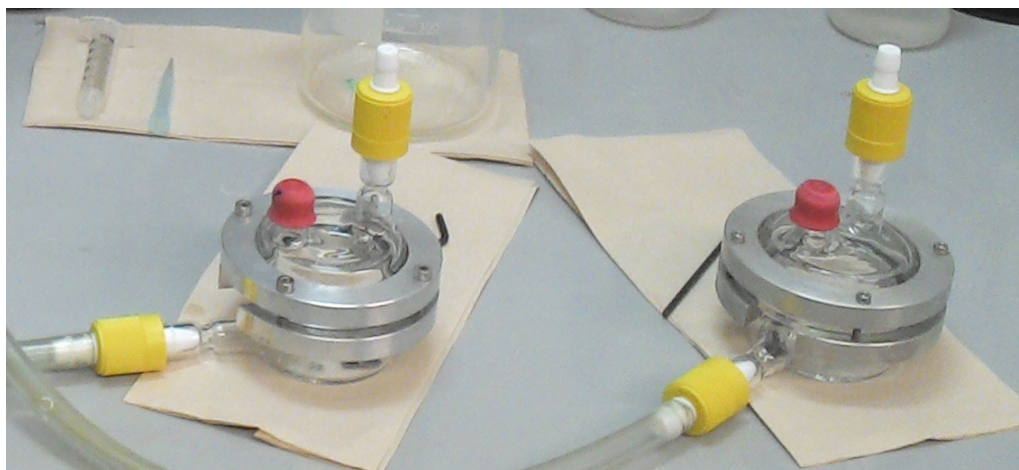


Figure 3.10: Photograph of two reaction cells containing cantilever chips and silicon wafers, being degassed by a nitrogen gas flow.

Silicon wafers and AFM cantilever chips were transferred to the base of the custom-made reaction cell before the lid was clamped on and the cell was degassed by attaching a nitrogen line to the lower Young's tap so that the gas flowed through the cell and out of the top tap (the reaction cell and degassing set up is shown in Figure 3.10). Anhydrous toluene, initiator and triethylamine were injected into a degassed Schlenk tube with ground glass top and stopper and stirred for a minute or two to mix well. The Young's taps on the reaction cell were closed and the initiator mixture injected into the cell via the Suba-Seal. The seal was then covered with Parafilm and the cell placed in the refrigerator for 6 hours at 5°C. The initiated wafers and cantilever chips were then rinsed with toluene and absolute ethanol and dried under a gentle nitrogen stream.

Polymerization of *tert*-butyl methacrylate brushes

The wafers and AFM cantilevers were placed into the reaction cell and degassed for 20 minutes. The taps were then closed and the cell transferred to an oil bath at 50°C. Copper chloride and a magnetic stir bar were added to a degassed Schlenk tube and exposed to nitrogen flow for a further 15 minutes. The 1,4-dioxane was degassed separately using a sparger then injected into the Schlenk tube and mixed with the copper chloride. The *N,N,N',N'',N'''*-pentamethyldiethylenetriamine was

also added to the Schlenk tube at this point.

The *tert*-butyl methacrylate was degassed using the sparger before being added to the Schlenk tube. Once the nitrogen flow to the Schlenk tube containing the mixture was stopped, the side arm tap was closed and the main stopper clipped in place. The mixture was stirred for another few minutes then left for 30 minutes to an hour to let any particulates settle. The particulate-free mixture was then injected into the reaction cell and Parafilm placed over the Suba-Seal. The cell was left in the oil bath overnight.

Following removal from the cell, wafers and AFM cantilevers were cleaned using 1,4-dioxane and dilute acetic acid (1:9 glacial acetic acid to water). They were then rinsed with water and ethanol and dried under a gentle nitrogen stream.

Hydrolysis to poly(methacrylic acid) brushes

The wafers and cantilever chips were placed in the reaction cell while *p*-toluenesulfonic acid and 1,4-dioxane were mixed in a glass vial using a magnetic stirrer. The solution was then poured over the samples and the reaction cell closed. The cell was placed in a pre-heated oil bath at 90°C and left for 24 h.

Once the cell was removed from the oil bath and cooled, the samples were cleaned using 1,4-dioxane and ethanol and dried under a gentle nitrogen stream. They were stored in clean 5 cm Petri dishes until use.

3.3.2 Improved PMAA brush synthesis route

The synthesis route described above failed to provide brushes of sufficient quality and homogeneity, and there was significant variation between different batches. A new method (which still used surface-initiated ATRP) was therefore adopted, and all of the data presented as part of the *Leishmania* results were obtained using tips coated by this route. This method, developed by Paul Chapman at the University of Sheffield, allowed for greater control of the polymer brush length and was more reliable [217]. It also had fewer complicated steps so the chance of dropping or breaking cantilevers during rinsing or drying between reaction stages was reduced.

The reagent quantities required to coat 10 cantilevers and 4 – 6 control wafers in 2×5 cm Petri dishes and $2 \times$ reaction cells are given below in Table 3.2 (the cantilevers and wafers were kept in their allocated groups throughout the process to reduce variability between cantilevers from the same cell at the end of the synthesis). Dry reagents used in the polymerization were stored in a dessicator to retain viability and absolute ethanol and methanol were used interchangeably when rinsing.

All required glassware and silicon wafers were cleaned the day before the synthesis by RCA and piranha, respectively. The inhibitor (250 ppm hydroquinone monomethyl ether) was also stripped from the monomer the previous day by passing it through an alumina column (Al_2O_3) with glass wool at the base to prevent contamination of the product with Al_2O_3 . The stripped MAA was kept in the fridge overnight and defrosted before use. The working temperature of the lab where the synthesis was completed was generally 8 – 14°C, so the MAA generally had to be defrosted in another laboratory.

Table 3.2: Reagents for improved PMAA brush synthesis.

Amount	Reagent
Formation of APTES layer	
40 ml	toluene $\geq 99.5\%$
0.4 ml	(3-aminopropyl)triethoxysilane (APTES) 99 %
Initiation	
40 ml	dichloromethane $\geq 99.5\%$
0.4 ml	triethylamine $\geq 99\%$
0.4 ml	α -bromoisobutyryl bromide 98 %
Polymerization of MAA	
10 ml	methacrylic acid (MAA) 99 % (inhibitor removed)
20 ml (approx.)	6 M sodium hydroxide ($\geq 98\%$ made up with DI water)
10 ml	methanol $\geq 99.8\%$
0.23 g	copper(I) chloride 97.0 %
0.13 g	copper(II) chloride 97.0 %
1.1 g	2,2'-bipyridyl $\geq 99\%$

APTES layer formation

Before starting the APTES coating, the vacuum oven (BINDER GmbH, Germany) was turned on and set to 120°C, and the uninhibited MAA was removed from the fridge. Ten MLCT cantilevers (Bruker AFM Probes, USA) from an unopened box were placed into a clean 5 cm glass Petri dish and exposed to oxygen plasma for 15 min immediately before use. The cantilevers were then divided between two clean Petri dishes, and the silicon control wafers were added (generally 3 per dish).

In a clean flask, the toluene and APTES were mixed well for approximately 1 min using a magnetic stirrer, before being poured over the cantilevers and silicon wafers. The Petri dishes were filled as much as possible without causing overflow, and 40 ml of the solution was sufficient for this when 2×5 cm Petri dishes were used. The Petri dishes were covered with their lids and left for 30 min before the cantilevers and wafers were rinsed well with toluene and dried under a nitrogen gas flow. Once dry, they were placed in 2 clean 5 cm glass Petri dishes, and transferred to the vacuum oven. The pressure was reduced to ~ 0.1 mbar and the substrates were annealed under vacuum for 30 min at 120°C, after which a test wafer was removed for ellipsometer and optical tensiometer analysis.

Initiation

The dichloromethane, triethylamine and α -bromoisobutyryl bromide (α -BiBB) were mixed well in a clean flask for approximately one minute using a magnetic stirrer, before being poured over the APTES-coated substrates. The chemical structures of these components and of the resulting ATRP initiator layer can be found in Appendix B, on page 243. Again, the dishes were filled as much as possible without spilling to reduce the amount of oxygen to which the mixture was exposed. The Petri dishes were covered with their lids and left for 30 min, at which time the cantilevers and wafers were rinsed well with dichloromethane and ethanol and dried under a nitrogen gas flow. A test wafer was removed for analysis by ellipsometry and optical tensiometry and the remaining wafers and cantilever chips were transferred

into the reaction cells (see Figure 3.10).

Growth of the poly(methacrylic acid) brush

While the substrates were being coated with the initiator, the MAA was changed into its sodium salt by adding 6 M sodium hydroxide to 10 ml of uninhibited MAA in a clean glass flask. Sodium hydroxide was gradually added via a glass Pasteur pipette, while the solution was stirred and monitored by a pH meter. The change in pH tended to be gradual up until approximately pH 7.5, at which point it would change very quickly and so the sodium hydroxide was added drop-wise from that point. When the solution reached pH 9, it warmed up and gained a very slight yellow hue and was ready to use in the polymerization. The flask containing the MAA salt was sealed using a Suba-seal and degassed by nitrogen flow for 30 min. 10 ml methanol was added to a separate flask and degassed in the same way, and the reaction cells containing the initiated wafers and cantilever chips were also connected to a gentle nitrogen flow at this point to start degassing.

Once degassed, the copper chlorides and 2,2'-bipyridyl were quickly added to the flask containing the methanol, and the mixture was stirred and degassed for a further 10 min. Note: when the dry reagents were added the solution changed to dark brown in colour. If it did not turn brown, but instead changed to bright blue, it was likely that the copper(I) chloride had oxidized and that the reaction would fail.

The methacrylic acid salt solution was then added to the flask containing the methanol, copper chlorides and 2,2'-bipyridyl via a degassed syringe and 6 inch needle, at which point the solution became slightly lighter in colour, though still a fairly dark, reddish-brown. This mixture was degassed for 15 min before being sonicated for 2 min to dissolve any remaining particulates.

10 ml of this final mixture was injected into each reaction cell using a degassed syringe and 6 inch needle, and the Young's taps on the reaction cells were closed (sometimes this was done before injecting the solution and it did not affect the outcome of the synthesis). The cells were inspected to check for any floating can-

tilevers, and, if present, the cell was agitated slightly in an attempt to sink them, as cantilevers needed to be submerged in order to grow consistent PMAA brushes. This was not always successful, but there were generally no more than 2 floating cantilevers per synthesis and sinking became more effective with practice.

The cells were then left for 20 min. After this time, they were opened and the cantilevers and wafers rinsed well with methanol and water before being dried under a gentle nitrogen flow. The cantilevers were then visually inspected; any that appeared partially coated (i.e. cantilevers which had been floating on the surface of the monomer solution), or that had sustained substantial damage to one or more of the five cantilevers on the chip edge where the cantilever selected for AFM experiments was situated, were discarded. Those that were fully submerged during the polymerization and with a full compliment of intact cantilevers (for example the cantilever pictured in Figure 3.13 on page 113) were stored in a glass Petri dish before glycosylation. The control wafers were kept separately so that they could be taken for optical tensiometry and ellipsometry measurements.

3.3.3 Conversion of poly(methacrylic acid) brushes to glycopolymer brushes

While the PMAA-coated cantilevers were kept for up to one month before use, sugar-coating was completed a maximum of 3 days before the cantilever was used for AFM. The reagents and quantities required for the glycosylation of the PMAA brushes are indicated in Table 3.3. The sugar amine solutions were made by Dr Ahmed Eissa at Durham University and either used as received, or diluted accordingly before use when supplied as more concentrated stock. The structures of glucose-amine and galactose-amine, a reaction scheme showing the conversion to glycopolymer brush from PMAA and a cartoon of the glycopolymer brush are shown in Figure 3.11 on page 109.

NHS and EDC were weighed out in clean 7 ml glass vials, and 5 ml of water was added to each. The separate solutions were then sonicated until completely dissolved. 3.5 ml of each was then added to a third vial and the combined solution mixed by sonication and manual agitation. The mixed solution was transferred into a

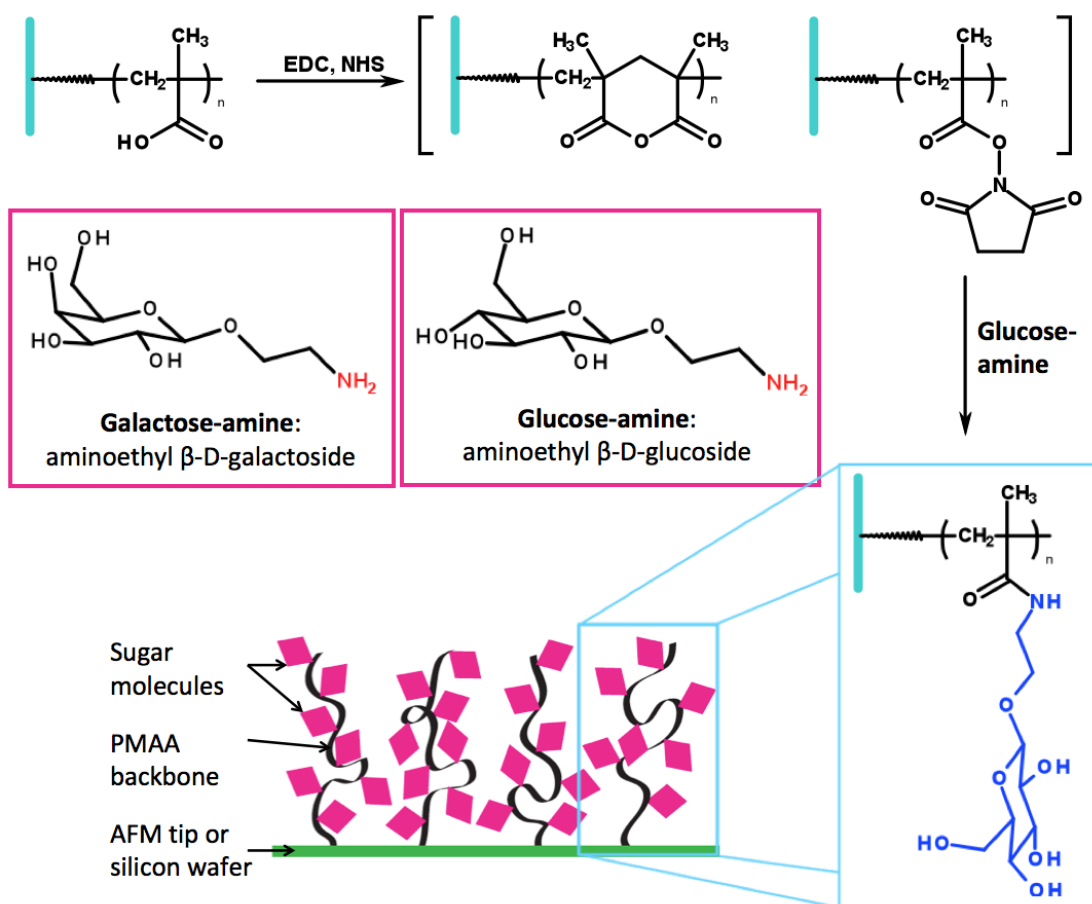


Figure 3.11: The pink boxes contain the chemical structures of glucose-amine and galactose-amine as used for the *Leishmania* parasite experiments. The reaction scheme proceeding clockwise from top shows PMAA glycosylation via EDC/NHS treatment and subsequent exposure to glucose-amine. The bottom image is a cartoon of the glycopolymer brush. Chemical structures provided by Dr Ahmed Eissa of Durham University.

Table 3.3: Reagents for conversion of PMAA to glycopolymer brush.

Amount	Reagent
0.096 g	<i>N</i> -(3-dimethylaminopropyl)- <i>N</i> '-ethylcarbodiimide hydrochloride (EDC) $\geq 98.0\%$
0.115 g	<i>N</i> -hydroxysuccinimide (NHS) 98 %
10 ml	water (5 ml each for the EDC and NHS)
Sugar amines: $\sim 150\ \mu\text{l}$ per cantilever chip	
10 mg ml ⁻¹	glucose-amine
10 mg ml ⁻¹	galactose-amine

clean 5 cm polystyrene Petri dish and the control wafer and required cantilevers were added. The dish was closed and left for 2 h, after which the wafer and cantilevers were rinsed well with water and dried under a gentle nitrogen flow.

In a new polystyrene Petri dish, approximately $\sim 150\ \mu\text{l}$ of the required sugar amine was carefully dropped onto the cantilevers and enough sugar amine was added to the control wafer to coat the whole surface. The dish was closed and left to coat to saturation overnight. The cantilevers and wafer were then rinsed well with water and dried under a gentle nitrogen flow.

3.3.4 PMAA and glycopolymer brush characterization

All control samples were measured using the white light ellipsometer and the optical tensiometer on the day of the synthesis, after all PMAA brush-associated reaction stages were complete. This information was recorded to check for consistency between tip batches. All batches used for experiments contained within this thesis met the general requirements set for the average water contact angle, θ_{av} , of the finished PMAA brush; $\theta_{\text{av}} < 48^\circ$, and had a brush thickness $> 4\ \text{nm}$.

Ellipsometry

Ellipsometry was conducted using a white light M-2000V ellipsometer and EC-400 control (J. A. Woollam Co. Inc, USA). One long measurement and two standard measurements were taken at different points on the control wafer and the measured thicknesses typically agreed to within 1 nm. The data were fitted using using the

CompleteEASE[®] software and a three-layer model: silicon, 2 nm native oxide and a Cauchy layer, where the standard Cauchy layer represented the PMAA. In this work, PMAA brush thickness is defined as the thickness of the Cauchy layer minus the measured thickness of the initiator layer (typically 1 – 2 nm, fitted with the same model).

The first batch of the seven made using the improved method was left for 30 min and the brushes grew to 100 nm. Only one of these cantilevers was used for the parasite experiments, and the adhesion results were consistent with the repeats obtained using much shorter brushes. Following this first successful batch, the polymerization time was reduced to 20 min, which was sufficient to grow brushes with a thickness of 10-20 nm when measured by ellipsometry in air, although there was some variability in this depending on the colour of the copper(I) chloride used in the reaction: when fully effective, it was grey to white in colour, but over time the reactivity decreased as it began to oxidize and became more greenish in hue. This meant that although more controlled than the initial synthesis method, a 20 min incubation resulted in PMAA brushes with various dry thicknesses (t) in the range $5 \text{ nm} \leq t \leq 40 \text{ nm}$, although most batches, including 19 of the 29 cantilevers used to gather the data presented in this work, had PMAA brushes between 8 and 15 nm thick. Of the 29 cantilevers, seven had PMAA layers $> 18 \text{ nm}$ thick (all $\leq 40 \text{ nm}$ apart from one from the first batch) and three cantilevers had PMAA layers with thicknesses in the range $5 \text{ nm} \leq t < 8 \text{ nm}$.

Both reaction cells were opened, and therefore the reaction exposed to air, after 20 min of polymerization, but cantilevers and control wafers in the second cell generally grew longer brushes (e.g. 14 nm compared to 8 nm) due to the time delay caused by rinsing and drying the contents of cell one before starting cell two (typically this was 10 to 15 min for five cantilevers and two wafer sections). Therefore, both the batch and the cell number of the cantilever in question were recorded in relation to the adhesion experiment for which they were used.

Contact angle

Water contact angle and droplet volume measurements were taken using an Attension Theta optical tensiometer (Biolin Scientific, Sweden) and fitted using the associated software. A pure water droplet with volume (V) $10 \mu\text{l} \leq V \leq 21 \mu\text{l}$ was gently dropped onto the surface via the in-built glass syringe and needle and, after waiting 1 – 2 s for the droplet to stop vibrating and undergo any rapid initial spreading, 200 image frames were recorded at 16 ms intervals. These data were then averaged to provide the left and right contact angles, from which an average contact angle was calculated and the droplet volume was estimated.

There was some variation in contact angles between the same reaction stage in different batches, but in general the APTES layer water contact angle was in the range $45^\circ \leq \theta_{\text{av}} \leq 74^\circ$; the initiator layer hydrophobicity increased in all cases to a value in the range $69^\circ \leq \theta_{\text{av}} \leq 86^\circ$ (all but one batch $< 80^\circ$); and the PMAA brush was much more hydrophilic in all cases, giving angles in the range $13^\circ \leq \theta_{\text{av}} \leq 48^\circ$ (all but one batch $< 41^\circ$), with thicker brushes from the second reaction cell to be opened and rinsed from a given batch typically having smaller contact angles and therefore greater hydrophilicity.

Changes associated with glycosylation

Even without ellipsometry or optical tensiometry measurements, the success of the coating could generally be ascertained by observation of the change in hydrophilicity of the control wafer and cantilevers between the EDC/NHS coating stage and the addition of the sugar amine. Figure 3.12, on page 113, gives an example of this from an early cantilever batch (PMAA thickness of the order of 40 nm). The left-hand image shows a cantilever chip and control wafer that have both been completely immersed in the EDC/NHS solution, rinsed and dried, and placed together in a new Petri dish. At this point, the cantilever is fully immersed in sugar amine solution, but the control wafer has only had one drop added towards one end (areas containing the sugar solution are outlined in purple). The right hand image shows the same control

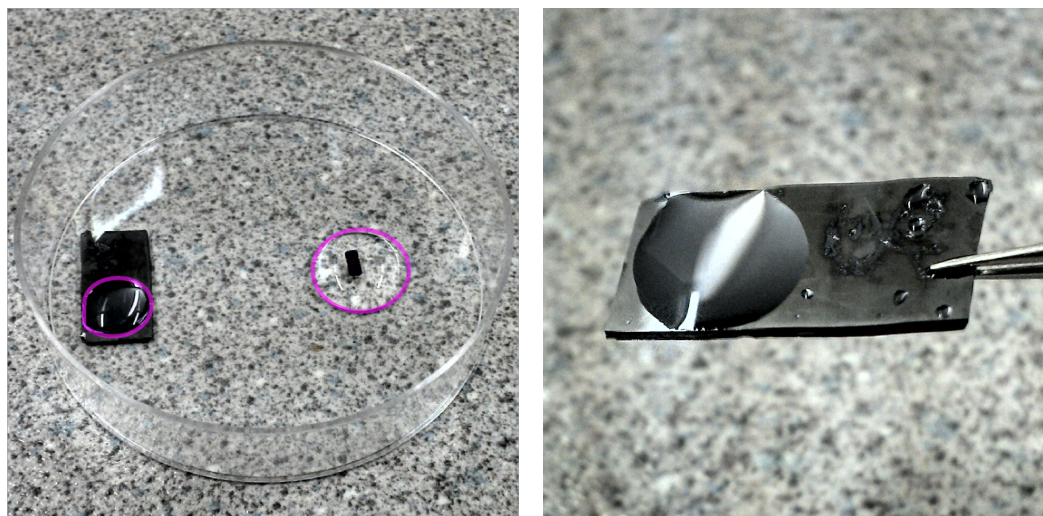


Figure 3.12: Photos illustrating the addition of galactose to an EDC/NHS functionalized PMAA brush. Left: just after the addition of galactose-ethyl-amine to the brush-functionalized wafer (left) and cantilever chip (right). The cantilever chip was covered with approximately 200 μl of 10 mg ml^{-1} saccharide solution and approximately 100 μl of this solution was also dropped onto one end of the wafer. The extent of the sugar amine drops is outlined in purple. Right: a photo that was taken after rinsing well with $18.2\text{ M}\Omega$ DI water but before drying under a nitrogen gas flow. It shows the different hydrophilicity levels of the area of brush coated with galactose-ethyl-amine compared to the surrounding EDC/NHS functionalized brush. The area retaining water is in the same position as the sugar solution in the left image, indicating successful glycopolymer formation.



Figure 3.13: Galactose glycopolymer-coated MLCT cantilever chip in position in the AFM cantilever holder. The chip appears to have a coating and all 5 cantilevers (1 rectangular and 4 triangular, with different lengths and spring constants) are undamaged. This cantilever is the one shown in the left-hand image of Figure 3.12, above.

wafer after it has been rinsed well with water, but before drying under nitrogen flow. The water on the surface clearly prefers being in contact with the brush on one part of the surface, which corresponds exactly with the location at which the sugar amine was added. As the glycopolymer is more hydrophilic than the EDC/NHS-modified PMAA, it suggests that the glycosylation has been successful. Note that due to its depth of several tens of nanometres, the polymer brush is visible to the naked eye as a film-like sheen covering the homogenous silicon (this is especially evident in the area of the control wafer where this surface has been scratched during handling). Figure 3.13 shows the cantilever chip coated alongside the test wafer when loaded into the cantilever holder of the AFM, and shows that all five cantilevers are still intact.

Besides the visible changes, the PMAA control wafers were measured again with the ellipsometer and optical tensiometer after the addition of sugar, so the increase in thickness and change in water contact angle associated with this reaction could be monitored. By tracking the changes for the individual samples, it could be seen that the property modifications varied between the samples, however, overall, the thickness of the brush was seen to increase by an average of just under 40%, corresponding to an average thickness increase of approximately 6 nm, and the water contact angle was reduced by between 24% and 42%.

When developing the protocol for the addition of sugars to the PMAA brush (samples made using the original synthesis method of hydrolysis from *Pt*BMA to PMAA), ellipsometry and optical tensometer measurements were combined with Fourier-transform infrared spectroscopy with attenuated total reflectance (FTIR-ATR) and Raman spectroscopy. These data were obtained during a collaboration visit to develop and refine the methodology under supervision by Prof. Neil Cameron and Dr Ahmed Eissa at Durham University. The data obtained during this visit are summarized in Table 3.4 and in Figure 3.14 on page 116.

Brush thickness and water contact angle were measured using laser ellipsometry and a manual telescope-based set up, respectively. The results of this are given below, and although the PMAA brush samples were made using the original synthesis

method, an increase in dry brush thickness and significant decrease in water contact angle were observed, which is consistent with the measurements of the batches used for AFM experiments and made using the different polymerization route.

Table 3.4: Thickness and water contact angle during glycopolymer conversion of brush made using initial synthesis route.

	Film thickness (nm)	Water contact angle (°)
PMAA brush	81 ± 2	52 ± 3
EDC/NHS-treated brush	72 ± 2	55 ± 5
Glucose glycopolymer brush	140 ± 3	17 ± 1

It is clear from Figure 3.14 that the glucose-modified brushes differed from the precursor brushes as characterized by the addition of a broad peak in both the FTIR-ATR and Raman spectroscopy data at around 3400 cm^{-1} (between 3000 cm^{-1} and 3700 cm^{-1}). This peak was attributed to OH bonds in the polymer layer, which suggest the presence of sugar molecules bound to the PMAA and is consistent with the successful attachment of glucose ethyl amine to the EDC/NHS treated PMAA brushes. Both graphs also show a small but clear peak at 1700 cm^{-1} which is attributed to carboxyl groups and is conserved for all samples except the FTIR-ATR data for the PtBMA sample.

The FTIR-ATR, Raman spectroscopy, water contact angle and ellipsometry data all combine to give strong evidence that the glycosylation of the precursor PMAA brushes was successful. The final addition to the portfolio of evidence supporting the presence of sugars on the cantilever tips in addition to the control wafers is in selective binding control experiments, which are presented in Section 5.2 on page 177.

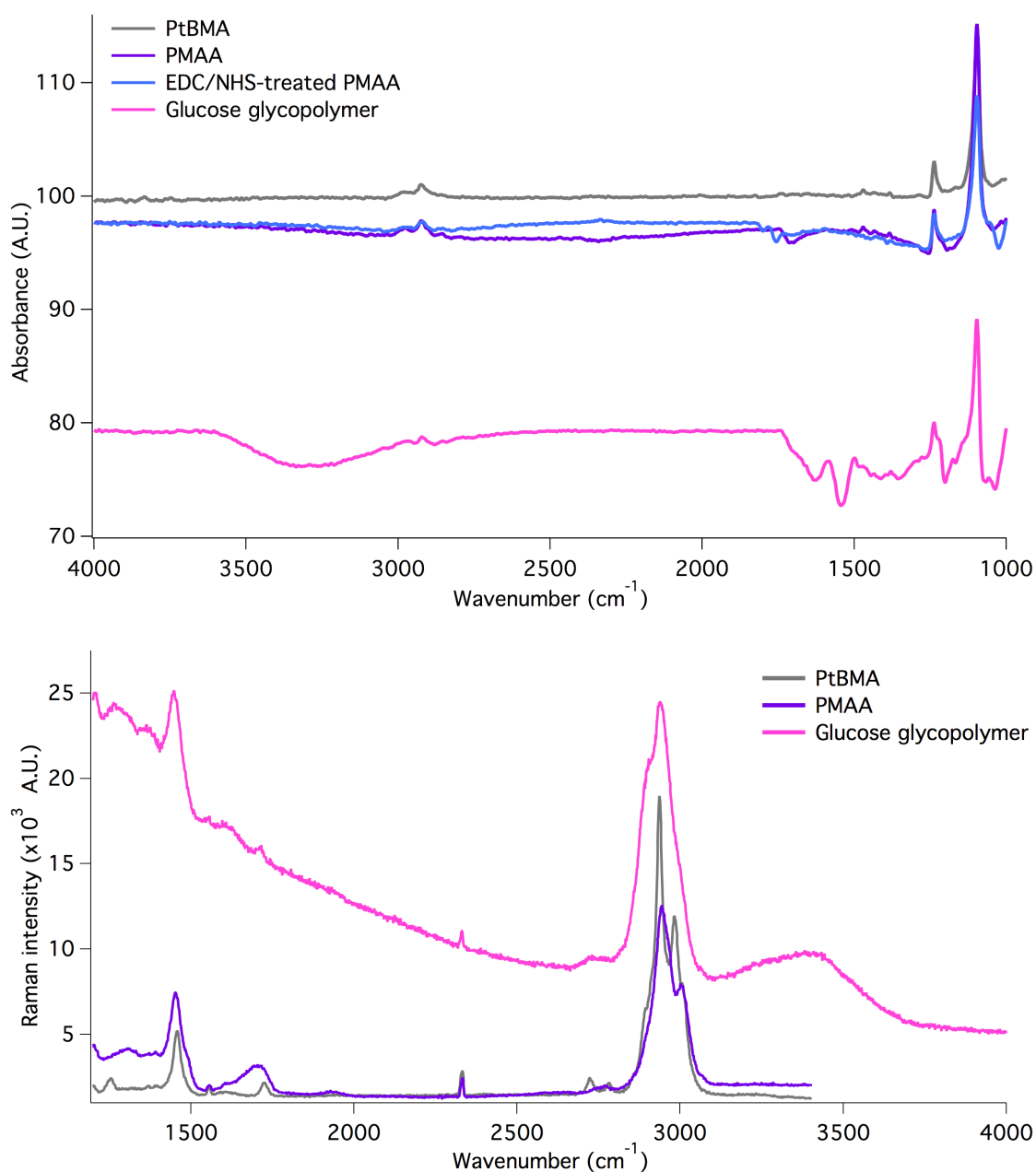


Figure 3.14: Top: FTIR-ATR data showing different absorbance spectra and bottom: Raman spectroscopy data showing intensity profiles of different stages in fabricating glucose glycopolymer brushes corresponding to the FTIR-ATR data. There is a clear distinction between the glycopolymer and the precursor brushes in the addition of a large, broad peak between 3000 cm⁻¹ and 3700 cm⁻¹ in both the FTIR-ATR and Raman spectroscopy data. This peak is attributed to the presence of OH bonds associated with the sugar molecules, and amine groups. The data also shows a small peak at 1700 cm⁻¹ which is attributed to carboxyl groups and is conserved for all samples except the FTIR-ATR data for the PtBMA sample. Note that the direction of the wavenumber axis is reversed between the two graphs.

3.4 Overcoming AFM issues

3.4.1 Vibration and noise

When imaging with nanometre height resolution and taking force curves where the expected forces correspond to a few nanometres of movement in the laser spot on the photodiode, noise is one of the key challenges to overcome. In this project, the signal to noise ratio was sufficient for the observed adhesion events to be clearly visible above the noise limit.

To reduce noise in the system, the AFM was set up on an air table, which significantly reduced vibrational noise by isolating the apparatus from the controller and light source (containing a fan) and other vibrations which would be transferred to the table through the floor. The AFM was also covered with a custom-made polystyrene box with pyramidal-textured lining, which reduced sound-based noise by dampening any noise within the chamber. The MFP-3D was in a small lab on its own which meant that it could be shut off from the main lab, helping to further reduce noise of acoustic origin.

3.4.2 Evaporation

Because the set up was not enclosed and because room temperature was generally around 27°C, when working in liquid, the imaging buffer underwent evaporation over a number of hours. If no measures had been taken to regulate ion levels, it would have led to increased salt concentrations which could have affected measured adhesion interactions due to different osmotic pressures in and around the cells and therefore increased screening of electrostatic forces.

To minimise this effect, the buffer quantity was monitored and, when it had noticeably decreased, it was diluted with fresh buffer; some liquid was then removed and then the level was topped up again with more fresh buffer. Typically, bacterial samples were immersed in between 0.3 and 0.4 ml of buffer due to the smaller sample area and to minimise direct contact of the buffer with the tape used to immobilize the sample. Parasite samples were immersed in approximately 0.5 ml of PBS. Imaging

time was kept to an absolute maximum of 6 h.

3.4.3 Drift in AFM force maps

Scanner drift during a force map can be caused by a number of factors including changes in ambient temperature (generally the equipment will warm up during use) and sometimes not having enough buffer when working in liquid. An example of the issues this causes is shown in Figure 3.15 where a 1.7 μm force map of a pair of bacteria (MUA-coated cantilever on FP22 *S. pneumoniae*) was obtained, but when the imaging area was offset to centre on the bacteria and the scale reduced to 800 nm to obtain a larger scale force map, they were not in the map. At this point, the AFM was switched into tapping mode and a larger 2 μm image was taken. The bacteria were located in one corner of the image and zooming in was much more effective in this case (presumably because the image was acquired over a much shorter time than the force map: approximately 8 min compared to 28.5 min), resulting in the 900 nm image shown in Figure 3.15. The image and the force map contain the same bacteria: the general shape features are still identifiable, but a clear distortion can be seen in the force map. This distortion was caused by drift and meant that by the time the scan had finished (moving upwards), the relocation, relative to the coordinates of the tip at the end of the map, was no longer sufficient to relocate on top of the bacteria because it did not account for the additional drift. This is one of the most extreme examples of drift encountered in this project, but it illustrates the problem well.

There was no temperature regulation in the laboratory, but the MFP-3D was in a small room on its own which helped to minimise changes in temperature caused by the use of other machines and varying numbers of people entering and leaving. However, the scanner head produced heat while running, and therefore created its own temperature gradient, which could increase the chance of drifting, especially when first turned on, or when put into contact with a cold sample (the buffer used for an experiment was allowed to adjust to the temperature of the AFM lab before use in order to reduce this second factor). Generally, drift was not too much of a

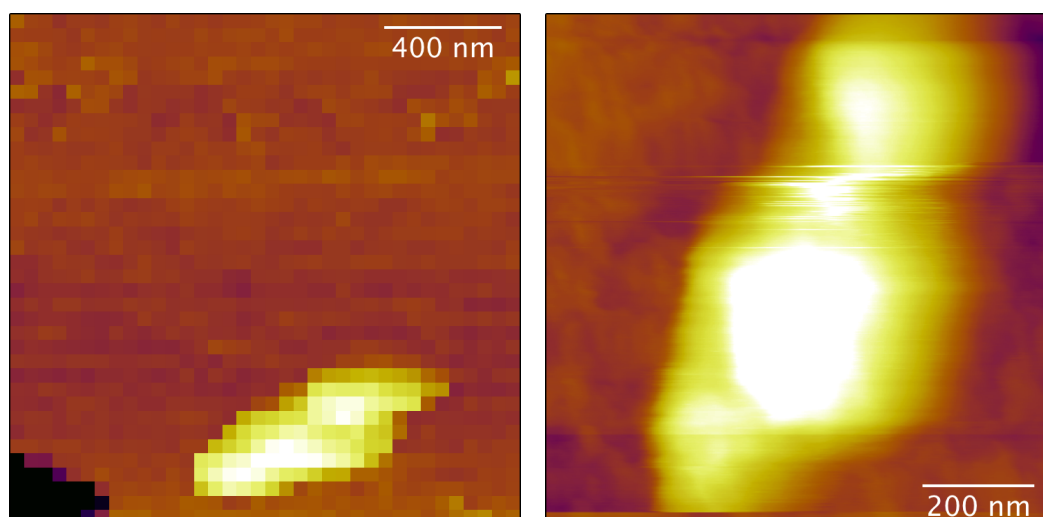


Figure 3.15: Left: 36×36 pixel height map of FP22 *S. pneumoniae* in PBS on a polycarbonate membrane. Map acquired from the bottom up. Right: tapping mode height image taken after failing to locate the bacteria in a subsequent force map. 512×512 pixels, image acquired from the top down. The force map image is clearly distorted, with the AFM moving further left with each row, resulting in a distortion of the bacteria image.

problem, especially in the parasite work, but on one or two bacteria experiments it presented more difficulties than usual. If drifting was noticed in an experimental session, in order to prevent the problems described above, as soon as a bacterium-like shape started to appear, the force map was paused, and the coordinates for the next map set using the “zoomzoom” function in the AFM software, before the map size and number of force points were adjusted as desired. At this point, the current force map was cancelled and the new, zoomed in force map was started, with the tip not having to move far from its current position to start the new scan.

3.4.4 Tip contamination

Tip contamination with molecules other than the one of interest is a serious point to consider when it comes to using chemically modified tips for FS. When probing the surface to see how the sample responds to the molecule coating the tip, fouling of this surface is most undesirable. To try and minimise the risk of this occurring during these experiments, all materials used in the experiment were thoroughly cleaned and kept in a sealed container such as a PS Petri dish when not in use to prevent dust settling. The cantilever holder was cleaned before each experiment by sonication in

IMS and water, before being thoroughly dried under a nitrogen gas flow. Following this, the holder was placed under a UV light (254/365 nm. Model UVLS-24 EL, UVP, Cambridge, UK) for 15 min.

Biological samples, by their nature, are at risk of having free or loose polymeric material alongside cells. To reduce the chance of this material or loose cells becoming attached to the tip, samples were prepared with a relatively low density of cells (i.e. mainly comprising isolated cells with areas of substrate in between them) and rinsed well before being used in the AFM to dislodge any loose material. This also ensured that the cells were well enough attached to the substrate to undergo mapping with minimal lateral movement, allowing for more accurate mapping.

The main defense employed against tip contamination was visual monitoring of the force curves obtained on the substrate over the course of the experiment; if any major change in the response of the tip occurred, the cantilever was deemed to have been compromised and no further data was taken. For this reason, and also to limit the effects of buffer evaporation and maximize the chance of mapping live cells, bacteria experiments were limited to a maximum of 6 hours of AFM (the bacteria were more difficult to locate so most of this time was taken imaging areas free of biological material) and *Leishmania* experiments to 5 h of AFM.

3.5 Selection of AFM parameters

It is crucial to decide upon the values of different AFM parameters before starting an experiment where several different combinations of tips and samples are compared, since features such as dwell time, applied force, loading rate (related to cantilever spring constant and approach/retraction velocity) and contact area are known to have an effect on the measured adhesion [10, 214, 218, 219] and therefore the conditions of the experiment must remain consistent throughout the work. Because of this, it can be difficult to directly compare results with those in the literature, as what can initially appear to be a similar experiment can, in some cases, result in quite marked variation in adhesive force.

The parameters used for force spectroscopy were determined through a combina-

tion of literature surveying, advice from Dr Alsteens, who was working at Université catholique de Louvain at the time, and optimizing settings, such as applied force, dwell time and force distance, in initial experiments (such as the one discussed in Section 4.2 on page 137). These final comparisons were necessary in order to obtain clean approach curves whilst applying enough force to find adhesion events between the tip and the cell. It was also important to ensure that the tip was retracted far enough from the surface for the majority of all curves to have ceased interacting with any surface polymers. This is why although the applied force is the same for the *S. pneumoniae* and *Leishmania* work, the retraction distance used was double the length in the *Leishmania* work as these cells tended to interact more strongly with the coated cantilevers, and the interaction lengths could extend up to ~ 400 nm from the cell surface (see Figure 5.19 on page 218), whereas the pneumococcal interactions tended to stay within the first 100 nm or so (see Figure 4.3 on page 142). Therefore, a force distance of 500 nm was selected for the bacterial work, and a force distance of 1.00 μm was used for the parasite work. As the rate was kept constant at 0.99 Hz, this meant that the z -velocity of the AFM cantilever increased from 992 nm s^{-1} to 1.98 $\mu\text{m s}^{-1}$ (these were the default velocities when a rate of 1 Hz was entered along with the selected distances).

Dwell time when the tip is on the surface allows molecules to diffuse, rearrange and bind, which can increase the chance of detecting a strong positive binding interaction: the detection frequency of Als3 adhesin binding on *Candida albicans* germ tubes more than doubled when the dwell time was increased from 100 ms to 2 s [170]. Longer dwell time is preferable for detecting more binding events, but comes at the cost of force map time. Work using dwell times of between 100 ms and 250 ms has given good adhesion results [101, 172, 220], so 240 ms was selected in this work.

In terms of the applied force, one major criteria for consideration was the level of indentation and cell damage likely to occur at high applied forces. 250 pN applied force is commonly used for AFM force studies of bacteria [31, 103, 172]. In some cases, patterns in the adhesive interactions were only visible when a maximum applied force

of 250 pN was used, as in the work of Andre *et al.*, where increasing the maximum applied force from 250 pN to 500 pN resulted in higher frequency of recognition events and therefore loss of peptidoglycan line resolution, which they were targeting with a specific moiety [204]. A maximum applied force of 250 pN was therefore selected for use in this work.

Soft cantilevers ($< 50 \text{ pN nm}^{-1}$) were used for both the bacteria and parasite experiments, as the spring constant of the cantilever should be fairly well matched to the stiffness of the sample and the expected forces [192]: since bacteria are soft and the expected forces are within the range of tens to hundreds of piconewtons, a stiff cantilever would not be sensitive enough to sense these forces. However, in the case where the adhesion force is tens to hundreds of nanonewtons, the cantilevers used here would not be appropriate to measure the interactions, as the strength of that adhesion is sufficient to bend the cantilever so severely that the cantilever is unable to detach from the surface between one force curve and the next. This occurred when the Olympus biolevers were used in air on glass (data not included in this work) and, in some cases, between the glycopolymer-coated Bruker MLCT AFM tips and the PEI-coated substrate used for the parasite experiments, resulting in the appearance of a snow-like effect in a small number of zoomed out topographical maps, such as the bottom right image in Figure 5.11 on page 200.

Combined, these parameters are fairly consistent with those used in the literature, and have been tailored to the exact system being probed, allowing for adhesive interactions to be measured appropriately on both the *S. pneumoniae* bacteria and *Leishmania* parasites.

3.6 AFM data processing

3.6.1 Calculating height maps using force data

The height map calculated by the software uses the distance moved by the z -piezo stack at the point where the trigger force is reached (i.e. the maximum z -piezo extension in the curve, calculated by multiplying the z -piezo sensor voltage by the

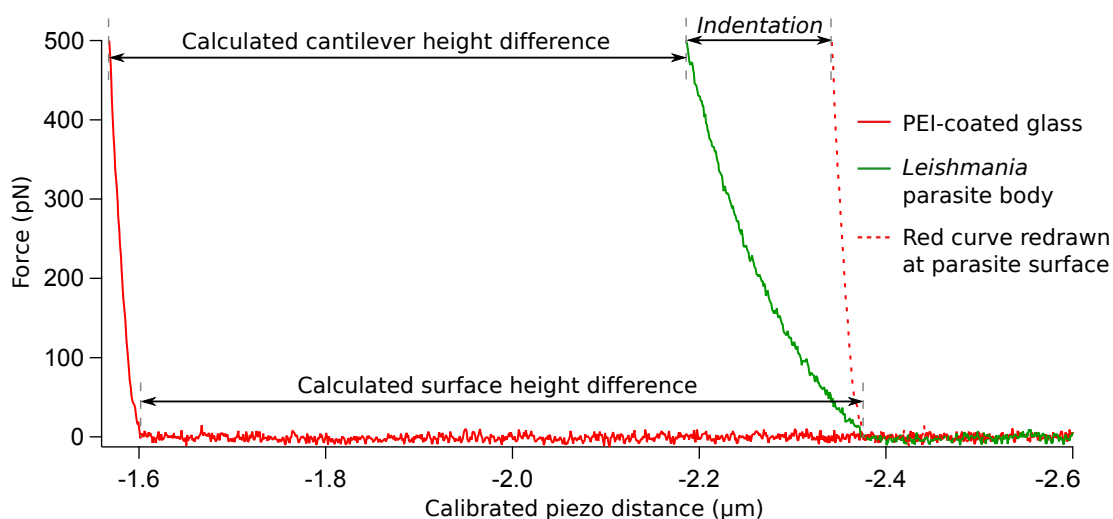


Figure 3.16: Approach force curves taken on (green) and off (red) of a *Leishmania* parasite, in PBS media and using a PMAA-coated tip. To aid the eye, the curve taken on the hard surface has been copied and placed on top of the comparable section of the curve taken on the parasite (dashed red line). This shows the different indentations caused by the tip applying the same force on the hard and soft samples. The figure also shows the height difference between the two curves according to the in-built software macro (cantilever height difference), and the indentation independent surface height difference obtained using the corrected macro to give a better recreation of the sample topography in the force map.

calibration constant of the sensor). This means that the height value will depend on the softness of the sample; if indentation were to occur, the piezo would extend further than on a rigid sample, reading out an artificially low height for softer features (see Figure 2.3 on page 47). This is clearly important for biological samples, especially in terms of the *Leishmania* parasites on PEI-coated glass used in part of this project, where there is a clear difference between force curves obtained on the parasite and on the hard substrate, as demonstrated by the two example curves in Figure 3.16 taken using a PMAA-coated tip on a wild type leptomonad *Leishmania mexicana* parasite (for information about the different lifecycle stages see Figures 1.9 and 1.10 on page 28). This discrepancy between surface height difference and the standard calculated height difference (‘calculated cantilever height difference’ in Figure 3.16) could have an impact when masking areas during data analysis to determine which force curves should be included in analysis of forces measured on the cell. To rectify this issue, a height calculation method coded by my colleague Ross Carter was employed (the code is included in Appendix A on page 242). This method evaluates the sample height as the distance at which the

tip touches the surface instead of at the full extension of the z piezo during approach ('calculated surface height difference' in Figure 3.16).

3.6.2 Force curve baseline correction

Little processing was applied to the force-distance curves themselves, other than to subtract a linear baseline from the curve, when not doing so would result in a false positive or negative binding event. The adhesive force measured using the difference between the average of the force at the furthest retraction distance from the surface and the lowest point in the retraction curve is only valid when the 'zero force' defined at the furthest retraction distance is the same as the 'zero force' relative to interaction event, i.e. the curve baseline is parallel to the x -axis. A baseline where the measured force has a positive gradient as the tip retracts from the sample can result in pixels within the force map reporting an adhesion force of similar scale to true binding events for a curve which contained no binding events. Equally, a negative baseline slope as the tip retracts from the surface could mask or reduce the scale of positive binding events depending on the severity of the baseline slope and the size of the binding event: if the difference between the baseline at the cell surface and at the furthest retraction distance is greater than the magnitude of a binding event, the pixel corresponding to the curve will show a false negative.

To prevent these effects impacting the force distributions within the close-up maps, all of the curves within the masked area of the maps were checked for baseline slope and any which deviated beyond the noise threshold of the force curve ($\sim \pm 15$ - 20 pN) were corrected using the 'line subtract' function within the Asylum Research software. These modified maps were then saved in a separate file and the height and adhesion maps re-drawn to remove false events.

3.7 DDT and MUA AFM control experiments

Control experiments were undertaken to compare DDT-DDT, MUA-MUA and DDT-MUA interactions in water (Figure 3.17 on page 125) and PBS (Figure 3.18 on page 128). Experiments were undertaken using freshly-coated DDT and MUA can-

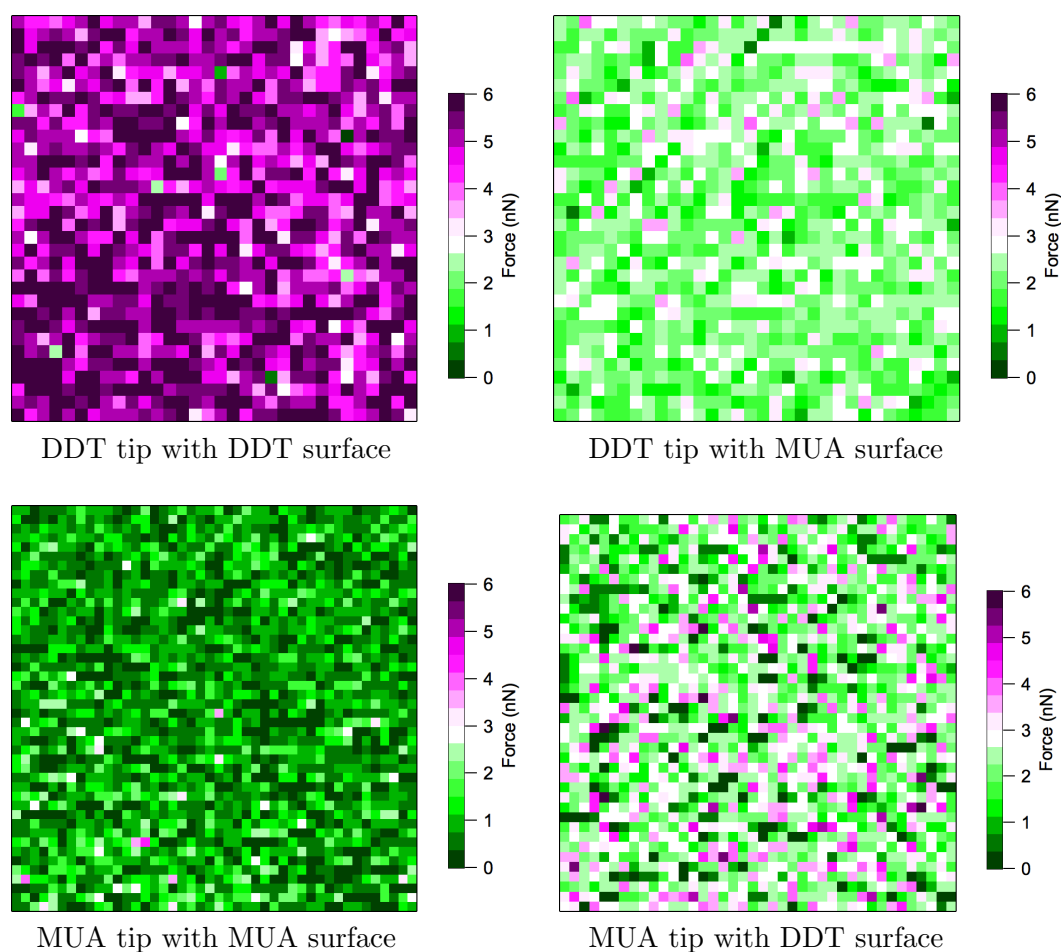


Figure 3.17: Force maps taken in water using thiol-modified tips and self-assembled monolayers. All force maps are 1.5 μm across and were taken using an applied force of 250 pN and dwell time of 240 ms. DDT is a neutral and hydrophobic CH_3 -terminated alkanethiol, whereas MUA is OH-terminated, which can hold a negative charge when the H^+ ion has dissociated, and is more hydrophilic.

tilevers, and gold-coated silicon wafers which were coated with DDT or MUA at the same time as the cantilevers. The water experiments were conducted in 18.2 M Ω DI water, and the experiments in PBS were conducted in the sterile PBS used for the bacteria experiments.

The DDT cantilevers were more hydrophobic than the MUA cantilevers and, when immersed in aqueous solutions, the cantilevers sometimes flipped back and attached to the cantilever chip rather than extending into solution. This could be minimised by adding a small drop of liquid to the cantilever before introducing it to the hydrated sample.

The adhesion force maps in Figure 3.17 are representative of several similar maps

and show that all of the SAM-coated surfaces have a random distribution of high and low forces across an area of $1.5 \mu\text{m} \times 1.5 \mu\text{m}$, with no clear areas of higher or lower adhesion. All maps are presented with the same scale for ease of comparison. The highest adhesion was observed between the DDT tip and the DDT surface: a $\text{CH}_3\text{-CH}_3$ -based interaction with an average force of $5.10 \pm 0.03 \text{ nN}$. The smallest adhesive forces were observed between the MUA tip and MUA surface: a COOH-COOH -based interaction with an average force of $0.89 \pm 0.01 \text{ nN}$. The maps showing different SAMs on the tip and surface had an intermediate interaction strength $2.26 \pm 0.02 \text{ nN}$ and $2.32 \pm 0.03 \text{ nN}$ for the DDT being on the tip and the surface, respectively. The uncertainty values presented are the standard error, but the difference in the force variability between the two maps is more clearly demonstrated by the higher standard deviation in the force data when the DDT was on the sample: 1 nN compared to 0.6 nN . The reason for this difference is unclear, but since the average forces were almost within standard errors of each other, this discrepancy is not important. The histograms of the forces tended to have a fairly normal distribution, except for the MUA-MUA map which had a more skewed distribution but still had a clear peak just below 1 nN .

The above results are consistent with others in the literature, such as in the work of Vezenov *et al.*, where stiffer cantilevers were used, but the pattern of adhesion strength between SAMs in pure water measured using AFM matched that shown here, with $\text{CH}_3\text{-CH}_3$ interactions being by far the strongest and COOH-COOH interactions being the weakest [221]. The scale of $\text{CH}_3\text{-COOH}$ interactions was intermediate, but closer in value to the adhesion strength measured between two hydrophilic surfaces than hydrophobic ones. The values are also close to those found by Sinniah *et al.*, where, by examining the presented force curves, adhesion force values were obtained using applied forces of 1 nN for the MUA-coated tips, and up to 6 nN for the DDT-coated tips [218]. Given that higher applied forces were used, it is expected that their reported adhesion values would be slightly larger than those in this work. Their adhesion forces of $12.5 \pm 4.4 \text{ nN}$ for $\text{CH}_3\text{-CH}_3$ interactions and $2.3 \pm 1.1 \text{ nN}$ for COOH-COOH interactions in water (the given uncertainty is

the standard deviation of the force data) are consistent with the control experiment data presented above, so long as the conditions of increased applied force are noted.

The magnitude of the measured interaction in water involving the DDT tips can also be compared to an experiment by Alsteens *et al.* [101], where the interaction of a hydrophobic CH₃-terminated tip with a mixed SAM-covered surface where the ratio of OH- and CH₃-terminated molecules was varied. The tip used in the experiment had a spring constant of approximately half that of the cantilevers used here and the applied force and dwell time is unknown, so, again, the exact values are not directly comparable with this experiment. However, in water, Alsteens' experiment returned a CH₃-CH₃ interaction value of just over 9 nN, and an OH-OH interaction value of < 1 nN, which is of the same scale as the interactions shown in Figure 3.17, albeit for a slightly different hydrophilic tip chemistry (-OH versus -COOH terminated). The paper also suggested that some portion of the measured forces might come from entropic changes associated with the reorganization of water molecules near hydrophobic surfaces as well as direct tip-sample interactions, and it is quite possible that solvent-organization and the hydrophobic force can partly explain the high measured forces between the two CH₃-terminated surfaces in the sample map presented in Figure 3.17. This idea is reinforced by the work of Ma *et al.*, who found that interactions between hydrophobic molecules (1-decane thiol SAMs) in buffer were dramatically reduced by the addition of methanol, which is known to disrupt the reorganization of water at non-polar surfaces, to the AFM imaging buffer [222]. They proposed that addition of 60 vol% methanol was sufficient to block 85 % of hydrophobic interactions.

The PBS experiments were conducted to see how the interaction between the different SAMs changed when in a solution containing ions, which are known to affect both electrostatic and hydrophobic interactions (see Section 1.1.1 on page 3). This also allowed comparison of the magnitude of these interactions with the SAM-*S. pneumoniae* interactions presented in Section 4.3.2.

As for the measurements in water, the DDT-DDT forces have a normal distribution, with the MUA-MUA interactions having a more skewed distribution. The

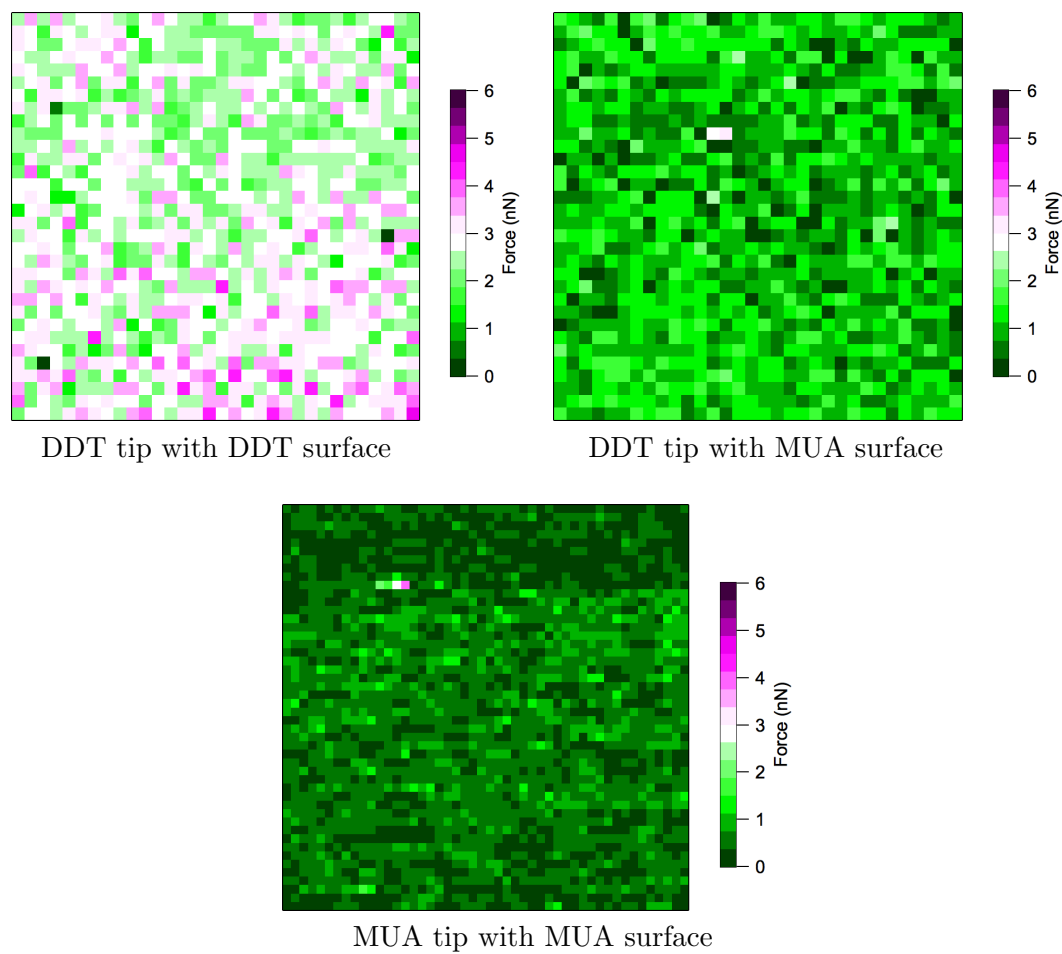


Figure 3.18: Force maps taken in PBS using thiol-modified tips and self-assembled monolayers. Force maps for the DDT-functionalized tip are 1.5 μm across, and the force map taken with the MUA-functionalized tip is 2 μm across. All were taken using an applied force of 250 pN and dwell time of 240 ms.

pattern in the average adhesion strengths shown in Figure 3.18 also follows that in water, with DDT - DDT giving the strongest interaction, DDT - MUA in the middle, and MUA - MUA having the weakest interaction. The magnitude of the interactions were approximately halved in all cases (average forces reduced from 5.1 nN to ~ 2.7 nN, 2.3 nN to ~ 1.0 nN and 0.89 nN to ~ 0.44 nN for DDT - DDT, DDT - MUA and MUA - MUA respectively). This is likely to be due to the charged ions screening the electrostatic interactions involved in the COO^- -based interactions for MUA, and affecting the restructuring of water molecules for the hydrophobic force involved in CH_3 -based interactions [222, 223].

All of these control experiments were taken using DDT- or MUA-coated cantilevers of comparable spring constant ($20 \text{ pN nm}^{-1} \leq k \leq 30 \text{ pN nm}^{-1}$) to those used for the *S. pneumoniae* experiments, and the same loading rate, applied force and dwell time. Therefore, the magnitude of these forces could be compared to those measured on the bacteria to ascertain how much the adhesion forces vary between a stiff, homogenous surface and the complex biological surface of the bacteria.

Chapter 4

Streptococcus pneumoniae results

4.1 Introduction

This chapter combines the results of AFM force mapping on capsulated and unencapsulated type 2 pneumococci and hydrophilic and hydrophobic surfaces. Several features of the data, including the median force and the parameters from finite mixture model fits of the log₁₀ force data, are used to compare the different bacterium-tip combinations, and these results are discussed in detail in Section 4.3 on page 154.

A brief literature survey is included to bring some context to the values measured on *Streptococcus pneumoniae*, which has not previously been investigated using AFM (Section 4.1.1). This section also includes a more detailed look at some of the surface molecules of *S. pneumoniae* (Section 4.1.2), to elucidate the different factors contributing to the measured adhesion forces.

To illustrate the selection of parameters during data gathering and analysis, Section 4.2 contains a single experiment as an example. The experiment, between D39 capsulated pneumococci and a hydrophilic MUA cantilever, was chosen because it contains multiple force maps of the same pair of cells which were obtained using a range of different parameters. Following this example, the data for the experiment with *S. pneumoniae* will be summarized, and the key findings presented.

4.1.1 Comparative bacterial hydrophobicity studies: context for adhesion properties of *S. pneumoniae*

No AFM force experiments have been performed on *Streptococcus pneumoniae*, so no direct intra-species comparisons can be made between this work and published data. However, SAM-coated AFM tips have been used to investigate the microscopic surface properties of other bacteria, allowing the adhesion properties of *S. pneumoniae* measured in this work to be given some context.

Genus *Streptococcus* bacteria

Group B streptococci (β -haemolytic human pathogens) have been studied using AFM with various tip chemistries including fibronectin [224] and specific antibody probes for group B carbohydrate and capsular polysaccharide [220]. As a control, bare silicon nitride tips, which are slightly hydrophilic in character, were used to probe the bacteria, resulting in between 3 and 7% of interaction forces containing an adhesive event at retraction distances of tens of nanometres away from the cell surface (this percentage could be considered similar to the proportion of data points associated with the second, higher force Gaussian distribution fitted to the *S. pneumoniae* data) [220]. The above interactions were measured in the same buffer, and using the same applied force, tip speed, and mechanical trapping approach as used to immobilize bacteria in this work. Based on this, it could be expected that pneumococci would not interact particularly strongly with the hydrophilic MUA cantilever.

Several different strains of *Streptococcus mitis* with varied hydrophobicity have been probed using an uncoated silicon nitride tip in both water and 0.1 M KCl buffer [225]. The applied force appears to be much larger than that used in this work, with force-distance curves presenting forces of ~ 9 nN at maximum indentation. The spring constant of the AFM cantilevers used were also stiffer than in this work. The force curves showed a repulsive force on approach from separation distances of up to 33 nm for some strains, and contained multiple adhesive force

events after sample indentation. These multiple binding events were attributed to polymers of different lengths on the bacterium, including the sparse fibrils which extend hundreds of nanometres out into the solution. The average adhesion force did not appear to be reduced when KCl buffer was used instead of water, but this trend was not observed for all of the bacterial strains. It is therefore likely that the hydrophilic MUA cantilever will experience a repulsive force as it approaches the *S. pneumoniae* cell surface, rather than jumping into contact, and that the majority of measured adhesive interactions will occur within the first hundred nanometres from the surface, as the pneumococcus does not express the very long fibrils present on *Streptococcus mitis*.

Other bacteria

The apathogenic bacterium *Staphylococcus carnosus* has been used as a whole cell probe on hydrophilic (silicon wafers with a native oxide layer) and hydrophobic (octadecyltrichlorosilane, OTS, which has a CH₃ tailgroup and forms monolayers on silicon) surfaces [226]. OTS and silicon samples were used so that ligand-receptor binding did not contribute to the adhesion measurements. Therefore, the cells were probing the adhesion due to surface energies, driven by van der Waals and electrostatic forces, and the hydrophobic interaction. *S. carnosus* was found to bind much more strongly to the hydrophobic surface than to silicon with its native oxide layer (~ 3 nN compared to 30 – 50 pN, which was close to the experimental resolution). This was attributed to the relative proportions, properties and arrangement of proteins in the bacterial cell wall. Because the substrates differed only by a 2.6 nm-thick SAM, the van der Waals forces were similar, and as both the bacterium and the silicon surface held a net negative charge, electrostatic forces between the bacterium and the surface were repulsive. It was therefore concluded that hydrophobic forces between the cell wall proteins and the sample surface were the dominating adhesive force, the value of which exceeded the other two main force contributions by an order of magnitude. This holds for the pneumococcal work, since both the capsule and cell wall have a net negative charge, and therefore the predominant electrostatic

interaction is expected to be repulsive, although there are positively charged regions on some surface molecules. From this, it would be predicted that the hydrophilic, negatively charged tip will interact only weakly with the surface if the contribution from electrostatic repulsion is a significant factor in pneumococcal adherence. As a result of this, the hydrophobic tip would be expected to interact more strongly with the bacterium, assuming that hydrophobic moieties are available to bind to the AFM tip.

The hydrophobic properties of four strains of *Staphylococcus epidermidis* have been compared by mechanically trapping them in polycarbonate membranes and mapping them using silicon nitride and ODT-coated AFM tips, with a maximum applied force of 250 pN, in water [103]. When mapped using silicon nitride tips, the two biofilm-forming strains showed more adhesive events (homogeneously distributed across the surface) and a greater mean adhesive force than the two biofilm-negative strains: 203 ± 66 pN and 273 ± 78 pN compared to 181 ± 64 pN and 154 ± 32 pN for the two biofilm-positive and biofilm-negative strains, respectively. The means reported appear to be of Gaussian fits to histograms, excluding non-adhesive events. When the hydrophobic tip was used, this trend was reversed, with a larger proportion of positive binding events seen in the biofilm-negative strains, and the mean adhesion forces were typically 150 pN and 200 pN for biofilm positive and negative strains, respectively. A similar comparison can be made for the capsulated and unencapsulated type 2 pneumococci used in this work, to examine any trends in adhesive behaviour which are associated with the presence of capsule on the bacterial surface.

The link between macroscopic and microscopic hydrophobicity of *Acinetobacter venetianus* and *Rhodococcus erythropolis* has been explored by combining contact angle measurements with FS on APTES-immobilized cells using 11-mercapto-1-undecanol (-OH terminated) and 1-octadecane thiol (ODT, -CH₃ terminated) functionalized AFM tips [102, 175]. Measurements were made in a 0.1 M phosphate buffer solution using cantilevers with comparable spring constants to those used in this work. *A. venetianus* is a Gram negative bacteria with hydrophobic pili, which

showed multiple adhesion interactions at different extension distances, randomly distributed across the cell, with the largest adhesion forces being approximately 2 nN. *R. erythropolis* is a hydrophobic Gram positive bacterium with a compact capsule, which showed single, gradual rupture events. Increased forces were measured at one end of the cell, with a force gradient along the long axis of the bacillus rising up to maximum forces of ~ 4 nN. Neither bacterial strain exhibited adhesion to the hydrophilic tip [102]. DLVO models of the results failed to accurately represent the data and this failure was believed to be due, in part, to steric interactions involving extracellular structures such as pili and the capsule [175]. This illustrates that AFM is capable of detecting patterns of adhesion across a bacterium. The forces measured on these bacteria are stronger than would be expected on the pneumococcal surface in this work, as the forces measured in PBS during the SAM control experiments were of the order of 1 nN, and so to measure similar forces on the bacterium would mean that the complex bacterial surface behaved very similarly to a surface comprised of a single type of molecule.

In another example, hydrophobic bacteria were probed with hydrophobic (DDT, CH₃ terminated) AFM tips. The weakly Gram positive, mycolic acid-rich *Mycobacterium bovis* gave adhesion forces of ~ 3 nN, uniformly distributed across the cell surface (measurements were made in water using applied forces of < 1 nN on mechanically trapped cells) [101]. By comparing this data with data obtained using the CH₃ tip and a mixed CH₃/OH terminated monolayer, the forces measured on the bacteria were consistent with those measured on a mixed SAM containing 40% hydrophobic groups, which suggests a highly hydrophobic cell surface, consistent with the presence of exposed mycolic acids in the cell wall. Because a DDT tip was used, the force measurements were unaffected by electrostatic interactions. The fact that the cell surface resembled a mixed monolayer containing both hydrophobic and hydrophilic groups showed that even hydrophobic bacteria need to be predominantly composed of hydrophilic biomolecules. As the pneumococcus is generally considered to be a hydrophilic bacterium (see the following section), it is predicted that interaction with the hydrophobic AFM tip will not be as strong as the interactions of *M.*

bovis or other hydrophobic bacteria with a similar tip.

4.1.2 A detailed look at the properties of selected pneumococcal surface molecules

In terms of the charge and hydrophobic properties of these various cell elements, the capsule is negatively charged (ζ -potential = -11.3 mV measured in PBS at pH 7.0 [108]) and D39 bacteria have been shown to be highly hydrophilic through a non-polar hydrocarbon binding test, with negligible binding to hexadecane [108], although local hydrophobicity will vary depending on the proteins and other molecules in a given region. Since each AFM force curve probes tens of nanometres at a time, it is possible that the hydrophobic interaction will still be an important factor in cell adhesion, even though the capsulated bacteria are very hydrophilic on a macroscopic scale. An unencapsulated D39 derivative was found to have higher hydrophobicity than D39, with $\sim 30\%$ of cells adhering to hexadecane [108]. In a similar test for the pneumococcus' close relative *Streptococcus mitis*, a capsulated strain was shown to have $\sim 7\%$ adhesion to hexadecane, with an unencapsulated derivative also showing an increase in hydrophobicity, with $\sim 20\%$ adherence [205]. This suggests that the capsule of type 2 *S. pneumoniae* is better at masking the underlying molecules than that of *S. mitis*, since both unencapsulated mutants were more hydrophobic than their capsulated counterparts, but the scale of the difference was larger for *S. pneumoniae*. This suggests that the forces measured on the unencapsulated pneumococci with the hydrophobic tip could be larger than those measured in the capsulated pneumococci, due to the hydrophilic capsule obscuring potential hydrophobic binding sites.

The array of virulence factors which might be encountered by the AFM tip are summarized in Figure 4.1. Note that the capsule is not defined in this figure, but, by comparison with Figure 1.5 on page 19, it can be assumed that the capsular depth is sufficient to leave the tips of the three choline-binding proteins (CBPs) exposed whilst covering most of the other molecules.

It appears that CBPs have a large impact on the properties of unencapsulated

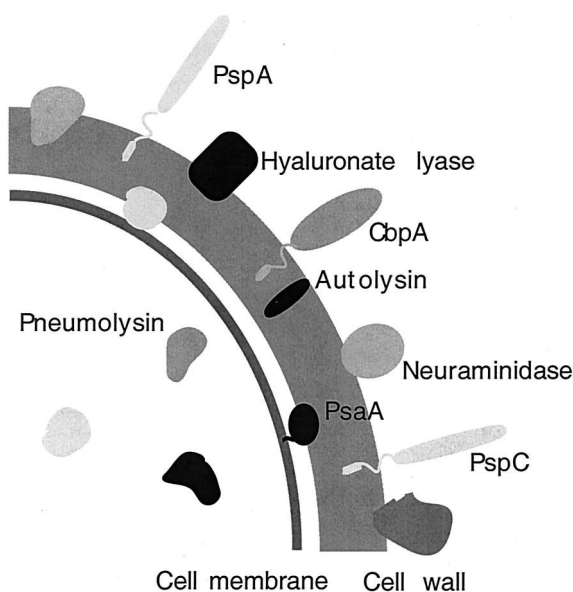


Figure 4.1: A more detailed look at the location of various virulence factors in relation to the pneumococcal cell wall (capsule not shown), showing molecules which could interact with the AFM tip and contribute to the measured adhesive forces. Reproduced with permission from [60].

pneumococcus: Swiatlo *et al.* compared the ζ -potentials and hydrophobicity of both capsulated and unencapsulated type 2 *S. pneumoniae* with equivalent bacteria which were incapable of anchoring CBPs to their surface, and as such were deficient in proteins such as PspA, CbpA and PspC (see Figure 4.1) [108]. In the capsulated bacteria, the differences between the CBP mutant and the wild type strain were small, with a change of -1.0 mV in the ζ -potential, and no discernible difference in the hydrocarbon binding assay. However, in the case of the unencapsulated derivative, the ζ -potential changed from -13.3 mV to -23.6 mV, showing that the CBPs contribute a net positive charge to surface electrochemistry, and therefore have a role in stabilization of the negatively charged capsule [60]. There was also a marked difference in hydrocarbon binding, with three times more cells adhering to the hexadecane, meaning that nearly all of the CBP-deficient mutant cells bound to oil. This suggests that the CBPs are significantly more hydrophilic than the peptidoglycan and teichoic acid-based cell wall, which is logical due to the polar characteristic CBP molecules (see Section 1.2.1).

The reason why CBP-deficient unencapsulated bacteria are highly electronegative is because the peptidoglycan of the cell wall is crosslinked by teichoic acid.

Teichoic acid is negatively charged at pH 7.4 because the phosphate groups within the phosphodiester bonds between the teichoic acid monomers have a pK_a of between 1 and 3 [107, 227], meaning that at pH 7.4, the phosphate will be ionized, giving it a net negative charge of 3 (PO_4^{3-}). The net electronegative charge in capsulated *S. pneumoniae* bacteria is because the capsular polysaccharide contains acidic groups such as the D-glucuronic acid at the terminus of the single sidechain in the repeating unit of the type 2 pneumococcal capsule [94]. The type 2 capsule also contains 2 D-glucose and 3 L-rhamnose residues per repeating unit, which are capable of hydrogen bonding and are hydrophilic in nature [94].

As the majority of surface molecules are hydrophilic in nature (this is a requirement of macroscopic hydrocarbon binding tests showing negligible binding for capsulated bacteria and low binding for an unencapsulated mutant), the force contribution from the hydrophobic interaction is likely to be relatively small due to the low density of hydrophobic elements on the cell surface. However, indentation of the surface during the force curve could expose more hydrophobic-binding sites to the AFM tip. This might mean that the background DDT adhesion forces are lower than the background forces for MUA, especially as the DDT-coated AFM tip is insensitive to electrostatic interactions and hydrogen bonding.

4.2 Sample experiment: D39 *Streptococcus pneumoniae* and MUA

The experiment described in this section is characteristic of the experiments that generated the data presented later in this chapter, but, since it was an early experiment, it contains maps obtained using a range of different applied forces and dwell times on the surface. It also contains two examples of trapped cells: a cell in a hole, and its partner cell which is predominantly on top of the substrate. These two cells have been analysed individually because they were clearly separated. In this work, diplococci were only treated as two separate cells if the boundary between them was very well defined. This was in order to prevent complications due to the challenge of

drawing a boundary between cells based on a relatively low-resolution height map.

Combined, the series of consecutive height maps presented in Figure 4.2 illustrate the process of locating a cell, zooming in on it, and the effects of repeated mapping on the cell pair. The corresponding force maps are also presented, in Figure 4.7, different masks are illustrated, and various characteristics of the data and the individual force curves are also discussed within this section.

4.2.1 Locating a cell pair and testing their tolerance of repeated mapping

Figure 4.2 on page 139 shows the height data from a series of force maps of the same pair of cells. These images have been included because they show that the area is generally stable over time, with drift causing slight distortion, as shown by the subtle differences in the shape of the cell in the hole, for example between C and D. The figure also shows that the height is fairly consistent between the maps, which have all had a linear plane fit applied (using the Asylum Research software) to the entire map in the y (top to bottom) direction to correct for a slant on the image. With the plane fit applied, the height of the cell out of the hole remains at > 300 nm.

The figure also shows the process of locating and zooming in on a cell: in 4.2A, a $7\ \mu\text{m} \times 7\ \mu\text{m}$, 32×32 pixel map is shown, which has high enough resolution to identify an area of interest (in this case, the cell pair is located towards the lower portion of the image, highlighted by the blue circle) whilst including a number of possible sites (holes, the round black features) in the map. Mapping was used to locate the bacteria as opposed to imaging because both contact and tapping mode tended to cause cells to detach soon after being encountered. One time-saving improvement which was applied in subsequent experiments was to remove the dwell time in these large “locator” maps. Once found, any cells could then be zoomed in upon and mapped using the desired parameters, giving a sufficient number of force curves on the bacterium surface for statistical analysis to be performed.

The map shown in Figure 4.2B was taken immediately after the one presented

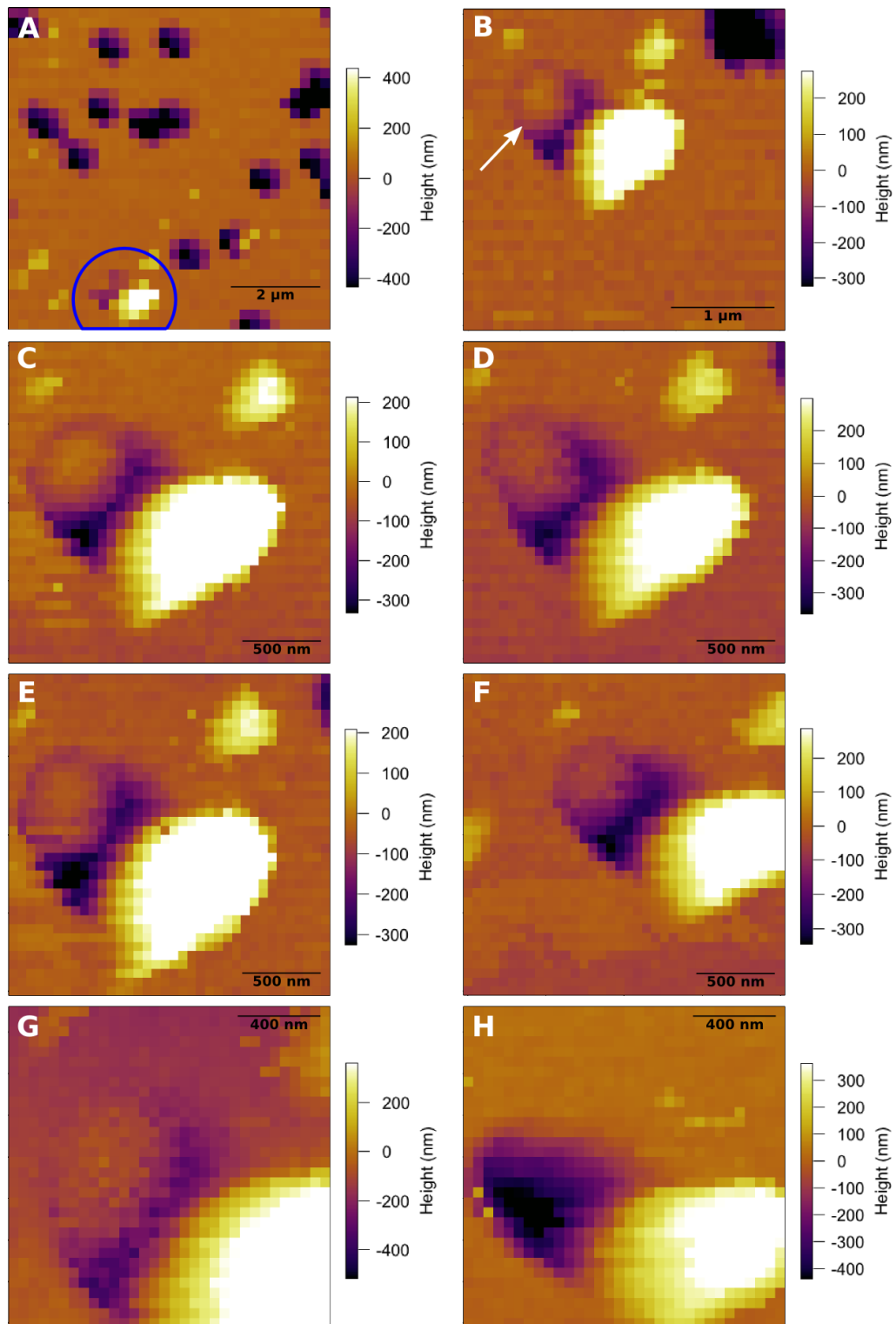


Figure 4.2: Consecutive height maps of a pair of D39 pneumococci obtained with various applied forces and dwell times on the surface, as given in Table 4.1 on page 141. On the larger scale map (image A), the cell pair is highlighted by a blue circle, and the cell in the hole, which is gradually forced down into the membrane pore by repeated mapping, is indicated by a white arrow in image B.

in 4.2A by applying an offset to the map position and decreasing the map size (in later experiments, the “nice zoomzoom” function in the Asylum Research software was used, with similar success). This map contained 32×32 pixels but the size was reduced to $3 \mu\text{m} \times 3 \mu\text{m}$, which allowed closer inspection of the cell pair without the new map being so small that the cell drifting out of the frame became an issue. In 4.2C, the scan size was reduced again to $2 \mu\text{m}$ and the number of pixels increased to 36×36 pixels. This meant that there were enough force curves on the bacteria for useful information to be extracted, and for the interaction to be mapped spatially across the cell’s surface.

The maps in Figure 4.2C-F all have the same size and resolution, and the final two maps (4.2G and H) have a scan size of $1.5 \mu\text{m} \times 1.5 \mu\text{m}$ containing 32×32 pixels. In this case, drift and inaccurate repositioning caused a large part of the more exposed cell to be cut out of the map region (4.2G). This is not ideal because the sampled surface forces no longer cover the entire exposed cell surface, but the map can still give an impression of the forces, assuming that the mapped area is representative of the entire cell surface, i.e. if the cell has a fairly homogeneous or randomized distribution of forces. In 4.2H, the map location is improved, but the cell in the hole is no longer visible, suggesting that the repeated mapping and application of forces to the cell have been sufficient to push it deeper into the hole. This is noticeable from Figure 4.2F onwards and could be partially explained by the different force curve characteristics observed on the cell in the hole, the cell on the surface, and the polycarbonate membrane (substrate), as shown in Figure 4.3 on page 142.

The maps shown in Figure 4.2 were obtained using different parameters, which are summarized in Table 4.1.

Although different parameters were used for the different maps, this did not seem to have too much of an effect on the appearance of the height maps. It could be argued that the most distorted cell image is that in Figure 4.2D, which was obtained using the longest dwell time, suggesting that increased dwell time on the surface, and therefore maps which take longer to complete, could be linked to increased drift

Table 4.1: Force curve parameters for the maps shown in Figure 4.2. All force curves were taken with a retraction distance of 500 pN and a tip z -speed of 992.06 nm s^{-1} .

Image	Applied force (pN)	Dwell time (ms)
A	500	240
B	500	240
C	500	240
D	500	510
E	500	0
F	500	240
G	250	240
H	700	240

severity. However, the map taken with no dwell towards the surface (4.2E) does not appear significantly different to the other maps, suggesting that this effect is more pronounced when long dwell times are used. Drift is also more apparent on the smaller maps (4.2G and H), so for the bacteria experiments, a compromise was made in order to obtain the highest number of force points on the bacterium without the map being so small that it drifted out of the map range.

4.2.2 Location-dependent force curve features

Figure 4.3 on page 142 shows a force-distance curve representative of those taken on the polycarbonate membrane (green trace), the cell on the substrate (pink trace), and the cell trapped in the membrane (blue trace). There are three graphs, A, B and C, each containing three sample curves from the force maps presented in Figure 4.7 parts E, A and D, respectively. The curves in Figure 4.3 had an applied force of 500 pN and were taken with a dwell time on the surface of 0 ms (A), 240 ms (B) and 510 ms (C). Some traces had a linear line subtracted to correct for baseline slope and all were offset so that the baseline was at 0 pN and the contact point was at approximately 0 nm (baseline subtraction can partially explain why there is some difference in the applied forces). Note that the applied force decreases slightly over time during a dwell on the surface for the curves taken on the cells, resulting in more hysteresis in these curves.

Force curves obtained on different types of material within the same force map tend to have different characteristics (see Section 2.1.2 on page 46). Briefly: because

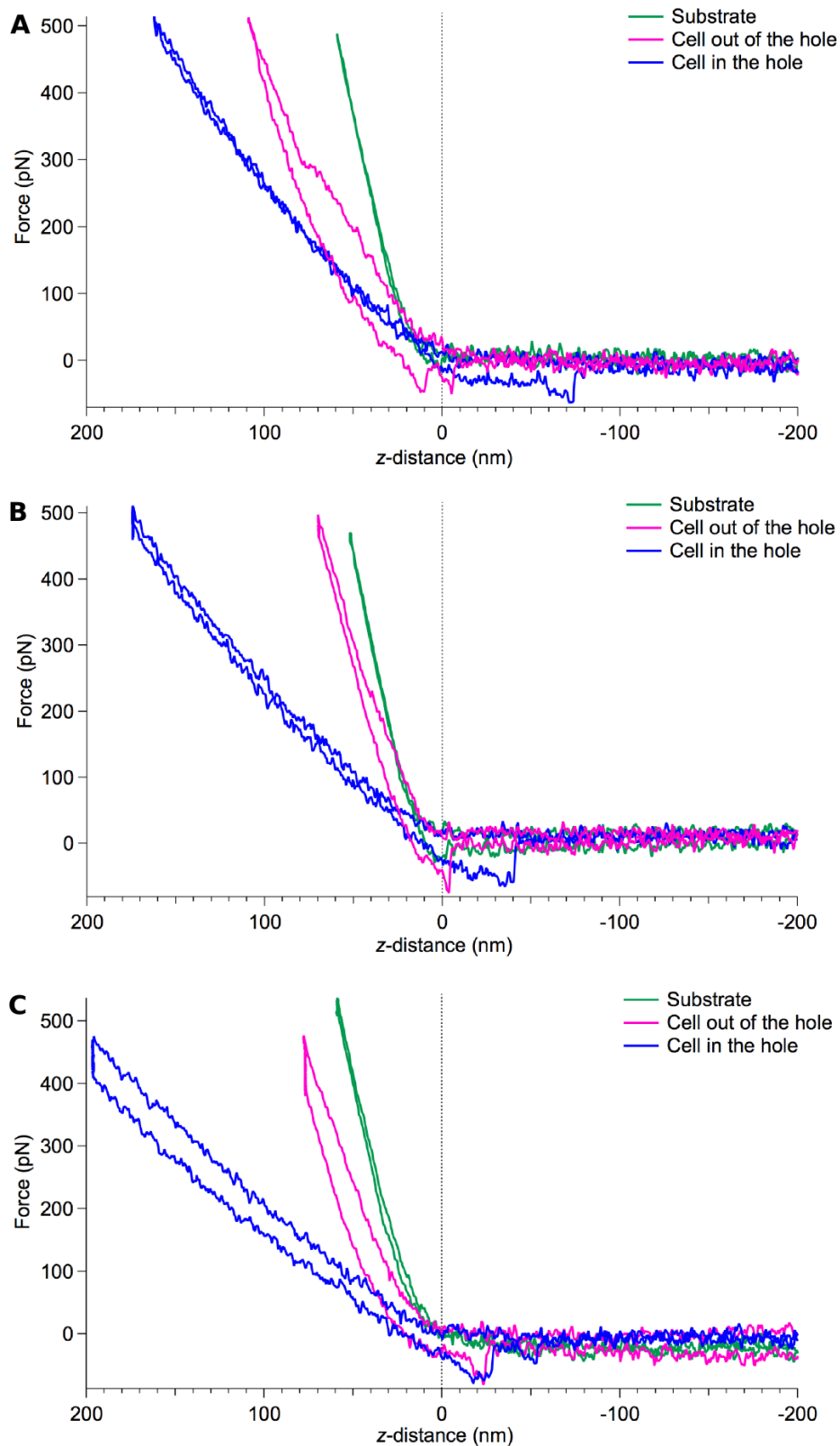


Figure 4.3: Typical force-distance curves taken with an MUA-coated tip in three different locations on a *Streptococcus pneumoniae* D39 sample: on the polycarbonate substrate (green trace), on a bacterium supported by the polycarbonate membrane (pink trace), and on a bacterium mechanically trapped in a hole in the polycarbonate membrane (blue trace). In each case the AFM tip applied a force of ~ 500 pN to the sample, but for different periods of time: A) 0 ms, B) 240 ms and C) 510 ms. Both the approach and retraction curves are shown and the x -axis has been cropped to make the portion of the curve around the sample surface clearer.

the polycarbonate membrane is comparatively rigid compared to the bacteria, it is expected to have a steeper gradient on the indenting portion of the force curve (z -distance > 0 nm) and for the indentation portion to mostly be linear. In contrast, the bacterium is expected to experience greater indentation (i.e. the left-most point on the curve is further away from z -distance = 0 nm) and the indentation portion is more likely to be non-linear. These features are clearly evident when looking at the green and pink traces on the graphs in Figure 4.3 (a similar pattern can be seen for approach curves taken on *Leishmania* parasites, an example of which is shown in Figure 3.16 on page 123). The exact level of indentation varies slightly depending on where the force curve is taken on the cell, but the difference between curves taken on the cell and the polycarbonate surface is clear and the curves shown in Figure 4.3 are typical of each type. Jumps in the indentation portion of the approach curve (e.g. the pink trace in 4.3A) can be due to slippage of the tip on the surface or rearrangement of molecules leading to areas of higher and lower resistance as the tip is pressed into the cell.

The blue traces on the graphs in Figure 4.3 show a force curve taken on the cell in the hole, whereas the pink traces are from the cell predominantly on the substrate. These blue force-distance curves show more indentation than the pink curves, which is likely to be due to the applied force causing the cell to move slightly into the hole and could explain why the cell disappears completely from the height map when the highest force of 700 pN was applied after six previous close-up maps (Figure 4.2H).

The force-distance curves taken on the cells also show examples of the type and scale of interaction forces that were identified as strong positive adhesion interactions. In this case, adhesion forces were no greater than 100 pN in magnitude, and the amount of extension before the pull off force varied between the events. In the case of the cell in the hole in Figure 4.3A (blue trace), a plateau-type extension is observed before the molecule is stretched out and finally the tip detaches from the cell approximately 70 nm from the point defined here as the cell surface (z -distance=0 nm). The curve on the cell in the hole shown in 4.3B shows an event

with shorter extension (~ 40 nm), whereas the curve in 4.3C shows two distinct binding events, one ~ 30 nm from the surface and a second, lower force event just over 50 nm from the surface. This graph also shows a binding event on the cell out of the hole, of similar magnitude to the first peak on the blue trace, and at a similar extension of 20 – 30 nm. Interaction events between the tip and the cells occurred for all map conditions tested in this experiment, and there appeared to be some difference in the measured adhesion forces (discussed in Section 4.2.5 on page 151). All of the adhesion events were clearly above the noise threshold in the data which was approximately 20 pN.

It should be noted that the analysis presented in this chapter is based on the adhesion force maps calculated by the Asylum Research software, which evaluates the adhesion force based on the largest interaction event (see Sections 2.1.2 and 2.1.3 on pages 46 and 49, respectively for discussion of this). Therefore, although the force curves contain information about the distance moved away from the sample before detachment occurs and can include multiple interaction events within a single curve, this additional detail about the character of the tip-sample interaction (e.g. number and size of multiple events, extension before bond rupture) is not used here. However, the information remains within the force-distance curve data and could be exploited at a future time.

4.2.3 Where to draw the line: selection of mask boundaries

In order to use the data provided by the force curves, masks must be applied to discount data from areas of the sample which aren't on the cell. Figure 4.4 on page 145 gives three examples of mask drawing for the first close-up map taken of the cell pair (500 pN applied force and 240 ms dwell towards the surface).

Masks were initially drawn on the height map using the iterative mask function in the Asylum Research software (any plane-fits should be applied before this step). This selected any material protruding above the sample substrate and was a useful starting point from which to select the best mask for the given map. The mask was tailored to the map in question so that the maximum number of data points

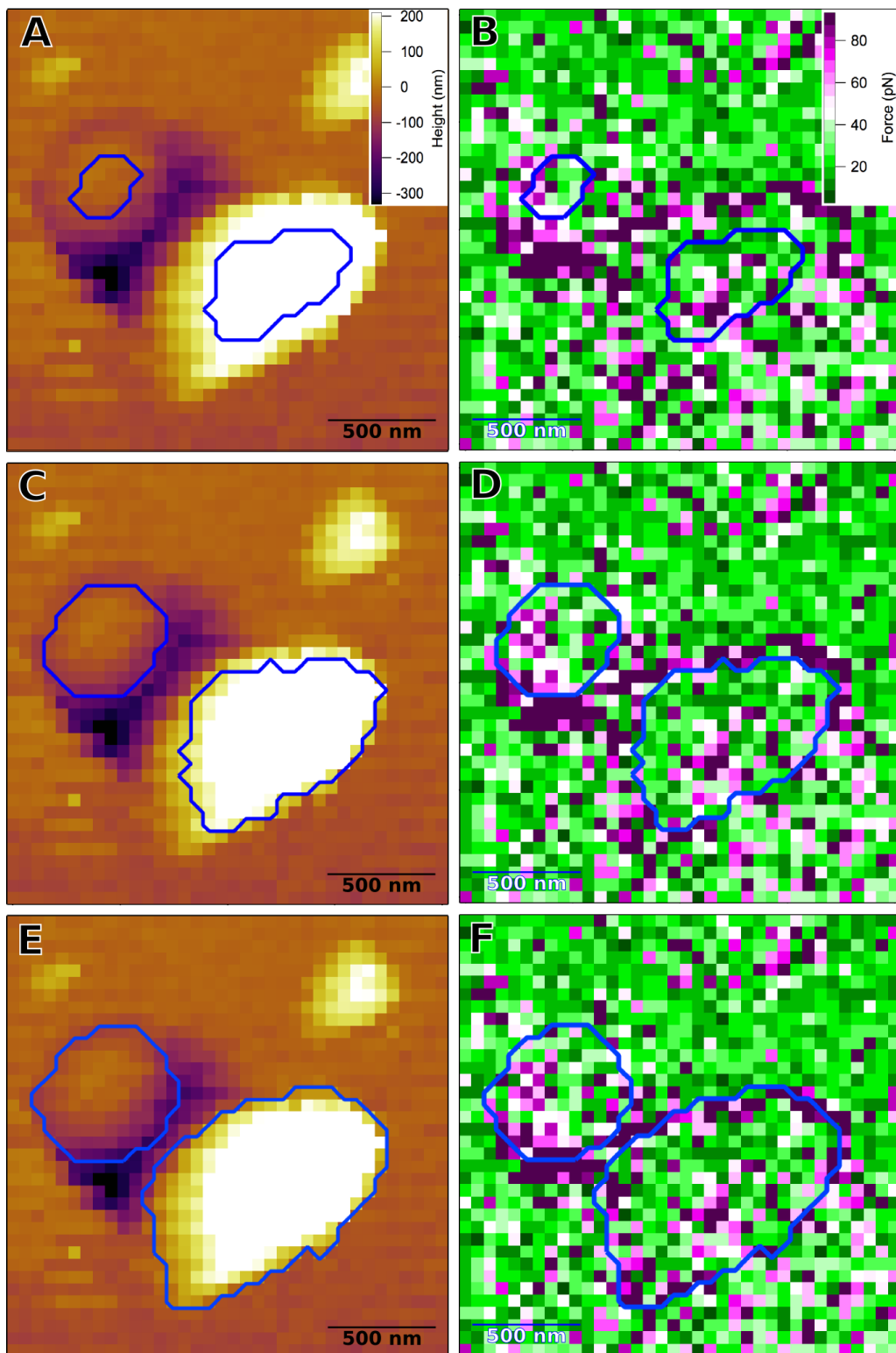


Figure 4.4: The same height (left) and force (right) map of a pair of D39 pneumococci used to illustrate three different mask thresholds (blue lines). A and B show a mask which is too small: all data points are on the cells but there are too few data points for use in statistical analysis. C and D show a suitable mask: constrained to the cell top but including as many force points as possible. The mask in E and F is too large, including data points on the steep edges of the cell. Force curves obtained in these edge regions tend to generate higher adhesion forces (purple force points) due to increased contact area between the tip and the sample.

on the cell were included whilst minimizing the influence of artificially high forces measured along the perimeter of the cell due to increased contact area between the side of the tip and the cell, and messier curves (often a result of tip slippage on steep cell edges and when in contact with softer material). This phenomenon is illustrated in Figure 4.4F where, towards the top of the cell on the surface and the lower edge of the cell in the hole, a ring of high force points along the cell edge is included in the drawn mask.

The mask should include as many points as possible on the surface of the cell without including edge areas with uncharacteristic lines of high forces to allow for more accurate statistical fitting. In Figure 4.4B, whilst all data points are safely on the top middle of the cell, because only a small number of force points are included, it is not a fair representation of the cell adhesion distribution and the mask on the cell on the surface includes a relatively high proportion of white, pink and purple positive interaction events compared to the population of adhesion forces in the masks presented in 4.4D and F. The best mask to use for this map is therefore the one illustrated in 4.4C and D. All *S. pneumoniae* force maps were treated in this manner in order to best extract their force data. The *Leishmania* parasite work did not require as much mask drawing because the cells were much larger and therefore in most cases a zoomed in map of $1.5\ \mu\text{m} \times 1.5\ \mu\text{m}$ and 28×28 pixels was either mostly or all on the parasite surface (see Section 5.5).

4.2.4 Can data from different maps of the same cell be combined?

In some cases, to make sure the entire cell was within the map area, a larger scan size was used (e.g. $\sim 2\ \mu\text{m} \times 2\ \mu\text{m}$ for a single cell or cell pair, as in this case), and the proportion of the map covered by the cell was not ideal. However, in some cases, the same cell or pair could be mapped multiple times. In this section, the validity of combining the data obtained in these repeat maps is assessed using the example of two maps which were obtained using an applied force of 500 pN and dwell time of 240 ms on the same pair of D39 pneumococci with an MUA-coated tip (the force maps of which are shown in Figure 4.7C and D on page 152). The maps were not

obtained consecutively, but had two maps taken in between (the maps in question are C and F according to the notation in Figure 4.2 and Table 4.1).

Figure 4.5 on page 148 shows different parameters extracted from the data and fits of the data for the cell out of the hole (top graph) and the cell in the hole (bottom graph), and the bars correspond to results from the different maps: navy blue being the first map, pink being the second map (which had fewer force points in the mask than the first map for both cells), and purple representing results obtained when using the combined data from both maps. The force parameters used for comparison are the median of the raw force data, and the force evaluated from either a single Gaussian or double Gaussian finite mixture model fitted to the histogram of the \log_{10} of the adhesion data. It is clear from the graphs that the combined map results are in between the results from the separate maps and that, in the case of the cell in the hole, where the second map provided insufficient data to fit using either Gaussian model, combining the two maps allows the data from the second map to be included in the analysis. Note that the median force is similar in value to the mean force of the single Gaussian fit, and that the two mean adhesive forces in the double Gaussian model are either side of the median force, as would be expected.

In Figure 4.6 (page 150), the effect of combining maps is considered in terms of the stability of finite mixture model fits. The figure shows a two component Gaussian model applied to the data on the cell out of the hole from A) map 1, B) map 2 and C) maps 1 and 2 combined. The graph on the left shows the first Gaussian component in red and the second in green, rendered on top of the histogram automatically produced as part of the analysis in the statistical software ‘R’. The second column of graphs shows the cumulative distribution function (CDF) of the raw data, normalized to 1, and the graphs on the right hand side show this plotted against the CDF calculated from the model data. The straighter the diagonal line, the better the model describes the data. The cleanest theoretical vs. empirical CDF plot is that in 4.6C, showing the combined data. In the other graphs, map 2 (4.6B) shows more deviations from a straight line than map 1 (4.6A). This demonstrates that although a 2-component Gaussian fit describes all of these maps, the best fit is

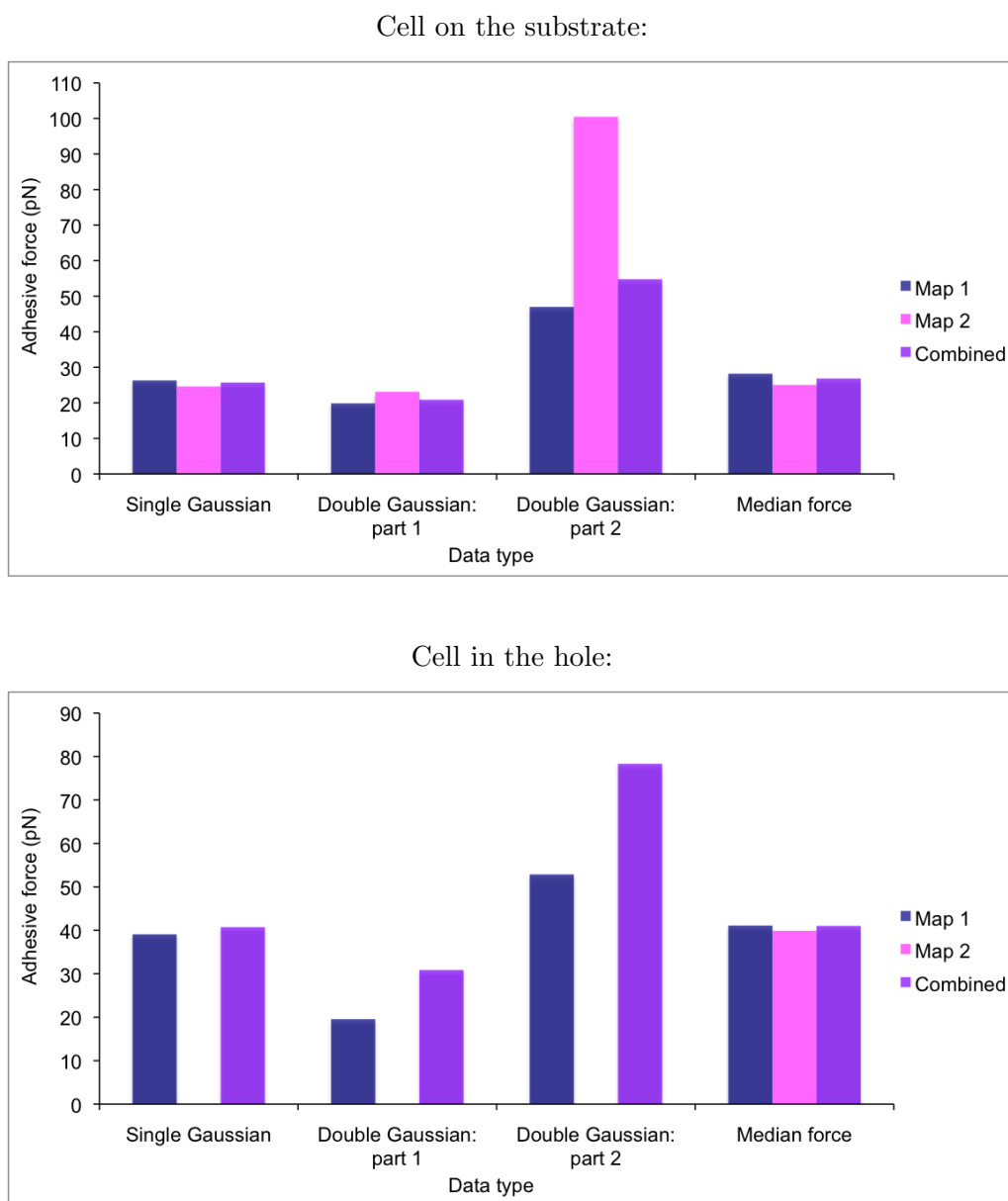


Figure 4.5: Graphs comparing different force measures including Gaussian fits (either a single Gaussian or a finite mixture model of two Gaussians, both being applied to a histogram of the force data) and the median of all the masked force map data for two separate force maps and their combined data. The data were obtained in a single experiment, on the same D39 pneumococci with an MUA-coated tip, using an applied force of 500 pN and a dwell time on the surface of 240 ms (images C and D in Figure 4.7 on page 152). The top graph compares data obtained on the cell predominantly resting on the substrate, and the lower graph compares data obtained on the cell in the hole. Note that there are no Gaussian fit data for the cell in the hole from map 2. This is due to only a small number of force points being obtained on the cell and therefore the data proving very difficult to fit with either one or two Gaussian curves. Map 2 had fewer data points for either cell than map 1.

of the combined data, which is a logical result given that there are more data points to fit.

In Figure 4.5, the single Gaussian, first Gaussian component and median values are all very similar, particularly in the case of the cell out of the hole. There is more variation between the means of the second Gaussian component, but given that this second component is shallower and broader in this case, this in itself is unsurprising. The fact that the values in three out of four conditions are very similar between the separate and combined maps, along with the improved fit of the finite mixture model for the combined map data, makes a very strong case in favour of combining repeat maps of the same cell.

It is therefore clear that there is more benefit in combining maps than in selecting one or the other to represent the bacterium in question. For the pneumococcus work, where recorded, force data from consecutive maps (no more than 3) of the same bacterium (taken immediately after one another compared to the case presented here where there was a break of approximately one hour between the end of the first map and the start of the second) have been combined in order to give a more representative sample of the forces across the surface, both when used to draw histograms for fitting, and when extracting the median force from the data.

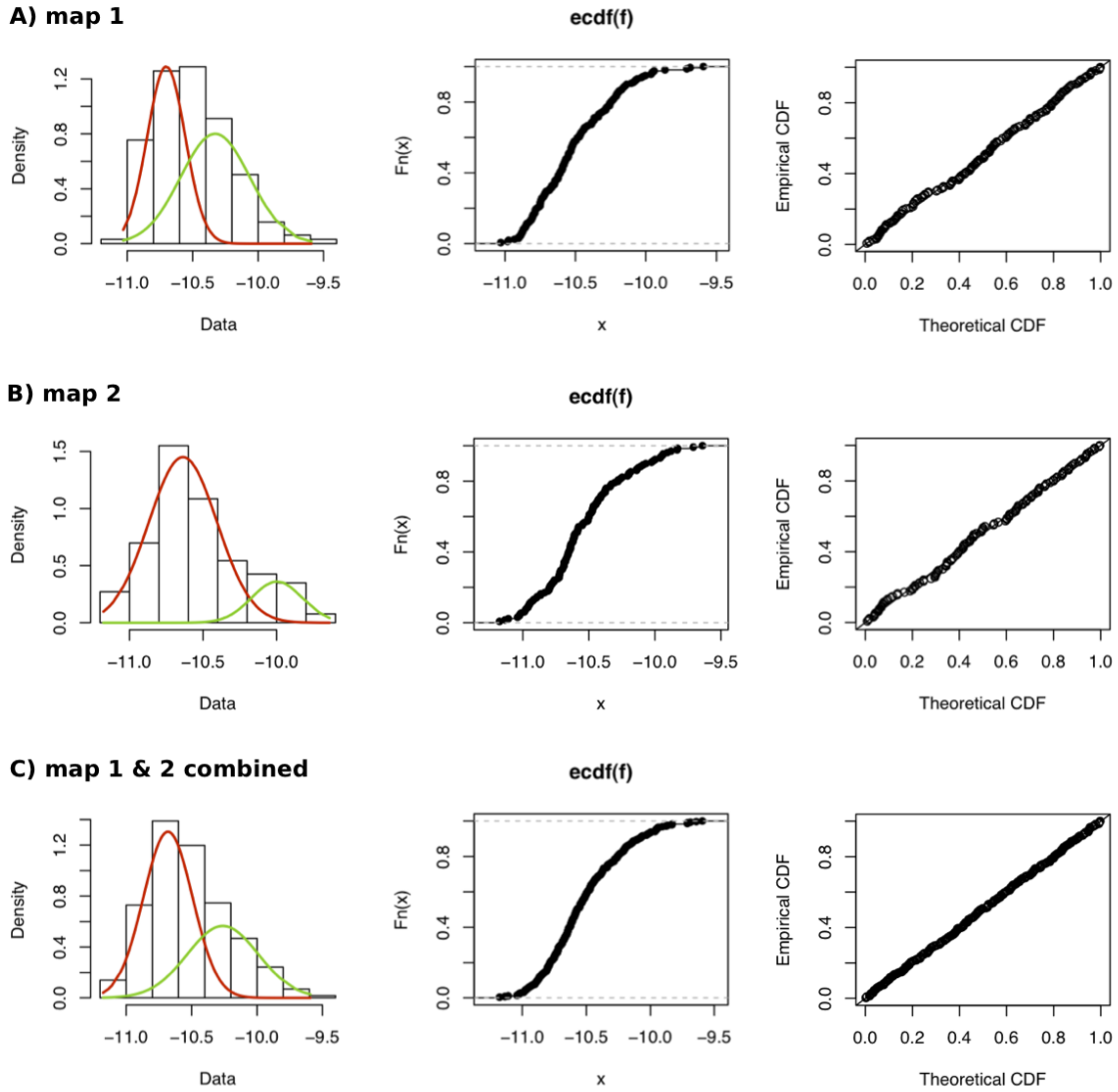


Figure 4.6: Comparison of finite Gaussian mixture model fits of data from the cell out of the hole in map 1 and map 2, and the fit of the combined data from both maps (A, B and C, respectively). The left hand graphs show the location of both Gaussian components (G_1 in red and G_2 in green) on a histogram of the \log_{10} force data, the middle graphs show the (normalized) empirical cumulative distribution function (CDF) of the \log_{10} force data (i.e. using the raw data), and the third graphs plot this empirical CDF against the theoretical CDF of the fit (i.e. the CDF as calculated using the model data). The closer this third graph is to a straight, diagonal line, the better the fit. For both individual maps, the third graph deviates from a straight line in several places, but the combined map data gives much better alignment. All fits were stable with two Gaussian components, but the combined data was modelled more accurately.

4.2.5 The effect of different forces and dwell times on the measured peak adhesive force

Figure 4.7 shows the masked force maps of both cells when applying different forces for assorted dwell times, given in white text as part of the image label. The strong, positive binding events (white, pink and purple) appear in clusters on the cell surface, although in images 4.7C and D, which were taken with the same parameters but with map start times approximately 1.5 hrs apart, these high force regions are not co-located, particularly on the cell in the hole (the smaller cell on the left hand side), where the high forces appear to swap from the left hand side to the right hand side of the cell. However, their force distributions are fairly similar (see Figure 4.6 on page 150).

By visually inspecting the maps, which are all presented with the same force scale, it is clear that increased dwell time for the same force leads to a higher proportion of curves showing an adhesive interaction (note the marked difference between Figure 4.7B and D in particular), and it also appears that for the same dwell time but increased applied force, there is also some increase in the frequency of positive interactions. This is further explored in Figure 4.8 on page 153, where different force measures are presented as a function of applied force (top) and dwell time (bottom).

In Figure 4.8, only the first Gaussian component for the cell out of the hole has been included for the 500 pN, 510 ms dwell condition because the second component had a mixing proportion, λ_2 , of 0.02, suggesting that there was only a 2% likelihood that data were associated with this peak (i.e. it was extremely small). This compares to $\lambda_2 = 0.53$ for the distribution shown in Figure 4.6A and $\lambda_2 = 0.16$ for the distribution shown in Figure 4.6B. The double Gaussian fit was also unstable, so the point has just been included for guidance (because the second component was so small, the resulting model is similar to a single Gaussian fit). The double Gaussian fit of the cell in the hole for 500 pN, 510 ms dwell was too unstable to be included at all.

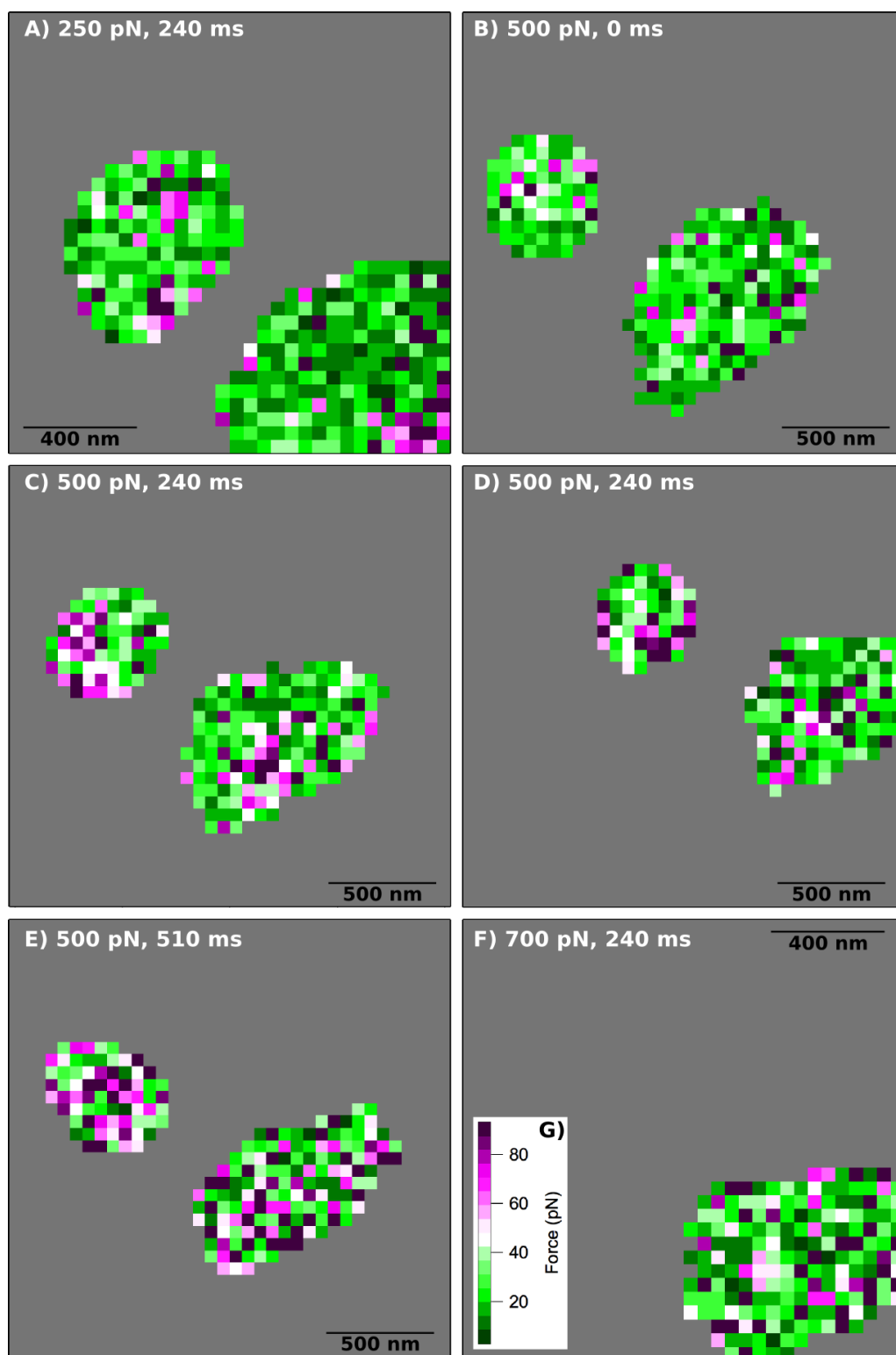


Figure 4.7: Force maps of a pair of D39 pneumococci obtained with various applied forces and dwell times on the surface using an MUA-coated AFM tip. The force scale inset to image F is the same for all images.

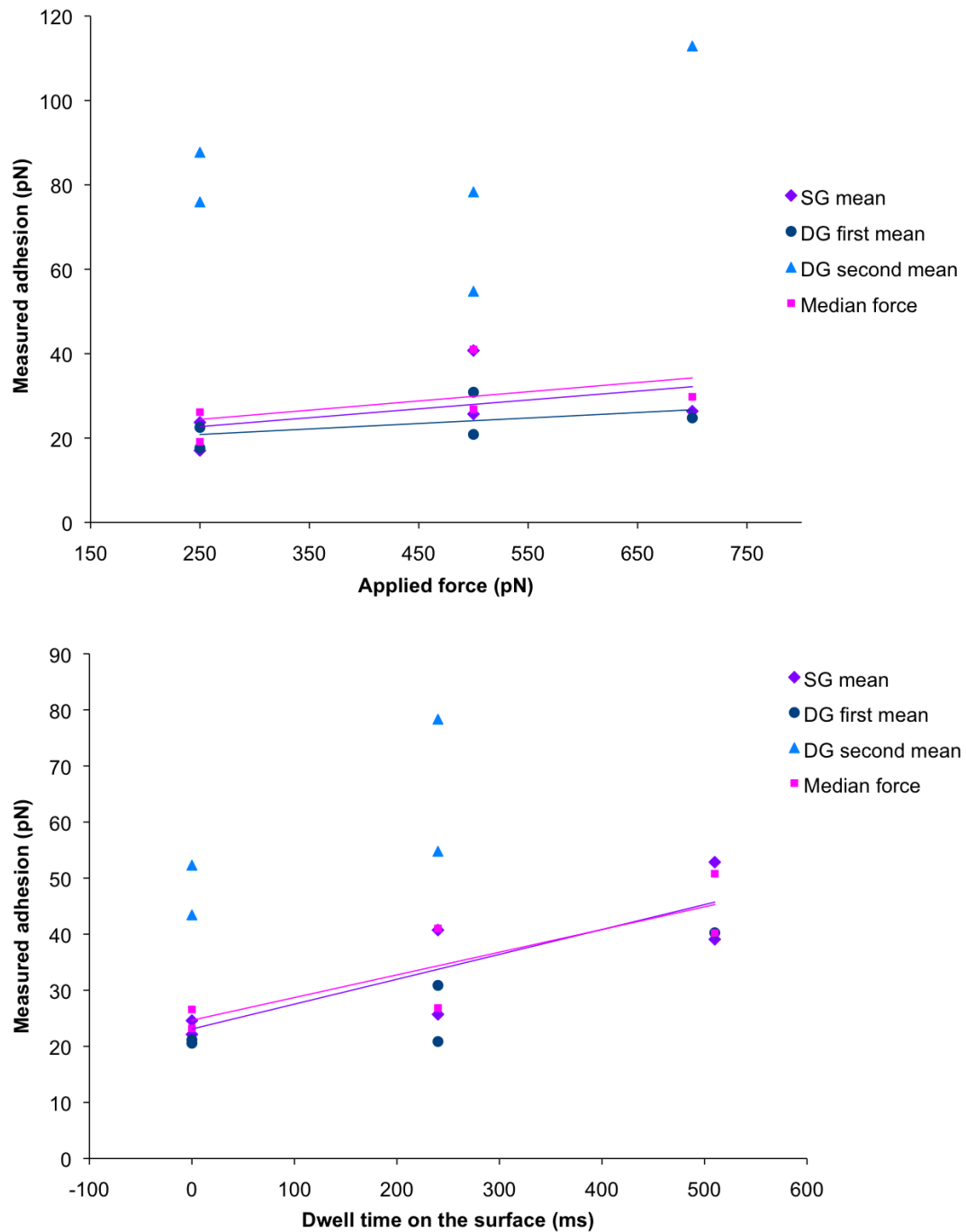


Figure 4.8: Graphs showing adhesive force measures for the same pair of bacteria when measured using different forces (top) and different dwell times (bottom). The two data for each condition are from the cell in the hole and the cell out of the hole. Linear lines of best fit are to guide the eye when observing how the median force, single gaussian (SG) fit and, in the case of varied applied force, the mean of the first Gaussian component of the finite mixture model (or “double Gaussian”, DG) change with the different parameters. The data in the top graph were obtained with a 240 ms dwell on the surface, and the bottom graph was obtained using an applied force of 500 pN.

4.2.6 Can a single Gaussian fit be compared with the first Gaussian component of a finite mixture model?

From the graphs in Figure 4.8 it is clear that the mean force of the first component of the finite mixture model is much closer to the mean of the single Gaussian than that of the second component. In addition, the median of the force data, the mean forces of the single Gaussian and first component of the double Gaussian all appear to increase with both increasing applied force (Figure 4.8A) and increasing dwell time (Figure 4.8B), whereas there is no clear relationship between the mean of the second component of the finite mixture model and increasing applied force (Figure 4.8A, pale blue triangles). The forces associated with the second component of the mixture model are also significantly higher than the other forces, particularly in the case of 250 pN applied force and 240 ms dwell; the map parameters used throughout the rest of this chapter. It is therefore reasonable to compare the mean force resulting from a single Gaussian fit of the \log_{10} force data histogram with the mean force calculated from the first component of a Gaussian finite mixture model of \log_{10} force data in other maps, in the case where a multiple-Gaussian fit is unstable (i.e. when the histogram data is clearly unimodal). For certain bacterium-tip combinations, very few maps presented data showing a bimodal distribution, so, in order to draw meaningful conclusions and compare the different *S. pneumoniae* data sets, single Gaussian fits of normal \log_{10} force histogram data were considered alongside the first Gaussian component of the FMM model for non-normal \log_{10} force distributions, except when the discussion pertained solely to bimodal distributions (e.g. Sections 4.3.3 and 4.3.4).

4.3 Results: comparison of interactions between capsulated and unencapsulated *Streptococcus pneumoniae* and tips coated with hydrophilic or hydrophobic surfaces

In this section, data summarizing the experiments conducted on *Streptococcus pneumoniae* are presented and discussed. By comparing various qualities of the data, a

picture of microscopic bacterial adhesion properties can be built up and considered in terms of different surface properties and forces. The discussion will be split into subsections which are in the form of questions to be answered.

4.3.1 Does the bacterial adhesion vary between capsulated and unencapsulated bacteria, and hydrophobic and hydrophilic surfaces?

Figure 4.9 on page 156 shows the average values of three different force measures: the median force, the mean of either a single gaussian model (G_s) or the first component of a two component finite mixture model (G_1), and the mean of the second component of the finite mixture model (G_2). All Gaussian-derived values originate from models applied to a histogram of the \log_{10} force data. For ease of comparison, the mean of the Gaussian model has been converted back to a force (the Gaussian mean in terms of \log_{10} force is defined as μ_k , where k is the number of the component). The error bars on the graph show the standard error in the data, which consists of a minimum of six cells for each combination, taken during a minimum of three independent experiments. The number of data points in series G_2 is lower because the \log_{10} force histogram of some cells could not be modelled effectively using more than one component (see Section 2.3.1 on page 54). The proportion of the cell population with multiple force distributions for the different cell-tip combinations is shown in Figure 4.14 on page 168. In the case of D39 *Streptococcus pneumoniae* probed using an MUA-coated AFM tip, only one cell showed a stable bimodal distribution, so this point is represented by a dashed column and a diamond marker in the colour of the relevant data series for the graph. This improves the ease of comparison with other data, but clearly separates the datum from other values which represent a larger cell population.

Figure 4.9 shows that the median force and first Gaussian mean of the data are within the standard error of one another for all cell-tip combinations, however, there does seem to be some difference between the scale of the force between the different combinations. For both capsulated and unencapsulated bacteria, the median and G_s/G_1 mean forces measured using a hydrophilic MUA-coated tip are higher

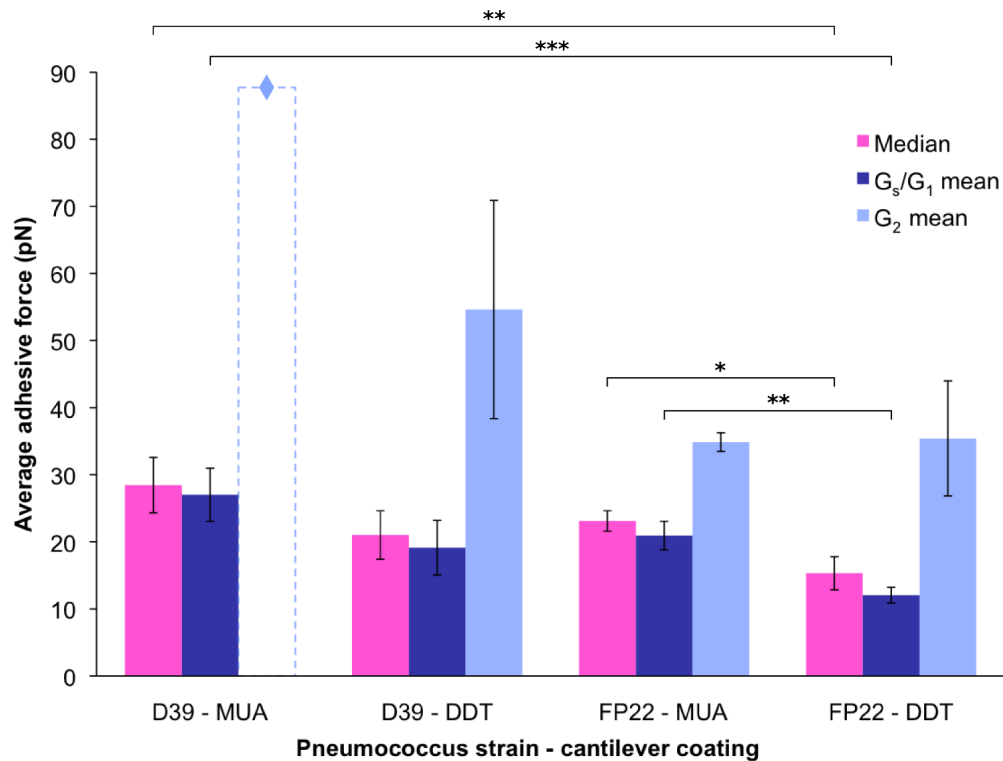


Figure 4.9: A graph showing the difference between averages of three force measures for the capsulated (D39) and unencapsulated (FP22) *S. pneumoniae* strains, and hydrophobic (DDT) and hydrophilic (MUA) tip coatings. The median force is shown in pink, the mean force of either a single Gaussian fit, or the first Gaussian fit of a finite mixture model is shown in dark blue (G_s/G_1 mean), and the mean force of the second Gaussian component of the finite mixture model is given in pale blue (G_2 mean). The error bars on the graph show the standard error in the data. Only one cell showed a bimodal \log_{10} force distribution in the D39-MUA category, so this datum is represented by a dashed bar with a diamond marker. Statistically significant differences are indicated by stars according to the scale in Table 2.1 on page 60.

than those measured using a hydrophobic DDT-coated tip, although this difference is only significant in the case of FP22 (p -value = 0.0037). Also, for the same tip coating, the capsulated D39 bacteria have higher median and G_s/G_1 forces than the unencapsulated FP22 bacteria, although none of these differences are statistically significant. It is possible that this trend is repeated for the mean value of the higher force Gaussian component, G_2 , however, there is more spread in this data for the DDT-coated cantilevers and more cells expressing bimodal \log_{10} force distributions would be required for the D39-MUA combination in order to confirm this. The mean value of G_2 is consistent between the unencapsulated FP22 *S. pneumoniae* bacteria and both tip types, with a magnitude of 35 pN, although the magnitude of the difference between G_2 and G_s/G_1 is greater when a DDT-coated probe was used.

Since the capsule is able to reduce deposition of opsonins and other biomolecules [59,90,91], it is perhaps surprising that the low level adhesion forces measured using both the hydrophilic and hydrophobic AFM tips were higher for the capsulated bacteria than for the unencapsulated bacteria. However, this could be explained by the nature of the material probed during experiments on the two cell types: the capsule is not crosslinked and is therefore soft compared to the rigid, heavily crosslinked peptidoglycan of the cell wall, which provides the cell structure [85]. Because the applied force is the same for all the experiments, it is logical that the tip will indent further into the capsulated cell surface than the unencapsulated cell surface, and therefore more molecules on the tip will interact with the cell. This was confirmed by comparing force - distance curves from across a range of bacteria included in the analysis, which are shown in Figure 4.10 on page 158.

In Figure 4.10, the approach portion of several force - distance curves representing both the A) capsulated and B) unencapsulated cell population are presented, and the range of the different indentation depths is illustrated by the grey box overlaid on the graphs (indentation is indicated by positive z -distance values). The curves, representing the central region of different cells from across 3 experiments, are taken from the experiments using the DDT-coated tip, so electrostatic repulsion by the

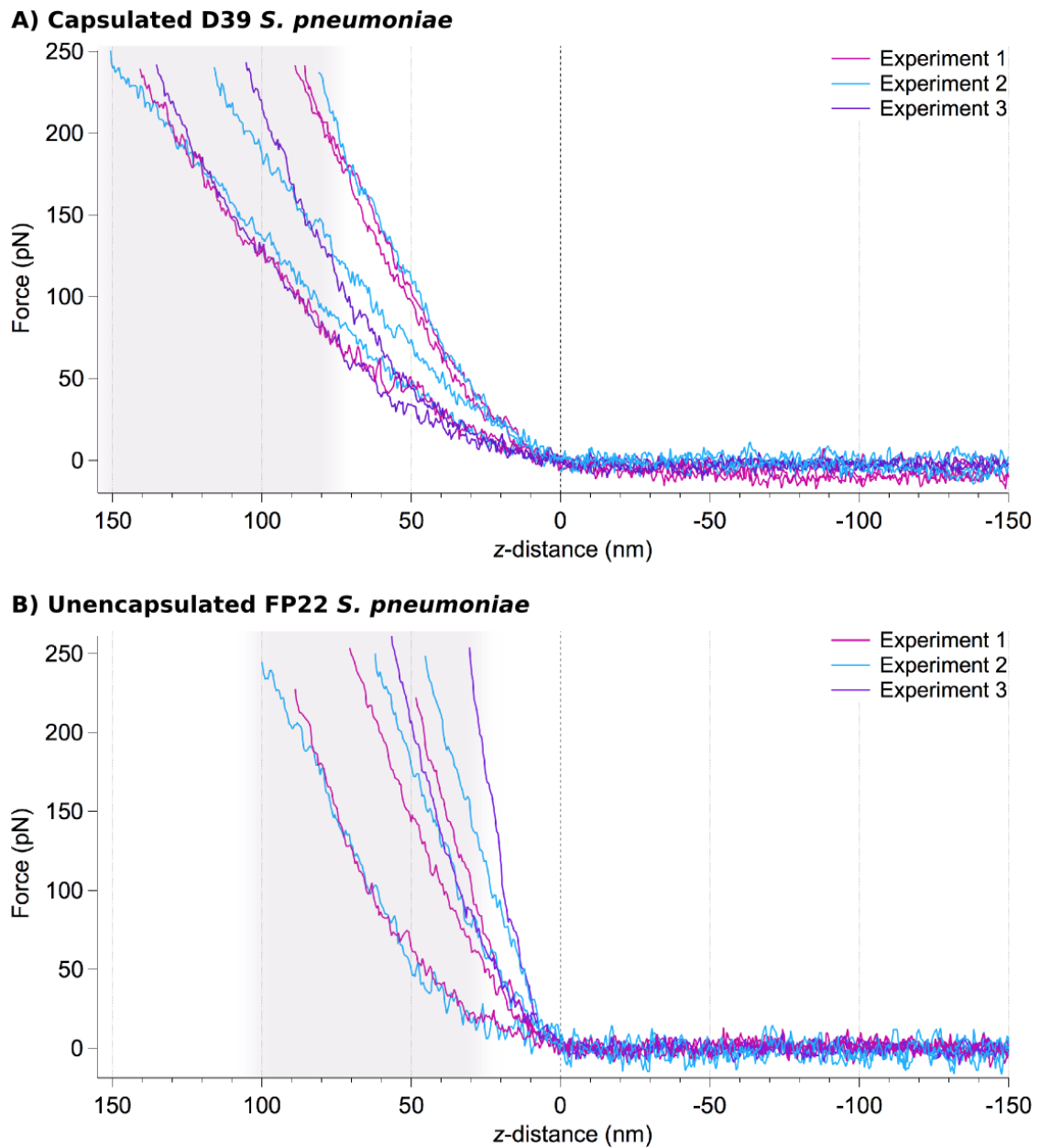


Figure 4.10: force-distance approach curves (the dwell and retraction portions of the curve are not shown) taken from the central region of different bacteria across 3 experiments on A) capsulated and B) unencapsulated bacteria. The curves were measured using a DDT-coated, hydrophobic tip to eliminate effects due to electrostatic charge. 2 or 3 curves from the highest regions of different cells are shown, illustrating the range of indentation depths observed on the bacteria population. For ease of comparison, the range of indentation distances is overlaid with a grey box. The variation in indentation depths is similar between the capsulated and unencapsulated bacteria, but the capsulated bacteria are indented ~ 50 nm more than the unencapsulated bacteria. The slope of the indentation portion of the force-distance curves is steeper on the FP22 bacteria, confirming that the cell wall surface is stiffer than the capsulated surface of the D39 bacteria.

negatively charged cell wall and capsule did not impact the indentation depths. The force curves taken on the capsulated bacteria (4.10A) have indentation depths ranging from 80 nm to 150 nm, with a shallow slope. In contrast, the curves taken on the unencapsulated bacteria (4.10B) have indentation depths ranging from 30 nm to 100 nm and a steeper slope, showing that the material being indented has a higher Young modulus than the material in graph A [17].

Neither of the graphs in Figure 4.10 show a sudden change in gradient in the final indentation portion of the approach curve, showing that the type of material being probed has not changed (force-distance AFM curves have been shown to have discontinuous gradient changes when probing polymer films containing layers of different stiffness [228]). This suggests that the cell wall has not been breached in the case of the FP22 bacteria (in addition to the lack of significant gradient change, the peptidoglycan layer is predicted to be 160 nm thick [82], making the measured indentations of up to 100 nm well within this limit), and that the capsule is at least as thick as the maximum indentation depths in the case of the D39 bacteria. This suggests that the capsule is at least 90 nm thick and, in some cases, at least 150 nm thick. This is consistent with the EM and TEM images presented in Figure 1.6 on page 21, which estimated that the capsule of D39 bacteria was between 100 nm and 200 nm thick (TEM [59] and EM [97] image, respectively).

As the indentations are within the capsular thickness for D39 and within the cell wall thickness for FP22, it can be assumed that the molecules interacting with the AFM tip in the case of D39 bacteria include those in the capsule, the upper portions of proteins which extend beyond the capsule and some molecules that protrude a good distance into the capsule (above the cell wall). In the case of the unencapsulated bacteria, both molecules within and protruding from the cell wall are being probed (see Section 4.1.2). The main difference between the two strains is therefore that the capsular polysaccharides probed in the case of D39 are replaced with peptidoglycan, teichoic acid and other additional molecules which are either embedded in (or do not protrude more than a few nanometres beyond) the cell wall. Additionally, in unencapsulated bacteria, the entire length of proteins which

were only partly exposed on the capsulated bacteria will be fully exposed, since production of these should be unaffected in the unencapsulated derivative strain.

For both strains, the G_s/G_1 forces were larger when measured using an MUA probe than when using a DDT probe (although the difference was only statistically significant for FP22). DDT carries no charge and is strongly hydrophobic, whereas MUA has a hydrophobic chain with a hydrophilic end group ($-\text{COOH}$) which will be ionized to $-\text{COO}^-$ in pH 7.4 PBS. Therefore, the DDT-coated tip is vulnerable to fewer forces than MUA. This could lead to a lower background in the adhesion force data. It should be noted that the noise in the data is approximately ± 10 pN but varies slightly between curves and experiments, with some particularly noisy curves imposing an upper limit of ± 13 pN, and some of the cleaner curves having ± 5 pN fluctuations from the baseline. Since the adhesion forces are calculated by subtracting the average of the final points of the baseline of the retraction curve from the lowest point in the curve, it is possible that force-distance curves with no binding events have an effective adhesion of ~ 10 pN. This means that a proportion of the force values associated with the G_1 mean originate from zero force events and, in the case of FP22-DDT, which has the lowest and most consistent (i.e. smallest uncertainty) G_s/G_1 adhesive force of all of the categories and combinations (12 ± 1 pN), the G_1 Gaussian fit is likely to include a large number of force curves containing no clear adhesive interactions. The fact that the first and second Gaussian fits of the \log_{10} force data for FP22-DDT predict that data is shared approximately evenly between the two distributions (see Figure 4.12 on page 166) suggests that approximately 50% of the force curves detect one of these positive binding events, with an adhesive peak well above the noise threshold in the data.

The mean G_2 adhesion force was the same when measured using the DDT and MUA probes and FP22 bacteria, but the relative difference between G_s/G_1 and G_2 was greater in the case of DDT: the overall strength of strong positive binding interactions was similar (e.g. between the hydrophobic probe and hydrophobic regions of bacteria molecules, or the negatively charged probe and positively charged regions of bacterial proteins), but the low-force interactions were smaller when using the

neutral, hydrophobic probe. This is likely to be due to the DDT tip being sensitive to fewer types of force.

4.3.2 How do the forces measured on the bacteria compare to those measured as part of the control experiments?

The scale of the forces measured in the control experiments between two SAMs was much larger than those measured on the bacteria (see Section 3.7, and specifically Figure 3.18 on page 128), with the DDT- DDT experiment in particular showing very high average adhesion forces of ~ 2.7 nN, which is just under 100 times the average of the adhesion force values recorded here: 47 ± 7 pN and 25 ± 4 pN for D39 and FP22, respectively. Here, ‘average’ values are the mean of the average forces of all data from the individual maps, presented with the standard error from inter-cell variation. The D39- DDT average force is higher because it was the combination that most readily expressed a bimodal distribution and so had more contributions from high force adhesion events. The comparatively small average forces measured on *S. pneumoniae* using a DDT-coated tip are at least partly due to the bacteria being macroscopically hydrophilic and therefore there are very few hydrophobic regions exposed on the cell surface, leading to a lower frequency of positive interaction events in the biological system, compared to 100 % positive interactions between the DDT tip and DDT surface under the same experimental conditions. Steric hindrance by the capsular polysaccharides and surface proteins is also a factor exclusive to the bacteria experiments. Steric repulsion contributes a repulsive force between the bacterium and the tip [12] (reducing the strength of interaction events [14], see Section 1.1.1 on page 3), and solvated, bulky biopolymers and hydrophilic proteins on the cell surface can potentially obscure hydrophobic binding sites (reducing binding event frequency). The DDT probe and the hydrophilic, negatively charged MUA SAM still showed larger adhesion forces (~ 1 nN) than those measured on the bacteria, suggesting that the same biopolymer-related effects are also present in this case.

The MUA - MUA control experiment had the weakest binding force at ~ 0.44 nN,

and included some events with no positive binding interactions. This value is the closest to those measured on *S. pneumoniae* with the coated tips, however, the control experiment value is still 14 times higher than the average forces here (35 ± 7 pN and 28 ± 5 pN for MUA probes and D39 and FP22, respectively), again, suggesting a role for steric hindrance in reducing the average interaction forces measured on cells compared to the MUA SAM. As both the cell and the MUA SAM are negatively charged, electrostatic repulsion between the tip and the sample is a factor in both cases, and so other factors, such as steric hindrance, must contribute to the lower bacterial forces.

4.3.3 Does the shape of the Gaussian distribution vary between the two FMM components?

Figure 4.11 illustrates the widths of the two fits in a bimodal distribution (G_s data is therefore not included) and is a measure of the spread of the data associated with each Gaussian component. Full conclusions cannot be drawn from D39 - MUA alone, however, it appears that for both D39 and FP22, the widths of the two components are essentially equivalent when the MUA-coated tip is used. In contrast, when the DDT tip is used, the second Gaussian component, G_2 is broader, suggesting a larger force range than when MUA is used (especially given that these Gaussian distributions were fitted to the logarithm of the force data). This difference is most striking in the case of the unencapsulated FP22 bacteria and DDT-coated tip, where there is also less variation in the width of G_2 (and therefore a smaller error bar on the graph) compared to the capsulated D39 bacteria probed with the same tip. The uncertainty in both the mean and the width of the second component for D39 - DDT was larger than in the other cases, showing that the increased variation between cells in terms of G_2 mean force is reflected in the width of the G_2 component.

The fact that there is more variation in the width of G_2 (i.e. larger uncertainty in the value) for the capsulated than the unencapsulated bacteria, when probed with DDT, means that for some cells the distribution of the second component is narrower, and for other cells it is broader. This could either be due to the D39

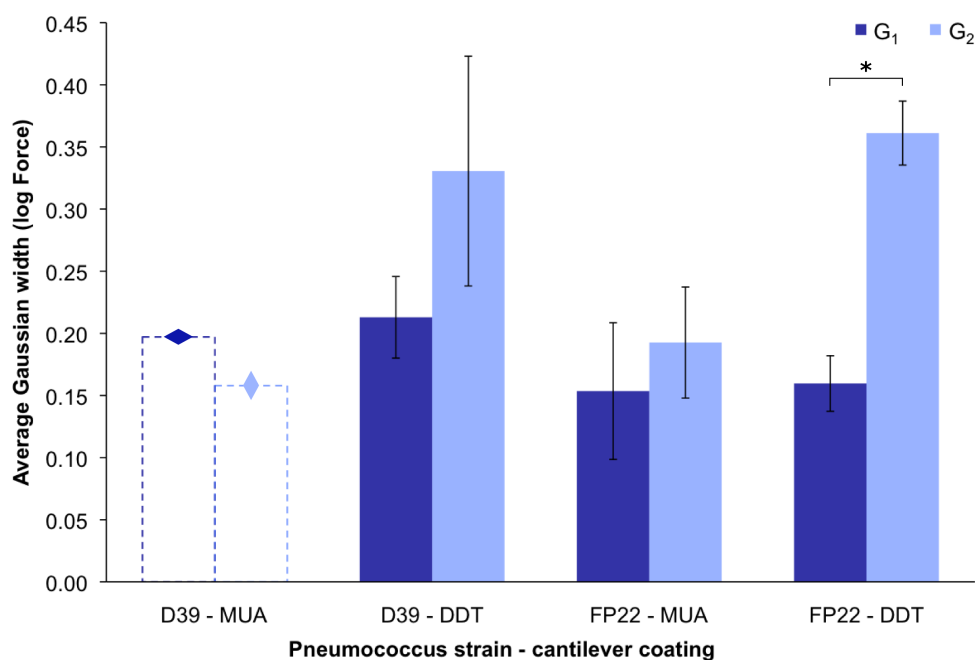


Figure 4.11: Graph showing the comparative widths of the first and second Gaussian components (G_1 and G_2 , respectively) fitted to the \log_{10} force data of the capsulated and unencapsulated *S. pneumoniae* strains and the hydrophobic and hydrophilic tip coatings. Since the D39 - MUA combination only contains one data point, it is represented using dashed bars and diamond markers.

bacteria having a more heterogeneous population, or it could be due to steric hindrance from the capsular polysaccharides restricting access to possible binding sites to varying degrees. The scale of this effect differs depending on the density and thickness of surface polymers (see Section 1.1.1), i.e. the capsular polysaccharide, and this has been shown to vary across cells within bacterial populations of the same age [229, 230]. These populations are intrinsically heterogeneous, with cell-to-cell differences in both surface macromolecules and individual growth rates [231].

For both strains, the width of the two Gaussian components resulting from probing with the hydrophilic tip are of similar size to the width of the first component, but in the case of DDT the width of the second component is larger, particularly in the case of FP22, where it is almost twice the width. This suggests that there is a larger range of force sizes within the strong positive interaction category, especially since the mean force of the first Gaussian distribution is close to the force attributed to background noise in the force curves. A wide range of high force values could be due to the nature of the interactions causing the adhesion forces. In the case

of DDT, positive interactions are likely to be due to hydrophobic bonding, which could occur with either the end molecules in the SAM, or, where there are faults in the SAM these interactions could also occur along the hydrocarbon chain of the DDT. The interaction will be stronger if more molecules are involved, so if the probe is indenting a region of the cell with a higher density of hydrophobic groups then the strength of the force will increase, since hydrophobic forces are additive [39]. Therefore, the size range of positive binding forces measured with a hydrophobic tip could be considered a measure of the heterogeneity in the distribution of isolated hydrophobic moieties and clusters of hydrophobic groups across the cell surface.

The breadth of the larger force component G_2 appears to be unaffected by the presence of capsule, as the value is consistent between FP22 and DDT cells for a given tip type. This suggests that the breadth of the range of high force values is unaffected by the presence of capsular polysaccharide.

4.3.4 Is there a difference between the relative proportion of force points attributed to the first and second Gaussian distributions?

The proportion of the bimodal histogram data attributed to the first and second Gaussian components is shown in Figure 4.12. The larger the proportion of pale blue (G_2) in the column, the greater the fraction of data points attributed to the second, wider force range, Gaussian component. Therefore, the value of the G_2 mean is more important for the cell-tip combinations whose columns contain a larger portion of pale blue than for those which are mainly dark blue. For FP22-DDT, just under 50% of data are attributed to G_2 , and in the case of FP22-MUA this increases to 57% (although the standard error is larger in this case). For the D39-DDT combination, only around 30% of the data is associated with the second component and in the one case illustrated for D39-MUA, this is even less, so the majority of data was part of the G_1 distribution. Despite this, the fit of the \log_{10} force histogram of the one multimodal D39-MUA cell-tip combination clearly shows a bimodal distribution with a distinct population of forces centred round a larger force, as shown in Figure 4.13 on page 166. In this case the two distributions are

clearly separate from one another such that $\mu_2 - \mu_1 > \sigma_1 + \sigma_2$, since $\mu_2 - \mu_1 = 0.70$ and $\sigma_1 + \sigma_2 = 0.36$. In some cases, multiple distributions in the \log_{10} force histograms are not as well defined, and instead are manifested as a skew on the histogram data, such as in the case of Figure 4.6C on page 150, where $\mu_2 - \mu_1 < \sigma_1 + \sigma_2$ ($\mu_2 - \mu_1 = 0.42$ and $\sigma_1 + \sigma_2 = 0.46$).

The fact that the unencapsulated bacteria have a more even allocation of points between the two distributions reinforces the suggestion that the capsule has a role in obscuring active binding sites, therefore reducing the ratio for D39. In the case of D39-DDT, electrostatic screening of positive charges within the capsule is not a factor because the probe is uncharged, providing further evidence that the capsule is able to block positive binding sites, e.g. hydrophobic moieties on proteins anchored in the cell wall or elements within the cell wall itself, through steric hindrance, and through hydrophilic polysaccharides reducing hydrophobic forces.

The fact that the proportion of data associated with G_2 is even less in the case of D39-MUA and only one cell of those mapped showed a stable bimodal distribution, could be attributed to additional electrostatic forces due to the negative charge of the AFM tip. In addition to the steric repulsion affecting the experiments on capsulated bacteria, because the capsule is also negatively charged, electrostatic repulsion might mean that the higher force events are more rare when an MUA-coated tip is used. This is a similar result to that found by Beaussart *et al.* [220] on capsulated group B streptococci when only a few events registered a high binding force when the cells were probed using a hydrophilic silicon nitride cantilever, which also has a slight negative charge [232].

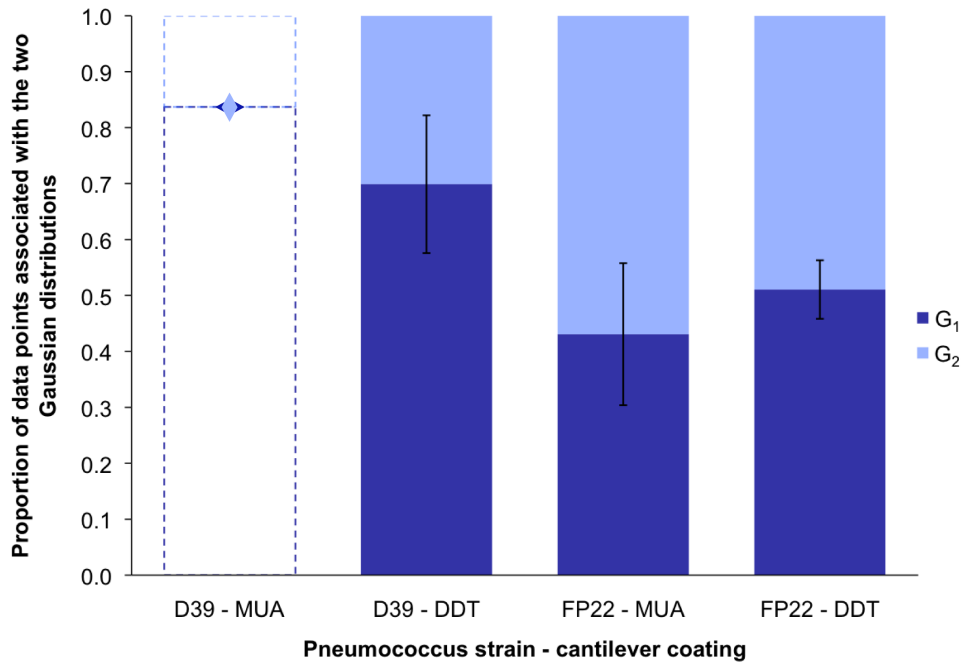


Figure 4.12: Graph showing the likelihood of a force curve being attributed to the first or second distribution in the histogram of the \log_{10} force data, for the capsulated and unencapsulated *S. pneumoniae* strains and the hydrophobic and hydrophilic tip coatings. Since the D39 - MUA combination only contains one data point, it is represented using dashed bars and diamond markers.

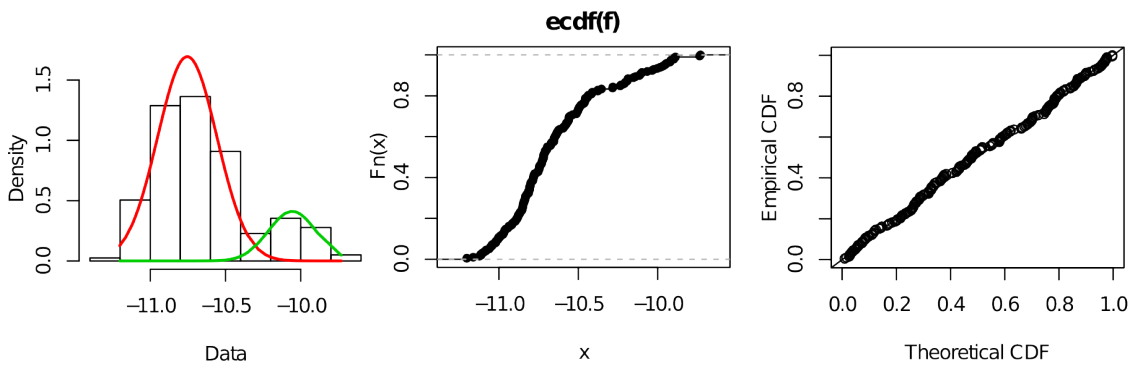


Figure 4.13: Graphs generated from the two component Gaussian finite mixture model of the \log_{10} force histogram for the D39 *S. pneumoniae* cell that showed a stable bimodal distribution when probed using MUA. The left hand graph shows the location of both Gaussian components on the \log_{10} force histogram, the middle graph shows the (normalized) empirical cumulative distribution function (CDF) of the \log_{10} force data (i.e. using the raw data), and the third graph plots this empirical CDF against the theoretical CDF of the fit (i.e. the CDF as calculated using the model data). Note that, in this case, the two distributions are clearly separated, with $\mu_2 - \mu_1 > \sigma_1 + \sigma_2$.

4.3.5 Is there a difference in the number of cells showing a bimodal distribution between the different tip-cell combinations?

Whilst the previous two sections have purely considered the data from cells where the force distribution was bimodal, another facet of this interaction is how likely it is that these multimodal distributions will be found. Figure 4.14 illustrates this by showing the proportion of cells included in the analysis which exhibited a bimodal distribution. The cell-tip combination least likely to show a bimodal distribution was D39 - MUA, with one cell out of seven being bimodal. In the case of the one cell whose \log_{10} force data could be stably fitted with a two-component finite mixture model, although there were clearly two distinct force populations, only one fifth of the data was attributed to the second, higher force component (see Figure 4.13).

Generally, it appears that mapping *S. pneumoniae* bacteria with the hydrophobic, uncharged DDT is more likely to result in a bimodal force distribution than mapping with hydrophilic, negatively charged MUA, with $\geq 50\%$ of cells exhibiting a bimodal distribution for the DDT compared to $< 43\%$ for the MUA. Within this subset, the capsulated D39 bacteria were the most likely to show bimodality, with 17% more of the cell population expressing this quality compared to its unencapsulated derivative. However, it should be noted that for the DDT cantilever, the number of events attributed to G_2 was substantially lower for unencapsulated FP22 bacteria than for D39.

One question is why D39 is so much more likely to have a single distribution when probed with MUA than when probed with DDT. As the cells were grown in the same way, from the same base stock, and the data were collected across seven experiments for each combination, this feature is likely to be due to the interactions between the tip and the cell rather than any cell population-related issue. This leaves electrostatic repulsion as the most likely reason for the reduction in the number of high force events. The pneumococcal capsule is known to be negatively charged along the length of the polymers which form this protective outer layer [108], and with indentation depths of > 80 nm, there will be a high net negative charge density surrounding the tip, which will outnumber interactions between the tip and

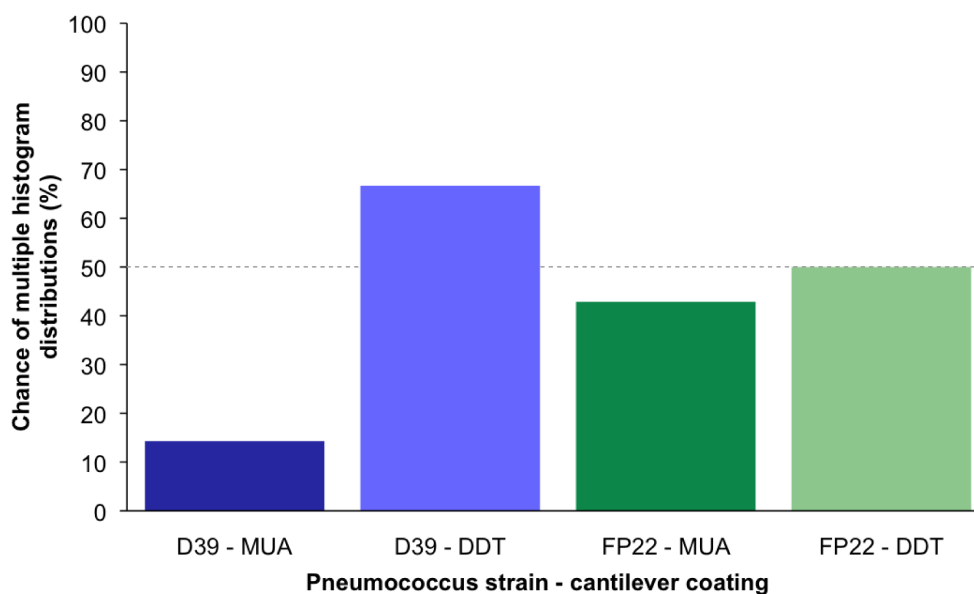


Figure 4.14: Graph showing the likelihood of the histogram of the \log_{10} force data having a bimodal distribution, for the capsulated and unencapsulated *S. pneumoniae* strains and the hydrophobic and hydrophilic tip coatings. The dashed line indicates a 50% chance of finding a bimodal distribution.

positively charged regions of the surface, effectively screening this positive interaction and reducing the net attractive force applied to the tip by the cell [222]. High force electrostatic events can therefore only occur when in areas where the overall negative charge density is reduced.

The chance of finding high force components in force maps taken on the unencapsulated bacteria is also lower for MUA than DDT, although in this case the scale of the difference is much smaller. The cell wall also has a net negative charge, particularly the teichoic acid molecules, but since the scale of the reduction is much smaller in this case, either charge screening is less dominant here or steric hindrance is reduced due to the lack of solvated capsular polysaccharides. A smaller negative charge density surrounding the AFM tip could be due to the lower indentation depths resulting from the increased stiffness of the cell wall compared to the capsule (see Figure 4.10 on page 158), meaning that the surface area in contact with the cell is lower, so although the net negative charge density is slightly higher than in the capsule [108], positively charged molecules are not competing with such a high area of negatively charged molecules up the sides of the tip. In addition, the positively

charged molecules are closer to the pneumococcal cell wall, so that in the case of the capsulated bacteria, except perhaps in the case where there is an extremely dense area of PspA, the top few tens of nanometres of the capsulated bacteria surface, and therefore indent, are very negative charge rich.

4.3.6 Are the larger forces, i.e. those associated with the secondary peak, distributed randomly or in a pattern on the bacterium surface?

As for the sample experiment (see Figure 4.7 on page 152), there was no clear pattern of G_2 forces distributed across cell surfaces, suggesting that they have a more homogeneous surface, and that the adhesins probed in this work are randomly distributed across the surface. This is consistent with the force distributions observed on other Gram positive bacteria including the work of Alsteens [101], Hu [103] and Dorobantu [102] which was discussed in Section 4.1.1.

4.4 Conclusions and interpretation of results

Combined, the different aspects of the adhesion force distributions measured on capsulated D39 and unencapsulated FP22 bacteria paint a picture of the adhesive interactions between the two strains and hydrophilic, negatively charged surfaces and hydrophobic, neutral ones. These conclusions are summarized below.

The frequency of positive binding events was reduced on capsulated *S. pneumoniae* compared to unencapsulated *S. pneumoniae*. Despite this, the measured adhesion forces were larger and more widely varied than those on unencapsulated bacteria. This could partly be due to the smaller indent on FP22 bacteria reducing the contact area between the tip and the cell and therefore reducing the number of potential binding sites. For the DDT cantilever the benefits of larger contact area could be compounded by the additive nature of hydrophobic interactions, which are predicted to be the dominant source of observed binding events in this case. Additive hydrophobic interactions are likely to lead to the observed width of the G_2 component, and could be explained by clustering of hydrophobic groups

in certain nanoscopic areas of the cell surface. Initial binding of pneumococci to mucosal cell surfaces is known to occur through interactions between surface glycoconjugates [233], which are then reinforced by protein-protein interactions, such as binding of the pneumococcal adherence and virulence factor (PavB) to fibronectin and plasminogen on the surface of nasopharyngeal cells [97]. It is therefore possible that hydrophobic bonding could have a role in this initial adhesive phase, or could enhance specific ligand-receptor interactions by interacting with hydrophobic moieties on the extracellular matrix of nasopharyngeal cells. Hydrophobic interactions have been shown to play an important role in staphylococcal attachment, with more hydrophobic surfaces showing increased staphylococcal adhesion, and human fibronectin (HFN) was also able to bind to both hydrophobic and hydrophilic surfaces, increasing the levels of bacterial adhesion compared to the HFN-free surface [234]. One of the bacterial species used in that study, *Staphylococcus epidermidis*, was the one which showed the most similar adhesion forces to those measured in this work, when probed with hydrophobic (ODT) and hydrophilic (Si_2N_2) AFM tips [103].

The variation in the values of the median force and the means of the two Gaussian components in the finite mixture model was larger for the capsulated bacteria than for the unencapsulated bacteria. This is likely to be due to more variation in the capsulated cell population: a thicker and more dense layer of capsular material will lead to increased steric repulsion, and if the capsule is thicker than the length of the CBPs, this could also increase electrostatic screening, with the positively charged regions of the proteins being further below the surface. Variation in capsular properties has been reported for various bacteria, and is consistent with the different D39 bacteria imaged using AFM in buffer in the early stages of this work, where some were shown to have a very soft, hydrated and extensive capsule, and others a neat but rough surface consistent with a thinner capsule [220] (Figure 3.8 on page 95). Having bacteria within a population with different amounts of capsular material bound to the surface could be an advantage in terms of successful host colonization. Hammerschmidt *et al.* proposed that serotype 3 pneumococci at the

point of establishing adhesion to epithelial cells appear to either have less dense capsules or to be devoid of them altogether, and that a thick capsule re-grows once the pneumococcus has, at least partially, been internalized by the epithelial cell [235]. This suggests that variation in capsular thickness and density is important in establishing an infection, and once initial adhesive contact has been made, the capsule regains its role as a protector from complement deposition.

All of the measured forces between *S. pneumoniae* and SAM-coated tips were much lower than the values reported for other bacteria (Section 4.1.1), where most interactions, particularly between hydrophobic bacteria and hydrophobic tips, showed adhesion forces of the order of nanonewtons [101, 102, 226]. Even the hydrophilic *Staphylococcus epidermidis* bacteria studied by Hu *et al.* had characteristic adhesion values of hundreds of piconewtons [103]. However, it should be noted that the work of Hu *et al.* was undertaken in water, which has been shown to elicit higher adhesion forces compared to the same experiment conducted in a buffer solution for several *Streptococcus mitis* strains [225], and this trend is likely to be reflected when using other streptococcus strains such as *S. pneumoniae*. Lower adhesion values in PBS compared to DI water were also observed during the DDT and MUA control experiments presented in Section 3.7. Reduction in forces due to increased ionic concentration and pH is unlikely to account for the full 3–7 times reduction in average forces measured using a CH₃-terminated tip in this work compared to forces measured by Hu *et al.*, but this difference could be further added to by the contrasting methods used to calculate average force: here, all force curves were included in calculated averages, whereas Hu *et al.* determined averages solely from curves containing positive adhesive interactions.

Unencapsulated mutants derived from D39 bacteria were shown to be more hydrophobic than D39 by Rukke *et al.* [205], however, the average adhesive forces measured when bacteria were probed with the DDT-coated cantilever were higher for D39-DDT (47 ± 7 pN) than for FP22-DDT (25 ± 4 pN). This could be due to the positioning of hydrophobic moieties on the surface: in the hydrocarbon binding tests used to estimate hydrophobicity, surface exposed molecules dominate the

binding interaction, but in AFM experiments the forces are measured at and below the sample surface. This could mean that the more hydrophobic regions on the D39 bacteria are ~ 100 nm below the surface, which is within the range of the AFM probe, but is not useful for the hydrocarbon tests. This is consistent with the D39 capsule's well-known role as a phagocytic inhibitor [59], and strengthens the hypothesis that modulation of capsular properties at different points in the infection cycle and between bacteria is important for successful host colonization [235].

These results link some features of pneumococcal behaviour during infection *in vivo* to fundamental forces dependent on the character of different molecules on the bacterium's surface. One of the elements not addressed during these experiments is the effect opsonization would have on measured interactions with capsulated bacteria. It would be expected that opsonized D39 bacteria would have a higher frequency of adhesive binding events with the AFM tip given that they are more easily phagocytosed, and it would be interesting to compare this in terms of non-specific forces measured by the DDT and MUA cantilevers.

In addition to probing non-specific interactions, it might also be useful to measure the adhesive forces between the bacteria and selected molecules that are predicted to have a role in selective binding, such as fibronectin, and compare the scale of these specific interactions with the non-specific interactions probed here.

4.5 Summary

The results of this work establish the capsule as a limiting factor in access to binding sites, modifying the availability of different proteins on the bacterial surface to enable colonization of the human host, and suggest that below the capsular surface there are molecular sites capable of hydrophobic binding, which is consistent with the known role of non-specific interactions in the initial attachment of pneumococci to mucosal cells. The results also provide further evidence that capsular reduction is a key process in this interaction, allowing hydrophobic moieties on the bacterium to bind to the extracellular matrix of mucosal cells, highlighting the importance of the pneumococcal capsule in pathogenesis.

The measured adhesive interactions were all fairly weak, being mostly < 100 pN in size, and were distributed randomly across the cell, indicating that there is no clear adhesive polarity or preferred orientation of the bacterium in initial attachment to host cells. This is not unwarranted given the bacterium's spherical shape, and suggests that a combination of similar, weak interactions across the cell surface add together to bring cells close enough to enable specific protein-protein binding to come into effect and stabilize the bacterium on the cell surface.

The negatively charged, hydrophilic tip was less likely to show a bimodal force distribution, and this effect was greater for the capsulated bacteria, suggesting that the combination of steric hindrance and electrostatic repulsion have a key role in reducing adhesive interactions between the bacteria and other surfaces.

Overall, this work suggests a role for additive hydrophobic adhesive interactions in the establishment of infection through binding to mucosal cells, and further elucidates how the capsule helps pneumococcus evade the immune system through steric repulsion and electrostatic screening of specific binding sites below the capsular surface.

Chapter 5

Leishmania results

5.1 Introduction

The nature of the interaction between live intra- and inter-species *Leishmania* parasite variants and two distinct glycopolymers with a shared backbone is investigated in this work, through the application of AFM force spectroscopy in buffer. If strong adhesion is found between sand fly midgut-adhesive parasites and the galactose glycopolymer, and if this relationship is stronger than with the glucose glycopolymer, GalNAc (which has been proposed as a potential candidate for LPG-independent binding in permissive sand fly vectors [142]) would be confirmed as a key molecule for disease transmission via permissive sand flies. Permissive vectors are crucial to establishing leishmaniasis in new areas where it was not previously endemic, and therefore understanding the methods of parasite-sand fly binding and disease transmission has potential relevance to disease control. This is of particular importance when sand fly-mediated leishmaniasis is primarily anthroponotic; relying on human to human transmission rather than infection from a non-human mammalian reservoir, such as in the case of *Leishmania donovani*, an anthroponotic visceral leishmaniasis-causing species which is transmitted by the permissive vector *Phlebotomus argentipes* in the Indian subcontinent [236].

Leishmania major is well known for its relationship with the specific sand fly vector *P. papatasi*, which is only capable of carrying *L. major* [142]. In contrast, *L. mexicana* is typically carried by the rodentophilic vector *Lutzomyia olmeca*

olmeca [237], which also carries *Leishmania chagasi*, a parasite with similar, but not identical, LPG [238]. The fact that the natural vector for *L. mexicana* is also able to carry another species suggests that the parasite-vector combination is not as species-specific as that of *L. major* and *P. papatasi*.

In terms of their LPG, all species share the same phosphodisaccharide repeat: Gal(β 1,4)Man(α 1)-PO₄, which makes up the LPG backbone (note that the phosphodiester bond will confer negative charge to the LPG) [239,240], and inter-species variation is due to the number, size and type of sugars attached to this backbone in the form of sidechains (the cap at the end of the LPG furthest from the parasite body also varies between species). In midgut-adhesive lifecycle forms, *Leishmania mexicana* contains additional β -glucose residues in approximately one third of repeat units [139], whereas *L. major* has significantly bulkier sidechains (see Figure 1.12) containing one to four residues of β -galactose appended to a single repeat unit (it is the sidechain of β 1,3Gal which is recognised by PpGalec in *P. papatasi* [240]). Some of these β -galactose sidechains are also terminated with arabinose [241]. The caps also differ between *L. mexicana* and *L. major*: the *L. mexicana* cap is predominantly made up of mannose residues with the following trisaccharide structure: Gal(β 1,4)[Man(α 1,2)]Man(α 1) [239, 240], whereas the *L. major* cap has a simple Man(α 1,2)Man(α 1) structure [240].

Parasites with more complex LPG are thought to bind to their specific vectors via a lectin exposed on the sand fly midgut which is selective for lifecycle stage-specific LPG sidechain or cap groups [139, 241, 242]. The LPG of midgut-adhesive lifecycle stages (i.e. procyclics, leptomonads and nectomonads) is thought to be equivalent [243], but undergoes modifications, in all parasite species, during metacyclogenesis, when the parasites transform into the final metacyclic sand fly stage. Metacyclogenesis appears to induce production of longer LPG, up to twice its original length in the case of species such as *L. donovani* and *L. major*, and can trigger alterations in the nature of the sidechains [139]. In the case of *L. major* this is known to be accompanied by arabinosyl capping of the galactose sidechains. These combined alterations are thought to induce structural conformation changes which

mask the terminal cap and obscure adhesive moieties along the length of the LPG, both of which can mediate binding to the sand fly midgut [241].

The exact structure of *L. mexicana* LPG following metacyclogenesis is unknown [139], but in *L. infantum*, which also has β -glucose residues as sidechains to approximately one third of LPG repeat units, but has a galactosylated and glucosylated cap rather than a mannose-based one, the length of the LPG backbone increases and expression of β -glucose residues is reduced, both along the sidechain and in the cap [139]. *L. chagasi*, the other parasite species carried by *L. mexicana*'s natural vector, is believed to bind to the gut of *Lutzomyia longipalpis* via its glucose sidechains, as these are similarly downregulated following metacyclogenesis [244].

All of the above features have been key in the elucidation of the role of LPG in binding to sand fly midguts, but LPG1⁻ mutants of *L. major* and *L. mexicana* were able to survive normally in permissive vector *Lu. longipalpis*, but LPG-deficient *L. major* failed to survive in its natural host *P. papatasi* [130, 142]. The differing success of LPG-deficient parasites in the two types of vector has been associated with the expression of β -galactose and *N*-acetyl-D-galactosamine on the epithelium of permissive, but not specific vectors [143, 245]. Another factor supporting the proposed sand fly galactose-mediated binding is that lectin-like activity has been reported on *L. donovani* (glucose and galactose) [246] and *L. mexicana* (galactose) [247].

Interestingly, a recent competitive binding study found that LPG-deficient *L. mexicana* procyclics bound less effectively to *Lu. longipalpis* midgut sections than the wild type equivalent, with mutants making up 25% of the bound parasites [144]. This suggests that LPG could have a role in the adhesion of *L. mexicana* procyclics to permissive sand fly midguts, and therefore LPG-deficient parasites might exhibit decreased adhesion compared to the wild type parasites. The study also used parasites which had an intact LPG coat but were deficient in GPI-anchored surface proteins, including glycoprotein 63 (gp63). The surface of *Leishmania* parasites is coated by a glycocalyx, which contains LPG, proteophosphoglycan and glycoproteins, of which gp63 is the most prominent and extensive, appearing across the

whole parasite body, flagellar pocket and flagellum [141,248]. In the *Lu. longipalpis* midgut binding assay, gp63-deficient mutants were significantly out-competed by those which were not gp63-deficient, with 99 % of bound parasites being wild type. Additionally, expression of gp63 has been shown to increase in *Leishmania* parasites that were repeatedly passaged through sand flies, which also suggests that this might be a keystone molecule in parasite-sand fly adhesion [249]. This raises interesting questions about the molecules involved in binding to permissive vector midguts, and suggests that other GPI-anchored cell surface glycoconjugates could also function as ligands or receptors for midgut binding [144].

Various types of *Leishmania mexicana* parasites including different lifecycle stages, both adhesive to the sand fly midgut (procyclics, nectomonads, leptomonads) and the infectious metacyclic form which is believed to adhere to promastigote secretory gel¹ were used in this work. Midgut and PSG-adhesive wild type parasites were probed using both galactose and glucose glycopolymers, and both LPG-deficient mutants of *L. mexicana* midgut-adhesive parasites and the add-back mutant were probed using galactose-modified tips. Finally, midgut-adhesive *Leishmania major* was also probed using the galactose-modified tips. By examining different properties of the adhesion force distribution across these different parasite-tip combinations, it is possible to compare the behaviour of the different lifecycle stages, evaluate the importance of LPG in glycopolymer adhesion and assess whether adhesion is conserved between two species. The *Leishmania mexicana* results (FMM analysis) will be considered in Section 5.7, and the relationship between *Leishmania major* nectomonads and similar *Leishmania mexicana* parasites will be included in Section 5.10.

5.2 Glycopolymer-lectin binding experiments

To establish whether the saccharides on the glycopolymer-functionalized AFM tips were capable of selective binding, and to confirm that it was possible to measure these interactions with the AFM, lectin binding experiments were undertaken. Mica surfaces were coated with lectins either specific to glucose (conA) or galactose (SBA)

¹M. Rogers, private communication.

using the method described in Section 2.6, and force maps were obtained on freshly cleaved mica, the lectin-coated mica and then on the lectin-coated mica but with a blocking agent added to the imaging buffer to reduce or eliminate specific binding. The results of these experiments are presented below.

The force maps were all $1.5\ \mu\text{m} \times 1.5\ \mu\text{m}$ in size and mostly contained 32×32 pixels (a few maps contained 36×36 pixels). The force curve parameters were the same as used for the *Leishmania* parasite experiments: experiments were conducted in PBS buffer, with a z -velocity of $2.0\ \mu\text{m s}^{-1}$, z -distance of $1\ \mu\text{m}$, applied force of $250\ \text{pN}$ and dwell time of $240\ \text{ms}$ on the surface. The tips used for the different experiments came from different glycopolymer coating batches and had spring constants in the range $17 < k < 27\ \text{pN nm}^{-1}$. Three independent experiments were conducted for both glycopolymers, and these results are summarized by Figures 5.2 and 5.3 on pages 182 and 185, respectively, which include the individual averages from force maps taken in different locations on the sample and under the various conditions described on the x -axes (the graphs include 4 galactose-mica maps, 9 galactose-SBA maps, 6 galactose-SBA + free galactose-amine maps; 4 glucose-mica maps, 10 glucose-conA maps, 3 glucose-conA + free conA maps and 3 glucose-conA + free glucose-amine maps).

Figure 5.1 on page 180 shows example maps from a single glucose (left) and galactose (right) experiment, presented using the same colour scale throughout. The top two images (A and B) show force maps obtained in PBS using the glycopolymer tip and a mica substrate, showing very little interaction in the case of glucose, and the majority of the surface showing no interaction with the galactose tip (the proportion of force events for maps taken in different conditions is explored further in Figure 5.3). The middle pair of force maps (C and D) show the interaction, in PBS, of the glycopolymer tip with its specific lectin-coated surface, with strong positive interactions evenly spread across the sample, suggesting an even lectin coverage and positive specific sugar-lectin binding events. The final pair of images show force maps recorded using the same tip and lectin sample (i.e. $E = C$ and $F = D$), but maps E and F were obtained with a blocking agent added to the PBS buffer.

In both cases there is a clear difference in the level of adhesion between the tip and the sample in unmodified PBS and in “blocked” buffer, with the addition of the blocking agent causing a reduction in adhesion to levels close to that of the uncoated mica. In the case of the glucose glycopolymer, conA (0.1 mg ml^{-1} conA dissolved in syringe-filtered, sterile PBS) was used as the blocking agent, and this map was taken approximately 1 h after the addition of the blocking agent. Experiments using glucose-amine as the blocking agent showed similar results to the use of conA (see Figure 5.2A and Figure 5.3A), so it was determined that the sugar amine used to functionalize the PMAA brush was also a suitable blocking agent at a concentration of 10 mg ml^{-1} . Due to the limited availability of SBA, 10 mg ml^{-1} galactose-amine was therefore used as the blocking agent for the galactose experiments (the map in Figure 5.1F was taken approximately 1 h after the addition of the “blocked” buffer). Note that both sugar blocking solutions were made by adding concentrated sugar-amine (35 and 100 mg ml^{-1} in water for the galactose-amine and glucose-amine, respectively) to syringe-filtered, sterile PBS. Although the buffer used for the blocking experiments was slightly diluted, the reduction in measured adhesion was far too large to be due to this decrease in ionic concentration (the ionic concentration of the PBS was reduced by $\sim 30\%$ for the galactose-amine blocking solution, and 10% for the glucose-amine blocking solution).

The differences in the adhesion for different conditions can be summarized by combining all of the data obtained in the force maps across the 3 independent experiments for each type and taking the average. This, combined with the associated standard error on each result, gives the results presented in Table 5.1.

Table 5.1: Glycopolymer-lectin binding results: average peak adhesive force. The blocking agent concentrations (in PBS) were 0.1 mg ml^{-1} for conA and 10 mg ml^{-1} for both saccharide solutions.

	Glucose glycopolymer	Galactose glycopolymer
Mica	$17.5 \pm 0.6 \text{ pN}$	$21 \pm 1 \text{ pN}$
Lectin	$76 \pm 1 \text{ pN}$	$113 \pm 2 \text{ pN}$
Lectin + free lectin	$25.4 \pm 0.4 \text{ pN}$	N/A
Lectin + free sugar-amine	$24.2 \pm 0.7 \text{ pN}$	$21.3 \pm 0.6 \text{ pN}$

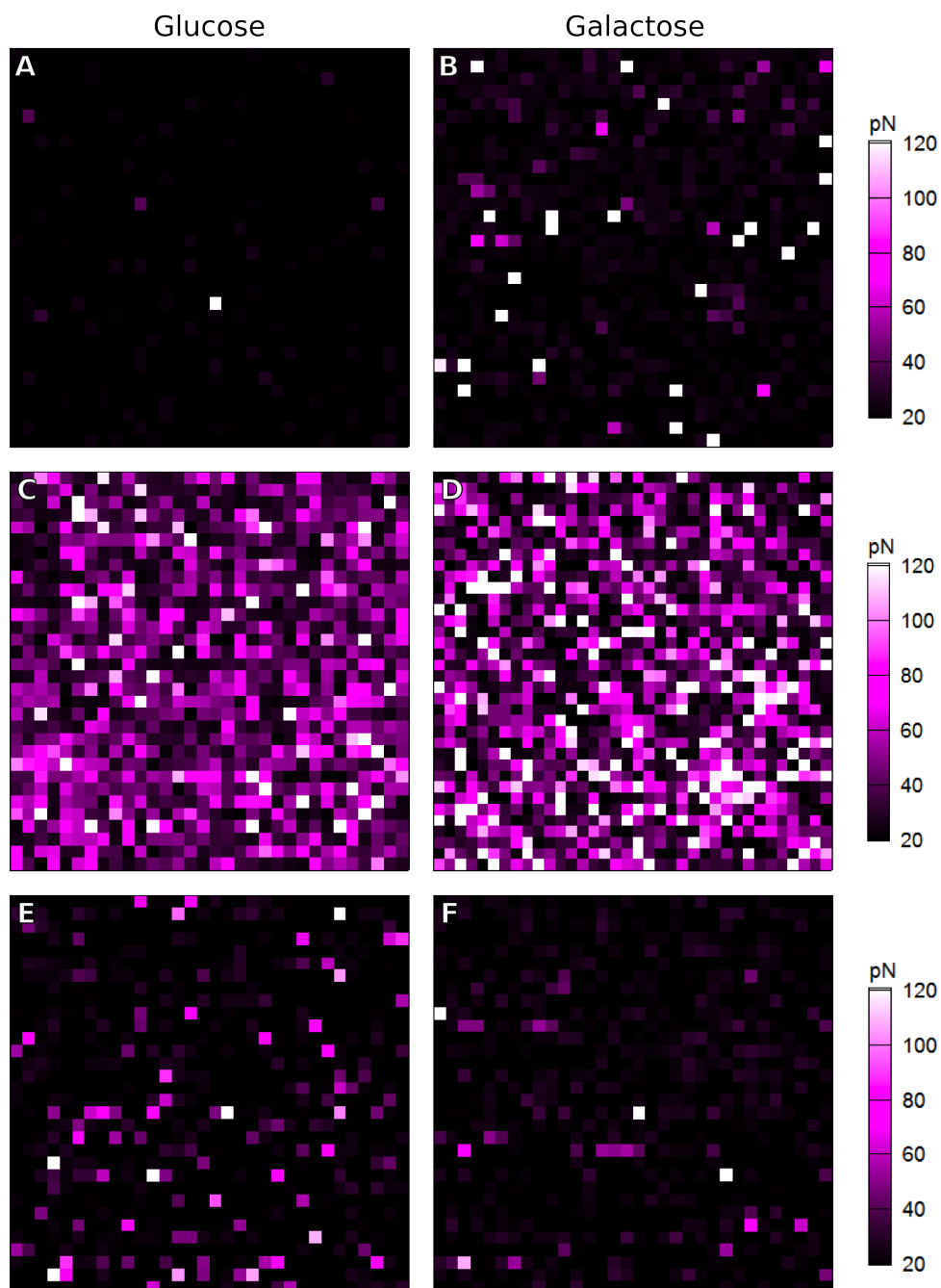


Figure 5.1: Representative force maps from the glucose (A, C and E) and galactose (B, D and F) glycopolymer control experiments. A and B show force maps obtained on mica using the glucose and galactose glycopolymers, respectively, C was obtained using a glucose glycopolymer tip on a conA-coated surface whereas D was obtained using a galactose glycopolymer tip on an SBA-coated surface. E is the same set up as C, but with free conA added to the PBS buffer. F is the same tip-sample combination as D, but with free galactose-amine added to the buffer. All maps are $1.5 \mu\text{m}$ across and the force scale is the same throughout. Each set of maps (A, C and E, and B, D and F) was obtained during a single experiment using a single glycopolymer tip.

The interaction was stronger between the galactose glycopolymer and the SBA surface than the glucose glycopolymer and the conA surface, and the addition of free galactose-amine reduced the binding interactions to the same level as with bare mica (a reduction of $\sim 81\%$) in the case of the galactose glycopolymer tip. Blocking was also successful for the glucose glycopolymer experiments, with a reduction of $\sim 67\%$ in the average adhesion force upon the addition of free conA, and a reduction of $\sim 68\%$ upon the addition of free glucose-amine (compared to an effective reduction on mica of $\sim 77\%$). The difference in the size of the reduction is not significantly different for the two blocking methods, suggesting that they are equally effective. In experiments with both sugars, there was more variation in the average force per individual force map for the stronger force glycopolymer-lectin combinations than for the reduced force combinations, as shown in Figure 5.2. The spread in the data is likely to be due to variation in the lectin surface coating: in some cases, there were areas of higher and lower adhesion on the sample, particularly in the case of the SBA-coated surface. In one experiment, approximately $2.5 \times$ as much SBA than normal was used when making the sample, leading to force curves with very high adhesion levels (including the top two points in Figure 5.2B). Variation could also be due to different amounts of sugar being available for binding on the glycopolymer-coated tip, which could depend on the length and density of the polymer brush which might vary between different PMAA brush synthesis batches. To prevent this effect from influencing the measured parasite adhesion, both the control experiments and experiments on parasites were repeated using AFM tips from different PMAA batches. Even with the variation in adhesion between the individual maps, the differences between the measured average peak adhesive force (the pixel value in the force map) of the glycopolymer and the lectin in PBS compared to the mica or blocked experiments was statistically significant. It is therefore reasonable to state that the glycopolymer tips are capable of binding selectively to their complementary lectins and that the levels of non-specific adhesion to mica are very low, typically giving results which are close to the noise threshold in the data of $10 - 20$ pN.

The individual force curves obtained during the glycopolymer-lectin binding

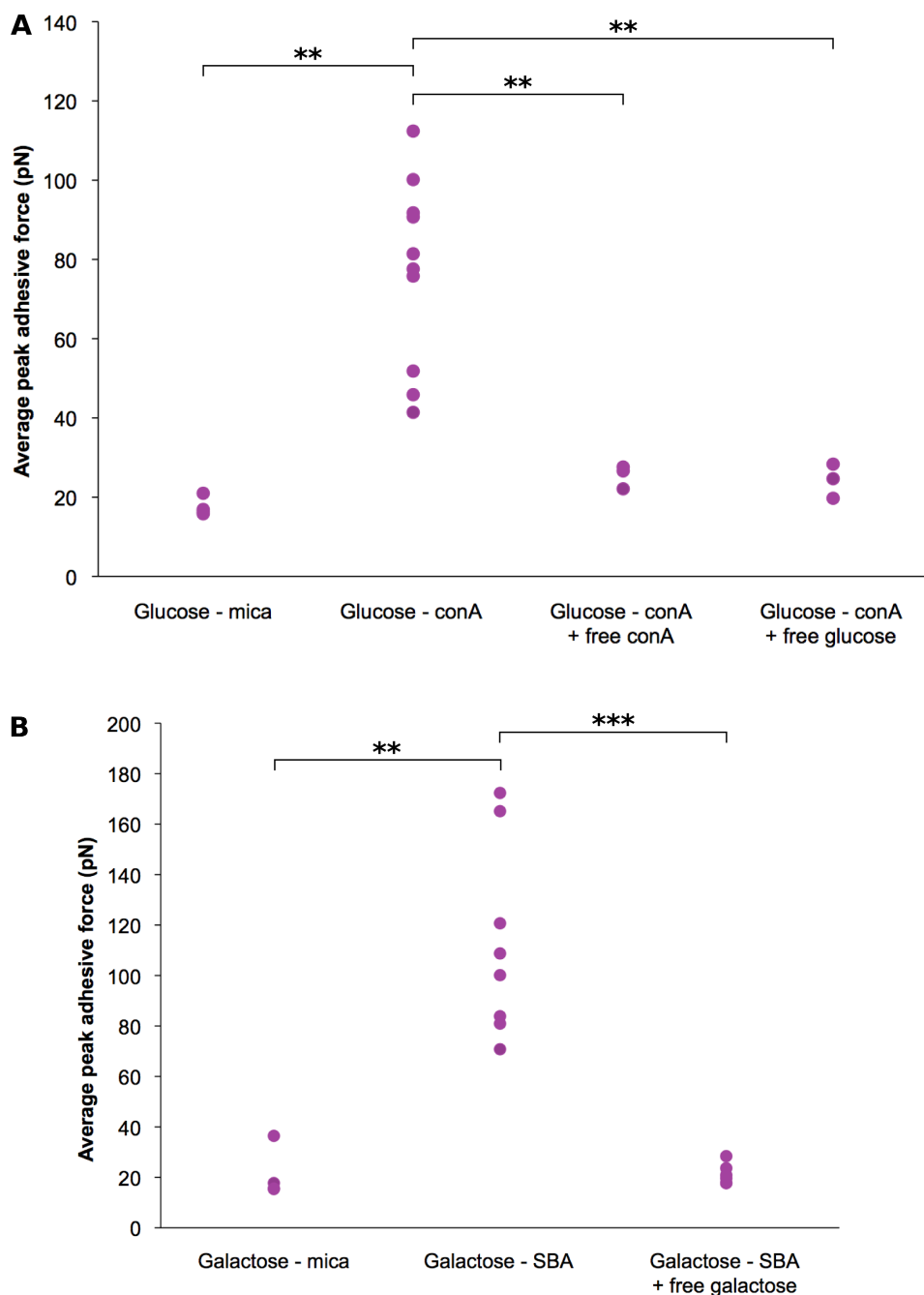


Figure 5.2: Graphs showing the average adhesive force for different force maps taken as part of the glycopolymer-lectin experiments. A) shows results obtained using the glucose glycopolymer-coated AFM tips and B) the equivalent experiment for the galactose glycopolymer-coated AFM tips. The x -axis categories give the glycopolymer type and the sample surface, and the second line of the axis categories indicates whether the PBS buffer had had anything added to it. Negative (low force) controls include interaction with uncoated mica, and interactions with the lectin-coated surface in a buffer supplemented with either free lectin or sugar-amine. In both cases the glycopolymer interacted strongly with the surface coated in its partner lectin. Statistically significant differences are indicated by stars according to the level of significance, as described in Section 2.3.4.

experiments are not presented in this work, but contained a mixture of single, double and multi-peak interactions with predominantly non-linear extension before detachment events. The character of the positive binding curves was similar to the range presented in Figure 5.19 on page 218. This type of binding profile is characteristic of specific binding events [44] and the scale of the adhesive forces is consistent with those measured using a porcine galactose-containing (α -GalNAc-containing) glycopolymer and an SBA-coated mica surface (it is difficult to compare the exact value because in that case individual binding events were modelled and arranged in relation to the loading rate calculated using the gradient of the force-time curve immediately before the bond rupture force, and a different buffer was used) [163]. The individual binding events in the porcine mucin experiments were of the order of 200 pN, which is close to the overall average interaction strength of 113 ± 2 pN measured in this work (note that this value was calculated using all of the force curves within the maps, which included non-adhesive force curves as well as those containing events), and is closer still to the average force measured in the experiments on the SBA samples which had a higher SBA concentration, and therefore denser lectin surface coverage, which had average forces closer to 170 pN.

The final comparison included here is the proportion of force curves which had a peak adhesive force > 30 pN. Since 30 pN is a little above the noise threshold of the data, the force curves included in the count will include at least one positive binding interaction: a higher proportion of curves with events > 30 pN means that the tip was interacting more strongly with the sample. Figure 5.3 shows this, calculated for both the glucose (A) and galactose (B) data, and, as for the average adhesive force, the differences are statistically significant between the larger proportion of curves with adhesive interactions > 30 pN for the sugar-lectin category, and the smaller proportion in both the blocked and mica experiments. The mica experiments had the fewest adhesive curves > 30 pN in both cases, the proportion being $< 10\%$, for both sugars. The blocked experiments also had a small proportion of high forces, with $< 25\%$ for blocked glucose and $< 20\%$ for blocked galactose. The sugar-lectin experiments in PBS resulted in significantly higher proportions of high forces

with galactose + SBA containing $> 40\%$ forces > 30 pN (again, note the larger spread in the data here associated with different levels of SBA on the sample) and the same measure for glucose and conA maps being $> 55\%$, the larger percentage suggesting fuller sample surface coverage for the conA experiments compared to the SBA experiments. The observed reduction in the number of high force events in the blocked maps is further evidence of the reduction in binding associated with blocking specific interactions between the tip and the sample, strengthening the case that the glycopolymer-coated AFM tips are a suitable candidate for investigating whether specific binding events play a part in *Leishmania* parasite adhesion to the sand fly midgut. By using AFM force spectroscopy with glycopolymer brush-coated tips, specific sugar-binding interactions involving lectins on the sample were detected and the strength of the adhesive force could be measured. The same parameters were used on the parasite sample, so if there were any appropriate lectins on the parasite surface, they should be detected and contribute to the parasite adhesion profile.

The galactose glycopolymer used in this work should be a suitable candidate to check for GalNAc-binding (*N*-acetyl- α -D-galactosamine-binding) activity on the parasite surface, because although a different lectin, HPA, was used to identify the molecules expressed in the midguts of permissive sand flies [142,245], SBA is specific for α -GalNAc (*N*-acetyl-D-galactosamine) [163] and bound strongly to the galactose glycopolymer in this experiment. Since both lectins are specific for GalNAc, the parasites should be capable of binding to the sugar residues on the glycopolymer-coated tip.

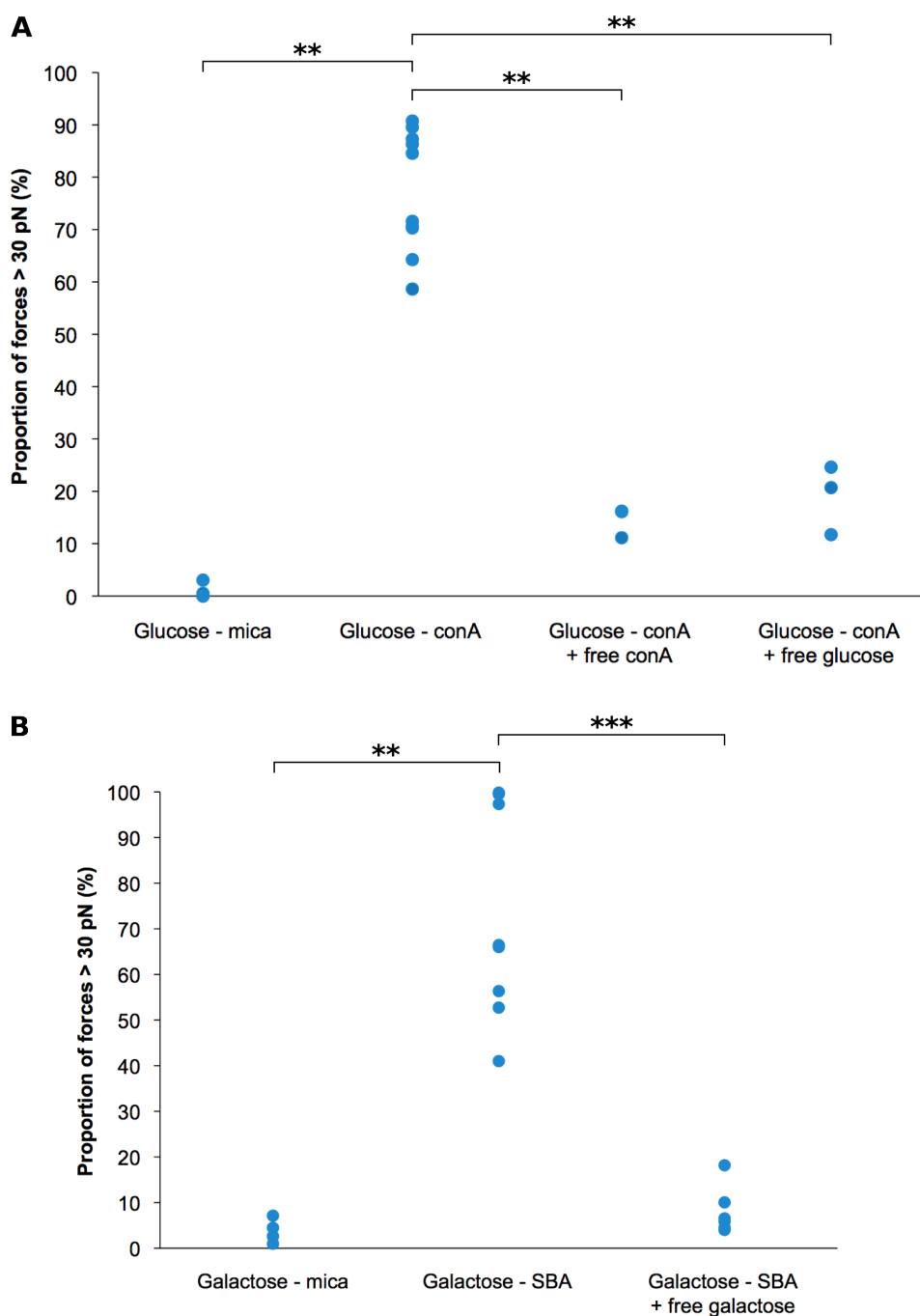


Figure 5.3: Graphs showing the proportion of force curves in individual glycopolymer control experiment force maps which measured adhesive forces > 30 pN. The proportion of force events > 30 pN in maps taken using A) a glucose glycopolymer-coated AFM tip and B) a galactose glycopolymer-coated AFM tip. The x -axis categories give the glycopolymer type and the sample surface, and the second line of the axis categories indicates whether the PBS buffer had had anything added to it. Negative controls include interaction with uncoated mica, and interactions with the lectin-coated surface in a buffer supplemented with either free lectin or sugar-amine, which all had a low proportion ($< 25\%$) of binding events > 30 pN in size. In both cases, the glycopolymer interacted strongly with the surface coated in its partner lectin, with all but one map having $> 50\%$ of curves above the 30 pN threshold. Statistically significant differences are indicated by stars according to the level of significance, as described in Section 2.3.4.

5.3 Dry *Leishmania mexicana* AFM images

As in the work on *S. pneumoniae*, during the initial phase of the work, AFM images were obtained in air. These parasites were cultured *in vitro*, having been passaged several times after harvest from a murine host, and therefore had reverted to a generic promastigote morphology before use in the AFM. Examples of these images are presented in Figure 5.4 on page 187. As the cells are incompatible with suspension in pure water, after harvesting by centrifugation they were resuspended in a dilute PBS solution, at which point some of the cell suspension was dropped onto a clean glass slide and left to dry for 1 – 2 hours before being transferred to an AFM for imaging. These images were taken using silicon nitride cantilevers and contact mode on a Dimension 3100 AFM (Figure 5.4A, B and C) and on the MFP-3D (Figure 5.4D). Some of the debris and fern-like patterns visible in the images are due to the crystallization of salts from the weak buffer.

The images presented in Figure 5.4 were selected because of the differing character of the parasites. In Figure 5.4A, the parasite has a fairly smooth, cylindrical body, with the flagellum appearing to emerge from the parasite approximately 1 μm from the anterior end of the body, suggesting that it is either covered by the thin region of the flagellar pocket [250] or that the pocket has been damaged during dehydration. This contrasts to the upper right parasite of the group in Figure 5.4D which has a much more tapered, wrinkled body and whose flagellum appears to thicken and be crossed by a series of structural bands before joining the main parasite body. This body type is consistent with other parasites in the same frame, with a thicker body region towards the anterior end and the flagellum being clearly covered by the flagellar pocket. The soft, sack-like bodies in Figure 5.4D appear very similar to published SEM images of *Leishmania mexicana* parasites from an *in vitro* culture during the process of cell division [250]. Figure 5.4B and C show the deflection and height images, respectively, of another group of parasites. Here, the central parasite has a twisted body, which might be due to flagellar rotation as the sample dried. As in image D, it shows that the dehydrating parasite body is insufficiently stiff to be able to hold its shape and suggests the presence of ridges or folds running along

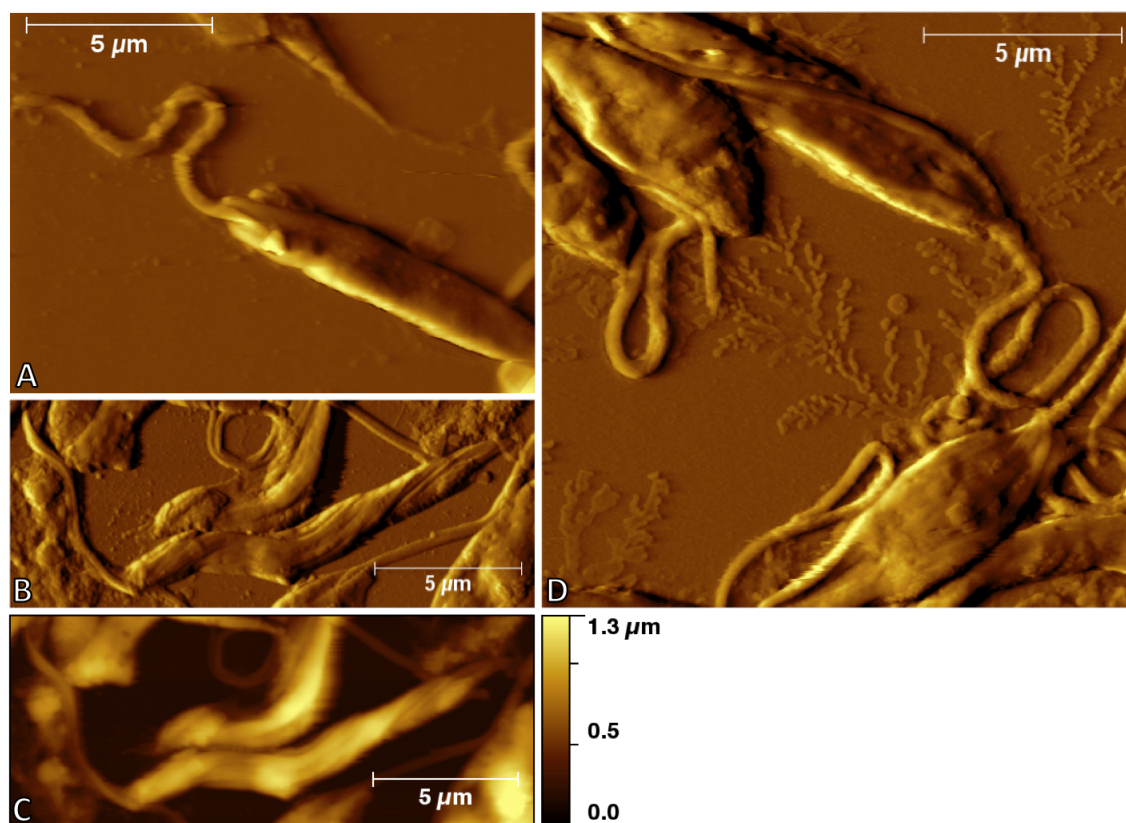


Figure 5.4: Contact mode deflection (A, B and D) and height (C) AFM images of *Leishmania mexicana* paramastigotes on a glass substrate. Images were taken in air using a silicon nitride tip with a nominal radius of 20 nm and $k = 0.03 \text{ N m}^{-1}$. Image A shows a single parasite whilst the other images contain groups. Image D includes detail of the join between the flagellum and parasite body and some fern-like patterns due to dried salt crystals are also visible in this image. The parasites appear symmetrical along their length and are similar in appearance to those in Figure 1.11. The larger parasite in image B and C shows a rotational twist along its length. This could be due to the parasite trying to move as the sample dried. Note that the colour scale is only valid for image C: since deflection images are obtained using an ‘error’ signal (see Section 2.1), they are useful for clear rendering of detailed surface features, but quantification of the images is difficult.

the length of the parasite body. These features are also present in reported SEM images of *L. mexicana* [251].

5.4 *Leishmania mexicana* AFM images in PBS: cell damage

The PEI-coated surfaces were so successful for immobilizing the parasites that it was decided to see if the parasites were stable enough for imaging as well as force mapping. Figure 5.5 shows an example of this for a *Leishmania mexicana* parasite imaged using a silicon nitride cantilever in PBS. The soft parasite body shown in the images is clearly deformed by the movement of the AFM tip across the cell surface, with the highest points on the parasite being pulled along in the direction of movement of the cantilever, even though tapping mode was used to obtain the image. Although tapping mode should reduce the lateral force on a sample, when a sample is very soft or has long molecules extending from it, interaction with the tip can be strong enough to pull the surface in the direction of tip movement. Force curves taken with SiN cantilevers during the earlier stages of this work interacted strongly with the parasite (data not shown), which might partly explain this distortion.

All of the images in Figure 5.5 are of the same parasite, which was imaged twice: a and b show the height and deflection trace images from the first scan (i.e. the tip was moving from left to right as the data were recorded), whereas images c and d are both deflection images from the second scan, in this case showing data recorded during the trace and retrace tip movements, respectively. The first scan shows a high, soft parasite body which is more distorted at its posterior end. By the time the second scan was undertaken, although some biological material is still well attached to the substrate, the surface polymers at the highest points on the cell are being moved more than in the first scan, and some material appears to have been lost completely, leaving a thin layer of material exposed, which has a closely-packed lined structure running along the length of the parasite (areas within the white ovals). There is a ring of smooth material around the edge of the parasite

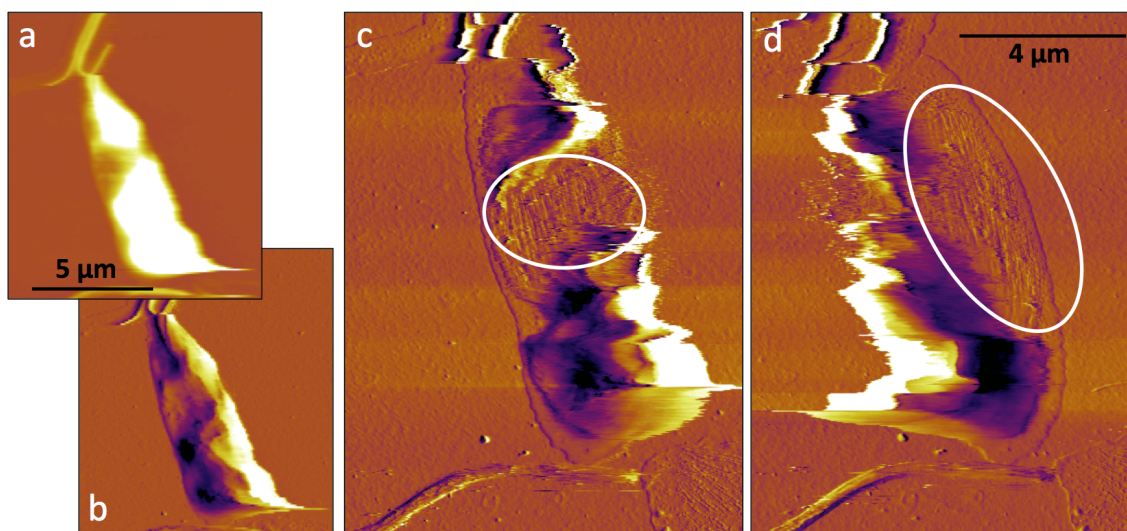


Figure 5.5: Tapping mode AFM images of a wild type *Leishmania mexicana* nectomonad on a 0.2 wt % PEI-coated substrate taken in PBS using a silicon nitride tip with a nominal radius of 20 nm and $k = 0.03 \text{ N m}^{-1}$. Trace (a, b and c) and retrace (d) height (a) and deflection (b, c and d) images) showing cell damage, highlighted using white ovals, after imaging. The first image (a and b) already shows soft, highly flexible surface material, which appears to have been severely damaged in places after imaging, resulting in a thin layer of material with ridges running along the long axis of the parasite visible in images c and d. These two images were obtained in a single scan, showing the data obtained as the tip moved from left to right (c) and from right to left (d) across the sample. This shows the level of force being applied to the polymers on the parasite, which are highly distorted according to the direction of tip movement, even when imaged using tapping mode.

body, which could be made of LPG from the parasite's outer surface, and the ridged, textured material is confined within this smooth outer ring, suggesting that parts of the cell have been removed or severely damaged, exposing this thin, textured layer which is likely to be part of the outer cell structure of the parasite that is not typically exposed on the outer surface (the entire parasite surface is smooth in the deflection image from the first scan).

Although this raises interesting questions about the internal structuring of the parasite and how the parasite copes with external forces, and shows that AFM could also have a role in exploring the textures and arrangement of structural biomolecules within the parasite, in the context of this work the internal parasite structure is of little importance. Therefore, no further AFM images were obtained and it was decided that force mapping alone would be used to locate the cell within the map region, in order to avoid unnecessary cell damage by lateral tip movement while in contact with the cell surface. Unlike these AFM image scans, repeated force maps could be obtained which showed very little difference in topography, including shape and cell height, so it was determined that cell damage caused by mapping was not significant.

5.5 Systematic mapping approach: maps of the whole parasite and maps of the centre of the parasite

Because the parasites are several microns long and were immobilized on transparent substrates, the inbuilt optical microscope could be used to reduce the amount of time spent “fishing” for cells, thereby reducing the amount of non-essential contact between the tip and the sample and decreasing the chance of biofouling or tip damage. It was possible to identify parasites using the 40× objective lens on the MFP-3D optical microscope, and to select parasites with appropriate morphology for the lifecycle stage, and which were unencumbered by other parasites or cell debris. By focusing on the parasites and engaging the AFM tip close to the surface, then noting the position of the AFM tip, withdrawing the AFM head and using

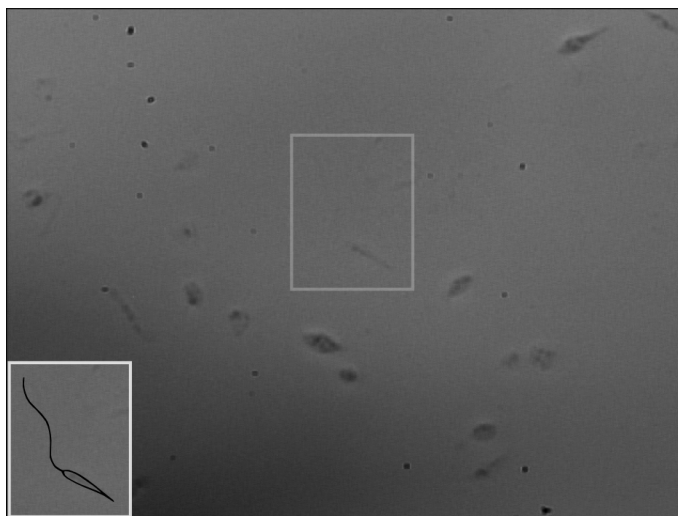


Figure 5.6: Image taken from the video feed from the MFP-3D in-built microscope at $40\times$ magnification of a *Leishmania mexicana* metacyclic-rich parasite sample on a PEI-coated glass substrate in PBS. Inset: the image is not particularly clear, so the approximate outline is drawn in black over the parasite selected for mapping (outlined by the white box in the main image). AFM maps taken on this parasite are shown in Figure 5.7 on page 192.

the manual sample stage adjusters to position the sample (and parasite) close to the location of the engaged tip, when the AFM head was lowered into the engaged position for the second time, a map could be started which was highly likely to contain the parasite (assuming it was well adhered to the surface and not moved by the approaching AFM tip). This initial force map typically used force curves with no dwell time and contained 28×28 pixels across $10 \mu\text{m} \times 10 \mu\text{m}$.

Parasites with an active flagellum (either wholly or ‘twitching’ at the anterior end, see Figure 5.8) were selected over those whose flagellum was firmly bound to the surface because it was highly likely that these parasites with a motile flagellum were still alive (one of the characteristics that makes AFM an ideal choice for examining binding at a single cell level). After a few lines of height data were obtained on the parasite in this initial map, the exact location of the parasite relative to the force map area could be worked out based on the topographical features in the force map and a screen shot of the microscope feed taken prior to the AFM tip being lowered. At this point, the map was paused, and the map position offset (and size adjusted if necessary) using the AFM software to ensure that the majority of the parasite body was in the frame, the scan size being adjusted accordingly. A

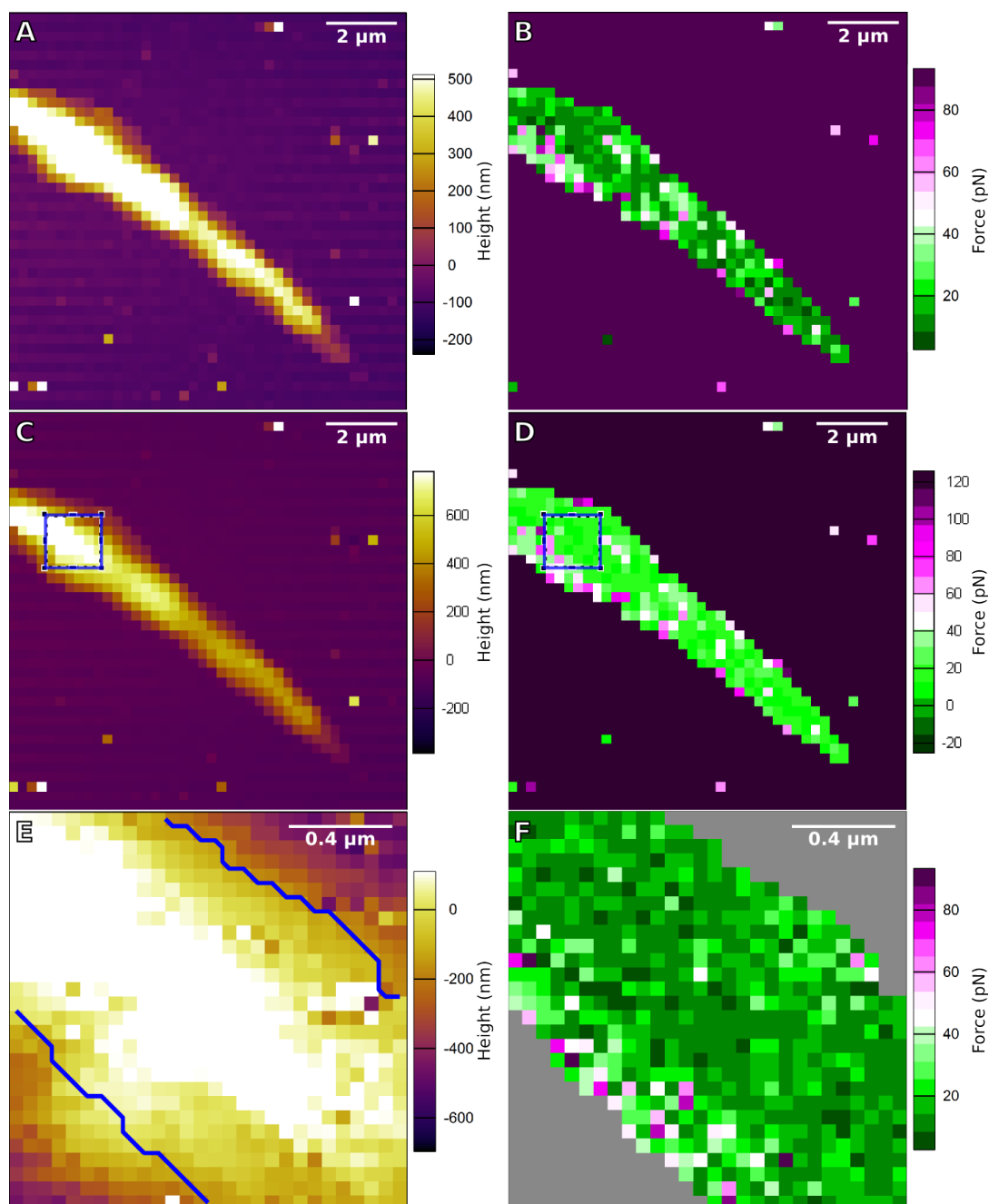


Figure 5.7: AFM height (A, C and E) and force (B, D, F) maps of a *Leishmania mexicana* metacyclic parasite taken in PBS using a glucose-glycopolymer-coated AFM tip. This figure shows the process used to investigate the adhesive properties of the parasite: Firstly, the optical image in Figure 5.6 was used to engage the AFM tip close to the parasite, and a map was taken which included the body of the parasite. This is shown in images A and B, and the height here is the contact point rather than the indentation depth (see Figure 3.16 on page 123). Note the high forces measured on the PEI substrate. The next row of images (C and D) show the area on the parasite selected for a closer-in $1.5 \mu\text{m} \times 1.5 \mu\text{m}$ map in terms of the height and force maps. The area selected was typically towards the centre of the parasite, or on the widest section, as in this case. The bottom image pair (E and F) show the zoomed-in contact point map with a mask applied so that the force curves considered in this case are solely on the upper portion of the parasite. The maps were all taken using the same force curve parameters and the adhesion pattern is conserved between the large and small-scale maps.

large map of the parasite was then obtained, typically $10\ \mu\text{m} \times 10\ \mu\text{m}$ (depending on the lifecycle stage of the parasite, since the length varied significantly between the lifecycle stages, with some procyclics being half the length of the nectomonad parasites). The large scans typically contained 36×36 or 40×40 pixels, depending on the scan size, and were obtained using a tip z -speed of $1.98\ \mu\text{m s}^{-1}$ with a relative trigger force of 250 pN and dwell time towards the surface of 240 ms. The full z -distance travelled during approach/retract cycles was $1\ \mu\text{m}$. The AFM was set to closed-loop operation.

Once a map had been obtained across the whole parasite body, in order to have more force curves for analysis, a zoomed-in map was taken towards the centre of the parasite, on an area where the adhesion forces were typical of those across the whole body. This map was obtained using the same force curve parameters, but the map size was typically reduced to $1.5\ \mu\text{m}$ and the number of pixels to 28×28 . In most cases, the entirety of the zoomed-in map was on the body of the parasite, so masks were rarely used, although in the case of metacyclic parasites, masks were sometimes necessary, as in Figure 5.7.

The spring constants of the cantilevers used for the *Leishmania* work were measured using the thermal noise method during the calibration procedure outlined in Section 2.4.1 and were within the range $14 < k < 35$ pN. The majority of cantilevers had spring constants lying between 20 and 30 pN.

5.5.1 Optical images of parasites with a motile flagellum but attached body

As stated in the previous section, in some cases, parasites were observed that had an active flagellum. Some videos of such parasites were taken, and stills from two of these films have been extracted and put together in Figure 5.8 in order to show the kind of movements witnessed. The first group of images, set A, shows a parasite sample where the tip is retracted away from the surface, and the second group of images, set B, shows a different parasite sample and in this case the tip is engaged on top of the parasite and a force map is being taken. The flagellum continued

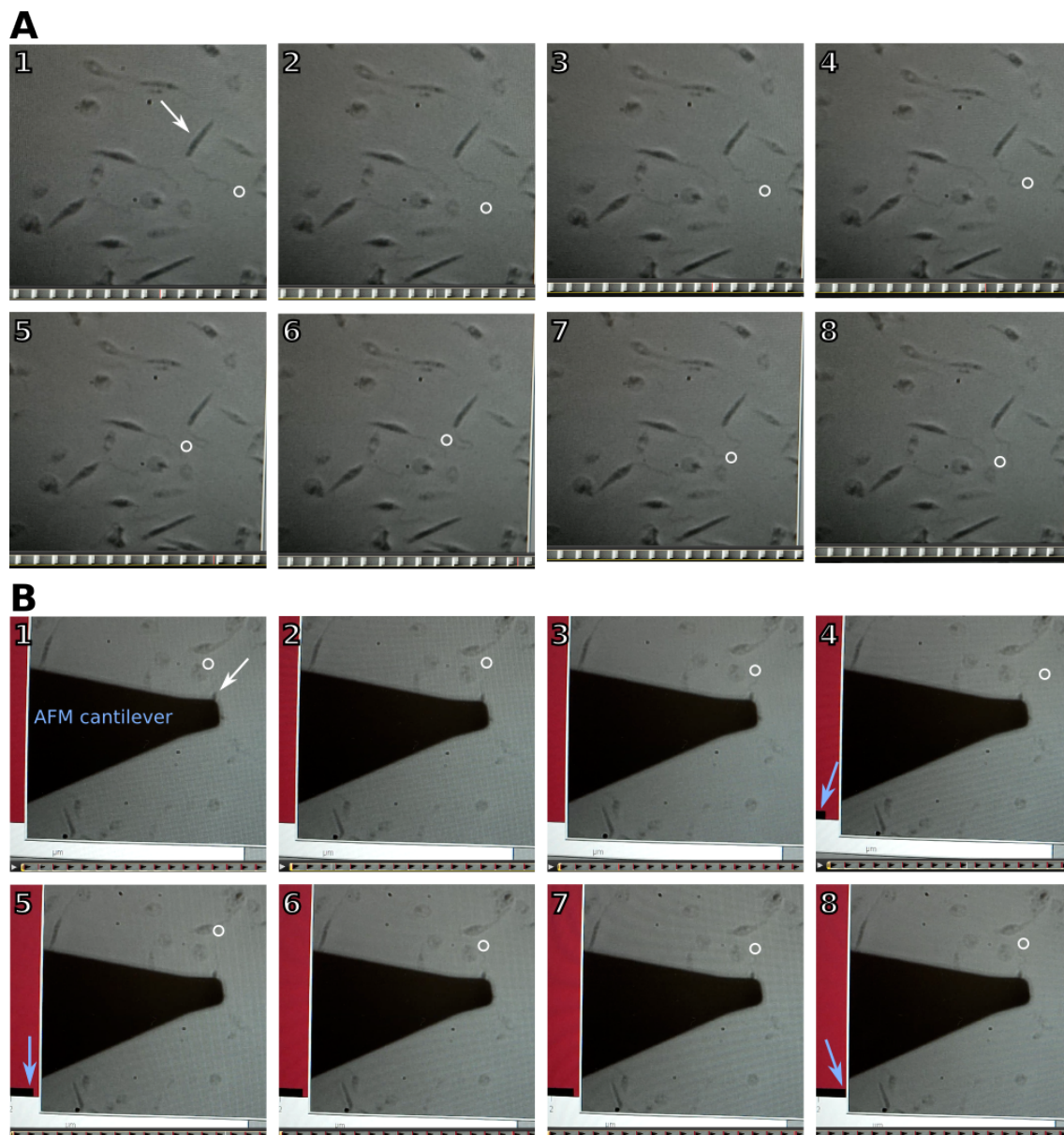


Figure 5.8: Still images taken from a video of the computer screen, including the optical output from the MFP-3D in-built microscope at $40\times$ magnification. *Leishmania* parasites can be seen moving their flagellum even while a force map is being taken (image set B). Parasites are attached to a PEI-coated glass substrate in PBS. The images are numbered in chronological order (a bar showing the position of the frame in the film is at the bottom of the image). The white arrows indicate the position of the body of the parasite of interest, and the last visible point of the flagellum (i.e. the anterior assuming the entire length is within the focal plane) has been overlaid with a white circle to aid visualisation of its movement relative to the other image features. The images have been arranged so that the parasite body is located at the same point within each grid location of a single image set. The pale blue arrows in image set B indicate the progression of an active preliminary force map (the microscope light was always turned off when acquiring data) by the addition of new pixels in the force map frame which is partially visible behind the window showing the microscope feed.

to move while the force map was being obtained, as shown by the addition of new pixels in the force map window just visible to the left of the microscope feed window (highlighted by pale blue arrows). In both cases, the images have been arranged so that the parasite is in approximately the same position relative to the image grid, and, as the contrast in the images is fairly low, for ease of visualisation, the end of the flagellum as visible in the still has been identified by a white circle. It is clear by looking at the location of the end of the flagellum, and the shape of the whole flagellum, that it is moving in a directed manner rather than just drifting in the buffer.

The flagellar bend shapes captured in the images are consistent with those shown in a high resolution video study of swimming *Leishmania major* promastigotes [252], where a characteristic distribution of flagellar and ciliary-type beating, along with pauses in the movement cycle were identified. Flagellar beating caused sinusoidal-type waves along the flagellum which appeared to be generated at the anterior end of the flagellum (this form of beating leads to forward motion), whereas asymmetrical ciliary beats moved from the base to the tip of the flagellum and were responsible for rotating the parasite body, changing its direction. The video corresponding to Figure 5.8A shows a combination of rapid movement in the portion of the flagellum towards the tip, beyond a point midway along, where it appears to be stuck to the substrate (the location of the severe U-shaped bend in image 5), and slower, more sudden flagellar-base-initiated “flicks”. The flagellar shapes within image set A indicate both flagellar- (3 and 4) and ciliary-type (5 and 6) movement, as well as shapes which could be due to a contribution of both, or due to restricted movement (as a result of flagellum-surface attachment points) or interaction with other objects on the sample. This suggests that the parasite is attempting to detach itself from the PEI-coated surface using the entire range of movement at its disposal.

The video corresponding to Figure 5.8B shows that, in this case, the flagellum is not attached to the substrate at any point along its length, and the movement is slower but smoother than in Figure 5.8A. The flagellar waves in image set B appear to be more symmetrical, suggesting that at that point in time the parasite

was mainly using flagellar-type beating to try and move away from the tip rather than ciliary-type beating to reorient itself. However, these images only represent some of the film of the parasites, and a wider sample over a longer time would be required to draw any firm conclusions from these observations other than that at least a proportion of parasites were able to survive the conditions used to prepare the parasite sample and that AFM force mapping did not kill parasites that were alive prior to being mapped (there are several films of parasites before and after being mapped twice (full body and close-up) with a glycopolymer-coated tip, and the flagellum remained active in all cases).

5.6 Parasite morphologies

The parasites used for the experiments were aliquotted and frozen at a given time point in the first or second passage following being harvested from a murine model in order to be rich in a single lifecycle phase, or morphology. The large scale force maps, although not as detailed as AFM images, still provide useful information about the shape of the parasites, and a selection of parasites of each type are included in the following pages. Procyclic parasites (Figure 5.9) tended to have less visible flagella, and are more rounded in shape, with shorter bodies ($\sim 6 \mu\text{m}$). The leptomonad and nectomonad parasites (Figures 5.10, 5.11 and 5.12) were the largest, having longer bodies (generally $> 11 \mu\text{m}$) with a more elongated shape but maintaining breadth of $\sim 2 \mu\text{m}$, some having a thicker region towards the flagellum end. They also had long flagella (the length of these is not clear in the AFM images, but was apparent when viewing the video feed from the microscope). The metacyclic phase parasites were different again (Figure 5.13), with parasites maintaining a long body ($\sim 10 \mu\text{m}$) and long flagellum, but being narrower ($1 - 2 \mu\text{m}$ wide) and devoid of the thick region near the flagellum base. The morphologies observed are consistent with the type descriptors in Figure 1.9 on page 28, although the lengths of the parasite bodies vary slightly from those in the figure. No significant topographical differences were observed between the nectomonad/leptomonad LPG1^- mutant and its add-back (Figures 5.11 and 5.12, respectively), or with the *L. mexicana* nectomonad/leptomonad

mutants and the *L. major* nectomonad parasites (Figure 5.10).

The height maps were calculated using the contact point rather than the software default of ‘height after indentation’ (see Section 3.6.1). A snow-like appearance on the substrate in some of the height maps is not due to physical features, but is a map artefact due to the interaction with the PEI substrate being sufficiently large that the tip was still attached to the surface at the start of the second curve in the pair, giving an artificially large height. As discussed in the previous section, in some parasites, although the body was well attached to the substrate, the flagellum was not well attached and could be seen moving when observed using the optical microscope. This sometimes resulted in flagella not being observed in the force map, or “noisy”-type height data around the anterior end of the parasite body (as in the bottom right image of Figure 5.10). The figures are arranged by the order of the lifecycle stages in the sample: procyclic - nectomonad/leptomonad - metacyclic.

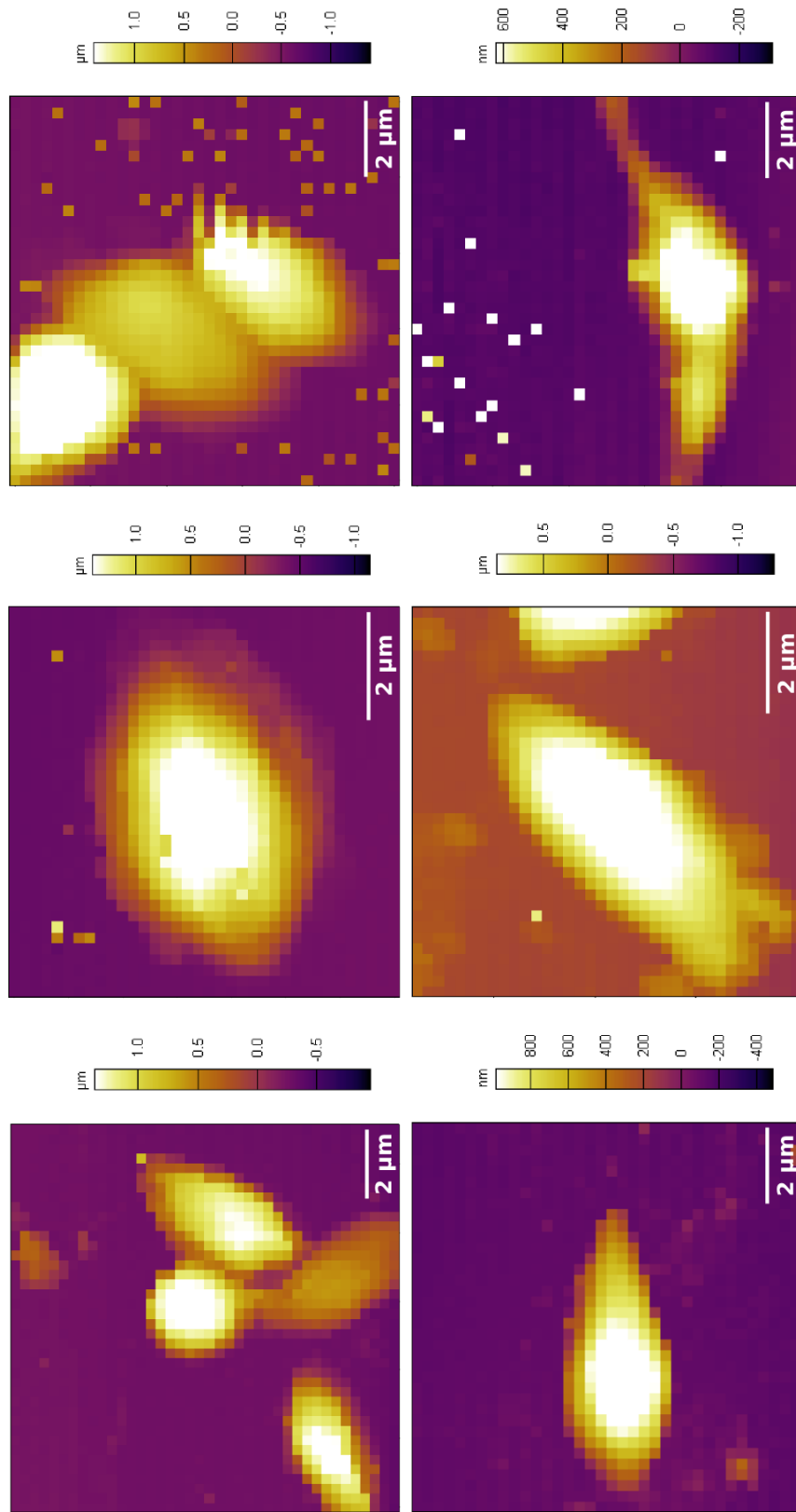


Figure 5.9: Wild type *Leishmania mexicana* procyclic parasites. Six zoomed-out maps showing topographical features calculated using the force-distance curves on each pixel. Maps were selected from across independent experiments and are representative of the parasite sample used in this work. Maps were taken using both glucose and galactose glycopolymer-coated AFM tips.

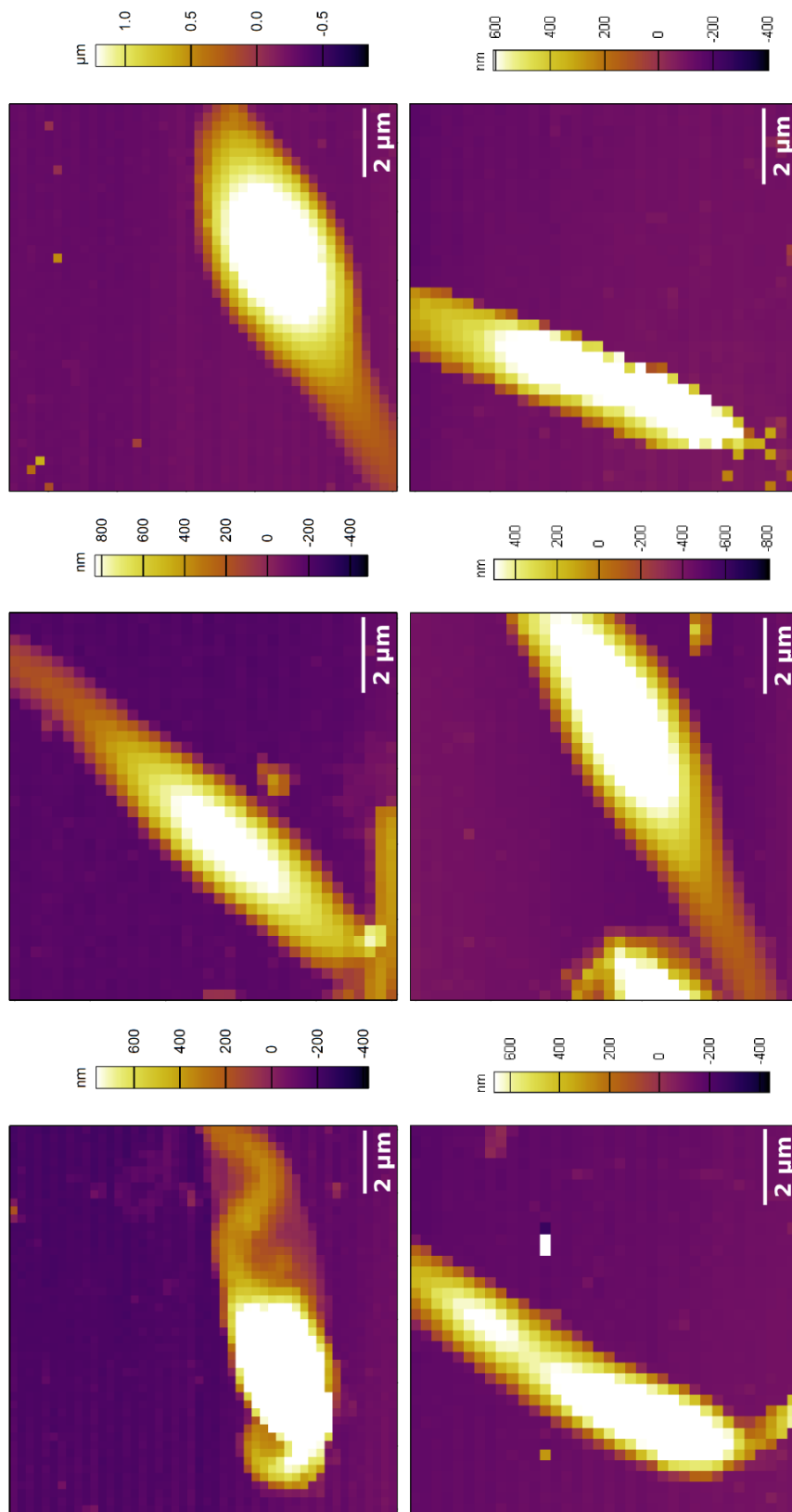


Figure 5.10: Wild type *Leishmania major* nectomonad parasites. Six zoomed-out maps showing topographical features calculated using the force-distance curves on each pixel. Maps were selected from across independent experiments and are representative of the parasite sample used in this work. Maps were taken using galactose glycopolymer-coated AFM tips.

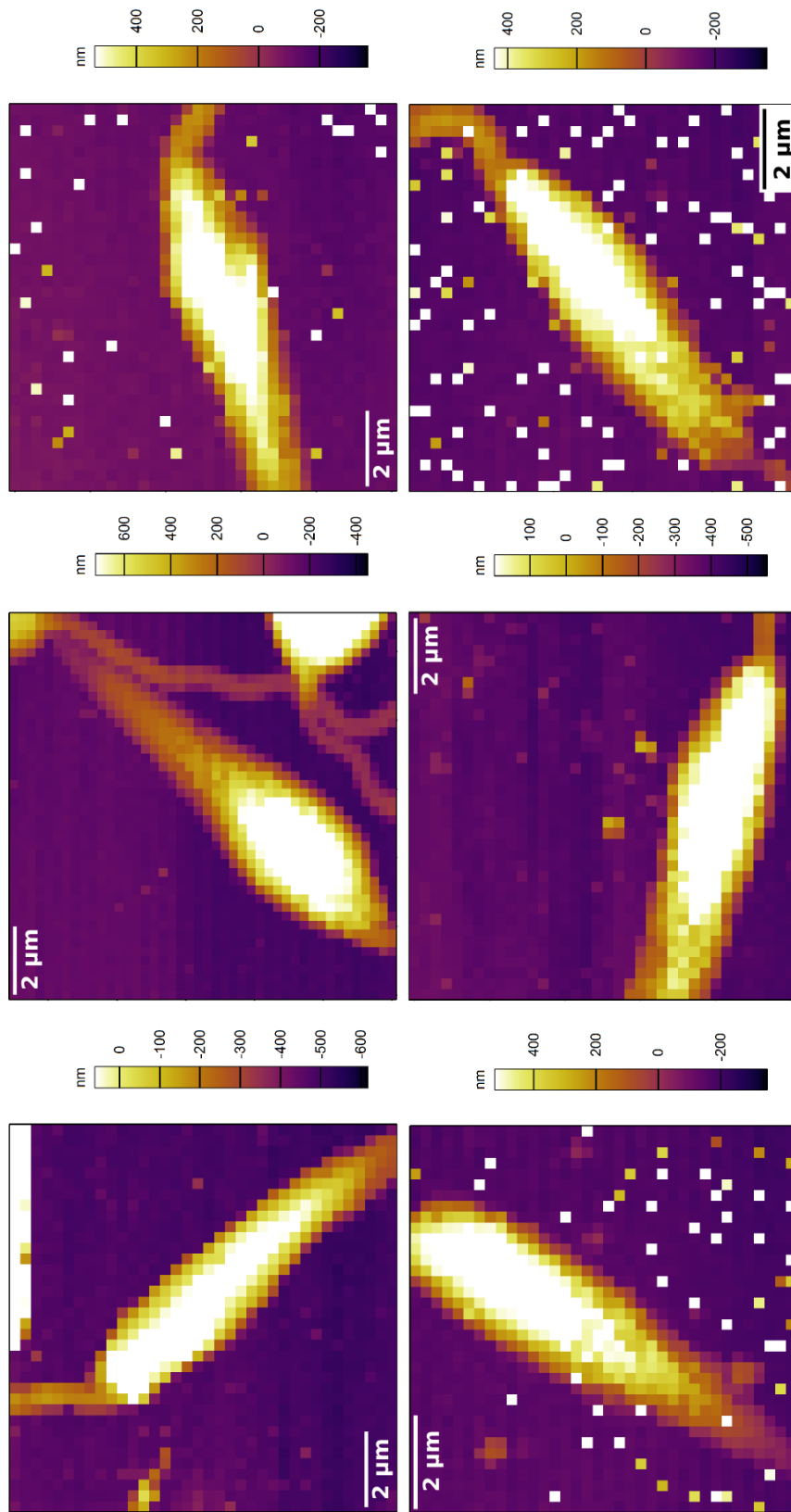


Figure 5.11: LPG1⁻ mutant *Leishmania mexicana* leptomonad parasites. Six zoomed-out maps showing topographical features calculated using the force-distance curves on each pixel. Maps were selected from across independent experiments and are representative of the parasite sample used in this work. Maps were taken using galactose glycopolymer-coated AFM tips.

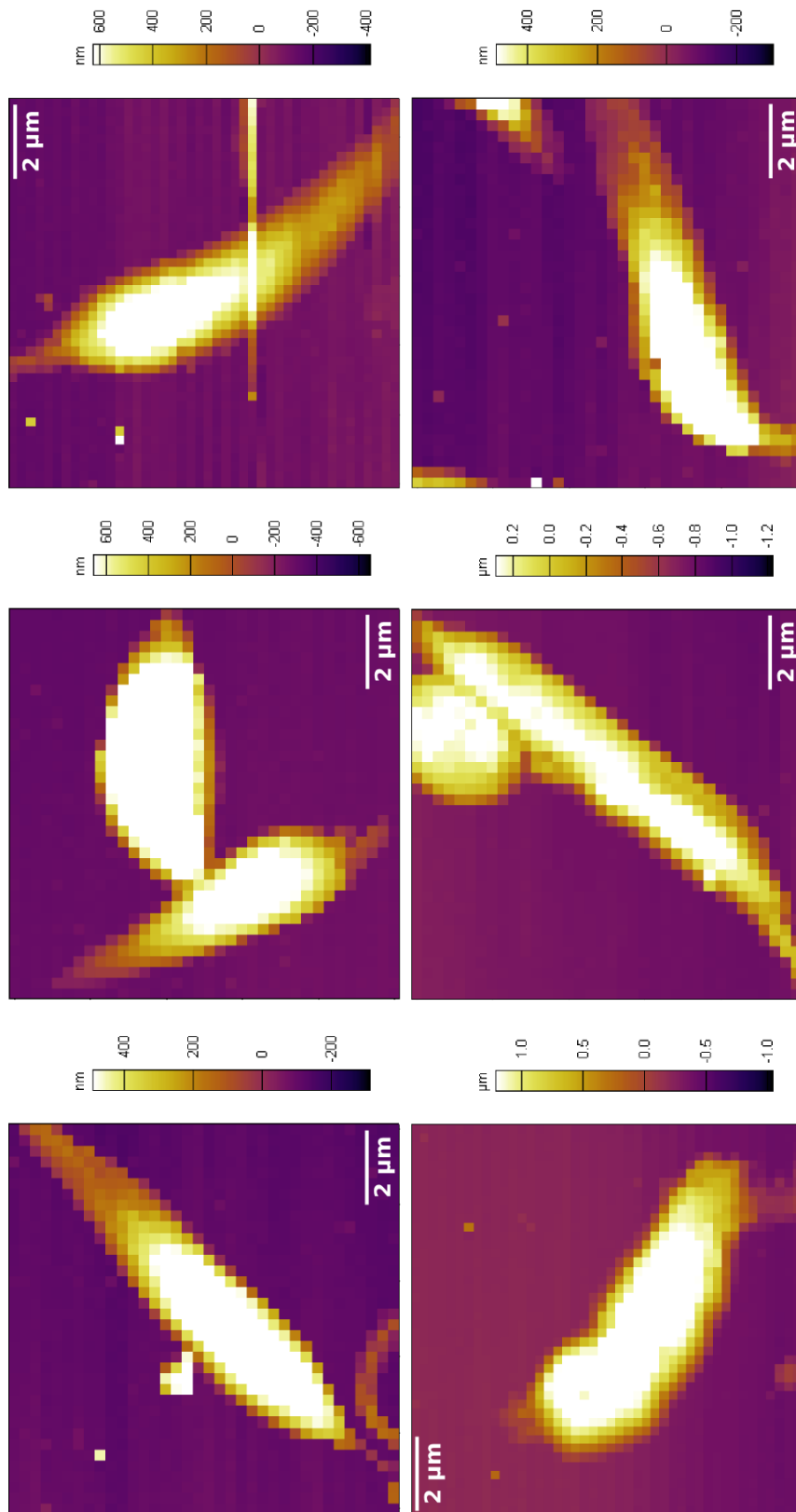


Figure 5.12: LPG1⁻ add-back *Leishmania mexicana* nectomonad/leptomonad parasites. Six zoomed-out maps showing topographical features calculated using the force-distance curves on each pixel. Maps were selected from across independent experiments and are representative of the parasite sample used in this work. Maps were taken using galactose glycopolymer-coated AFM tips.

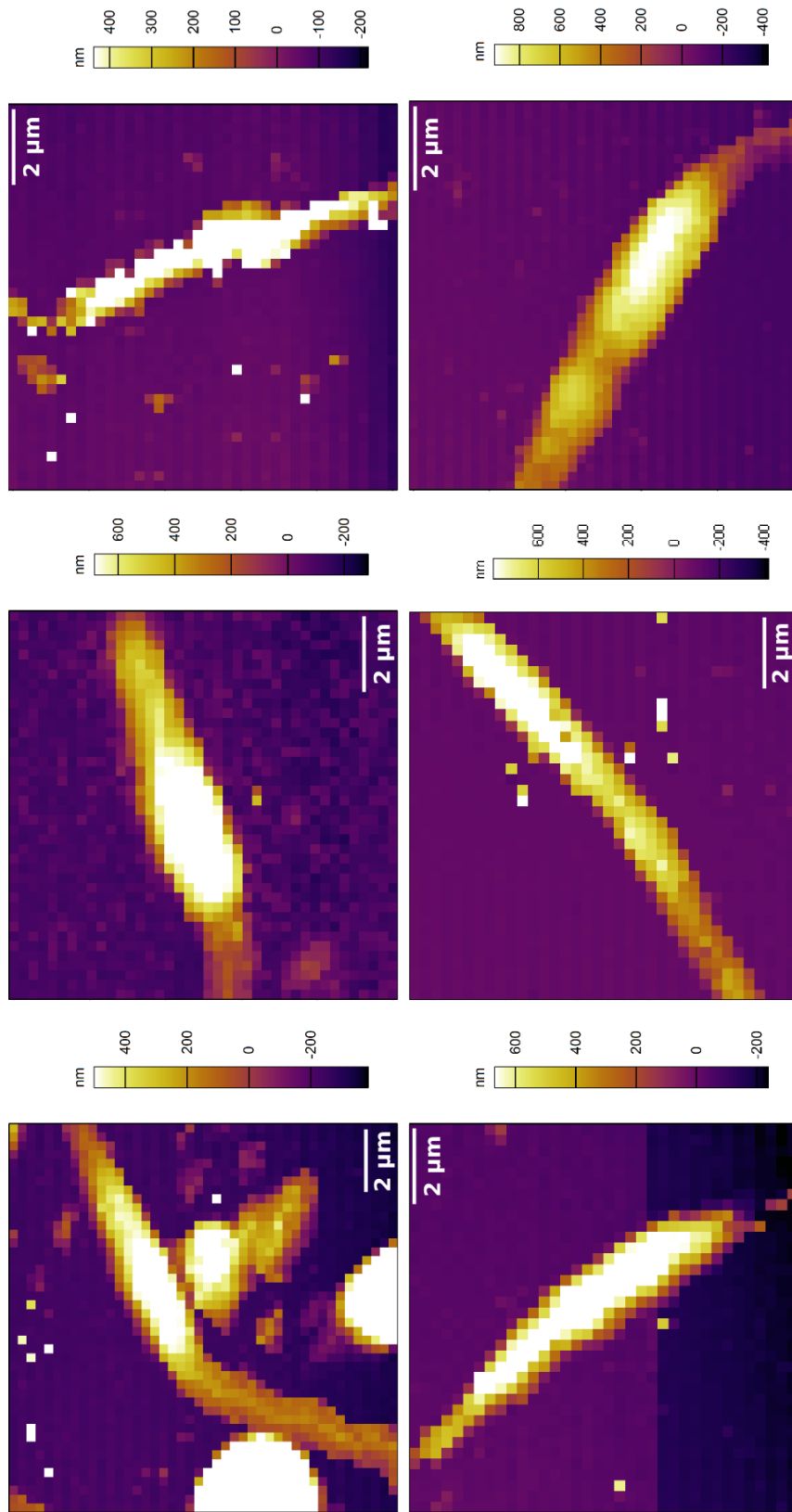


Figure 5.13: Wild type *Leishmania mexicana* metacyclic parasites. Six zoomed-out maps showing topographical features calculated using the force-distance curves on each pixel. Maps were selected from across independent experiments and are representative of the parasite sample used in this work. Maps were taken using both glucose and galactose glycopolymer-coated AFM tips.

5.7 *Leishmania mexicana*

A similar approach has been adopted here as for the *S. pneumoniae* work, using a combination of parameters to compare the adhesion profiles obtained from the force map data. The pixelated peak adhesive force data has been processed in two main ways: firstly, a finite mixture model (FMM) has been applied to the \log_{10} force distributions, which revealed some differences in the data, but since the model is stochastic in nature and takes account of all of the force-distance curves, including those with no binding interactions between the tip and the parasite, high force adhesion events could be masked in the FMM results, or the distributions skewed to lower forces in cases where non-interactive curves predominate. Therefore, an alternative comparison route has also been used which calculates a mean force purely using forces with positive binding interactions, through the addition of a minimum force threshold. This also allows determination of an effective force per μm^2 , which combines the adhesive forces measured in the map (above a given threshold) and therefore gives an estimation of the overall interaction strength in an AFM map of an equivalent $1 \mu\text{m}^2$ parasite surface area for different parasite-tip combinations.

5.7.1 Finite-mixture model analysis

Comparison of mean forces of the Gaussian components

Figure 5.14 summarizes the FMM adhesion results for the *Leishmania mexicana* parasites: G_1 , G_2 and G_3 represent the means of different Gaussian components in the FMM (the mean force of the k^{th} Gaussian component is also referred to as μ_k , where $1 \leq k \leq 3$), and the median force is also included to give a sense of which component is dominant. In most cases, the median is clearly higher than the G_1 mean, so a good proportion of the adhesion data is associated with the higher force G_2 or G_3 components. The two categories where this is not the case can be taken to be the lowest force combinations: WT metacyclic *L. mexicana* parasites probed with a glucose glycopolymer-coated tip and LPG-deficient leptomonad *L. mexicana* parasites probed with a galactose glycopolymer-coated tip. The highest

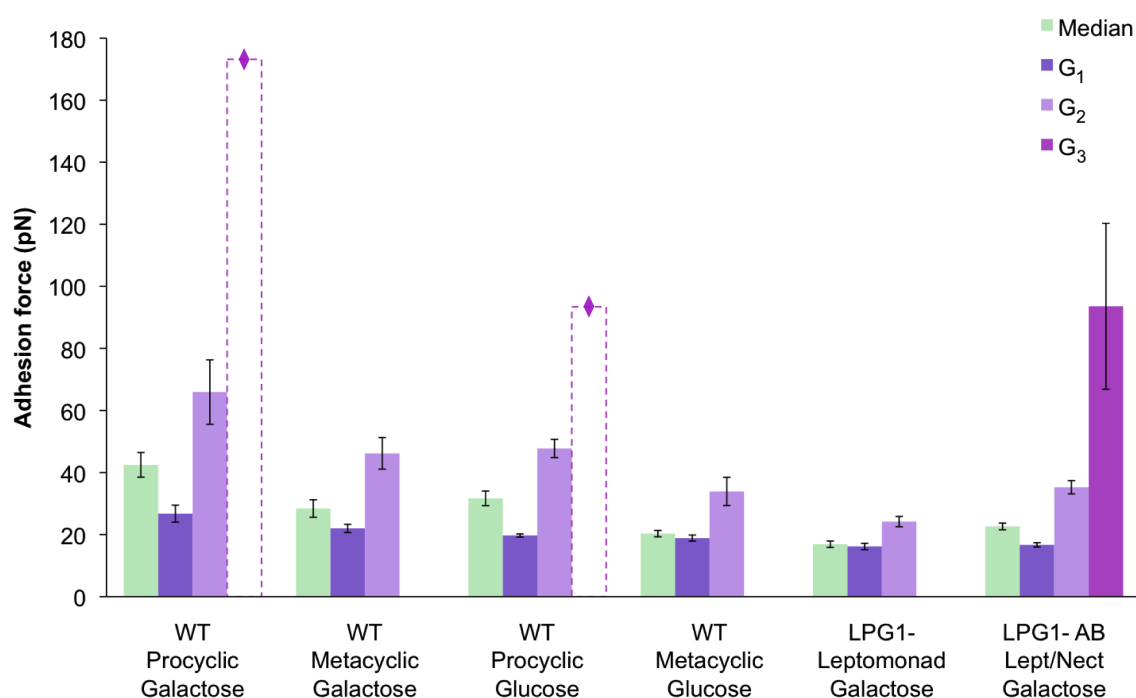


Figure 5.14: Graph comparing the mean forces of the components of the FMM applied to *Leishmania mexicana* - glycopolymer force data. Error bars show the standard error in the population and the dashed bars with a diamond marker represent a single parasite. The first of the three lines in the x -axis categories indicates whether the parasites are wild type or mutants, middle line gives the lifecycle stage of the parasites (NB: metacyclics are infectious and highly motile, with chemically modified LPG compared to the other types. Lept/Nect is an abbreviation of leptomonad/nectomonad), and the bottom line indicates the glycopolymer type used to probe the parasites. If the significant differences were indicated on the graph, as in the *S. pneumoniae* work, the graph would be unclear due to the number of different categories. The p -values corresponding to the measures shown in this graph can therefore be found in Appendix C on page 246.

force parasite-tip combination, with the largest median force and G_2 component, is the wild type *L. mexicana* procyclic parasite probed with a galactose glycopolymer-coated tip. The median force for this combination is significantly different to all of the other combinations ($p < 0.05$, see Appendix C, page 246), and the mean of the second Gaussian component is also larger than that of the other combinations, although this difference is not significantly different in the case of the G_2 component of the same parasite type with a glucose glycopolymer, or to the metacyclic WT parasite with a galactose glycopolymer.

The combination with the lowest value second component is the LPG-deficient leptomonad/nectomonad parasite probed with a galactose glycopolymer: this value is significantly different to all of the other combinations apart from the metacyclic WT parasite probed with glucose, although these two combinations are not directly comparable as they do not share a common factor other than parasite species.

The interaction between the WT metacyclic parasites and the two sugars suggests that this infectious form of the parasite interacts more strongly with galactose than with glucose, although, due to the variations in the behaviour of different parasites within the populations (particularly when probed using galactose: see Figure 5.15 on page 207), the differences in G_1 and G_2 are not significant between metacyclic parasites probed with galactose and glucose. However, the difference in the median force has a p -value of 0.022. The smaller G_2 mean of the WT metacyclic parasites + glucose is not significantly different to any value apart from the WT procyclics + galactose, but, again, it is not particularly useful to compare these two combinations as they do not share a common factor.

Perhaps the most interesting feature of the data presented in Figure 5.14 is that the removal of LPG from the parasite affects the measured adhesion values so strongly (compare the median and G_1 and G_2 means of the WT procyclics + galactose and LPG1⁻ leptomonads + galactose), suggesting that the interaction between galactose and the parasite is LPG-dependent. This is reinforced by the fact that the add-back LPG1⁻ mutants recover adhesion to galactose, restoring them to a wild type-like phenotype.

The FMM component means only partially describe the data, as they do not account for the distribution of the data between the components. To address this, both the mean force and the dispersity of the data are plotted as a function of the component weight in the following section.

Distribution of fit parameters according to the weight of the component

To illustrate the range of behaviour of the parasites within each category, Figures 5.15 and 5.16 plot the mean force and Gaussian width, σ , as a function of the component weight, with each data point on the graph representing a single parasite. If the forces and widths are similar for maps of different cells within the population (i.e. markers for component k are clustered together in the graphs) and similar proportions of data are attributed to the k^{th} component, then the cell population can be considered to be fairly homogeneous in terms of the FMM fits. It also follows that a wide variation in the data represents a more diverse population in terms of FMM modelling.

Graphs which have a higher concentration of G_2 points at higher λ values (WT procyclics and glucose/galactose: the middle and upper left-hand graphs in Figure 5.15) have the highest interaction levels, whereas when the G_2 points are clustered at lower λ values, the G_2 mean values are not as important because less of the data are attributed to the second Gaussian component (WT metacyclic + glucose, LPG1⁻ leptomonad + galactose: middle right and lower left graphs in Figure 5.15, respectively). In most cases, the third Gaussian component contains $< 10\%$ of the data within the sample and has a high force value (WT procyclics + glucose/galactose), except for the data from the LPG1⁻ AB leptomonads/nectomonads + galactose, where in one case the value of the mean of the third Gaussian component is much lower than the other two, being within the range of the G_2 mean for most other parasites, and containing $\sim 20\%$ of the force curve data. This large variation in the mean force of the G_3 component accounts for the large error bar in Figure 5.14.

The model showing the most variation in λ for G_2 is of the WT metacyclic

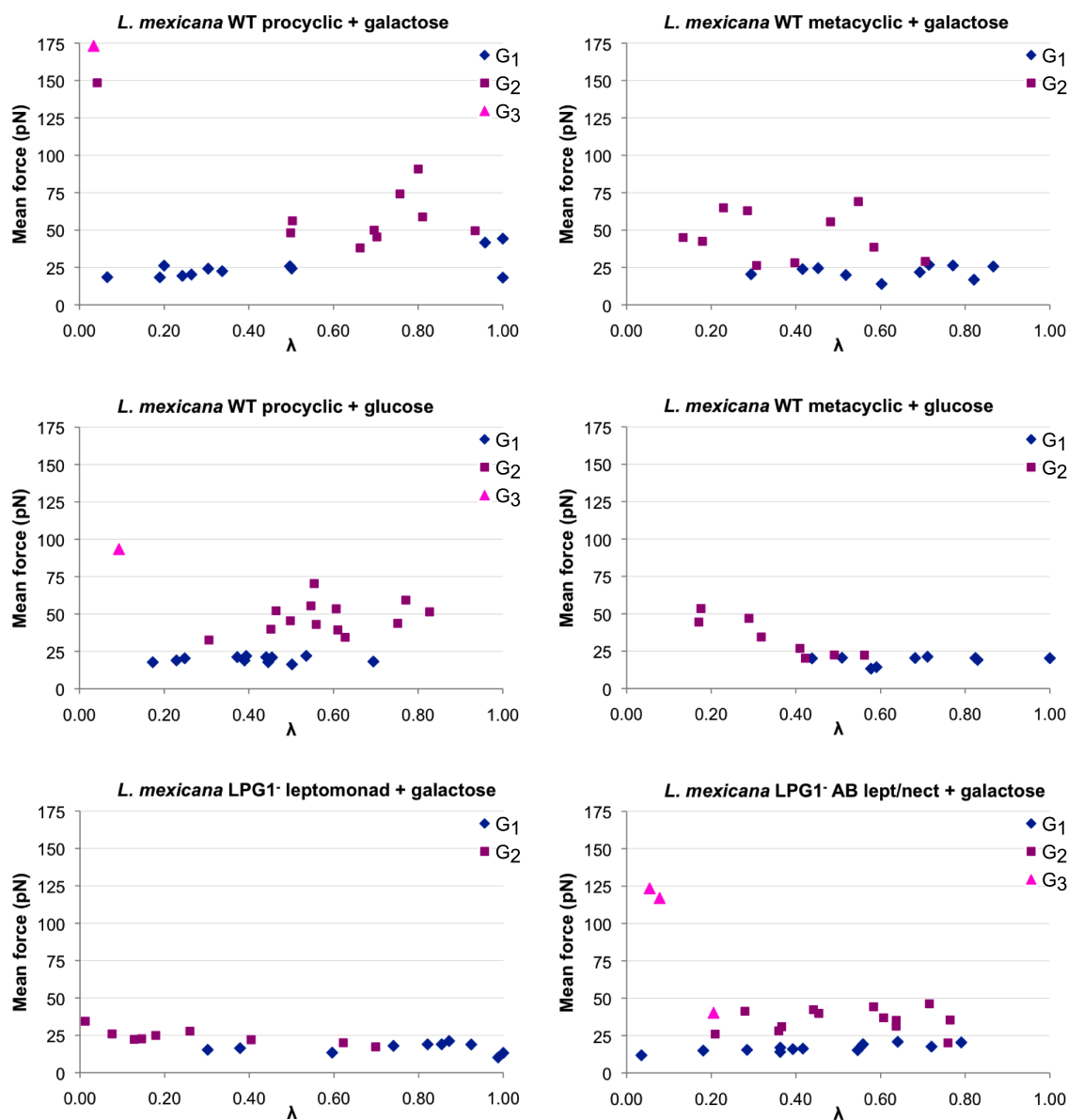


Figure 5.15: Graphs showing the mean forces of the components of the finite mixture model and their associated weights (λ) for different *Leishmania mexicana* - glycopolymer combinations. Each point within a series represents the data from a single parasite. The y -scales are the same for ease of comparison between the different combinations. Higher force combinations (e.g. WT procyclics + galactose/glucose) tend to have more variation in the G_2 mean force and a higher weighting attributed to the G_2 component than lower force combinations (e.g. WT metacyclics + glucose, $LPG1^-$ leptomonads + galactose). Additionally, the narrower the spread of data in the x -axis and the closer the data are to the same force, the more homogeneous the population, such as for WT procyclics + glucose.

parasites + galactose. While the left-hand portion of the graph appears similar for the WT metacyclics + glucose or galactose, in the case of galactose, there are some parasites which have a high proportion of data ($\gtrsim 50\%$) associated with a high force (50 – 75 pN) G_2 component. All of the parasites with a G_2 component > 50 pN belonged to the subpopulation identified as having patterned areas of high force (see Section 5.8), with only one ‘patterned’ parasite having a lower force G_2 component ($\mu_2 = 39$ pN, $\lambda_2 = 0.58$). These ‘patterned’ parasites could therefore represent a stickier subset of the population and could account for the high WT metacyclic-galactose interaction compared to the same parasite type’s interaction with glucose (no patterned high force regions were observed on parasites within this combination).

It should also be noted that there is more variation in the G_1 mean for the WT procyclic parasites + galactose than the other G_1 means. The reason for this becomes clear when looking at the upper left graph in Figure 5.15, where, unlike the other combinations, whose G_1 means all have a similar force value irrespective of the weighting proportion of the first component, G_1 components containing a larger proportion of data have a larger mean force than G_1 components containing less data. This difference is large enough that in some cases there is overlap between μ_1 and μ_2 for different cells, showing that, even when the lower force component is dominant, the *L. mexicana* procyclic promastigotes have a higher peak adhesive force than the other parasite types used in the study, when probed with a galactose glycopolymer. Note that two cells in this combination were unstable when fitted with multimodal distributions and therefore were fitted with a single distribution, having an effective λ value of 1.

The parasite-glycopolymer combination with the most even distribution of data between the two main Gaussian components is *L. mexicana* WT procyclics + glucose, where most cells had at least 20% of data points attributed to one of the main components and no parasites had data fitted with a single Gaussian. Also, the G_1 and G_2 means were fairly consistent within the population, suggesting that this combination was one of the most effectively modelled by the FMM approach, with

the behaviour of one parasite a reasonable predictor of another parasite within the same cell-tip combination.

In some cases, the mean force of the two components was very similar (WT metacyclic + glucose, and LPG1⁻ leptomonad + galactose), but in both of these combinations the fit for the G₂ component tended to be broader than that of the G₁ component (see Figure 5.16 on page 210). This, combined with the broadest of the components being associated with a smaller fraction of the force data (i.e. lower λ), suggests a skewed-type distribution, rather than a true bimodal distribution, with one clear peak with wide ranging but low frequency histogram bins extending on either side of the main peak (note that broader fits will encompass a greater amount high force data than a narrower fit with the same mean, as in the case of the more adhesive LPG1⁻ AB leptomonads/nectomonads + galactose compared to the LPG1⁻ leptomonads + galactose).

In general, Figure 5.16 suggests that in the majority of cases the second component is broader than the first, having the larger σ value of the two, although this is less clear in the case of WT procyclics + galactose, where the data are more widely spread, with heavily weighted G₁ components tending to be broader (upper left graph in Figure 5.16). In the case of WT metacyclics + galactose (upper right graph in Figure 5.16), there is a large overlap in the breadth of the two components and so in this case, to an approximation, both components will have the same dispersity.

The additional information these plots provide about the variation within the parasite population in adhesive response to galactose or glucose probes is a useful addition to the mean force data associated with the different FMM components, but it still does not combine all of the information into one easily comparable number. It is for this reason that, later in this chapter, an effective force per μm^2 is calculated (see Section 5.10), which can be used in combination with the FMM results to draw fuller conclusions from the force map results.

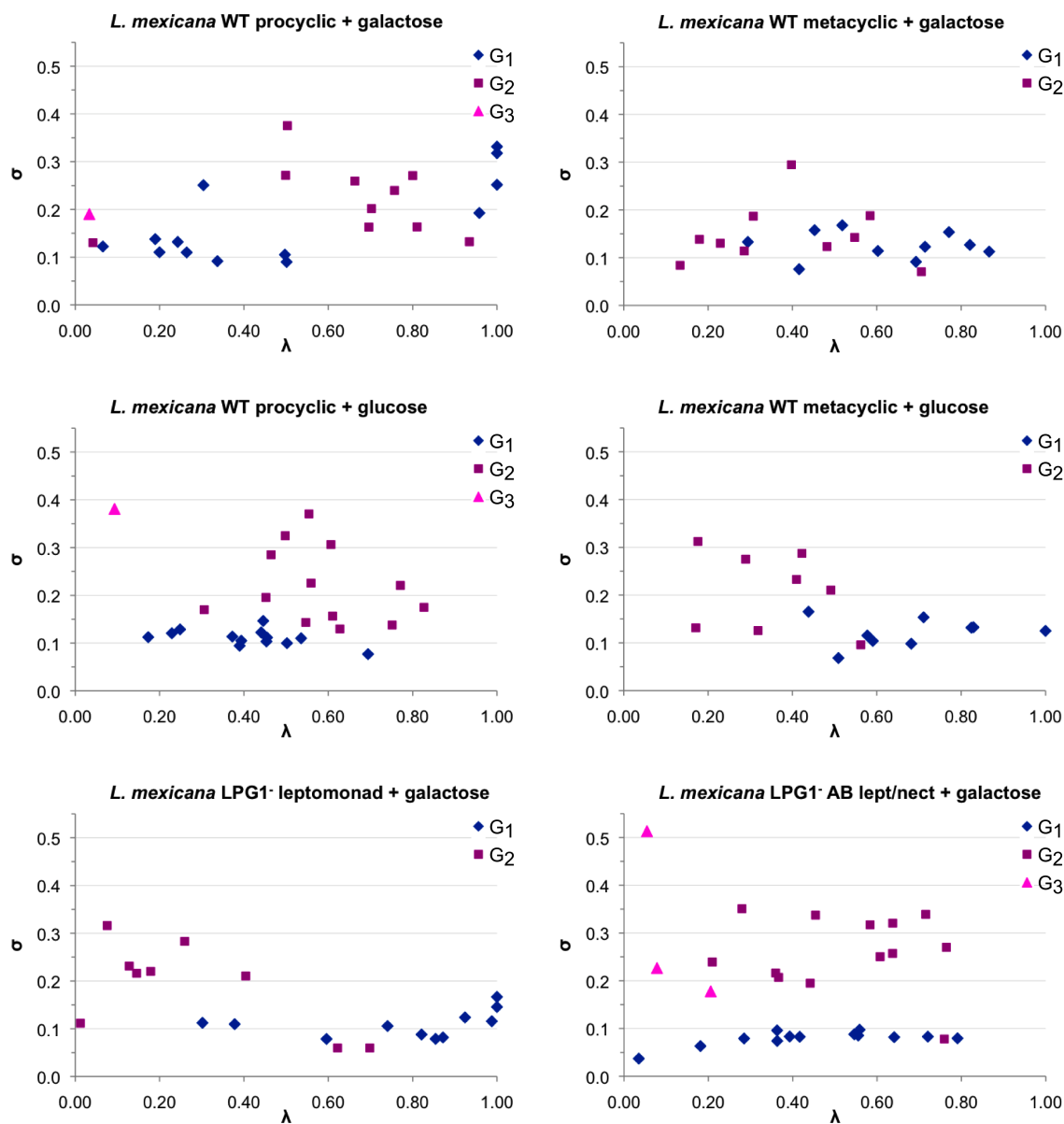


Figure 5.16: Graphs showing the widths (σ , in \log_{10} force) of the components of the finite mixture model and their associated weights (λ) for different *Leishmania mexicana* - glycopolymer combinations. Each point within a series represents the data from a single parasite. The y -scales are the same for ease of comparison between the different combinations. For most parasite-glycopolymer combinations, the G_2 component is wider than the G_1 component, apart from the WT metacyclics + galactose, where both components have a similar width, and the WT procyclics + galactose, where the G_1 components with $\lambda > 0.90$ are within the range of the G_2 widths.

5.8 Do any parasites show an uneven distribution of high forces across their surface?

If the proposed selective galactose-driven binding mechanism is responsible for the adhesion of *Leishmania* parasites to the midgut of the sand fly, the same interaction forces would not be expected between the WT procyclic parasites and the glucose glycopolymer-coated tip. However, the adhesion force measures showed that some procyclic parasites did exhibit adhesion to the glucose tip. Whilst the force maps obtained using the galactose tip on the WT *L. mexicana* procyclic parasites showed a random distribution of force-distance curves containing strong adhesion interactions across the parasite surface, the higher force maps resulting from experiments with the glucose tip tended to show patterned adhesion along the long axis of three parasites, illustrated in Figure 5.17 on page 212.

Similarly, since the adhesion of promastigotes to the sand fly midgut is stage specific, infectious metacyclic parasites would not be expected to adhere to galactose residues. However, the FMM results for WT *L. mexicana* metacyclics + galactose showed the presence of a bimodal distribution, where the G_2 mean force was larger than the “low-interaction” combinations (compare the value of G_2 in Figure 5.14 and the data distribution in Figure 5.15). Similarly to the WT procyclic parasites and glucose, a few parasites towards the higher-force end of the population showed a heterogeneous force distribution, with a line of higher force events along the long axis of the parasite. An example of this is shown in Figure 5.18 on page 213, where three maps are shown of the same parasite: the height and force data from a zoomed out map, then the height and force data from two consecutive zoomed-in maps. The line of high force is conserved between the map of the whole parasite and the first zoomed-in map, but is less clearly defined in the third map of the parasite. The reason for this is unclear, but it could be due to the timescale between the maps, as map A would have taken approximately 30 mins, map B just under 20 mins, and map C taking approximately 15 mins. It is possible that these high force regions have a limited lifetime, or it is possible that the parasite responded to the interaction with

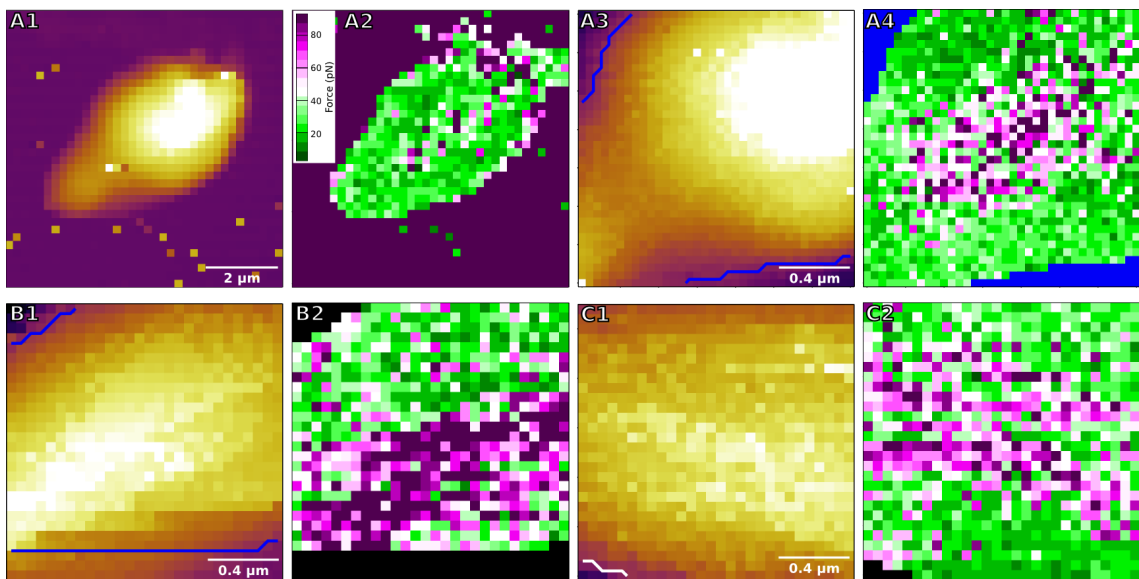


Figure 5.17: Patterning forces on three wild type *Leishmania mexicana* procyclic parasites probed with glucose glycopolymers. Maps A1-4 are of the same parasite, comprising topographical (1 and 3) and force maps (2 and 4) of the whole parasite body (1 and 2) and a close-up of the central region (3 and 4). There appears to be a line of high force along the centre of the long axis of the parasite which is conserved between the two maps. Maps B1 and B2 show the topography and force profile of a close-up section of a different parasite, which has a line of very high forces running in a line parallel to the parasite's long axis, and a similar pattern of high forces along the long axis is also present in the third parasite, shown in maps C1 and C2. The force scale is the same across all of the maps and is inset into A2. There are no clear topographical features that could explain these spatially-organized forces but it is possible that there are surface features which are not visible due to insufficient detail in the low resolution topographical map.

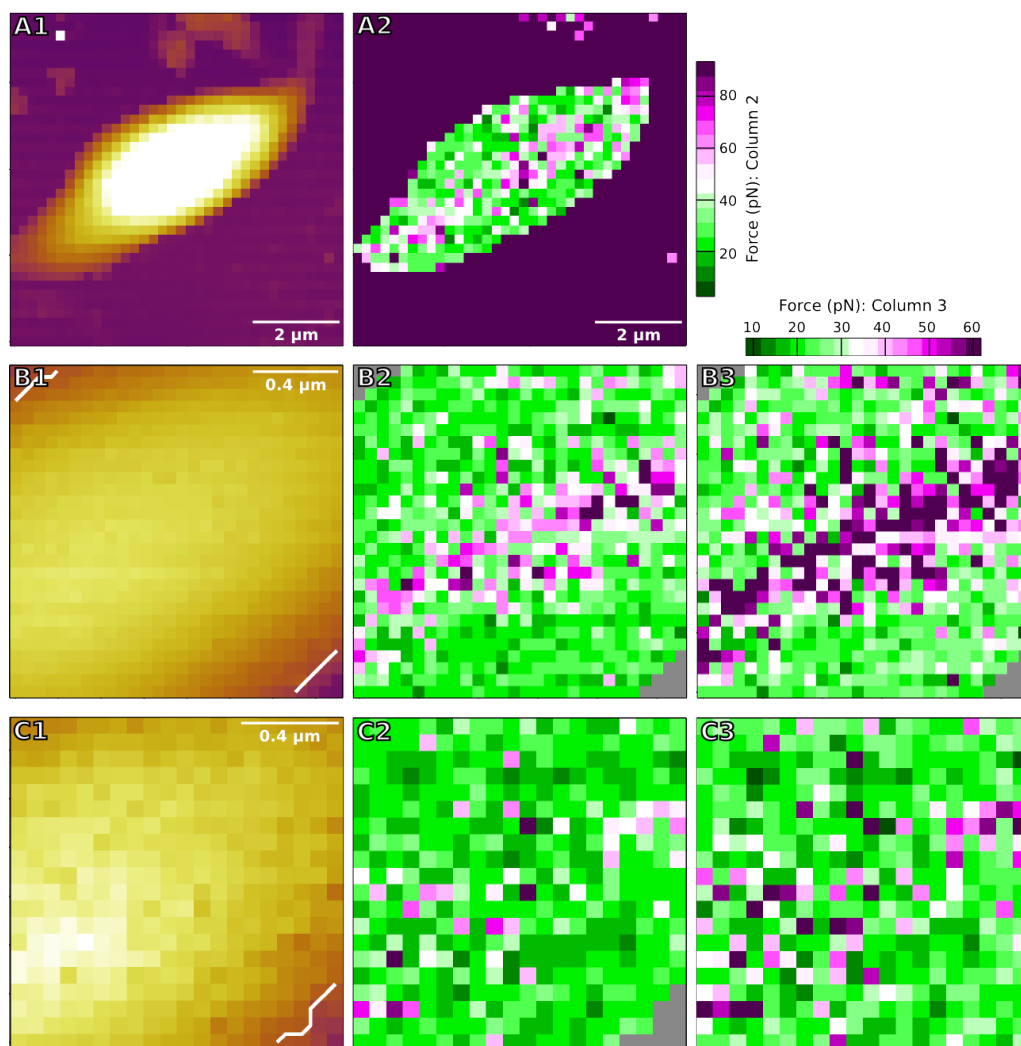


Figure 5.18: Patterned forces on a parasite from a wild type *Leishmania mexicana* metacyclic sample, probed with galactose glycopolymers. Maps A, B and C were obtained consecutively, and the pattern of higher adhesive interactions down the centre of the parasite was conserved between the zoomed-out image and the first close-up scan, but the high force line is less well defined in the third, map, which had fewer pixels across a slightly smaller area in the same position. The length scale is indicated on the height image for each map (A1, B1 and C1). The scale for the force maps in the middle column is given to the right of map A3, and the scale of the force maps in the right-hand column is given above map B3. The pattern of forces is more clearly defined when the scale is smaller, such that forces > 35 pN are indicated using the pink and purple range of the scale, as in column 3, but the highest forces (< 60 pN) appear to be present along the central line with lower adhesion forces surrounding them. There are no clear topographical features in the location of this high force region, but it is possible that this is due to insufficient detail in the topographical map due to the low resolution compared to an AFM image.

the AFM tip, triggering molecular changes or reorganization of molecules exposed on the cell surface.

These were the only two parasite-tip combinations to show clearly patterned forces, and it raises further questions about whether patterned forces exist on all parasite types, and the sample size was too small to see this effect for other combinations (although this is unlikely given that patterned parasites made up between 35 and 40% of the population where they were observed, across all three independent repeats), or whether these particular combinations of procyclics and glucose, and metacyclics and galactose, share some common response to the tips. However, since the patterning was seen in response to both galactose and glucose, the reason for this is unclear.

5.9 Multiple binding events within a single force-distance curve

Double, triple or multi-peak forces were common in maps for the following combinations: WT procyclic and leptomonad/nectomonad + galactose (in 4 independent experiments for this combination, 1 was performed using leptomonad/nectomonad parasites, rather than procyclics), WT procyclic + glucose, and LPG1⁻AB leptomonad/nectomonad + galactose. The relative proportions of single, double, triple and multi-peak curves have not been calculated in this work due to the focus on mapping the distribution of high and low peak adhesive forces across the parasite. It would be possible to calculate the proportion of different event types, and the characteristics of those events if a script was used which could extract extension distances before adhesion and count multiple events, rather than manual extraction of this information, which was not feasible for such large volume data as those in this work. However, the increased appearance of multi-peak curves for parasite-tip combinations which showed more interaction with the tip suggests that combinations exhibiting larger peak adhesive forces also have more force-distance curves containing multiple events. This further suggests that the moieties on the parasites

which are involved in adhesion to the glycopolymers are fairly dense, since multiple binding events represent multiple interactions occurring within the contact area between the tip and the sample.

A closer look at force curves from a single parasite.

As mentioned previously, the force curves making up the map of the parasite contain lots of information which is not extracted as part of the above analysis. Although the peak adhesive force is a useful measure of interaction characteristics, it is worth noting that these adhesive forces only account for the strongest interaction within a given force-distance curve. A sample of force-distance curves showing some of the range of different interactions observed within force curves from a single, adhesive parasite are briefly discussed here to improve understanding of the meaning of the conclusions made as a result of analysis of peak adhesive force data.

To illustrate the varied interaction events observed on a parasite which interacted strongly and positively with the tip, force curves showing different types of binding events, taken on a WT *Leishmania mexicana* procyclic parasite using a galactose-coated tip ($k = 26 \text{ pN nm}^{-1}$) are presented in Figure 5.19 on page 218. The x -axis on these graphs has been cropped as there were no additional force events beyond 600 nm from the cell surface and the reduced width allowed two graphs to be shown side-by-side on a single page. All of the curves contain clear interaction events. The left-hand column of graphs includes the approach curve, dwell on the surface, and retraction curve, whereas the graphs on the right-hand side only show the retraction curves for clarity.

On this parasite, the majority of curves contained at least one interaction event with the AFM tip, and the scale of these interactions was seemingly independent of the number of events: a single interaction could require the same unbonding force as an interaction which was part of a multi-event curve, such that there were high-force single events and curves containing two or three events each of 30 – 40 pN in size. Therefore, the curves shown here are not an exhaustive list, but demonstrate some of the observed features. There were very few adhesion events with short, linear

extension before pull-off, so the measured adhesive forces can be associated with binding interactions between molecules on the parasite and the glycopolymers on the AFM tip, rather than non-specific interactions [37, 164].

One thing to note with the observed molecule extensions in Figure 5.19 is that, although the following discussion takes the length/extension of the different force events to be the length of the stretched parasite surface molecule (and also takes zero distance to be the point at which the AFM tip crosses the zero force baseline on retraction from the surface [165]), there is likely to be some extension of the glycopolymer brush on the AFM tip, since polymer brushes are relatively elastic compared to a bare tip and even when in a good solvent will not be extended to their full chain length. All of these curves were taken in the same map and therefore using the same glycopolymer-coated tip in the same solvation conditions, so extension of the polymers on the tip should be fairly consistent across the images. However, if these individual force events were to be modelled and compared between the different experiments, where tips coated in different polymerization batches were used, the thickness of the polymer coating might have to be accounted for as brushes of different thicknesses could have varied elastic or extension properties [253]. The tip used in these experiments had a dry PMAA thickness of approximately 30 nm, as measured by ellipsometry of a control wafer, but in later experiments the PMAA thickness was generally lower, at between 5 and 10 nm (note that the actual brush thicknesses in the aqueous PBS would have been larger, as the glycopolymers are hydrophilic, and in addition the ellipsometry measurement here was taken prior to the glycosylation reaction). Despite variations in polymer chain length, the grafting density of brushes from different batches should be fairly constant because a grafting-from approach was used to grow the polymers from the surface and the water contact angles and thicknesses of the APTES and initiator layers were fairly consistent between polymerization batches.

Glycopolymer length and elasticity would need to be considered for detailed analysis of individual bond properties, for example if the observed peaks were fitted using the WLC model, where the extension profile of each event is used to evaluate

the physical properties of the biomolecule [26, 254], which would be related to the combined length of the glycopolymer and biomolecule in this case [219] (see Section 2.2). However, this work is focused on the variation of the size of the peak adhesion force between different tip-parasite combinations, which does not consider extension. Instead, in this case, the main feature required to be constant is the tip chemistry: the same reactive groups, sugar and PMAA backbone should be conserved for different batches of glucose or galactose glycopolymers. Therefore, so long as the tip surface is well populated with the relevant sugar molecule, which appears to be the case given the low water contact angle and increases in brush thickness after the glycosylation reaction (see Section 3.3.4), and the PMAA coating is thick enough to block non-specific interactions with the silicon nitride tip (given the lack of non-specific interactions observed in the lectin-binding control experiments using glycopolymer brush tip coatings of varied thickness), variation in polymer brush thickness should not have too great an impact on the measured forces.

Figure 5.19A shows a clean single event with non-linear extension, where the tip retracted a little over 50 nm from the cell surface before the bond broke as the tip applied a pull-off force of ~ 50 pN. Figure 5.19B is dominated by a single adhesion peak with non-linear extension to a longer distance of ~ 150 nm, where a much higher force of nearly 300 pN was required to break the attachment. This primary event is followed by two much smaller (~ 40 pN) detachment peaks. The remainder of curves included in the figure show increasing numbers of individual adhesion peaks, with C and D having two clearly defined, non-linear extensions followed by detachments at forces which are similar for both events within the curve, suggesting that the same type of molecule (i.e. with the same energetic barrier for detachment [40]) is bound to the tip on two occasions. This could occur either as two moieties along the same, long polymer, or similar moieties on two separate polymers interact with the tip in series (see Figure 5.20 on page 220).

The unbinding events in Figure 5.19E - H tend to occur at different forces, so could be due to different moieties interacting with the tip. For example, in graph E, two clear events with fairly linear extension occur at ~ 25 nm and ~ 90 nm from

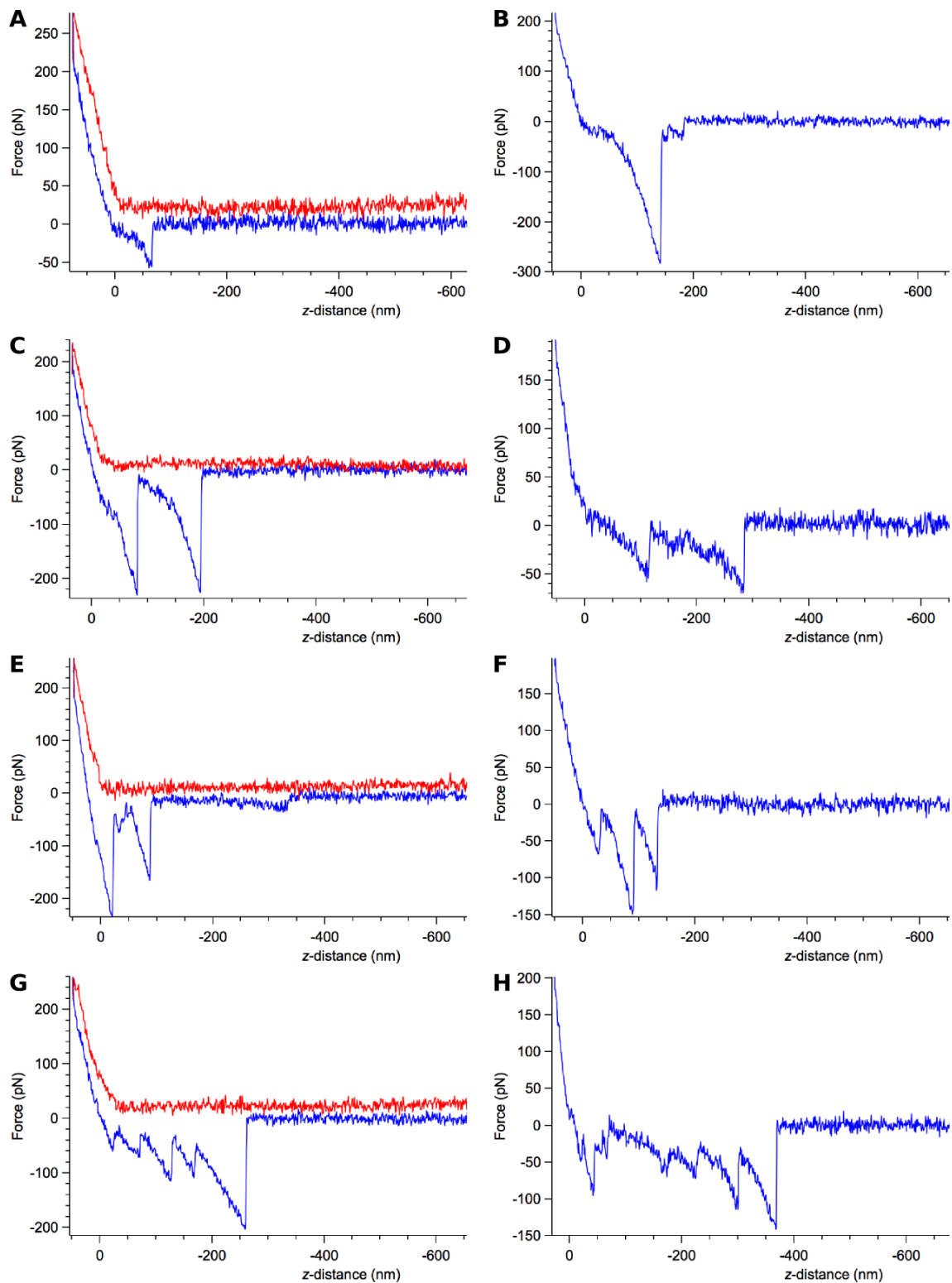


Figure 5.19: Different force curves taken from a force map obtained on a single WT *Leishmania mexicana* procyclic parasite probed with a galactose glycopolymer coated AFM tip ($k = 26 \text{ pN nm}^{-1}$). 250 pN applied force, 240 ms dwell towards the surface. Approach curves are red (where included) and retraction curves are blue. The zero force has been determined using the retraction curve.

the cell surface, whereas the final adhesive event in this graph is due to a very long molecule (~ 350 nm, assuming the moiety attached to the tip is at the end of the chain) which is bound to a moiety on the tip with an adhesive force of ~ 30 pN. This event would be just above the threshold implied during the calculation of average adhesive forces (> 20 pN), were it a single event within a curve (see Section 5.10). Long extensions (> 200 nm) tended to be found when multiple events were present in the force-distance curve, but there were a few cases on other cells within this tip-parasite combination which contained a single 20 – 40 pN unbinding event of a similar character to the third peak in Figure 5.19E.

Note that the z -distance on the graphs is related to the position of the cantilever, so does not take account of where the parasite biomolecule is attached to the AFM tip, or how far along the length of the glycopolymer chain it is attached, both of which could affect the difference between the actual length of the biomolecule up to the bond point and the z -distance of the extension. Additionally, the moiety interacting with the AFM tip could be at the far end of the biomolecule relative to the parasite surface, or somewhere along the length of the molecule. Biomolecules are highly complex and can have one or more binding sites along their length which can target different residues. Therefore, multiple interactions observed within a single curve can arise in different ways: either from several individual parasite surface molecules interacting independently with the glycopolymer tip, or from the same molecule interacting at different points along its length, or by a combination of the two. These two interaction types are illustrated in Figure 5.20, on page 220.

The force curves contain a wealth of information about the adhesive molecules probed during the AFM experiments, and although individual events are not analysed in detail in this work, it is possible to deduce that parasite-tip combinations which demonstrate higher adhesion, based on analysis of the peak adhesive force across their surface, are likely to also contain force events where multiple points on the same biomolecule or biomolecules are interacting during a single curve. The combination of lots of weak interactions can be as effective as a single strong interaction, and multivalent interactions are known to be important in generating

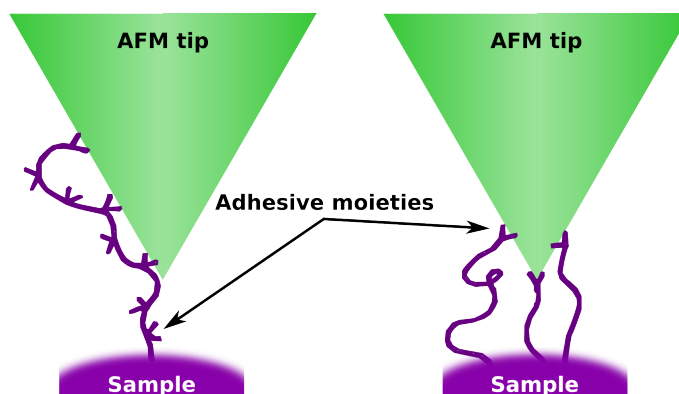


Figure 5.20: Schematic diagrams suggesting how multiple adhesion events could be measured in a single retraction curve through interaction of the AFM tip with either a single biomolecule or multiple biomolecules. In the left-hand example, a single biopolymer with multiple adhesive moieties along its length interacts with the tip at several points. In the right-hand image, three biomolecules with different lengths and an adhesive moiety at the termination of the molecule interact independently with the AFM tip. Different extension distances before bond rupture can be caused by molecules of different lengths, different lengths of biomolecule between tether points, and different binding positions within the area of the tip in contact with the surface. AFM tip coatings and sample molecules which are not interacting directly with the tip are not included for clarity. However, it should be noted that as there are sugar molecules distributed along the PMAA backbone throughout the glycopolymer brush tip coating, both of the multivalent interactions illustrated in the figure are also possible for the glycopolymer brush.

biologically relevant adhesion strength from individual, weak sugar-protein binding events [47], so events with smaller adhesive forces could still play an important role in the attachment of parasites to the sand fly gut midgut. Additionally, the shape of the force-distance curves suggest that even the strongest binding events of the order of hundreds of piconewtons are caused by specific binding events, due to the non-linear character of the extension [255], and that the forces are due to single events because the unbinding occurs suddenly, rather than incrementally [226]. Therefore, the peak adhesive force is a suitable measure of the range of interaction strengths which contribute to the adhesion of *Leishmania* parasites.

5.10 Analysis of *Leishmania* parasite adhesion using the mean adhesive force of FS curves containing binding events

This section uses a different method to assess the adhesion of different parasites to glycopolymers, by applying a given threshold to the force map data, and taking the average of the values above the threshold. These averages are also converted into an effective force per μm^2 , as described in Section 2.3.3. Figure 5.21 shows the average adhesive force calculated using the following data taken on the parasite: all force-distance curves, curves with a peak adhesive force above the noise threshold (> 20 pN), and curves with a peak adhesive force > 30 pN (i.e. ignoring the weakest binding events). The results for the different combinations are presented alongside the median force, which was also presented alongside the FMM results shown in Figure 5.14 on page 204.

The fact that the average interaction strength was not significantly different for the WT *L. mexicana* procyclics + galactose/glucose in any of the mean force results ($p > 0.05$) suggests that the main high force interactions are independent of the sugar type, agreeing with the FMM results. The mean adhesive force for the LPG1⁻AB *L. mexicana* leptomonads and nectomonads + galactose was also not significantly different to the WT procyclics + galactose for the mean force > 20 and 30 pN (p -values can be found in Appendix C on page 247), showing that although a higher proportion of force curves on the add-back parasites contained weaker interactions, once these were removed from the sample, the adhesive binding events contributing to the adhesion between the parasites and the galactose were of the same scale as those on the wildtype, suggesting that these sand fly midgut-adhesive types share a common binding mechanism or range of mechanisms with a similar bond strength. The fact that the differences between the means calculated above the thresholds are significantly different between these three high adhesion force combinations and all of the other parasite-tip combinations (except the > 20 pN mean for LPG1⁻AB *L. mexicana* l/n + galactose and WT *L. mexicana* metacyclics + galac-

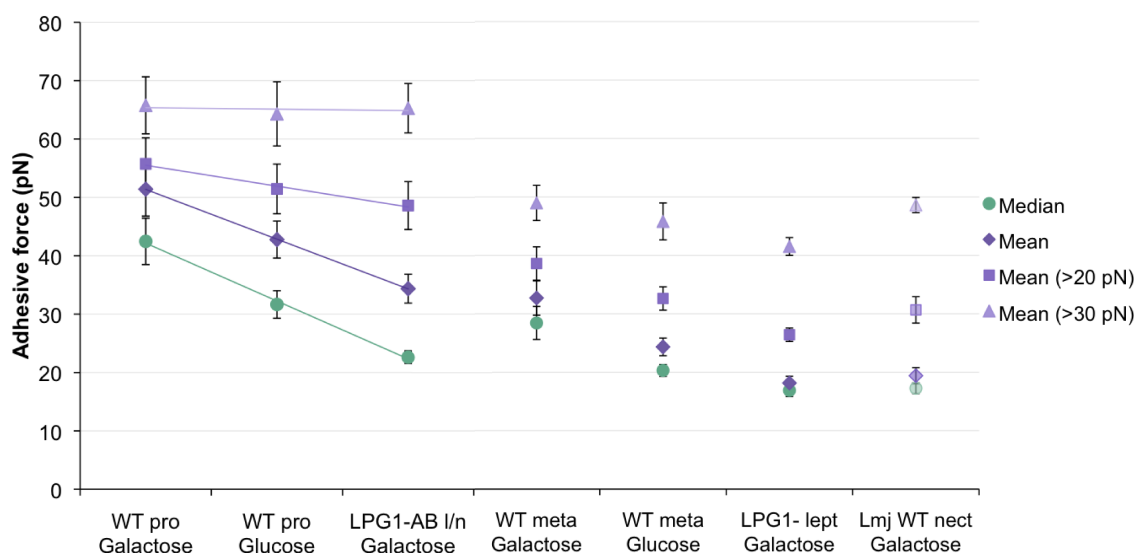


Figure 5.21: Graph comparing the median and mean forces of the different *Leishmania* parasite-glycopolymers combinations. Lines are drawn to guide the eye and highlight the trends in the data for the three combinations showing highest adhesion. For these categories, the differences between the means calculated using force curves including >20 pN or >30 pN force events are non-significant. The differences between the mean adhesive forces for WT procyclic parasites probed with galactose or glucose are also non-significant. However, the mean adhesive force of LPG1^- AB nectomonads/leptomonads + galactose is significantly different to the others (the differences between this category and WT procyclics + galactose or glucose have p -values of 0.02 and 0.04, respectively). Trends of relatively higher or lower forces between these parasite-tip combinations are consistent between all of the force measures, and most differences are significant (p -values can be found in Appendix C on page 247). Differences between the tip-cell combinations with lower adhesion are less pronounced, and in some cases are non-significant, such as between the WT metacyclic parasites + galactose and the LPG1^- AB leptomonad/nectomonad parasites + galactose.

Abbreviations: pro = procyclic, l/n = leptomonad/nectomonad, meta = metacyclic, lept = leptomonad and nect = nectomonad. Note that the results for wild type *Leishmania major* (Lmj) nectomonads have been included in this graph for comparison, using paler markers. Also note that the *L. mexicana* combinations have been arranged in order of decreasing interaction strength.

tose, which is non-significant) sets that the strongly and weakly adhesive parasites apart more clearly than the FMM results. This suggests that the metacyclic lifecycle stage of the WT *L. mexicana* parasites, the LPG-deficient parasites and the sand fly midgut-binding *L. major* parasites all lack something which is key to this high strength binding interaction. This raises interesting questions about the mechanism involved in the interaction between the parasites and sand fly midguts, particularly regarding the proposed conservation of binding between different parasite species, as the striking difference in behaviour of similar types of WT *L. mexicana* and *L. major* suggests that this might not be the case.

It is interesting to note that the parasite-tip combinations with the highest interaction forces in Figure 5.21 are also the combinations where at least one cell showed a stable trimodal distribution in the FMM analysis of the \log_{10} force data. The linear fits of the data from the adhesive combinations are drawn to guide the eye, and they show that the high force events have the same mean magnitude for all three categories, and that the means decrease for the other two calculated means. This drop illustrates the proportion of high force data, since the difference between the means calculated with different criteria indicates the proportion of high force events: if the mean drops significantly upon inclusion of 20 – 30 pN events, it shows that most force events are part of the weak binding force regime. If this mean decreases significantly again when all the data are considered, it shows that force-distance curves containing no clear interactions between the tip and the surface make up a greater proportion of the data. Note that the trend in decreasing average force matches that in the mean force of the second Gaussian component in the FMM analysis, with the WT procyclics + galactose having the highest value ($\mu_2 \approx 66$ pN) and LPG1⁻AB leptomonads/nectomonads + galactose having the lowest value ($\mu_2 \approx 35$ pN), with the WT procyclics + glucose lying in the middle ($\mu_2 \approx 45$ pN): see Figure 5.14 on page 204.

5.10.1 How do forces measured on *L. mexicana* compare to the lectin-binding control experiments?

In the control experiments, the lectin coating of the sample was fairly even, with most events registering adhesive interactions. In the parasites, even the most adhesive combinations contained curves with non-adhesive events, so to compare the control experiment data with the parasite data, the average force calculated using force-distance curves with a peak adhesive force above 20 or 30 pN was used. The relevant values are presented in Table 5.2.

Table 5.2: Average force for the lectin-binding control experiments compared to selected parasite-glycopolymer tip combinations. SBA is a galactose-specific lectin and conA is a glucose-specific lectin. The parasites used for the comparison are *Leishmania mexicana* wild type promastigotes, as they exhibited the highest adhesion levels to both glycopolymers.

Tip	Sample	Mean force (> 20 pN)	Mean force (> 30 pN)
Galactose	SBA	120 ± 13 pN	136 ± 13 pN
Galactose	<i>L. mex</i> WT pro	56 ± 4 pN	66 ± 5 pN
Glucose	conA	82 ± 8 pN	91 ± 9 pN
Glucose	<i>L. mex</i> WT pro	51 ± 4 pN	64 ± 5 pN

In all cases, the interactions between the glycopolymer-coated tip and the lectin surfaces were approximately twice that between the same type of tip and the parasite (the measured lectin interaction forces were smaller for conA than for SBA, so the apparent reduction in the force measured on parasites relative to those on the lectin surface was smaller when the glucose glycopolymer was used). Although the peak adhesive forces differ, they are of a similar magnitude, unlike in the *S. pneumoniae* work, where the SAM monolayer control experiments were of the order of nanonewton interactions rather than piconewtons (see Section 3.7). This suggests that the control experiments for the *Leishmania* work more accurately represent the cell surface, and suggests that the measured interactions could be due, at least in part, to specific lectin-sugar interactions. However, it would be expected that removal of LPG from the parasite surface would enhance access to lectins anchored to the cell, which is not the case in this work, since the LPG-deficient mutant showed

very little interaction with the glycopolymer tip. The difference between the average interaction force on the lectin samples and the parasites could be due to factors such as the rigidity of the surface, as the parasite is much more easily deformed than mica (see Figure 3.16: mica has a similar stiffness to glass), or the fact that the parasites are coated in an array of biomolecules, including proteins and polymers. As in the case of *S. pneumoniae*, these polymers will interact with the tip and, even if they are not involved in full binding interactions, they might attract or repel the AFM tip depending on factors such as steric hindrance and electrostatic interactions (see Section 1.1.1). If there is a repellent contribution, it could lower the bond energy barrier and lead to reduced interaction forces [17].

5.10.2 Effective force per unit area

When comparing the effective force over $1 \mu\text{m}^2$, the differences between the adhesive and non-adhesive combinations are much more marked than when comparing the average forces above the threshold, with the “less adhesive” combinations as defined in the above discussion becoming even more clearly separated from the rest of the parasite-tip combinations. This is because of the differing frequency of the relatively strong binding events in maps across the combinations, with all of the peak forces over 20 pN combining to give an effective binding force of $16 \pm 2 \text{ nN } \mu\text{m}^{-2}$ for the most well attached combination of *L. mexicana* WT procyclics + galactose, as shown in Figure 5.22 and the associated reductions in adhesion are given in Table 5.3.

Table 5.3: Differences between the effective force per μm^2 for selected parasite-tip combinations (for peak adhesive forces > 20 pN and including all parasites).

Sugar	Parasite types	% reduction	<i>p</i> -value
Galactose	<i>L. mex</i> WT pro \rightarrow WT meta	68	0.00034
Glucose	<i>L. mex</i> WT pro \rightarrow WT meta	56	0.00556
Galactose	<i>L. mex</i> WT pro \rightarrow LPG1 ⁻ l/n	82	0.00005
Galactose	<i>L. mex</i> LPG1 ⁻ AB lept \rightarrow LPG1 ⁻ l/n	71	< 0.00001
Galactose	<i>L. mex</i> WT pro \rightarrow <i>L. maj</i> WT nect	81	0.00039

The effective force per μm^2 is a measure of both the bond strength and the availability or population of active binding molecules on the parasite surface, and it

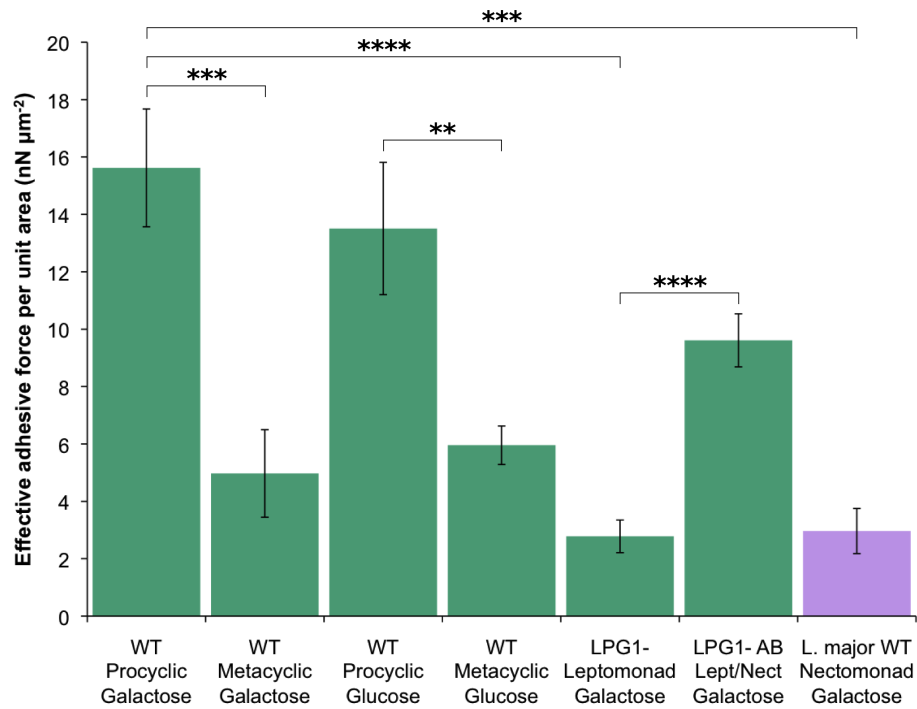


Figure 5.22: Effective areal force evaluated using force-distance curves with a peak adhesive force > 20 pN. Calculated using all parasites (including those with a patterned force distribution). Key significance values are indicated on the graph according to the scale in Table 2.1 on page 60. To separate the species, *Leishmania mexicana* parasite variants are in green, and *Leishmania major* parasites are shown in purple.

appears that this is significantly reduced in the case of the WT metacyclic *L. mexicana* parasites compared to their procyclic counterparts, when probed using either sugar (see Figures 5.22 and 5.23). The similarity of the effective adhesive force per unit area between the WT procyclics and the two sugars adds weight to the argument that specific galactose-mediated binding is not the dominant mechanism of attachment between the tip and the cantilever, or that at the very least it involves a sugar-binding molecule which is insensitive to the chemical and structural differences between galactose and glucose moieties on the glycopolymers (see Figure 3.11). However, there is a clear relationship between the parasite lifecycle stage and the scale of parasite surface forces, since parasites which have undergone metacyclogenesis show a significant reduction in the effective adhesive force per μm^2 . In addition, the reduction in adhesion for the galactose glycopolymer between the LPG1⁻AB and the LPG-deficient mutant is of a similar scale to the loss of adhesion during metacyclogenesis for the WT parasites.

Experiments were also undertaken using a sand fly midgut-adhesive form of WT *Leishmania major*, which has complex, galactose-rich LPG (see Figure 1.12) and is typically carried by *P. papatasi* as a specific vector-parasite combination. Interestingly, the adhesion measured between *L. major* parasites and the galactose glycopolymer was significantly lower than that of the equivalent experiment using *L. mexicana*. This effect was equivalent to the complete loss of LPG from the parasite surface, and the LPG-deficient *L. mexicana* and WT *L. major* had the lowest effective force per micron of all of the combinations tested in this work, further reinforcing the importance of LPG to parasite adhesion.

Figure 5.23 on page 228 considers the case where only peak adhesive forces above increasing minimum force thresholds are able to contribute to the adhesion between the parasite and an array of glycopolymer tips (with the pixel spacing used in the force maps) acting over an area of $1 \mu\text{m}^2$. Overall, the effective force decreases as larger and larger forces are considered, but what is interesting is that, whilst the differences between the three combinations with strongest adhesion remain fairly similar, suggesting that, to an approximation, they share the same pro-

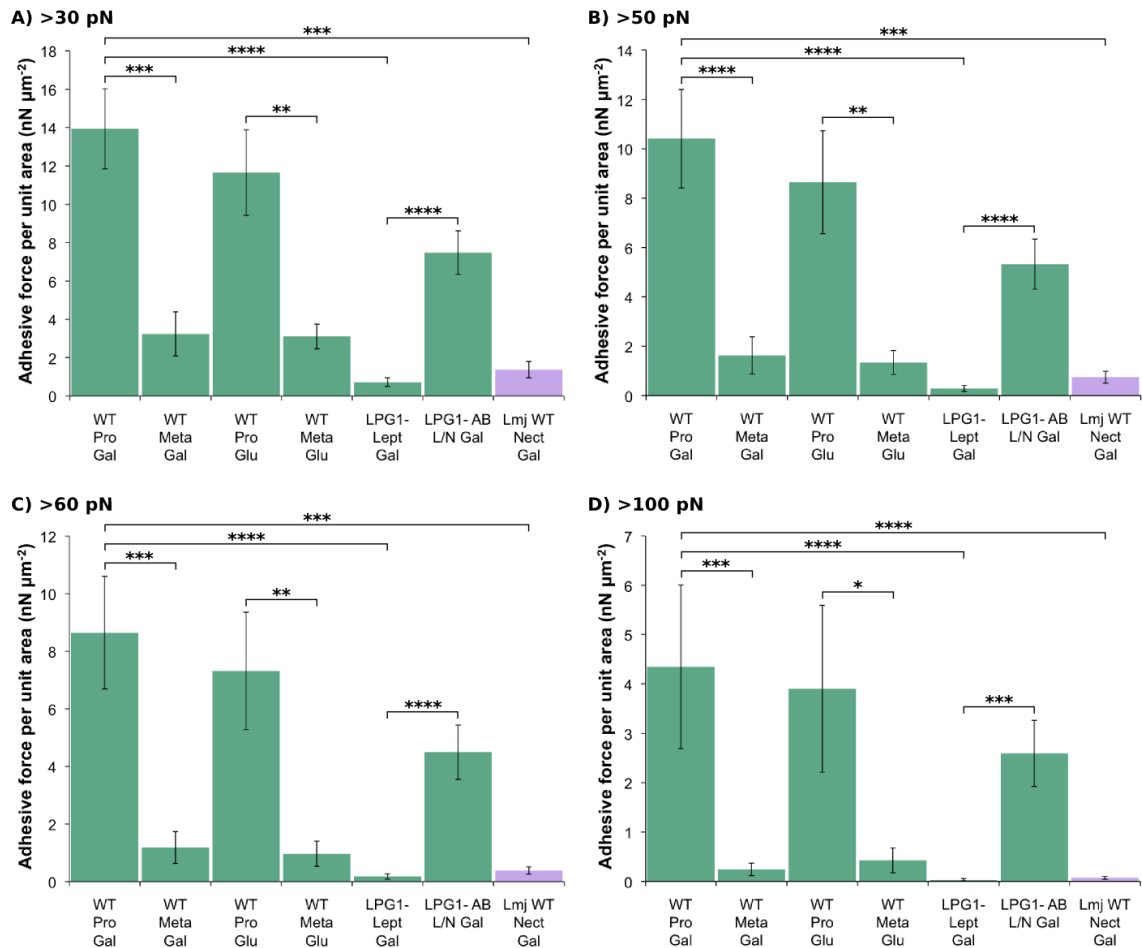


Figure 5.23: Effective areal force evaluated using the mean force calculated for peak adhesive forces above a range of thresholds. Key significance values are indicated on the graph according to the scale in Table 2.1 on page 60. Note that the value is slightly increased for the WT metacyclics and galactose, but due to the smaller error (because of the increased number of cells in the analysis), the decrease in adhesion relative to WT procyclics and galactose is actually of higher significance. To separate the species, *Leishmania mexicana* parasite variants are in green, and *Leishmania major* parasites are shown in purple.

portion of peak adhesive forces within given force ranges, even between using forces above 20 pN (Figure 5.22) and 30 pN (Figure 5.23A), the effective adhesion of the *L. mexicana* WT metacyclics with both glycopolymers drops off substantially, leaving *L. mexicana* WT procyclics + galactose and glucose, and *L. mexicana* LPG1⁻AB leptomonad/nectomonads + galactose as the clear front runners in terms of overall adhesive strength. These three combinations are also the only interactions which are effective when forces solely > 100 pN are used. In fact, for the galactose glycopolymer, the effective areal force for WT procyclics when only interactions > 100 pN are considered is the same as that of the WT metacyclics including all force events > 20 pN (compare Figure 5.23D and Figure 5.22). This clearly demonstrates that, in the strong adhesion combinations, parasites are able to bind to the AFM tip with single events which have a characteristic binding force in the region of those typically associated with lectin-sugar interactions, such as those seen in the control experiments (e.g. the average glycopolymer-lectin interaction strengths shown in the graphs in Figure 5.2), in sufficient numbers that the adhesion purely associated with these high strength interaction forces is still > 2.5 nN μm^{-2} .

The calculations used to evaluate the combined force over 1 μm^2 of parasite surface assume that the distribution of adhesive events across the surface is random and approximately even. This is true of most parasite maps, which had no clear trend in the adhesion distribution, but in some cases the parasites had a line of higher force running along the long axis of the parasite cell (see Section 5.8). Although it is likely that a 1 μm^2 area of the cell would contain this region, if the area was smaller this could become more problematic. The patterned parasites were within groups initially predicted to have less adhesion, and tended to have higher forces than other parasites within the same group. It is therefore not surprising that if these parasites are not included in the analysis, as in Figure 5.24, the values of the effective adhesive force per μm^2 for the WT metacyclics + galactose and the WT procyclics + glucose are lower than in Figure 5.22. This results in a larger decrease in adhesion between the WT *L. mexicana* procyclics and metacyclics + galactose, but a smaller decrease between the same parasite types and a glucose probe. These

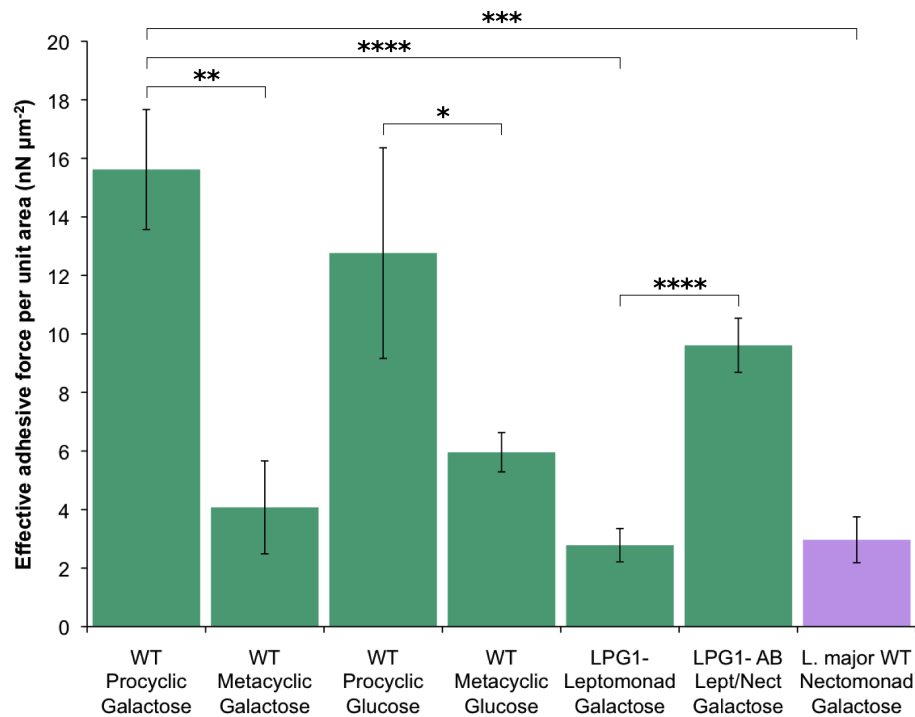


Figure 5.24: Effective areal force evaluated using force-distance curves with a peak adhesive force > 20 pN. Calculated using cells with a random force distribution only (omitting 4 and 5 parasites from the WT metacyclic - galactose and WT procyclic - glucose categories, respectively). Note that the effective force is slightly lower for the WT metacyclics + galactose than in Figure 5.22, but due to the larger error (because of fewer cells in the analysis), the decrease in adhesion relative to WT procyclics and galactose is of less significance, although $p < 0.05$. Key significance values are indicated on the graph according to the scale in Table 2.1 on page 60. To separate the species, *Leishmania mexicana* parasite variants are in green, and *Leishmania major* parasites are shown in purple.

differences are reported in Table 5.4. Because the associated uncertainty is higher due to the reduced sample size within these categories, the level of significance is slightly reduced when the patterned parasites have been excluded, and this is also given in the table.

Table 5.4: Differences between the effective force per μm^2 which are different when parasites with patterned regions of high force are excluded from the analysis (for peak adhesive forces > 20 pN).

Sugar	Parasite types	% reduction	<i>p</i> -value
Galactose	<i>L. mex</i> WT pro \rightarrow WT meta	74	0.00221
Glucose	<i>L. mex</i> WT pro \rightarrow WT meta	53	0.04640

It is therefore reasonable to conclude that the observed patterns in the effective areal adhesive force are present whether patterned parasites are included in the analysis or not, since although the scale of the reduction changes slightly (and the metacyclogenesis-associated reduction for WT *L. mexicana* procyclics + galactose is actually greater than the analysis including patterned parasites - see Table 5.3), the overall trends in the data are still the same.

5.11 Discussion and interpretation of results

In this section, trends in the measured adhesive response of different parasite-glycopolymer tip combinations, determined using both the FMM and threshold-based analysis, will be combined and discussed, and the possible biological causes outlined. The key observations have been divided into a series of statements, and the implication of these results is placed in the context of the current understanding of *Leishmania*-parasite binding mechanisms, which was discussed in 5.1.

Wild type *L. mexicana* procyclics interact strongly with both galactose and glucose glycopolymers.

The FMM results, average adhesion calculated above different thresholds, and the effective adhesive force per μm^2 , all show that WT procyclic *L. mexicana* para-

sites interacted strongly with both types of glycopolymer. The parasites exhibited an effective adhesive force per μm^2 of $15.6 \pm 2.1 \text{ nN } \mu\text{m}^{-2}$ with galactose and $13.5 \pm 2.3 \text{ nN } \mu\text{m}^{-2}$ with glucose (including patterned parasites and using all force events $> 20\text{pN}$). Additionally, for both combinations, the force associated with the G_2 component of the FMM was clearly separated from the G_1 component, although the distribution and width of these two main components varied depending on the glycopolymer type. This suggests that whilst the adhesion of the two combinations is similar, the profile of the peak adhesive force histograms differs for the two interactions, and so the character of the measured forces varies slightly when different sugars are used.

The high interaction of the WT procyclics was expected, since they are among the range of sand fly midgut-adherent lifecycle stages, and therefore are likely to interact strongly with moieties expressed on the sand fly gut epithelial cells, which include various sugar moieties. However, since it has been proposed that binding between *Leishmania* parasites and permissive vectors is due to a lectin on the parasite surface binding to GalNAc on the sand fly, and most lectins are specific for a single type of sugar, it is perhaps somewhat surprising that the parasites showed slightly lower but not significantly different levels of adhesion to the glucose glycopolymer compared to the galactose glycopolymer. From this result alone it is unclear whether the interaction between the glycopolymer and the parasite is due to lectins on the parasite surface, or due to interaction with other parasite surface molecules, such as LPG or other elements of the glycocalyx. The scale of the measured adhesion is comparable, if slightly smaller than that of the glycopolymer-lectin binding experiments (see Table 5.2), so it is quite possible that the individual binding events are due to sugar specific lectins on the parasite surface binding to sugar residues on the glycopolymer-coated AFM tip. As the binding appears to be insensitive to the chemical difference between the two sugars (the mean forces for the different conditions calculated using events > 20 or 30 pN were within the standard error of one another), if lectin-based interactions are the cause, it suggests that both glucose- and galactose-specific lectins are present and accessible on the procyclic parasite surface.

Alternatively, there could be an alternative dominant adhesion factor, potentially involving glycoproteins or proteophosphoglycan in the glycocalyx.

Metacyclogenesis reduces the peak adhesive force between wild type *L. mexicana* parasites and both galactose and glucose glycopolymers.

One of the most striking results was the sharp reduction in adhesion associated with parasites which had undergone metacyclogenesis (68 and 56 % for the effective adhesive force per μm^2 measured in the galactose and glucose experiments, respectively). This agrees with metacyclogenesis-associated changes releasing the parasites from their bond with the parasite midgut epithelium, which must occur as part of successful parasite carriage through any vector, be it specific or permissive. Even if the interaction between the AFM tip and the parasite is mediated by a parasite surface galectin, it follows that the typical metacyclogenesis-associated LPG modifications of increased polymer length and conformational changes would make it more difficult for sites on the parasite surface to be accessed through the LPG coat. This result therefore shows that AFM is a suitable method to detect stage-specific adhesion of *Leishmania* parasites, and gives weight to the adhesion values measured on the procyclic forms, as the level of adhesion dropped off so significantly when metacyclic parasite samples were used. If the AFM tips were measuring non-specific interactions, LPG modifications might not have caused such a large difference in adhesive behaviour (the negligible level of non-specific adhesion associated with the glycopolymer-coated AFM tips was also confirmed by the lectin - glycopolymer control experiments presented in Section 5.2).

Removal of LPG from the surface of sand fly midgut-adherent *L. mexicana* significantly reduces the peak adhesive force between the parasite and galactose-glycopolymers.

Perhaps the most surprising result of the FS experiments was the very low adhesive response of the LPG1^- parasites compared to their wild type equivalent (*LPG1* is in-

volved in biosynthesis of the core oligosaccharide LPG domain, so in the LPG1⁻ mutants, the LPG is effectively cleaved at the level of the parasite surface [256]), with an even larger reduction in the effective adhesive force over 1 μm^2 than the metacyclics (82 % compared to 68 %). This would not be expected if parasite-galactose binding was mediated by a factor excluding LPG, since its removal should facilitate easier access to these sites. In this case, the size of the adhesive force would be expected to remain constant due to the energetic barrier associated with breaking specific bonds, but the effective areal force would be expected to increase (due to more binding sites across the surface becoming available to bind with the tip, reducing the proportion of curves containing no binding interactions). Therefore, it can be concluded that the adhesion events measured in this work are LPG-dependent, although whether LPG is the molecule actually binding to the glycopolymers or whether it is required as part of a secondary binding mechanism is unclear. Whilst some work confirms the ability of LPG1⁻ mutants (*L. major*) to bind to GalNAc [142], one recent study suggested that in *L. mexicana*, LPG1⁻ parasites did not bind as effectively to sand fly midguts as their wild type counterparts [144], suggesting that LPG might indeed have a role even in binding to permissive sand fly vectors.

Patterned areas of high force are present on a number of parasites from two of the seven different parasite-glycopolymer combinations.

The reason for the appearance of a stripe of higher force adhesion interactions along the central, highest point of parasites within two out of the seven tip-parasite combinations is unclear, since there were no obvious topographical details revealed by the force maps on the patterned parasites (although these maps are rather low resolution compared to standard AFM images). The patterned force was typically conserved between the larger, zoomed out map, and the close-up map of the parasite body, although in the case of one patterned metacyclic parasite, which was mapped for a third time, the clear band of high force mostly disappeared (see Figure 5.18). This suggests that there might be a time frame associated with high force areas and therefore that they could be related to the reorganization of molecules on the

parasite surface, or the patterns could either form or dissipate in response to the parasite sensing the AFM tip.

The patterned metacyclic parasites were towards the higher-force end of the parasite population, and, as in the case of the parasite in Figure 5.18, patterned parasites tended to be wider than expected for the morphological type (see Figure 1.9). This suggests that they could potentially be parasite contaminants: other morphological types in the metacyclic-rich parasite sample. A small, adherent population in a generally non-adhesive population in one midgut binding assay was attributed to contaminant parasites which were determined (by visual inspection) to have morphological features different to the rest of the sample [135]. It is also possible that these higher-force stripes were also present on other parasites within the samples, but that the orientation of the parasite on the sample meant that this region was not within the area accessible by the AFM tip.

Regardless of combination, patterned parasites tended to be more adhesive than non-patterned parasites, with the effective areal force for both categories reducing when patterned parasites were excluded from the analysis (see Figures 5.22 and 5.24). This raises the question of whether these parasites, be they part of a sub-population or whether the patternation occurs due to an environmental response, should be included in the analysis. If they are not included, the strength of interaction (gauged using the effective areal force measure) between the WT procyclics and galactose is stronger than that with glucose, although this difference is not significant. Additionally, excluding patterned parasites from the analysis reduces the measured interaction between WT metacyclic parasites and galactose. However, because the general trends observed in the data remain the same, inclusion of these parasites in the analysis does not strongly impact the conclusions of this work.

Sand fly midgut-adherent *L. major* parasites show very low levels of adhesion to galactose glycopolymers compared to the *L. mexicana* equivalent.

This is not surprising given the more complex nature of the *L. major* LPG, which has developed to be compatible with its specific vector. The bulkier sidechains might

make it more difficult to reach adhesive moieties or lectins within the LPG coat, due to steric hindrance. Also, because the sidechains are predominantly made of galactose residues, like the galactose glycopolymer, the two similar polymers would not necessarily be expected to show high affinity, especially as both are hydrophilic molecules, which tend to maximise their contact with water.

The *L. mexicana* LPG has smaller, less frequent sidechains containing glucose residues, and so when probed with the galactose glycopolymer, the AFM tip does not encounter a surface which appears (to an approximation) similar to its own. This, combined with the smaller bulk of the LPG, could allow for more interpenetration of the glycopolymers on the tip and the parasite glycocalyx compared to *L. major*, and result in the higher adhesion values measured in this work.

Extensions to the work

Whilst the observations described above are informative about the nature of the interaction, the questions raised about the nature of the parasite-glycopolymer interaction could be answered by further experiments. Firstly, the addition of more glycopolymer types (e.g. mannose or arabinose) into the study would allow determination of whether or not there is any difference between other sugars and the galactose and glucose glycopolymers, which elicited a similar response from the WT *L. mexicana* procyclics and metacyclics. Further to this, it would be interesting to observe whether the reduction in adhesion associated with the *L. mexicana* LPG1⁻ mutants is mirrored in the same mutant of *L. major*, to establish whether any adhesion would be recovered when the bulky *L. major* LPG is removed from the parasite surface. This would be particularly interesting since LPG-deficient *L. major* has persisted in permissive sand flies (see Section 5.1). One extra experiment which might also be useful in terms of understanding the weak interaction between the galactose glycopolymer and the *L. major* surface would be to undertake further controls using glycopolymer-coated substrates as the sample. This would establish whether the glycopolymers interact with themselves or whether, as suspected, the interaction between like glycopolymers would be weak.

5.12 Summary

Overall, the combined results from the FMM and threshold-based mean force analysis revealed several key findings, which were discussed in detail in the previous section. These findings are summarized in the following statements:

1. Wild type *L. mexicana* procyclics interact strongly with both galactose and glucose glycopolymers.
2. Metacyclogenesis reduces the peak adhesive force between wild type *L. mexicana* parasites and both galactose and glucose glycopolymers.
3. Removal of LPG from the surface of sand fly midgut-adherent *L. mexicana* significantly reduces the peak adhesive force between the parasite and galactose-glycopolymers.
4. Patterned areas of high force are present on a number of parasites from two of the seven different parasite-glycopolymer combinations.
5. Sand fly midgut-adherent *L. major* parasites show very low levels of adhesion to galactose glycopolymers compared to the *L. mexicana* equivalent.

Combined, these features point to LPG playing a key role in the adhesion measured in this work, although it is unclear whether the strong adhesion measured between the WT *L. mexicana* procyclics and the glycopolymers is due to binding between the glycopolymer and LPG, or whether LPG has a role in assisting with binding to another molecule expressed on the parasite surface. Whilst the results do not directly support the prediction that a lectin on the parasite surface is responsible for binding to GalNAc residues on the sand fly midgut epithelium, they do show that *L. mexicana* is capable of interacting on a biologically-relevant scale with galactose and glucose-rich polymeric surfaces, especially when the effective areal binding force is considered, and that this adhesion is lost following metacyclogenesis. This therefore confirms that sugars expressed on the sand fly midgut are involved in some form of parasite lifecycle stage-specific binding, and could play an important role in the transmission of *Leishmania* parasites via permissive vector species.

Chapter 6

Conclusions

This work used force spectroscopy with chemically modified tips to investigate both non-specific and specific binding interactions of two different human pathogens. Whilst AFM is now part of the toolkit for examining adhesive interactions and mechanical properties of different bacteria and other cells, it has not previously been used to explore the adhesive properties of *S. pneumoniae* or *Leishmania* parasites. Existing methodologies were tailored to the two specific organisms and two different cell immobilization methods were used: mechanical trapping for the spheroidal pneumococcus, and physisorption on a positively charged substrate for the *Leishmania* parasites. For the *Leishmania* work, new glycopolymer synthesis routes and applications were developed through a collaboration with Professor Cameron (of Durham University at that time), tested using a lectin binding assay, and applied to the investigation of the methods used by *Leishmania* parasites to bind to the midguts of permissive sand fly vectors. The outcomes of this work are presented below.

The results of Chapter 4 established the capsule as a limiting factor in access to binding sites, modifying the availability of different proteins on the bacterial surface to enable colonization of the human host, and suggested that below the capsular surface there are molecular sites capable of hydrophobic binding, which is consistent with the known role of non-specific interactions in the initial attachment of

pneumococci to mucosal cells. The work also provided further evidence that capsular reduction is a key process in this interaction, allowing hydrophobic moieties on the bacterium to bind to the extracellular matrix of mucosal cells, highlighting the importance of the pneumococcal capsule in pathogenesis.

The measured adhesive interactions were all fairly weak, being mostly < 100 pN in size, and were distributed randomly across the cell, suggesting that there is no clear adhesive polarity or preferred orientation of the bacterium in initial attachment to host cells. This is not unwarranted given the bacterium's spherical shape, and suggests that a combination of similar, weak interactions across the cell surface add together to bring cells close enough to enable specific protein-protein binding to come into effect and stabilize the bacterium on the cell surface.

The negatively charged, hydrophilic tip was less likely to show a bimodal force distribution, and this effect was greater for the capsulated bacteria, suggesting that the combination of steric hindrance and electrostatic repulsion plays a key role in reducing adhesive interactions between the bacteria and other surfaces.

Overall, this work predicts a role for additive hydrophobic adhesive interactions in the establishment of infection through binding to mucosal cells, and further elucidates how the capsule helps pneumococcus evade the immune system through steric repulsion and electrostatic screening of specific binding sites below the capsular surface. This has implications in terms of colonization of the respiratory tract and invasive pneumococcal disease.

The combined results from the FMM and threshold-based mean force analysis in Chapter 5 revealed several key findings, which are summarized in the following statements:

1. Wild type *L. mexicana* procyclics interact strongly with both galactose and glucose glycopolymers.
2. Metacyclogenesis reduces the peak adhesive force between wild type *L. mexicana* parasites and both galactose and glucose glycopolymers.

3. Removal of LPG from the surface of sand fly midgut-adherent *L. mexicana* significantly reduces the peak adhesive force between the parasite and galactose-glycopolymers.
4. Patterned areas of high force are present on a number of parasites from two of the seven different parasite-glycopolymer combinations.
5. Sand fly midgut-adherent *L. major* parasites show very low levels of adhesion to galactose glycopolymers compared to the *L. mexicana* equivalent.

Combined, these features point to LPG playing a key role in the adhesion measured in this work, although it is unclear whether the strong adhesion measured between the WT *L. mexicana* procyclics and the glycopolymers is due to binding between the glycopolymer and LPG, or whether LPG assists with binding to another molecule expressed on the parasite surface. Whilst the results do not directly support the prediction that a specific lectin on the parasite surface is responsible for binding to GalNAc residues on the sand fly midgut epithelium, they do show that *L. mexicana* is capable of interacting on a biologically-relevant scale with galactose and glucose-rich polymeric surfaces, especially when the effective areal binding force is considered, and that this adhesion is lost following metacyclogenesis. This therefore confirms that sugars expressed on the sand fly midgut are involved in some form of parasite lifecycle stage-specific binding, and could play an important role in the transmission of *Leishmania* parasites via permissive vector species.

As a whole, this work reveals the role of the pneumococcal capsule in obscuring binding sites closer to the cell wall, and suggests that hydrophobic interactions could be involved in the early establishment or strengthening of other specific binding events which attach the bacterium to mucosal cells. It also shows that adhesion of *Leishmania mexicana* to glucose and galactose glycopolymers is stage specific, with strong adhesion for procyclic forms and weak adhesion for metacyclic forms, and suggests a role for LPG in the binding between parasites and glycopolymers. These adhesive properties are important in terms of understanding disease pathogenesis in both organisms: host colonization by *S. pneumoniae*, which is a prerequisite for inva-

sive bacterial infection, and transmission of leishmanial disease between mammalian hosts. In summary, AFM was used successfully to probe the adhesive properties of two independent organisms, both of which have extremely diverse surfaces, making them challenging targets for therapeutic drugs and vaccines (the capsular variation in *S. pneumoniae* and the inter-species LPG variation in *Leishmania* parasites). An AFM-based toolkit, using probes which have been predicted to be bound by the pathogen through other, more traditional biological assays, could aid in the discovery of adhesion and infection-related features which are common across the diverse genera. The combination of conventional studies of infection and transmission with quantitative AFM force data could therefore prove an effective way to identify and rank the importance of different adhesion targets, assessing whether they are species-specific or could be effective across a whole genus. This information could then be used to direct further research towards drugs and other disease control measures.

Appendix A

Force curve contact point calculation code

The code below was provided by Ross Carter to automate the process of identifying the non-indented sample surface height. The code was saved in the 'UserCalculated.ipf' Igor procedure file, making it accessible as an option when drawing force maps within the Asylum Research AFM software which runs in Igor Pro.

```
Function FMapCalcContactPoint2(Data,DataB,ParmWave)
    Wave Data          //Raw (z piezo displacement)
    Wave/Z DataB       //Deflection
    Wave/Z ParmWave    //not used

    variable surfindex = FindSurfaceIndex(DataB,Data,10)

    return(-Data[surfindex])

End

Function/S FMapCalcContactPoint2Info()
    String Output = "DataType:Raw;Section:Ext;DataTypeB:Defl;ParmWave:None;CalcType:Height;"
    return(output)

End
```

Appendix B

Chemical structures of molecules required for ATRP initiation

This appendix contains some chemical structures which are relevant to both the original and improved PMAA brush synthesis routes. Figure B.1 shows the key reagent molecules required to coat the silicon surfaces with an ATRP initiator: allyl-11-undecane bromoisobutyrate and triethylamine for the original synthesis method, and (3-aminopropyl)triethoxysilane (APTES) followed by α -bromoisobutyryl bromide (α -BiBB) and triethylamine for the revised method.

The main differences between the two initiator molecules is shown in Figure B.2, where they are illustrated in the same configuration and attached to a silicon substrate (shown in green). The APTES-based initiator is shorter, having only three CH₂ units compared to eleven for the original initiator. The oxygen in the original initiator is also substituted with NH. The initiator should fully cover the silicon substrate, meaning that the end group is most important as this will be exposed. This end group is unchanged between the two molecules.

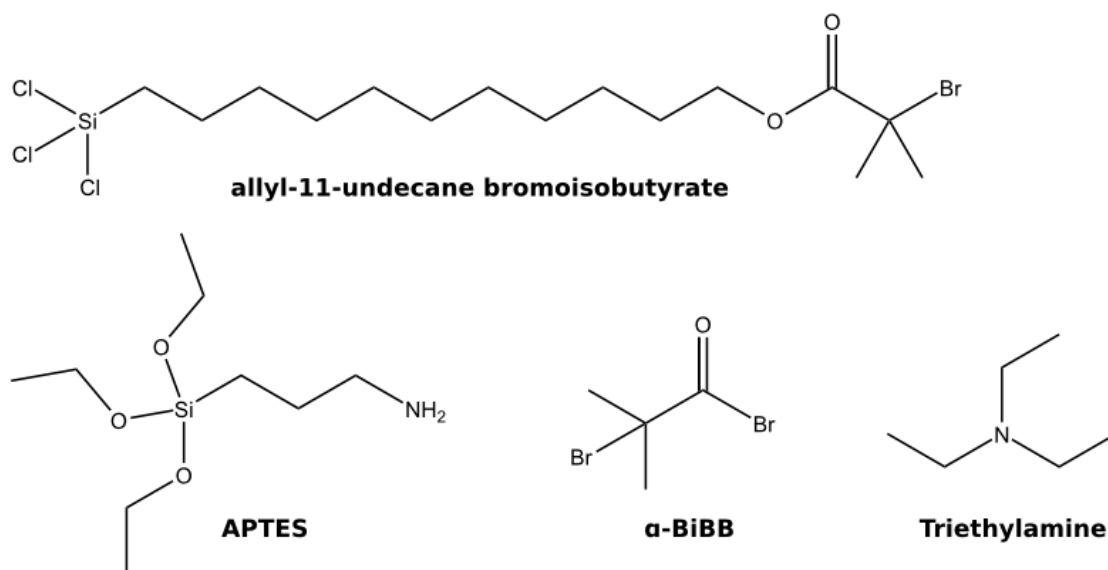


Figure B.1: Chemical structures of reagents required to initiate the silicon wafers and AFM cantilevers ready for ATRP.

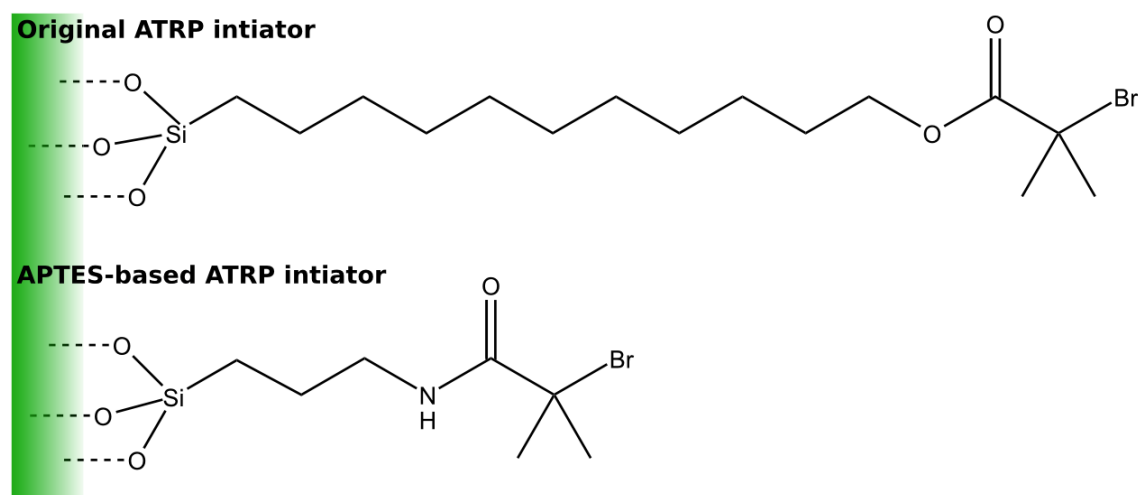


Figure B.2: Chemical structures of allyl-11-undecane bromoisobutyrate and the initiator molecule (formed over two reactions) used in the revised synthesis method. The molecules are illustrated attached to a silicon substrate (in green).

Appendix C

P-values for the *Leishmania* parasite comparisons

This appendix contains the p -values for the different combinations of parasite experiments. One-way ANOVA tests showed that all compared variables had significant variation between groups, and these tables elucidate this further, containing p -values for each combination, as evaluated using a two-tailed Mann-Whitney test with significance level of 0.05. The results are colour-coded by their significance, and the variable compared in each table is written at the top left of the table in blue capital letters.

MEDIAN FORCE:										
<i>P. TwoTail</i>										
	<i>L. mex</i> WT pro - Gal	<i>L. mex</i> WT meta - Gal	<i>L. mex</i> WT pro - Glu	<i>L. mex</i> WT meta - Glu	<i>L. mex</i> LPG1 ⁻ lept - Gal	<i>L. mex</i> LPG1 ⁻ lept - Glu	<i>L. mex</i> LPG1 ⁻ AB lept/nect - Gal	<i>L. mex</i> LPG1 ⁻ AB lept/nect - Glu	<i>L. major</i> WT nect - Gal	<i>L. major</i> WT nect - Glu
<i>L. mex</i> WT pro - Gal	0.01210	0.03488	0.02202	0.0018	0.00002	0.00026	0.00002	0.00022	0.00003	0.00022
<i>L. mex</i> WT meta - Gal	0.01210	0.03488	0.02202	0.0018	0.00002	0.00026	0.00002	0.00022	0.00003	0.00022
<i>L. mex</i> WT pro - Glu	0.34341	0.03488	0.02202	0.0018	0.00002	0.00026	0.00002	0.00022	0.00003	0.00022
<i>L. mex</i> WT meta - Glu	0.00144	0.00000	0.02202	0.00144	0.02004	0.00050	0.020311	0.00050	0.00051	0.00050
<i>L. mex</i> LPG1 ⁻ lept - Gal	0.00002	0.00000	0.00000	0.02004	0.00050	0.00050	0.00050	0.00050	0.00051	0.00050
<i>L. mex</i> LPG1 ⁻ AB lept/nect - Gal	0.08537	0.00699	0.00699	0.03998	0.72544	0.72544	0.72544	0.72544	0.72544	0.72544
<i>L. major</i> WT nect - Gal	0.00097	0.00008	0.00008	0.03998	0.72544	0.72544	0.72544	0.72544	0.72544	0.72544
<i>F₁</i>										
<i>P. TwoTail</i>										
<i>L. mex</i> WT pro - Gal	0.59291	0.02885	0.13055	0.08020	0.00040	0.00276	0.00040	0.00010	0.00077	0.00040
<i>L. mex</i> WT meta - Gal	0.59291	0.02885	0.13055	0.08020	0.00040	0.00276	0.00040	0.00010	0.00077	0.00040
<i>L. mex</i> WT pro - Glu	0.02885	0.13055	0.60053	0.09472	0.01836	0.00235	0.01836	0.00235	0.01113	0.01836
<i>L. mex</i> WT meta - Glu	0.08020	0.09472	0.60053	0.03103	0.03103	0.12642	0.03103	0.12642	0.05031	0.03103
<i>L. mex</i> LPG1 ⁻ lept - Gal	0.00040	0.00276	0.01836	0.03103	0.77621	0.77621	0.77621	0.77621	0.77621	0.77621
<i>L. mex</i> LPG1 ⁻ AB lept/nect - Gal	0.00010	0.00647	0.00235	0.12642	0.55163	0.55163	0.55163	0.55163	0.55163	0.55163
<i>L. major</i> WT nect - Gal	0.00077	0.01113	0.01113	0.05031	1.00000	1.00000	1.00000	1.00000	1.00000	1.00000
<i>F₂</i>										
<i>P. TwoTail</i>										
<i>L. mex</i> WT pro - Gal	0.12301	0.13055	0.73806	0.0306	0.00002	0.00026	0.00002	0.00005	0.00300	0.00002
<i>L. mex</i> WT meta - Gal	0.12301	0.13055	0.73806	0.0306	0.00002	0.00026	0.00002	0.00005	0.00300	0.00002
<i>L. mex</i> WT pro - Glu	0.13055	0.73806	0.05349	0.10110	0.00001	0.00507	0.00001	0.00507	0.00921	0.00001
<i>L. mex</i> WT meta - Glu	0.00306	0.10110	0.05349	0.13879	0.13879	0.80444	0.13879	0.80444	0.94972	0.00306
<i>L. mex</i> LPG1 ⁻ lept - Gal	0.00002	0.00026	0.00001	0.13879	0.00107	0.00107	0.00107	0.00107	0.14466	0.00002
<i>L. mex</i> LPG1 ⁻ AB lept/nect - Gal	0.00005	0.13055	0.00507	0.80444	0.00107	0.00107	0.00107	0.00107	0.28181	0.00005
<i>L. major</i> WT nect - Gal	0.00300	0.07268	0.00921	0.94972	0.14466	0.14466	0.14466	0.14466	0.28181	0.00300

0.01 < P ≤ 0.05
 0.001 < p ≤ 0.01
 0.0001 < p ≤ 0.001
 p ≤ 0.0001

AVERAGE FORCE:										
<i>P. TwoTail</i>										
	<i>L. mex</i> WT pro - Gal	<i>L. mex</i> WT meta - Gal	<i>L. mex</i> WT pro - Glu	<i>L. mex</i> WT meta - Glu	<i>L. mex</i> LPG1 ⁻ lept - Gal	<i>L. mex</i> LPG1 ⁻ lept - Glu	<i>L. mex</i> LPG1 ⁻ AB lept/nect - Gal	<i>L. mex</i> LPG1 ⁻ AB lept/nect - Glu	<i>L. mex</i> LPG1 ⁻ AB lept/nect - Gal	<i>L. mex</i> LPG1 ⁻ AB lept/nect - Glu
<i>L. mex</i> WT pro - Gal	0.00412	0.00412	0.11293	0.00012	0.00000	0.00000	0.00000	0.00000	0.00235	0.00003
<i>L. mex</i> WT meta - Gal	0.00412	0.00412	0.11293	0.00012	0.00000	0.00000	0.00000	0.00000	0.00235	0.00003
<i>L. mex</i> WT pro - Glu	0.02552	0.02552	0.02552	0.02202	0.00008	0.00008	0.00008	0.00008	0.03869	0.00003
<i>L. mex</i> WT meta - Glu	0.00012	0.02202	0.00008	0.00008	0.00000	0.00000	0.00424	0.00000	0.00256	0.05031
<i>L. mex</i> LPG1 ⁻ lept - Gal	0.00000	0.00001	0.00000	0.00424	0.00000	0.00000	0.00000	0.00000	0.00000	0.76643
<i>L. mex</i> LPG1 ⁻ AB lept/nect - Gal	0.00235	0.00210	0.03869	0.00256	0.00000	0.00000	0.00256	0.00000	0.00000	0.00005
<i>L. major</i> WT nect - Gal	0.00003	0.00210	0.00003	0.05031	0.00000	0.00000	0.76643	0.00000	0.00005	0.00005
AVERAGEIF FORCE > 20 pN:										
<i>P. TwoTail</i>										
	<i>L. mex</i> WT pro - Gal	<i>L. mex</i> WT meta - Gal	<i>L. mex</i> WT pro - Glu	<i>L. mex</i> WT meta - Glu	<i>L. mex</i> LPG1 ⁻ lept - Gal	<i>L. mex</i> LPG1 ⁻ lept - Glu	<i>L. mex</i> LPG1 ⁻ AB lept/nect - Gal	<i>L. mex</i> LPG1 ⁻ AB lept/nect - Glu	<i>L. mex</i> LPG1 ⁻ AB lept/nect - Gal	<i>L. mex</i> LPG1 ⁻ AB lept/nect - Glu
<i>L. mex</i> WT pro - Gal	0.00196	0.00196	0.54460	0.00005	0.00000	0.00000	0.00000	0.00000	0.31073	0.00005
<i>L. mex</i> WT meta - Gal	0.00196	0.00196	0.54460	0.00005	0.00000	0.00000	0.00000	0.00000	0.31073	0.00005
<i>L. mex</i> WT pro - Glu	0.54460	0.01778	0.01778	0.11275	0.00055	0.00055	0.00055	0.00055	0.68663	0.04347
<i>L. mex</i> WT meta - Glu	0.00005	0.11275	0.00077	0.00077	0.00000	0.00000	0.01247	0.00000	0.00891	0.43628
<i>L. mex</i> LPG1 ⁻ lept - Gal	0.00000	0.00055	0.00001	0.01247	0.00000	0.00000	0.00000	0.00000	0.00011	0.09518
<i>L. mex</i> LPG1 ⁻ AB lept/nect - Gal	0.31073	0.10101	0.68663	0.00891	0.00011	0.00011	0.00011	0.00011	0.00011	0.00335
<i>L. major</i> WT nect - Gal	0.00005	0.04347	0.00039	0.43628	0.00011	0.00011	0.09518	0.00011	0.00335	0.00335
AVERAGEIF FORCE > 30 pN:										
<i>P. TwoTail</i>										
	<i>L. mex</i> WT pro - Gal	<i>L. mex</i> WT meta - Gal	<i>L. mex</i> WT pro - Glu	<i>L. mex</i> WT meta - Glu	<i>L. mex</i> LPG1 ⁻ lept - Gal	<i>L. mex</i> LPG1 ⁻ lept - Glu	<i>L. mex</i> LPG1 ⁻ AB lept/nect - Gal	<i>L. mex</i> LPG1 ⁻ AB lept/nect - Glu	<i>L. mex</i> LPG1 ⁻ AB lept/nect - Gal	<i>L. mex</i> LPG1 ⁻ AB lept/nect - Glu
<i>L. mex</i> WT pro - Gal	0.00619	0.00619	0.86950	0.00319	0.00000	0.00000	0.00000	0.00000	0.83001	0.00038
<i>L. mex</i> WT meta - Gal	0.00619	0.00619	0.86950	0.00319	0.00000	0.00000	0.00000	0.00000	0.83001	0.00038
<i>L. mex</i> WT pro - Glu	0.86950	0.02552	0.02552	0.44697	0.00022	0.00022	0.00022	0.00022	0.57877	0.90483
<i>L. mex</i> WT meta - Glu	0.00319	0.44697	0.01113	0.01113	0.00000	0.00000	0.00000	0.00000	0.00193	0.06047
<i>L. mex</i> LPG1 ⁻ lept - Gal	0.00000	0.00000	0.00022	0.29473	0.00000	0.00000	0.00000	0.00000	0.00001	0.25808
<i>L. mex</i> LPG1 ⁻ AB lept/nect - Gal	0.83001	0.01778	0.57877	0.00193	0.00001	0.00001	0.00001	0.00001	0.00001	0.01381
<i>L. major</i> WT nect - Gal	0.00038	0.90483	0.06047	0.25808	0.00001	0.00001	0.00566	0.00001	0.01381	0.01381

0.01 < P ≤ 0.05
 0.001 < p ≤ 0.01
 0.0001 < p ≤ 0.001
 p ≤ 0.0001

Average Force per μm^2 (>20 pN)											
<i>P. TwoTail</i>											
	<i>L. mex</i> WT pro - Gal	<i>L. mex</i> WT meta - Gal	<i>L. mex</i> WT pro - Glu	<i>L. mex</i> WT meta - Glu	<i>L. mex</i> LPG1 ⁻ lept - Gal	<i>L. mex</i> LPG1 ⁻ lept - Gal	<i>L. mex</i> LPG1 ⁻ lept - Gal	<i>L. mex</i> LPG1 ⁻ lept - Gal	<i>L. mex</i> LPG1 ⁻ lept - Gal	<i>L. mex</i> LPG1 ⁻ lept - Gal	<i>L. mex</i> LPG1 ⁻ lept - Gal
<i>L. mex</i> WT pro - Gal	0.00034	0.00034	0.20354	0.00256	0.00005	0.00005	0.00005	0.00005	0.00005	0.00005	0.00005
<i>L. mex</i> WT meta - Gal	0.00034	0.00034	0.00518	0.66072	0.42617	0.42617	0.42617	0.42617	0.42617	0.42617	0.42617
<i>L. mex</i> WT pro - Glu	0.20354	0.00518	0.00556	0.00424	0.00011	0.00011	0.00011	0.00011	0.00011	0.00011	0.00011
<i>L. mex</i> WT meta - Glu	0.00256	0.66072	0.00556	0.00424	0.00011	0.00011	0.00011	0.00011	0.00011	0.00011	0.00011
<i>L. mex</i> LPG1 ⁻ lept - Gal	0.00005	0.42617	0.00011	0.00424	0.00000	0.00000	0.00000	0.00000	0.00000	0.00000	0.00000
<i>L. mex</i> LPG1 ⁻ AB lept/nlect - Gal	0.00860	0.04216	0.09085	0.00891	0.00000	0.00000	0.00000	0.00000	0.00000	0.00000	0.00000
<i>L. major</i> WT nect - Gal	0.00039	0.71970	0.00077	0.03147	0.76643	0.76643	0.76643	0.76643	0.76643	0.76643	0.76643
Average Force per μm^2 (>30 pN)											
<i>P. TwoTail</i>											
	<i>L. mex</i> WT pro - Gal	<i>L. mex</i> WT meta - Gal	<i>L. mex</i> WT pro - Glu	<i>L. mex</i> WT meta - Glu	<i>L. mex</i> LPG1 ⁻ lept - Gal	<i>L. mex</i> LPG1 ⁻ lept - Gal	<i>L. mex</i> LPG1 ⁻ lept - Gal	<i>L. mex</i> LPG1 ⁻ lept - Gal	<i>L. mex</i> LPG1 ⁻ lept - Gal	<i>L. mex</i> LPG1 ⁻ lept - Gal	<i>L. mex</i> LPG1 ⁻ lept - Gal
<i>L. mex</i> WT pro - Gal	0.00034	0.00034	0.26421	0.00144	0.00001	0.00001	0.00001	0.00001	0.00001	0.00001	0.00001
<i>L. mex</i> WT meta - Gal	0.00034	0.00034	0.00196	0.60378	0.07200	0.07200	0.07200	0.07200	0.07200	0.07200	0.07200
<i>L. mex</i> WT pro - Glu	0.26421	0.00196	0.00196	0.00256	0.00002	0.00002	0.00002	0.00002	0.00002	0.00002	0.00002
<i>L. mex</i> WT meta - Glu	0.00144	0.60378	0.00256	0.00116	0.00116	0.00116	0.00116	0.00116	0.00116	0.00116	0.00116
<i>L. mex</i> LPG1 ⁻ lept - Gal	0.00001	0.07200	0.00002	0.00116	0.00000	0.00000	0.00000	0.00000	0.00000	0.00000	0.00000
<i>L. mex</i> LPG1 ⁻ AB lept/nlect - Gal	0.00860	0.01471	0.09085	0.01113	0.00000	0.00000	0.00000	0.00000	0.00000	0.00000	0.00000
<i>L. major</i> WT nect - Gal	0.00012	0.27751	0.00027	0.03147	0.15194	0.15194	0.15194	0.15194	0.15194	0.15194	0.15194
Average Force per μm^2 (>50 pN)											
<i>P. TwoTail</i>											
	<i>L. mex</i> WT pro - Gal	<i>L. mex</i> WT meta - Gal	<i>L. mex</i> WT pro - Glu	<i>L. mex</i> WT meta - Glu	<i>L. mex</i> LPG1 ⁻ lept - Gal	<i>L. mex</i> LPG1 ⁻ lept - Gal	<i>L. mex</i> LPG1 ⁻ lept - Gal	<i>L. mex</i> LPG1 ⁻ lept - Gal	<i>L. mex</i> LPG1 ⁻ lept - Gal	<i>L. mex</i> LPG1 ⁻ lept - Gal	<i>L. mex</i> LPG1 ⁻ lept - Gal
<i>L. mex</i> WT pro - Gal	0.00008	0.00008	0.36216	0.00055	0.00000	0.00000	0.00000	0.00000	0.00000	0.00000	0.00000
<i>L. mex</i> WT meta - Gal	0.00008	0.00008	0.00151	0.54896	0.09311	0.09311	0.09311	0.09311	0.09311	0.09311	0.09311
<i>L. mex</i> WT pro - Glu	0.36216	0.00151	0.00151	0.00335	0.00004	0.00004	0.00004	0.00004	0.00004	0.00004	0.00004
<i>L. mex</i> WT meta - Glu	0.00055	0.54896	0.00335	0.02404	0.02404	0.02404	0.02404	0.02404	0.02404	0.02404	0.02404
<i>L. mex</i> LPG1 ⁻ lept - Gal	0.00000	0.09311	0.00004	0.02404	0.00000	0.00000	0.00000	0.00000	0.00000	0.00000	0.00000
<i>L. mex</i> LPG1 ⁻ AB lept/nlect - Gal	0.02948	0.00412	0.24278	0.00256	0.00000	0.00000	0.00000	0.00000	0.00000	0.00000	0.00000
<i>L. major</i> WT nect - Gal	0.00027	0.96824	0.00077	0.54570	0.08930	0.08930	0.08930	0.08930	0.08930	0.08930	0.08930
Average Force per μm^2 (>60 pN)											
<i>P. TwoTail</i>											
	<i>L. mex</i> WT pro - Gal	<i>L. mex</i> WT meta - Gal	<i>L. mex</i> WT pro - Glu	<i>L. mex</i> WT meta - Glu	<i>L. mex</i> LPG1 ⁻ lept - Gal	<i>L. mex</i> LPG1 ⁻ lept - Gal	<i>L. mex</i> LPG1 ⁻ lept - Gal	<i>L. mex</i> LPG1 ⁻ lept - Gal	<i>L. mex</i> LPG1 ⁻ lept - Gal	<i>L. mex</i> LPG1 ⁻ lept - Gal	<i>L. mex</i> LPG1 ⁻ lept - Gal
<i>L. mex</i> WT pro - Gal	0.00012	0.00012	0.61387	0.00018	0.00000	0.00000	0.00000	0.00000	0.00000	0.00000	0.00000
<i>L. mex</i> WT meta - Gal	0.00012	0.00012	0.00254	0.86123	0.06074	0.06074	0.06074	0.06074	0.06074	0.06074	0.06074
<i>L. mex</i> WT pro - Glu	0.61387	0.00254	0.00433	0.00433	0.00004	0.00004	0.00004	0.00004	0.00004	0.00004	0.00004
<i>L. mex</i> WT meta - Glu	0.00018	0.86123	0.00433	0.04602	0.04602	0.04602	0.04602	0.04602	0.04602	0.04602	0.04602
<i>L. mex</i> LPG1 ⁻ lept - Gal	0.00000	0.06074	0.00004	0.04602	0.00001	0.00001	0.00001	0.00001	0.00001	0.00001	0.00001
<i>L. mex</i> LPG1 ⁻ AB lept/nlect - Gal	0.05681	0.00196	0.41841	0.00193	0.00001	0.00001	0.00001	0.00001	0.00001	0.00001	0.00001
<i>L. major</i> WT nect - Gal	0.00012	0.62025	0.00077	0.75043	0.15095	0.15095	0.15095	0.15095	0.15095	0.15095	0.15095
Average Force per μm^2 (>100 pN)											
<i>P. TwoTail</i>											
	<i>L. mex</i> WT pro - Gal	<i>L. mex</i> WT meta - Gal	<i>L. mex</i> WT pro - Glu	<i>L. mex</i> WT meta - Glu	<i>L. mex</i> LPG1 ⁻ lept - Gal	<i>L. mex</i> LPG1 ⁻ lept - Gal	<i>L. mex</i> LPG1 ⁻ lept - Gal	<i>L. mex</i> LPG1 ⁻ lept - Gal	<i>L. mex</i> LPG1 ⁻ lept - Gal	<i>L. mex</i> LPG1 ⁻ lept - Gal	<i>L. mex</i> LPG1 ⁻ lept - Gal
<i>L. mex</i> WT pro - Gal	0.00034	0.00034	0.64985	0.00185	0.00001	0.00001	0.00001	0.00001	0.00001	0.00001	0.00001
<i>L. mex</i> WT meta - Gal	0.00034	0.00034	0.01203	0.59346	0.01157	0.01157	0.01157	0.01157	0.01157	0.01157	0.01157
<i>L. mex</i> WT pro - Glu	0.64985	0.01203	0.01104	0.01104	0.00011	0.00011	0.00011	0.00011	0.00011	0.00011	0.00011
<i>L. mex</i> WT meta - Glu	0.00185	0.59346	0.01104	0.01104	0.00011	0.00011	0.00011	0.00011	0.00011	0.00011	0.00011
<i>L. mex</i> LPG1 ⁻ lept - Gal	0.00001	0.01157	0.00011	0.01104	0.00000	0.00000	0.00000	0.00000	0.00000	0.00000	0.00000
<i>L. mex</i> LPG1 ⁻ AB lept/nlect - Gal	0.63949	0.01678	0.76211	0.01536	0.00029	0.00029	0.00029	0.00029	0.00029	0.00029	0.00029
<i>L. major</i> WT nect - Gal	0.00003	0.65744	0.00344	0.79671	0.08691	0.08691	0.08691	0.08691	0.08691	0.08691	0.08691

IGNORING PATTERNED PARASITE MAPS

Average Force per μm^2 (>20 pN)

<i>P. TwoTail</i>	<i>L. mex</i> WT pro - Gal	<i>L. mex</i> WT meta - Gal	<i>L. mex</i> WT pro - Glu	<i>L. mex</i> WT meta - Glu	<i>L. mex</i> LPG1 ⁻ lept - Gal	<i>L. mex</i> LPG1 ⁻ lept - Gal	<i>L. mex</i> LPG1 ⁻ AB lept/nect - Gal	<i>L. mex</i> LPG1 ⁻ AB lept/nect - Gal	<i>L. major</i> WT nect - Gal
<i>L. mex</i> WT pro - Gal	0.00221	0.08905	0.02930	0.00256	0.00005	0.00005	0.00005	0.00005	0.00039
<i>L. mex</i> WT meta - Gal	0.00221	0.08905	0.02930	0.00256	0.00005	0.00005	0.00005	0.00005	0.00039
<i>L. mex</i> WT pro - Glu	0.08905	0.02930	0.00256	0.00005	0.00005	0.00005	0.00005	0.00005	0.00039
<i>L. mex</i> WT meta - Glu	0.08905	0.02930	0.00256	0.00005	0.00005	0.00005	0.00005	0.00005	0.00039
<i>L. mex</i> LPG1 ⁻ lept - Gal	0.00005	0.00005	0.00005	0.00005	0.00005	0.00005	0.00005	0.00005	0.00039
<i>L. mex</i> LPG1 ⁻ AB lept/nect - Gal	0.00060	0.01246	0.37376	0.00891	0.00891	0.00891	0.00891	0.00891	0.00003
<i>L. major</i> WT nect - Gal	0.00039	0.86394	0.01522	0.03147	0.76643	0.76643	0.00003	0.00003	

Average Force per μm^2 (>30 pN)

<i>P. TwoTail</i>	<i>L. mex</i> WT pro - Gal	<i>L. mex</i> WT meta - Gal	<i>L. mex</i> WT pro - Glu	<i>L. mex</i> WT meta - Glu	<i>L. mex</i> LPG1 ⁻ lept - Gal	<i>L. mex</i> LPG1 ⁻ lept - Gal	<i>L. mex</i> LPG1 ⁻ AB lept/nect - Gal	<i>L. mex</i> LPG1 ⁻ AB lept/nect - Gal	<i>L. major</i> WT nect - Gal
<i>L. mex</i> WT pro - Gal	0.00140	0.14025	0.01998	0.00144	0.00001	0.00001	0.00001	0.00001	0.00012
<i>L. mex</i> WT meta - Gal	0.00140	0.14025	0.01998	0.00144	0.00001	0.00001	0.00001	0.00001	0.00012
<i>L. mex</i> WT pro - Glu	0.14025	0.01998	0.00144	0.00001	0.00001	0.00001	0.00001	0.00001	0.00012
<i>L. mex</i> WT meta - Glu	0.14025	0.01998	0.00144	0.00001	0.00001	0.00001	0.00001	0.00001	0.00012
<i>L. mex</i> LPG1 ⁻ lept - Gal	0.00001	0.00001	0.00001	0.00001	0.00001	0.00001	0.00001	0.00001	0.00012
<i>L. mex</i> LPG1 ⁻ AB lept/nect - Gal	0.00860	0.00472	0.41367	0.01113	0.00000	0.00000	0.00000	0.00000	0.15194
<i>L. major</i> WT nect - Gal	0.00012	0.52867	0.00551	0.03147	0.15194	0.15194	0.00027	0.00027	

Average Force per μm^2 (>50 pN)

<i>P. TwoTail</i>	<i>L. mex</i> WT pro - Gal	<i>L. mex</i> WT meta - Gal	<i>L. mex</i> WT pro - Glu	<i>L. mex</i> WT meta - Glu	<i>L. mex</i> LPG1 ⁻ lept - Gal	<i>L. mex</i> LPG1 ⁻ lept - Gal	<i>L. mex</i> LPG1 ⁻ AB lept/nect - Gal	<i>L. mex</i> LPG1 ⁻ AB lept/nect - Gal	<i>L. major</i> WT nect - Gal
<i>L. mex</i> WT pro - Gal	0.00029	0.12125	0.01265	0.00055	0.00000	0.00000	0.00000	0.00000	0.00027
<i>L. mex</i> WT meta - Gal	0.00029	0.12125	0.01265	0.00055	0.00000	0.00000	0.00000	0.00000	0.00027
<i>L. mex</i> WT pro - Glu	0.12125	0.01265	0.00055	0.00000	0.00000	0.00000	0.00000	0.00000	0.00027
<i>L. mex</i> WT meta - Glu	0.12125	0.01265	0.00055	0.00000	0.00000	0.00000	0.00000	0.00000	0.00027
<i>L. mex</i> LPG1 ⁻ lept - Gal	0.00000	0.00000	0.00000	0.00000	0.00000	0.00000	0.00000	0.00000	0.00027
<i>L. mex</i> LPG1 ⁻ AB lept/nect - Gal	0.02948	0.80444	0.00256	0.00256	0.00000	0.00000	0.00000	0.00000	0.00055
<i>L. major</i> WT nect - Gal	0.00027	0.45594	0.01522	0.04570	0.08930	0.08930	0.00055	0.00055	

Average Force per μm^2 (>60 pN)

<i>P. TwoTail</i>	<i>L. mex</i> WT pro - Gal	<i>L. mex</i> WT meta - Gal	<i>L. mex</i> WT pro - Glu	<i>L. mex</i> WT meta - Glu	<i>L. mex</i> LPG1 ⁻ lept - Gal	<i>L. mex</i> LPG1 ⁻ lept - Gal	<i>L. mex</i> LPG1 ⁻ AB lept/nect - Gal	<i>L. mex</i> LPG1 ⁻ AB lept/nect - Gal	<i>L. major</i> WT nect - Gal
<i>L. mex</i> WT pro - Gal	0.00029	0.37376	0.01998	0.00018	0.00000	0.00000	0.00000	0.00000	0.00012
<i>L. mex</i> WT meta - Gal	0.00029	0.37376	0.01998	0.00018	0.00000	0.00000	0.00000	0.00000	0.00012
<i>L. mex</i> WT pro - Glu	0.37376	0.01998	0.00018	0.00000	0.00000	0.00000	0.00000	0.00000	0.00012
<i>L. mex</i> WT meta - Glu	0.37376	0.01998	0.00018	0.00000	0.00000	0.00000	0.00000	0.00000	0.00012
<i>L. mex</i> LPG1 ⁻ lept - Gal	0.00000	0.00000	0.00000	0.00000	0.00000	0.00000	0.00000	0.00000	0.00012
<i>L. mex</i> LPG1 ⁻ AB lept/nect - Gal	0.05681	1.02823	0.00193	0.00193	0.00001	0.00001	0.00001	0.00001	0.15095
<i>L. major</i> WT nect - Gal	0.00012	0.71429	0.01522	0.75043	0.15095	0.15095	0.00018	0.00018	

Average Force per μm^2 (>100 pN)

<i>P. TwoTail</i>	<i>L. mex</i> WT pro - Gal	<i>L. mex</i> WT meta - Gal	<i>L. mex</i> WT pro - Glu	<i>L. mex</i> WT meta - Glu	<i>L. mex</i> LPG1 ⁻ lept - Gal	<i>L. mex</i> LPG1 ⁻ lept - Gal	<i>L. mex</i> LPG1 ⁻ AB lept/nect - Gal	<i>L. mex</i> LPG1 ⁻ AB lept/nect - Gal	<i>L. major</i> WT nect - Gal
<i>L. mex</i> WT pro - Gal	0.00088	0.59507	0.05861	0.00185	0.00001	0.00001	0.00001	0.00001	0.00003
<i>L. mex</i> WT meta - Gal	0.00088	0.59507	0.05861	0.00185	0.00001	0.00001	0.00001	0.00001	0.00003
<i>L. mex</i> WT pro - Glu	0.59507	0.05861	0.00185	0.00001	0.00001	0.00001	0.00001	0.00001	0.00003
<i>L. mex</i> WT meta - Glu	0.59507	0.05861	0.00185	0.00001	0.00001	0.00001	0.00001	0.00001	0.00003
<i>L. mex</i> LPG1 ⁻ lept - Gal	0.00001	0.00001	0.00001	0.00001	0.00001	0.00001	0.00001	0.00001	0.00003
<i>L. mex</i> LPG1 ⁻ AB lept/nect - Gal	0.63949	0.02672	0.91536	0.01536	0.00029	0.00029	0.00029	0.00029	0.08691
<i>L. major</i> WT nect - Gal	0.00003	0.59800	0.06224	0.79671	0.08691	0.08691	0.01076	0.01076	

Bibliography

- [1] G. Binnig, C. Quate, and C. Gerber, “Atomic Force Microscope.,” *Physical Review Letters*, vol. 56, no. 9, pp. 930–933, 1986.
- [2] G. Weder, N. Blondiaux, M. Giazzon, N. Matthey, M. Klein, R. Pugin, H. Heinzelmann, and M. Liley, “Use of Force Spectroscopy to Investigate the Adhesion of Living Adherent Cells.,” *Langmuir*, vol. 26, no. 17, pp. 8180–8186, 2010.
- [3] A. V. Bolshakova, O. I. Kiselyova, and I. V. Yaminsky, “Microbial surfaces investigated using atomic force microscopy.,” *Biotechnology Progress*, vol. 20, no. 6, pp. 1615–1622, 2004.
- [4] Y. F. Dufrêne, “AFM for nanoscale microbe analysis.,” *The Analyst*, vol. 133, no. 3, pp. 297–301, 2008.
- [5] Y. F. Dufrêne, “Using nanotechniques to explore microbial surfaces.,” *Nature Reviews Microbiology*, vol. 2, no. 6, pp. 451–460, 2004.
- [6] S. K. Lower, C. J. Tadanier, and M. F. Hochella Jr., “Measuring interfacial and adhesion forces between bacteria and mineral surfaces with biological force microscopy,” *Geochimica et Cosmochimica Acta*, vol. 64, no. 18, pp. 3133–3139, 2000.
- [7] A. Harimawan, A. Rajasekar, and Y. P. Ting, “Bacteria attachment to surfaces—AFM force spectroscopy and physicochemical analyses.,” *Journal of Colloid and Interface Science*, vol. 364, no. 1, pp. 213–218, 2011.
- [8] A. G. Végh, C. Fazakas, K. Nagy, I. Wilhelm, J. Molnár, I. a. Krizbai, Z. Szegletes, and G. Váró, “Adhesion and stress relaxation forces between melanoma and cerebral endothelial cells.,” *European Biophysics Journal*, vol. 41, no. 2, pp. 139–145, 2012.
- [9] C. Na, C. J. McNamara, N. R. Konkol, K. A. Bearce, R. Mitchell, and S. T. Martin, “The use of force-volume microscopy to examine bacterial attachment to titanium surfaces,” *Annals of Microbiology*, vol. 60, no. 3, pp. 495–502, 2010.
- [10] G. Haugstad, *Atomic Force Microscopy: Understanding Basic Modes and Advanced Applications*. Wiley-Blackwell, New Jersey, 1st ed., 2012.
- [11] B. Cappella and G. Dietler, “Force-distance curves by atomic force microscopy,” *Surface Science Reports*, vol. 34, no. 1-3, pp. 1–104, 1999.

- [12] M. R. Smyda and S. C. Harvey, "The entropic cost of polymer confinement," *Journal of Physical Chemistry B*, vol. 116, no. 35, pp. 10928–10934, 2012.
- [13] G. Gao, K. Yu, J. Kindrachuk, D. E. Brooks, R. E. W. Hancock, and J. N. Kizhakkedathu, "Antibacterial surfaces based on polymer brushes: investigation on the influence of brush properties on antimicrobial peptide immobilization and antimicrobial activity," *Biomacromolecules*, vol. 12, no. 10, pp. 3715–27, 2011.
- [14] N. I. Abu-Lail and T. A. Camesano, "Role of ionic strength on the relationship of biopolymer conformation, DLVO contributions, and steric interactions to bioadhesion of *Pseudomonas putida* KT2442.," *Biomacromolecules*, vol. 4, pp. 1000–1012, 2003.
- [15] J. Y. Wong, C. K. Park, M. Seitz, and J. Israelachvili, "Polymer-cushioned bilayers. II. An investigation of interaction forces and fusion using the surface forces apparatus.," *Biophysical Journal*, vol. 77, no. 3, pp. 1458–68, 1999.
- [16] J. M. Thwala, M. Li, M. C. Y. Wong, S. Kang, E. M. V. Hoek, and B. B. Mamba, "Bacteria Polymer Membrane Interactions: Atomic Force Microscopy and XDLVO Predictions," *Langmuir*, vol. 29, pp. 13773–13782, 2013.
- [17] J. N. Israelachvili, *Intermolecular and Surface Forces*. Elsevier Academic Press, third ed., 2011.
- [18] L. S. Dorobantu and M. R. Gray, "Application of atomic force microscopy in bacterial research.," *Scanning*, vol. 32, no. 2, pp. 74–96, 2010.
- [19] B. J. Berne, J. D. Weeks, and R. Zhou, "Dewetting and hydrophobic interaction in physical and biological systems.," *Annual Review of Physical Chemistry*, vol. 60, pp. 85–103, 2009.
- [20] L.-C. Xu, V. Vadillo-Rodríguez, and B. E. Logan, "Residence time, loading force, pH, and ionic strength affect adhesion forces between colloids and biopolymer-coated surfaces.," *Langmuir*, vol. 21, no. 16, pp. 7491–7500, 2005.
- [21] S. Ip, J. K. Li, and G. C. Walker, "Phase segregation of untethered zwitterionic model lipid bilayers observed on mercaptoundecanoic-acid-modified gold by AFM imaging and force mapping.," *Langmuir*, vol. 26, no. 13, pp. 11060–70, 2010.
- [22] J. Ubbink and P. Schär-Zammaretti, "Probing bacterial interactions: integrated approaches combining atomic force microscopy, electron microscopy and biophysical techniques.," *Micron*, vol. 36, no. 4, pp. 293–320, 2005.
- [23] M. Sletmoen, G. Maurstad, P. Sikorski, B. S. Paulsen, and B. Stokke, "Characterisation of bacterial polysaccharides: steps towards single-molecular studies," *Carbohydrate Research*, vol. 338, no. 23, pp. 2459–2475, 2003.
- [24] H. K. Webb, V. K. Truong, J. Hasan, R. J. Crawford, and E. P. Ivanova, "Physico-mechanical characterisation of cells using atomic force microscopy - Current research and methodologies.," *Journal of Microbiological Methods*, vol. 86, no. 2, pp. 131–139, 2011.

- [25] G. Francius, S. Lebeer, D. Alsteens, L. Wildling, H. J. Gruber, P. Hols, S. De Keersmaecker, J. Vanderleyden, and Y. F. Dufrêne, “Detection, localization, and conformational analysis of single polysaccharide molecules on live bacteria,” *ACS Nano*, vol. 2, no. 9, pp. 1921–1929, 2008.
- [26] C. Lv, C. Tan, M. Qin, D. Zou, Y. Cao, and W. Wang, “Low folding cooperativity of HP35 revealed by single-molecule force spectroscopy and molecular dynamics simulation,” *Biophysical Journal*, vol. 102, no. 8, pp. 1944–1951, 2012.
- [27] T. A. Camesano and N. I. Abu-Lail, “Heterogeneity in bacterial surface polysaccharides, probed on a single-molecule basis,” *Biomacromolecules*, vol. 3, no. 4, pp. 661–667, 2002.
- [28] X. Sheng, Y. P. Ting, and S. O. Pehkonen, “Force measurements of bacterial adhesion on metals using a cell probe atomic force microscope,” *Journal of Colloid and Interface Science*, vol. 310, no. 2, pp. 661–669, 2007.
- [29] C. J. Wright, M. K. Shah, L. C. Powell, and I. Armstrong, “Application of AFM from microbial cell to biofilm,” *Scanning*, vol. 32, no. 3, pp. 134–149, 2010.
- [30] A. Beaussart, S. El-Kirat-Chatel, P. Herman, D. Alsteens, J. Mahillon, P. Hols, and Y. F. Dufrêne, “Single-cell force spectroscopy of probiotic bacteria,” *Biophysical Journal*, vol. 104, no. 9, pp. 1886–1892, 2013.
- [31] S. El-Kirat-Chatel, A. Beaussart, C. D. Boyd, G. A. O’Toole, and Y. F. Dufrêne, “Single-cell and single-molecule analysis deciphers the localization, adhesion, and mechanics of the biofilm adhesin LapA,” *ACS Chemical Biology*, vol. 9, pp. 485–494, 2014.
- [32] A. Wargenau and A. Kwade, “Determination of Adhesion between Single *Aspergillus niger* Spores in Aqueous Solutions Using an Atomic Force Microscope,” *Langmuir*, vol. 26, no. 14, pp. 11071–11076, 2010.
- [33] X. Sheng, Y. P. Ting, and S. O. Pehkonen, “The influence of ionic strength, nutrients and pH on bacterial adhesion to metals,” *Journal of Colloid and Interface Science*, vol. 321, no. 2, pp. 256–264, 2008.
- [34] E. Dague, D. T. L. Le, S. Zanna, P. Marcus, P. Loubière, and M. Mercier-Bonin, “Probing in vitro interactions between *Lactococcus lactis* and mucins using AFM,” *Langmuir*, vol. 26, no. 13, pp. 11010–11017, 2010.
- [35] D. T. L. Le, Y. Guérardel, P. Loubière, M. Mercier-Bonin, and E. Dague, “Measuring Kinetic Dissociation/Association Constants Between *Lactococcus lactis* Bacteria and Mucins Using Living Cell Probes,” *Biophysical Journal*, vol. 101, no. 11, pp. 2843–2853, 2011.
- [36] D. J. Müller, M. Krieg, D. Alsteens, and Y. F. Dufrêne, “New frontiers in atomic force microscopy: analyzing interactions from single-molecules to cells,” *Current Opinion in Biotechnology*, vol. 20, no. 1, pp. 4–13, 2009.

- [37] P. Tripathi, A. Beaussart, G. Andre, T. Rolain, S. Lebeer, J. Vanderleyden, P. Hols, and Y. F. Dufrêne, “Towards a nanoscale view of lactic acid bacteria.,” *Micron*, vol. 43, no. 12, pp. 1323–1330, 2012.
- [38] M. Yizhak, “Effect of Ions on the Structure of Water: Structure Making and Breaking,” *Chemical Reviews*, vol. 109, pp. 1346–1370, 2009.
- [39] D. Tareste, F. Pincet, L. Lebeau, and E. Perez, “Hydrophobic forces and hydrogen bonds in the adhesion between retinoid-coated surfaces.,” *Langmuir*, vol. 23, no. 6, pp. 3225–3229, 2007.
- [40] C.-K. Lee, Y.-M. Wang, L.-S. Huang, and S. Lin, “Atomic force microscopy: determination of unbinding force, off rate and energy barrier for protein-ligand interaction.,” *Micron*, vol. 38, no. 5, pp. 446–461, 2007.
- [41] R. Nevo, C. Stroh, F. Kienberger, D. Kaftan, V. Brumfeld, M. Elbaum, Z. Reich, and P. Hinterdorfer, “A molecular switch between alternative conformational states in the complex of Ran and importin beta 1,” *Nature Structural Biology*, vol. 10, no. 7, pp. 553–557, 2003.
- [42] Y.-S. Lo, Y.-J. Zhu, and T. P. Beebe, “Loading-Rate Dependence of Individual Ligand-Receptor Bond-Rupture Forces Studied by Atomic Force Microscopy,” *Langmuir*, vol. 17, pp. 3741–3748, 2001.
- [43] M. Li, X. Xiao, L. Liu, N. Xi, Y. Wang, Z. Dong, and W. Zhang, “Atomic force microscopy study of the antigen-antibody binding force on patient cancer cells based on ROR1 fluorescence recognition.,” *Journal of Molecular Recognition*, vol. 26, no. 9, pp. 432–438, 2013.
- [44] A. Touhami, B. Hoffmann, A. Vasella, F. A. Denis, and Y. F. Dufrêne, “Aggregation of yeast cells: direct measurement of discrete lectin-carbohydrate interactions,” *Microbiology*, vol. 149, no. Pt 10, pp. 2873–2878, 2003.
- [45] P. Gunning, S. Chambers, C. Pin, A. L. Man, V. J. Morris, and C. Nicoletti, “Mapping specific adhesive interactions on living human intestinal epithelial cells with atomic force microscopy.,” *The FASEB Journal*, vol. 22, no. 7, pp. 2331–2339, 2008.
- [46] T. Osada, S. Takezawa, A. Itoh, H. Arakawa, M. Ichikawa, and A. Ikai, “The distribution of sugar chains on the vomeronasal epithelium observed with an atomic force microscope.,” *Chemical Senses*, vol. 24, no. 1, pp. 1–6, 1999.
- [47] M.-X. Hu and Z.-K. Xu, “Carbohydrate decoration of microporous polypropylene membranes for lectin affinity adsorption: comparison of mono- and disaccharides.,” *Colloids and Surfaces B: Biointerfaces*, vol. 85, no. 1, pp. 19–25, 2011.
- [48] S. R. S. Ting, G. Chen, and M. H. Stenzel, “Synthesis of glycopolymers and their multivalent recognitions with lectins,” *Polymer Chemistry*, vol. 1, no. 9, pp. 1392–1412, 2010.
- [49] J.-L. Chen, S. Lin, and L.-P. Lin, “Rhizobial Surface Biopolymers and their Interaction with Lectin Measured by Atomic Force Microscopy,” *World Journal of Microbiology and Biotechnology*, vol. 22, no. 6, pp. 565–570, 2006.

- [50] K. L. O'Brien, L. J. Wolfson, J. P. Watt, E. Henkle, M. Deloria-Knoll, N. McCall, E. Lee, K. Mulholland, O. S. Levine, and T. Cherian, "Burden of disease caused by *Streptococcus pneumoniae* in children younger than 5 years: global estimates.," *Lancet*, vol. 374, no. 9693, pp. 893–902, 2009.
- [51] T. van der Poll and S. M. Opal, "Pathogenesis, treatment, and prevention of pneumococcal pneumonia.," *Lancet*, vol. 374, no. 9700, pp. 1543–1556, 2009.
- [52] E. N. Miyaji, M. L. S. Oliveira, E. Carvalho, and P. L. Ho, "Serotype-independent pneumococcal vaccines.," *Cellular and Molecular Life Sciences*, vol. 70, no. 18, pp. 3303–3326, 2013.
- [53] J. M. Garcés, S. Tomás, J. Rubiés-Prat, J. L. Gimeno, and L. Drobnic, "Bacterial infection as a presenting manifestation of visceral leishmaniasis.," *Reviews of infectious diseases*, vol. 12, no. 3, pp. 518–519, 1990.
- [54] M. Endris, Y. Takele, D. Woldeyohannes, M. Tiruneh, R. Mohammed, F. Moges, L. Lynen, J. Jacobs, J. van Griensven, and E. Diro, "Bacterial Sepsis in Patients with Visceral Leishmaniasis in Northwest Ethiopia," *BioMed Research International*, vol. 2014, pp. 1–7, 2014.
- [55] D. Bogaert, R. de Groot, and P. Hermans, "*Streptococcus pneumoniae* colonisation: the key to pneumococcal disease," *The Lancet Infectious Diseases*, vol. 4, no. March, pp. 144–154, 2004.
- [56] J. R. Shak, J. E. Vidal, and K. P. Klugman, "Influence of bacterial interactions on pneumococcal colonization of the nasopharynx.," *Trends in Microbiology*, vol. 21, no. 3, pp. 129–135, 2013.
- [57] M. J. Walport, "Complement. First of two parts.," *The New England Journal of Medicine*, vol. 344, no. 14, pp. 1058–1066, 2001.
- [58] C. A. Janeway, P. Travers, M. J. Walport, and M. J. Schlomchik, "The complement system and innate immunity," in *Immunobiology: the immune system in health and disease*, Garland, New York, 5th ed., 2001.
- [59] C. Hyams, E. Camberlein, J. M. Cohen, K. Bax, and J. S. Brown, "The *pneumoniae* capsule inhibits complement activity and neutrophil phagocytosis by multiple mechanisms.," *Infection and Immunity*, vol. 78, no. 2, pp. 704–715, 2010.
- [60] M. J. Jedrzejas, "Pneumococcal virulence factors: structure and function.," *Microbiology and Molecular Biology Reviews*, vol. 65, no. 2, pp. 187–207, 2001.
- [61] K. K. Gosink, E. R. Mann, C. Guglielmo, E. I. Tuomanen, and H. R. Masure, "Role of Novel Choline Binding Proteins in Virulence of *Streptococcus pneumoniae*," *Infection and Immunity*, vol. 68, no. 10, pp. 5690–5695, 2000.
- [62] C. Rosenow, P. Ryan, J. N. Weiser, S. Johnson, P. Fontan, A. Ortqvist, and H. R. Masure, "Contribution of novel choline-binding proteins to adherence, colonization and immunogenicity of *Streptococcus pneumoniae*," *Molecular Microbiology*, vol. 25, no. 5, pp. 819–829, 1997.

- [63] R. Mukerji, S. Mirza, A. M. Roche, R. W. Widener, C. M. Cronney, D.-K. Rhee, J. N. Weiser, A. J. Szalai, and D. E. Briles, "Pneumococcal surface protein A inhibits complement deposition on the pneumococcal surface by competing with the binding of C-reactive protein to cell-surface phosphocholine.," *Journal of Immunology*, vol. 189, no. 11, pp. 5327–5335, 2012.
- [64] C. C. Daniels, T. C. Briles, S. Mirza, A. P. Håkansson, and D. E. Briles, "Capsule does not block antibody binding to PspA, a surface virulence protein of *Streptococcus pneumoniae*." *Microbial Pathogenesis*, vol. 40, no. 5, pp. 228–233, 2006.
- [65] S. Hammerschmidt, "Adherence molecules of pathogenic pneumococci.," *Current Opinion in Microbiology*, vol. 9, no. 1, pp. 12–20, 2006.
- [66] B. Ren, J. Li, K. Genschmer, S. K. Hollingshead, and D. E. Briles, "The absence of PspA or presence of antibody to PspA facilitates the complement-dependent phagocytosis of pneumococci in vitro.," *Clinical and Vaccine Immunology*, vol. 19, no. 10, pp. 1574–1582, 2012.
- [67] S. Ricci, A. Gerlini, A. Pammolli, D. Chiavolini, V. Braione, S. A. Tripodi, B. Colombari, E. Blasi, M. R. Oggioni, S. Peppoloni, and G. Pozzi, "Contribution of different pneumococcal virulence factors to experimental meningitis in mice.," *BMC Infectious Diseases*, vol. 13, p. 444, 2013.
- [68] T. B. Gang, D. J. Hammond, S. K. Singh, D. A. Ferguson, V. K. Mishra, and A. Agrawal, "The Phosphocholine-binding pocket on C-reactive protein is necessary for initial protection of mice against pneumococcal infection.," *The Journal of Biological Chemistry*, vol. 287, no. 51, pp. 43116–43125, 2012.
- [69] A. D. Ogunniyi, K. S. LeMessurier, R. M. A. Graham, J. M. Watt, D. E. Briles, U. H. Stroehrer, and J. C. Paton, "Contributions of pneumolysin, pneumococcal surface protein A (PspA), and PspC to pathogenicity of *Streptococcus pneumoniae* D39 in a mouse model.," *Infection and Immunity*, vol. 75, no. 4, pp. 1843–1851, 2007.
- [70] B. B. Mook-Kanamori, M. Geldhoff, T. van der Poll, and D. van de Beek, "Pathogenesis and pathophysiology of pneumococcal meningitis.," *Clinical Microbiology Reviews*, vol. 24, no. 3, pp. 557–591, 2011.
- [71] S. Ricci, R. Janulczyk, A. Gerlini, V. Braione, L. Colomba, F. Iannelli, D. Chiavolini, M. R. Oggioni, L. Björck, and G. Pozzi, "The factor H-binding fragment of PspC as a vaccine antigen for the induction of protective humoral immunity against experimental pneumococcal sepsis.," *Vaccine*, vol. 29, no. 46, pp. 8241–8249, 2011.
- [72] G. J. Boulnois, J. C. Paton, T. J. Mitchell, and P. W. Andrew, "Structure and function of pneumolysin, the multifunctional, thiol-activated toxin of *Streptococcus pneumoniae*." *Molecular Microbiology*, vol. 5, no. 11, pp. 2611–2616, 1991.
- [73] B. B. Bonev, R. J. Gilbert, P. W. Andrew, O. Byron, and A. Watts, "Structural analysis of the protein/lipid complexes associated with pore formation by the

- bacterial toxin pneumolysin.," *The Journal of Biological Chemistry*, vol. 276, no. 8, pp. 5714–5719, 2001.
- [74] H. M. Marriott and D. H. Dockrell, "Streptococcus pneumoniae: the role of apoptosis in host defense and pathogenesis.," *The International Journal of Biochemistry & Cell Biology*, vol. 38, no. 11, pp. 1848–1854, 2006.
- [75] J. C. Paton, B. Rowan-Kelly, and A. Ferrante, "Activation of human complement by the pneumococcal toxin pneumolysin.," *Infection and Immunity*, vol. 43, no. 3, pp. 1085–1087, 1984.
- [76] R. B. Alcantara, L. C. Preheim, and M. J. Gentry, "Role of Pneumolysin's Complement-Activating Activity during Pneumococcal Bacteremia in Cirrhotic Rats," *Infection and Immunity*, vol. 67, no. 6, pp. 2862–2866, 1999.
- [77] E. A. McNeela, A. Burke, D. R. Neill, C. Baxter, V. E. Fernandes, D. Ferreira, S. Smeaton, R. El-Rachkidy, R. M. McLoughlin, A. Mori, B. Moran, K. A. Fitzgerald, J. Tschopp, V. Pétrilli, P. W. Andrew, A. Kadioglu, and E. C. Lavelle, "Pneumolysin activates the NLRP3 inflammasome and promotes proinflammatory cytokines independently of TLR4.," *PLOS Pathogens*, vol. 6, no. 11, p. e1001191, 2010.
- [78] R. Haase, C. J. Kirschning, A. Sing, P. Schröttner, K. Fukase, S. Kusumoto, H. Wagner, J. Heesemann, and K. Ruckdeschel, "A dominant role of Toll-like receptor 4 in the signaling of apoptosis in bacteria-faced macrophages.," *Journal of Immunology*, vol. 171, no. 8, pp. 4294–4303, 2003.
- [79] R. Malley, P. Henneke, S. C. Morse, M. J. Cieslewicz, M. Lipsitch, C. M. Thompson, E. Kurt-Jones, J. C. Paton, M. R. Wessels, and D. T. Golenbock, "Recognition of pneumolysin by Toll-like receptor 4 confers resistance to pneumococcal infection.," *Proceedings of the National Academy of Sciences of the United States of America*, vol. 100, no. 4, pp. 1966–1971, 2003.
- [80] A. Srivastava, P. Henneke, A. Visintin, S. C. Morse, V. Martin, C. Watkins, J. C. Paton, M. R. Wessels, D. T. Golenbock, and R. Malley, "The apoptotic response to pneumolysin is Toll-like receptor 4 dependent and protects against pneumococcal disease.," *Infection and Immunity*, vol. 73, no. 10, pp. 6479–6487, 2005.
- [81] C. F. Rayner, A. D. Jackson, A. Rutman, A. Dewar, T. J. Mitchell, P. W. Andrew, P. J. Cole, and R. Wilson, "Interaction of pneumolysin-sufficient and -deficient isogenic variants of *Streptococcus pneumoniae* with human respiratory mucosa.," *Infection and Immunity*, vol. 63, no. 2, pp. 442–447, 1995.
- [82] A. Tomasz, "Surface components of *Streptococcus pneumoniae*." *Reviews of Infectious Diseases*, vol. 3, no. 2, pp. 190–211, 1981.
- [83] I. R. Poxton, E. Tarelli, and J. Baddiley, "The structure of C-polysaccharide from the walls of *Streptococcus pneumoniae*." *The Biochemical Journal*, vol. 175, no. 3, pp. 1033–1042, 1978.

- [84] N. Gisch, T. Kohler, A. J. Ulmer, J. Muething, T. Pribyl, K. Fischer, B. Lindner, S. Hammerschmidt, and U. Zaehring, “Structural reevaluation of *Streptococcus pneumoniae* lipoteichoic acid and new insights into its immunostimulatory potency,” *Journal of Biological Chemistry*, vol. 288, pp. 15654–15667, MAY 31 2013.
- [85] R. López, “Pneumococcus: the sugar-coated bacteria,” *International Microbiology*, vol. 9, no. 3, pp. 179–190, 2006.
- [86] C. M. Snapper, Y. Shen, A. Q. Khan, J. Colino, P. Zelazowski, J. J. Mond, W. C. Gause, and Z.-Q. Wu, “Distinct types of T-cell help for the induction of a humoral immune response to *Streptococcus pneumoniae*,” *Trends in Immunology*, vol. 22, no. 6, pp. 308–311, 2001.
- [87] J. R. Catterall, “*Streptococcus pneumoniae*,” *Thorax*, vol. 54, pp. 929–937, 1999.
- [88] M. Kalin, “Pneumococcal serotypes and their clinical relevance,” *Thorax*, vol. 53, no. 3, pp. 159–162, 1998.
- [89] U. Koppe, N. Suttorp, and B. Opitz, “Recognition of *Streptococcus pneumoniae* by the innate immune system,” *Cellular Microbiology*, vol. 14, no. 4, pp. 460–466, 2012.
- [90] M. Abeyta, G. G. Hardy, and J. Yother, “Genetic Alteration of Capsule Type but Not PspA Type Affects Accessibility of Surface-Bound Complement and Surface Antigens of *Streptococcus pneumoniae*,” *Infection and Immunity*, vol. 71, no. 1, pp. 218–225, 2003.
- [91] N. Noske, U. Kämmerer, M. Rohde, and S. Hammerschmidt, “Pneumococcal interaction with human dendritic cells: phagocytosis, survival, and induced adaptive immune response are manipulated by PavA,” *Journal of Immunology*, vol. 183, no. 3, pp. 1952–1963, 2009.
- [92] D. M. Weinberger, K. Trzciski, Y.-J. Lu, D. Bogaert, A. Brandes, J. Galagan, P. W. Anderson, R. Malley, and M. Lipsitch, “Pneumococcal capsular polysaccharide structure predicts serotype prevalence,” *PLOS Pathogens*, vol. 5, no. 6, p. e1000476, 2009.
- [93] L. Kenne, B. Lindberg, and S. Svensson, “The structure of capsular polysaccharide of the pneumococcus type II,” *Carbohydrate Research*, vol. 40, pp. 69–75, 1975.
- [94] F. Iannelli, B. J. Pearce, and G. Pozzi, “The type 2 capsule locus of *Streptococcus pneumoniae*,” *Journal of Bacteriology*, vol. 181, no. 8, pp. 2652–2654, 1999.
- [95] B. J. Pearce, F. Iannelli, and G. Pozzi, “Construction of new unencapsulated (rough) strains of *Streptococcus pneumoniae*,” *Research in Microbiology*, vol. 153, no. 4, pp. 243–247, 2002.
- [96] H. M. Marriott, K. A. Gascoyne, R. Gowda, I. Geary, M. J. H. Nicklin, F. Iannelli, G. Pozzi, T. J. Mitchell, M. K. B. Whyte, I. Sabroe, and D. H. Dockrell,

- “Interleukin-1 β regulates CXCL8 release and influences disease outcome in response to *Streptococcus pneumoniae*, defining intercellular cooperation between pulmonary epithelial cells and macrophages.,” *Infection and Immunity*, vol. 80, no. 3, pp. 1140–1149, 2012.
- [97] I. Jensch, G. Gámez, M. Rothe, S. Ebert, M. Fulde, D. Somplatzki, S. Bergmann, L. Petruschka, M. Rohde, R. Nau, and S. Hammerschmidt, “PavB is a surface-exposed adhesin of *Streptococcus pneumoniae* contributing to nasopharyngeal colonization and airways infections.,” *Molecular Microbiology*, vol. 77, no. 1, pp. 22–43, 2010.
- [98] F. Wartha, K. Beiter, B. Albiger, J. Fernebro, A. Zychlinsky, S. Normark, and B. Henriques-Normark, “Capsule and D-alanylated lipoteichoic acids protect *Streptococcus pneumoniae* against neutrophil extracellular traps.,” *Cellular Microbiology*, vol. 9, no. 5, pp. 1162–1171, 2007.
- [99] F. Ahimou, F. A. Denis, A. Touhami, and Y. F. Dufre, “Probing Microbial Cell Surface Charges by Atomic Force Microscopy,” *Langmuir*, vol. 18, pp. 9937–9941, 2002.
- [100] E. Dague, D. Alsteens, J.-P. Latgé, C. Verbelen, D. Raze, A. R. Baulard, and Y. F. Dufrêne, “Chemical force microscopy of single live cells.,” *Nano Letters*, vol. 7, no. 10, pp. 3026–3030, 2007.
- [101] D. Alsteens, E. Dague, P. G. Rouxhet, A. R. Baulard, and Y. F. Dufrêne, “Direct measurement of hydrophobic forces on cell surfaces using AFM.,” *Langmuir*, vol. 23, no. 24, pp. 11977–11979, 2007.
- [102] L. S. Dorobantu, S. Bhattacharjee, J. M. Foght, and M. R. Gray, “Atomic force microscopy measurement of heterogeneity in bacterial surface hydrophobicity.,” *Langmuir*, vol. 24, no. 9, pp. 4944–4951, 2008.
- [103] Y. Hu, J. Ulstrup, J. Zhang, S. r. Molin, and V. Dupres, “Adhesive properties of *Staphylococcus epidermidis* probed by atomic force microscopy.,” *Physical Chemistry Chemical Physics*, vol. 13, no. 21, pp. 9995–10003, 2011.
- [104] G. Francius, R. Henry, J. F. L. Duval, E. Bruneau, J. Merlin, A. Fahs, and N. Leblond-Bourget, “Thermo-regulated adhesion of the *Streptococcus thermophilus* Δ rgg0182 strain.,” *Langmuir*, vol. 29, no. 15, pp. 4847–4856, 2013.
- [105] E. W. van der Vegte and G. Hadziioannou, “Scanning force microscopy with chemical specificity: An extensive study of chemically specific tip-surface interactions and the chemical imaging of surface functional groups,” *Langmuir*, vol. 13, no. 16, pp. 4357–4368, 1997.
- [106] W.-C. Lin, S.-H. Lee, M. Karakachian, B.-Y. Yu, Y.-Y. Chen, Y.-C. Lin, C.-H. Kuo, and J.-J. Shyue, “Tuning the surface potential of gold substrates arbitrarily with self-assembled monolayers with mixed functional groups.,” *Physical Chemistry Chemical Physics*, vol. 11, no. 29, pp. 6199–6204, 2009.
- [107] W. W. Wilson, M. M. Wade, S. C. Holman, and F. R. Champlin, “Status of methods for assessing bacterial cell surface charge properties based on zeta potential measurements,” *Journal of Microbiological Methods*, vol. 43, pp. 153–164, 2001.

- [108] E. Swiatlo, F. R. Champlin, S. C. Holman, W. W. Wilson, and J. M. Watt, "Contribution of Choline-Binding Proteins to Cell Surface Properties of *Streptococcus pneumoniae*," *Infection and Immunity*, vol. 70, no. 1, pp. 412–415, 2002.
- [109] Y. Li, D. M. Weinberger, C. M. Thompson, K. Trzciski, and M. Lipsitch, "Surface charge of *Streptococcus pneumoniae* predicts serotype distribution.," *Infection and Immunity*, vol. 81, no. 12, pp. 4519–4524, 2013.
- [110] H. J. Busscher, B. van de Belt-Gritter, R. J. B. Dijkstra, W. Norde, and H. C. van der Mei, "*Streptococcus mutans* and *Streptococcus intermedius* adhesion to fibronectin films are oppositely influenced by ionic strength.," *Langmuir*, vol. 24, no. 19, pp. 10968–10973, 2008.
- [111] O. R. Millington, E. Myburgh, J. C. Mottram, and J. Alexander, "Imaging of the host/parasite interplay in cutaneous Leishmaniasis," *Experimental Parasitology*, vol. 126, pp. 310–317, 2010.
- [112] P. Desjeux, "The increase in risk factors for Leishmaniasis worldwide," *Transactions of the Royal Society of Tropical Medicine and Hygiene*, vol. 95, no. 3, pp. 239–243, 2001.
- [113] J. Alvar, I. D. Vélez, C. Bern, M. Herrero, P. Desjeux, J. Cano, J. Jannin, and M. den Boer, "Leishmaniasis worldwide and global estimates of its incidence.," *PloS One*, vol. 7, no. 5, p. e35671, 2012.
- [114] L. Savioli and D. Daumerie, *Second WHO report on neglected tropical diseases: Sustaining the drive to overcome the global impact of neglected tropical diseases*. WHO Press, 2013.
- [115] S. M. Beverley and D. E. Dobson, "Flypaper for parasites.," *Cell*, vol. 119, no. 3, pp. 311–312, 2004.
- [116] A. S. Nagle, S. Khare, A. B. Kumar, F. Supek, A. Buchynskyy, C. J. N. Mathison, N. K. Chennamaneni, N. Pendem, F. S. Buckner, M. H. Gelb, and V. Molteni, "Recent Developments in Drug Discovery for Leishmaniasis and Human African Trypanosomiasis," *Chemical Reviews*, vol. 114, pp. 11305–11347, 2014.
- [117] P. Desjeux, "Leishmaniasis: current situation and new perspectives," *Comparative Immunology, Microbiology and Infectious Diseases*, vol. 27, no. 5, pp. 305–318, 2004.
- [118] G. Mandell, J. Bennett, and R. Dolin, *Mandell, Douglas and Bennett's Principles and Practice of Infectious Diseases*. Elsevier US, 7th ed., 2010.
- [119] H. Kato, E. A. Gomez, A. G. Cáceres, H. Uezato, T. Mimori, and Y. Hashiguchi, "Molecular epidemiology for vector research on Leishmaniasis," *International Journal of Environmental Research and Public Health*, vol. 7, no. 3, pp. 814–826, 2010.
- [120] F. Chappuis, S. Sundar, A. Hailu, H. Ghalib, S. Rijal, R. W. Peeling, J. Alvar, and M. Boelaert, "Visceral Leishmaniasis: what are the needs for diagnosis,

- treatment and control?,” *Nature Reviews Microbiology*, vol. 5, no. 11, pp. 873–882, 2007.
- [121] R. Guha, D. Gupta, R. Rastogi, R. Vikram, G. Krishnamurthy, S. Bimal, S. Roy, and A. Mukhopadhyay, “Vaccination with *Leishmania* hemoglobin receptor-encoding DNA protects against visceral Leishmaniasis,” *Science Translational Medicine*, vol. 5, no. 202, p. 202ra121, 2013.
- [122] S. Kamhawi, “Phlebotomine sand flies and *Leishmania* parasites: friends or foes?,” *Trends in Parasitology*, vol. 22, no. 9, pp. 439–445, 2006.
- [123] A. M. Blagborough, T. S. Churcher, L. M. Upton, A. C. Ghani, P. W. Gething, and R. E. Sinden, “Transmission-blocking interventions eliminate malaria from laboratory populations,” *Nature Communications*, vol. 4, no. May, p. 1812, 2013.
- [124] K. Miura, E. Takashima, B. Deng, G. Tullo, A. Diouf, S. E. Moretz, D. Nikolaeva, M. Diakite, R. M. Fairhurst, M. P. Fay, C. A. Long, and T. Tsuboi, “Functional comparison of *Plasmodium falciparum* transmission-blocking vaccine candidates by the standard membrane-feeding assay,” *Infection and Immunity*, vol. 81, no. 12, pp. 4377–82, 2013.
- [125] P. A. Bates, “Transmission of *Leishmania* metacyclic promastigotes by phlebotomine sand flies,” *International Journal for Parasitology*, vol. 37, no. 10, pp. 1097–1106, 2007.
- [126] A. Rojas-Bernabé, O. Garcia-Hernández, C. Maldonado-Bernal, J. Delegado-Dominguez, E. Ortega, L. Gutiérrez-Kobeh, I. Becker, and M. Aguirre-Garcia, “*Leishmania mexicana* lipophosphoglycan activates ERK and p38 MAP kinase and induces production of proinflammatory cytokines in human macrophages through TLR2 and TLR4,” *Parasitology*, vol. 141, no. 6, pp. 788–800, 2014.
- [127] S. Kamhawi, M. Ramalho-Ortigao, V. M. Pham, S. Kumar, P. G. Lawyer, S. J. Turco, C. Barillas-Mury, D. L. Sacks, and J. G. Valenzuela, “A role for insect galectins in parasite survival,” *Cell*, vol. 119, no. 3, pp. 329–341, 2004.
- [128] P. Volf, J. Hostomska, and I. Rohousova, “Molecular crosstalks in *Leishmania*-sandfly-host relationships,” *Parasite*, vol. 15, no. 3, pp. 237–243, 2008.
- [129] M. E. Rogers, M. L. Chance, and P. A. Bates, “The role of promastigote secretory gel in the origin and transmission of the infective stage of *Leishmania mexicana* by the sandfly *Lutzomyia longipalpis*,” *Parasitology*, vol. 124, no. Pt 5, pp. 495–507, 2002.
- [130] M. E. Rogers, T. Ilg, A. V. Nikolaev, M. A. J. Ferguson, and P. A. Bates, “Transmission of cutaneous Leishmaniasis by sand flies is enhanced by regurgitation of fPPG,” *Nature*, vol. 430, no. 6998, pp. 463–467, 2004.
- [131] A. Warburg, “The structure of the female sand fly (*Phlebotomus papatasi*) alimentary canal,” *Transactions of the Royal Society of Tropical Medicine and Hygiene*, vol. 102, no. 2, pp. 161–166, 2008.

- [132] A. Ambit, K. L. Woods, B. Cull, G. H. Coombs, and J. C. Mottram, “Morphological events during the cell cycle of *Leishmania major*,” *Eukaryotic Cell*, vol. 10, no. 11, pp. 1429–1438, 2011.
- [133] D. E. Dobson, S. Kamhawi, P. Lawyer, S. J. Turco, S. M. Beverley, and D. L. Sacks, “*Leishmania major* Survival in Selective *Phlebotomus papatasi* Sand Fly Vector Requires a Specific SCG-Encoded Lipophosphoglycan Galactosylation Pattern,” *PLoS Pathogens*, vol. 6, no. 11, p. e1001185, 2010.
- [134] P. A. Bates, “*Leishmania*-sand fly interaction: progress and challenges,” *Current Opinion in Microbiology*, vol. 11, no. 4, pp. 340–344, 2008.
- [135] R. Wilson, M. D. Bates, A. Dostalova, L. Jecna, R. J. Dillon, P. Volf, and P. A. Bates, “Stage-specific adhesion of *Leishmania* promastigotes to sand fly midguts assessed using an improved comparative binding assay,” *PLoS Neglected Tropical Diseases*, vol. 4, no. 9, pp. 1–9, 2010.
- [136] S. Ramakrishnan, M. Serricchio, B. Striepen, and P. Bütikofer, “Lipid synthesis in protozoan parasites: a comparison between kinetoplastids and apicomplexans,” *Progress in Lipid Research*, vol. 52, no. 4, pp. 488–512, 2013.
- [137] D. L. Sacks, “*Leishmania*-sand fly interactions controlling species-specific vector competence,” *Cellular Microbiology*, vol. 3, no. 4, pp. 189–196, 2001.
- [138] C.-L. Forestier, Q. Gao, and G.-J. Boons, “*Leishmania* lipophosphoglycan: how to establish structure-activity relationships for this highly complex and multifunctional glycoconjugate?,” *Frontiers in Cellular and Infection Microbiology*, vol. 4, p. e193, Jan. 2015.
- [139] R. R. de Assis, I. C. Ibraim, P. M. Nogueira, R. P. Soares, and S. J. Turco, “Glycoconjugates in New World species of *Leishmania*: polymorphisms in lipophosphoglycan and glycoinositolphospholipids and interaction with hosts,” *Biochimica et Biophysica Acta*, vol. 1820, no. 9, pp. 1354–65, 2012.
- [140] B. A. Butcher, S. J. Turco, B. A. Hilty, P. F. Pimenta, M. Panunzio, and D. L. Sacks, “Deficiency in beta1,3-galactosyltransferase of a *Leishmania major* lipophosphoglycan mutant adversely influences the *Leishmania*-sand fly interaction,” *The Journal of Biological Chemistry*, vol. 271, no. 34, pp. 20573–20579, 1996.
- [141] N. Secundino, N. Kimblin, N. C. Peters, P. Lawyer, A. A. Capul, S. M. Beverley, S. J. Turco, and D. Sacks, “Proteophosphoglycan confers resistance of *Leishmania major* to midgut digestive enzymes induced by blood feeding in vector sand flies,” *Cellular Microbiology*, vol. 12, no. 7, pp. 906–918, 2010.
- [142] J. Myskova, M. Svobodova, S. M. Beverley, and P. Volf, “A lipophosphoglycan-independent development of *Leishmania* in permissive sand flies,” *Microbes and Infection*, vol. 9, no. 3, pp. 317–324, 2007.
- [143] A. Svárovská, T. H. Ant, V. Seblová, L. Jecná, S. M. Beverley, and P. Volf, “*Leishmania major* glycosylation mutants require phosphoglycans (lpg2-) but not lipophosphoglycan (lpg1-) for survival in permissive sand fly vectors,” *PLoS Neglected Tropical Diseases*, vol. 4, no. 1, p. e580, 2010.

- [144] L. Jecna, A. Dostalova, R. Wilson, V. Seblova, K.-P. Chang, P. A. Bates, and P. Volf, "The role of surface glycoconjugates in *Leishmania* midgut attachment examined by competitive binding assays and experimental development in sand flies.," *Parasitology*, vol. 140, no. 8, pp. 1026–32, 2013.
- [145] V. Ladmiral, E. Melia, and D. M. Haddleton, "Synthetic glycopolymers: an overview," *European Polymer Journal*, vol. 40, no. 3, pp. 431–449, 2004.
- [146] S. G. Spain, M. I. Gibson, and N. R. Cameron, "Recent advances in the synthesis of well-defined glycopolymers," *Journal of Polymer Science Part A: Polymer Chemistry*, vol. 45, pp. 2059–2072, 2007.
- [147] S. G. Spain and N. R. Cameron, "A spoonful of sugar: the application of glycopolymers in therapeutics," *Polymer Chemistry*, vol. 2, pp. 60–68, 2011.
- [148] J. Geng, G. Mantovani, L. Tao, J. Nicolas, G. Chen, R. Wallis, D. A. Mitchell, B. R. G. Johnson, S. D. Evans, and D. M. Haddleton, "Site-directed conjugation of "clicked" glycopolymers to form glycoprotein mimics: binding to mammalian lectin and induction of immunological function.," *Journal of the American Chemical Society*, vol. 129, no. 49, pp. 15156–15163, 2007.
- [149] S. Slavin, J. Burns, D. M. Haddleton, and C. R. Becer, "Synthesis of glycopolymers via click reactions," *European Polymer Journal*, vol. 47, no. 4, pp. 435–446, 2011.
- [150] C. Schatz and S. Lecommandoux, "Polysaccharide-Containing Block Copolymers: Synthesis, Properties and Applications of an Emerging Family of Glycoconjugates," *Macromolecular Rapid Communications*, vol. 31, no. 19, pp. 1664–1684, 2010.
- [151] S. R. S. Ting, E. H. Min, P. Escale, M. Save, L. Billon, and M. H. Stenzel, "Lectin Recognizable Biomaterials Synthesized via Nitroxide-Mediated Polymerization of a Methacryloyl Galactose Monomer," *Macromolecules*, vol. 42, no. 24, pp. 9422–9434, 2009.
- [152] M. Mammen, S.-k. Choi, and G. M. Whitesides, "Polyvalent Interactions in Biological Systems: Implications for Design and Use of Multivalent Ligands and Inhibitors," *Angewandte Chemie*, vol. 37, pp. 2754–2794, 1998.
- [153] Y. Miura, "Design and synthesis of well-defined glycopolymers for the control of biological functionalities," *Polymer Journal*, vol. 44, no. 7, pp. 679–689, 2012.
- [154] H. C. Kolb, M. G. Finn, and K. B. Sharpless, "Click Chemistry: Diverse Chemical Function from a Few Good Reactions.," *Angewandte Chemie*, vol. 40, no. 11, pp. 2004–2021, 2001.
- [155] J. Lazar, H. Park, R. R. Rosenkrantz, A. Böker, L. Elling, and U. Schnakenberg *Macromolecular Rapid Communications*, vol. 36, no. 16, pp. 1472–1478, 2015.
- [156] Y. C. Lee and R. T. Lee, "Carbohydrate-Protein Interactions: Basis of Glycobiology," *Accounts of Chemical Research*, vol. 28, no. 8, pp. 321–327, 1995.

- [157] N. R. Cameron, S. G. Spain, J. A. Kingham, S. Weck, L. Albertin, C. A. Barker, G. Battaglia, T. Smart, and A. Blanazs, “Synthesis of well-defined glycopolymers and some studies of their aqueous solution behaviour,” *Faraday Discussions*, vol. 139, p. 359, 2008.
- [158] J. J. Lundquist and E. J. Toone, “The cluster glycoside effect,” *Chemical Reviews*, vol. 102, no. 2, pp. 555–578, 2002. PMID: 11841254.
- [159] Z. Deng, S. Li, X. Jiang, and R. Narain, “Well-Defined Galactose-Containing Multi-Functional Copolymers and Glyconanoparticles for Biomolecular Recognition Processes,” *Macromolecules*, vol. 42, no. 17, pp. 6393–6405, 2009.
- [160] M.-G. Baek and R. Roy, “Relative Lectin Binding Properties of T-Antigen-Containing Glycopolymers: Copolymerization of N-Acryloylated T-Antigen Monomer vs. Graft Conjugation of Aminated T-Antigen Ligands onto Poly(N-acryloxysuccinimide),” *Macromolecular Bioscience*, vol. 1, no. 7, pp. 305–311, 2001.
- [161] A. Pfaff, V. S. Shinde, Y. Lu, A. Wittemann, M. Ballauff, and A. H. E. Müller, “Glycopolymer-Grafted Polystyrene Nanospheres,” *Macromolecular Bioscience*, pp. 199–210, 2010.
- [162] Y. Chen, G. Chen, and M. H. Stenzel, “Synthesis and Lectin Recognition of Glyco Star Polymers Prepared by Clicking Thiocarbohydrates onto a Reactive Scaffold,” *Macromolecules*, vol. 43, no. 19, pp. 8109–8114, 2010.
- [163] M. Sletmoen, T. K. Dam, T. A. Gerken, B. T. Stokke, and C. F. Brewer, “Single-molecule pair studies of the interactions of the alpha-GalNAc (Tn-antigen) form of porcine submaxillary mucin with soybean agglutinin,” *Biopolymers*, vol. 91, no. 9, pp. 719–728, 2009.
- [164] Voigtländer, Bert, *Scanning Probe Microscopy: Atomic Force Microscopy and Scanning Tunnelling Microscopy*. Springer-Verlag, Berlin Heidelberg, Germany., 2015.
- [165] F. Gaboriaud and Y. F. Dufrêne, “Atomic force microscopy of microbial cells: application to nanomechanical properties, surface forces and molecular recognition forces,” *Colloids and surfaces B: Biointerfaces*, vol. 54, no. 1, pp. 10–19, 2007.
- [166] T. Puntheeranurak, I. Neundlinger, R. K. H. Kinne, and P. Hinterdorfer, “Single-molecule recognition force spectroscopy of transmembrane transporters on living cells,” *Nature Protocols*, vol. 6, no. 9, pp. 1443–1452, 2011.
- [167] H. J. Busscher, W. Norde, and H. C. van der Mei, “Specific molecular recognition and nonspecific contributions to bacterial interaction forces,” *Applied and Environmental Microbiology*, vol. 74, no. 9, pp. 2559–2564, 2008.
- [168] V. Dupres, F. D. Menozzi, C. Locht, B. H. Clare, N. L. Abbott, S. Cuenot, C. Bompard, D. Raze, and Y. F. Dufrêne, “Nanoscale mapping and functional analysis of individual adhesins on living bacteria,” *Nature Methods*, vol. 2, no. 7, pp. 515–520, 2005.

- [169] C. Hentschel, H. Wagner, J. Smiatek, A. Heuer, H. Fuchs, X. Zhang, A. Studer, and L. Chi, “AFM-based force spectroscopy on polystyrene brushes: effect of brush thickness on protein adsorption.,” *Langmuir*, vol. 29, no. 6, pp. 1850–1856, 2013.
- [170] A. Beaussart, D. Alsteens, S. El-Kirat-Chatel, P. N. Lipke, S. Kucharíková, P. Van Dijck, and Y. F. Dufrêne, “Single-molecule imaging and functional analysis of Als adhesins and mannans during *Candida albicans* morphogenesis.,” *ACS Nano*, vol. 6, no. 12, pp. 10950–10964, 2012.
- [171] H. Handa, S. Gurczynski, M. P. Jackson, and G. Mao, “Immobilization and Molecular Interactions between Bacteriophage and Lipopolysaccharide Bilayers.,” *Langmuir*, vol. 602, no. 7, pp. 12095–12103, 2010.
- [172] K. P. Heim, R. M. a. Sullan, P. J. Crowley, S. El-Kirat-Chatel, A. Beaussart, W. Tang, R. Besingi, Y. F. Dufrene, and L. J. Brady, “Identification of a supramolecular functional architecture of *Streptococcus mutans* adhesin P1 on the bacterial cell surface,” *Journal of Biological Chemistry*, vol. 290, no. 14, p. jbc.M114.626663, 2015.
- [173] F. Gaboriaud, B. S. Parcha, M. L. Gee, J. A. Holden, and R. A. Strugnell, “Spatially resolved force spectroscopy of bacterial surfaces using force-volume imaging.,” *Colloids and Surfaces. B, Biointerfaces*, vol. 62, no. 2, pp. 206–13, 2008.
- [174] P. Polyakov, C. Soussen, J. Duan, J. F. L. Duval, D. Brie, and G. Francius, “Automated force volume image processing for biological samples.,” *PloS One*, vol. 6, no. 4, p. e18887, 2011.
- [175] L. S. Dorobantu, S. Bhattacharjee, J. M. Foght, and M. R. Gray, “Analysis of force interactions between AFM tips and hydrophobic bacteria using DLVO theory.,” *Langmuir*, vol. 25, no. 12, pp. 6968–6976, 2009.
- [176] Y. Chen, H. J. Busscher, H. C. van der Mei, and W. Norde, “Statistical Analysis of Long- and Short-Range Forces Involved in Bacterial Adhesion to Substratum Surfaces Measured Using AFM.,” *Applied and Environmental Microbiology*, vol. 77, pp. 5065–5070, 2011.
- [177] M. Castelain, E. Koutris, M. Andersson, K. Wiklund, O. Björnham, S. Schedin, and O. Axner, “Characterization of the biomechanical properties of T4 pili expressed by *Streptococcus pneumoniae*—a comparison between helix-like and open coil-like pili.,” *ChemPhysChem*, vol. 10, no. 9-10, pp. 1533–1540, 2009.
- [178] C. Bustamante, J. F. Marko, E. D. Siggia, and S. Smith, “Entropic elasticity of lambda-phage DNA.,” *Science*, vol. 265, no. 5178, pp. 1599–1600, 1994.
- [179] Y. Muroga, T. Yoshida, and S. Kawaguchi, “Conformation of poly(methacrylic acid) in acidic aqueous solution studied by small angle X-ray scattering.,” *Biophysical Chemistry*, vol. 81, no. 1, pp. 45–57, 1999.
- [180] A. J. Parnell, S. J. Martin, C. C. Dang, M. Geoghegan, R. A. L. Jones, C. J. Crook, J. R. Howse, and A. J. Ryan, “Synthesis, characterization and swelling

- behaviour of poly(methacrylic acid) brushes synthesized using atom transfer radical polymerization,” *Polymer*, vol. 50, no. 4, pp. 1005–1014, 2009.
- [181] P. Markiewicz and M. C. Goh, “Atomic force microscope tip deconvolution using calibration arrays,” *Review of Scientific Instruments*, vol. 66, pp. 3186–3190, 1995.
- [182] O. Dos Santos Ferreira, E. Gelinck, D. de Graaf, and H. Fischer, “Adhesion experiments using an AFM - Parameters of influence.,” *Applied Surface Science*, vol. 257, no. 1, pp. 48–55, 2010.
- [183] S. Sen, S. Subramanian, and D. E. Discher, “Indentation and adhesive probing of a cell membrane with AFM: theoretical model and experiments.,” *Biophysical Journal*, vol. 89, no. 5, pp. 3203–3213, 2005.
- [184] A. Suchodolskis, V. Feiza, A. Stirke, A. Timonina, A. Ramanaviciene, and A. Ramanavicius, “Elastic properties of chemically modified baker’s yeast cells studied by AFM,” *Surface and Interface Analysis*, vol. 43, no. 13, pp. 1636–1640, 2011.
- [185] R. L. Meyer, X. Zhou, L. Tang, A. Arpanaei, P. Kingshott, and F. Besenbacher, “Immobilisation of living bacteria for AFM imaging under physiological conditions.,” *Ultramicroscopy*, vol. 110, no. 11, pp. 1349–1357, 2010.
- [186] G. McLachlan and D. Peel, *Finite mixture models*. John Wiley & Sons Ltd., Chichester, England., 2004.
- [187] S. Frühwirth-Schnatter, *Finite mixture and Markov switching models*. Springer Science + Business Media, Paris, France., 2006.
- [188] D. W. Scott, “Scott’s rule,” *Wiley Interdisciplinary Reviews: Computational Statistics*, vol. 2, no. 4, pp. 497–502, 2010.
- [189] B. R. Martin, *Statistics for Physical Science: an Introduction*. Academic Press, Boston, USA., 1st ed., 2012.
- [190] R. J. Barlow, *Statistics: a guide to the use of statistical methods in the physical sciences*. John Wiley & Sons Ltd., Chichester, England., 1st ed., 1989.
- [191] E. Whitley and J. Ball, “Statistics review 6: Nonparametric methods.,” *Critical Care*, vol. 6, no. 6, pp. 509–513, 2002.
- [192] J. Friedrichs, K. R. Legate, R. Schubert, M. Bharadwaj, C. Werner, D. J. Müller, and M. Benoit, “A practical guide to quantify cell adhesion using single-cell force spectroscopy.,” *Methods*, vol. 60, no. 2, pp. 169–78, 2013.
- [193] D. B. Petropolis, J. C. F. Rodrigues, N. B. Viana, B. Pontes, C. F. A. Pereira, and F. C. Silva-Filho, “*Leishmania amazonensis* promastigotes in 3D Collagen I culture: an *in vitro* physiological environment for the study of extracellular matrix and host cell interactions.,” *PeerJ*, vol. 2, p. e317, 2014.
- [194] C. Hyams, K. Trzciski, E. Camberlein, D. M. Weinberger, S. Chimalapati, M. Noursadeghi, M. Lipsitch, and J. S. Brown, “*Streptococcus pneumoniae* capsular serotype invasiveness correlates with the degree of factor H binding

- and opsonization with C3b/iC3b.," *Infection and Immunity*, vol. 81, no. 1, pp. 354–363, 2013.
- [195] H. Barkhausen, "Zwei mit hilfe der neuen verstärker entdeckte erscheinungen," *Physikalische Zeitschrift*, vol. 20, pp. 401–403, 1919.
- [196] I. Tessmer, P. Kaur, J. Lin, and H. Wang, "Investigating bioconjugation by atomic force microscopy.," *Journal of Nanobiotechnology*, vol. 11, no. 1, p. 25, 2013.
- [197] H.-J. Butt and M. Jaschke, "Calculation of thermal noise in atomic force microscopy," *Nanotechnology*, vol. 6, pp. 1–7, 1995.
- [198] W. R. Bowen, R. W. Lovitt, and C. J. Wright, "Atomic Force Microscopy Study of the Adhesion of *Saccharomyces cerevisiae*," *Journal of Colloid and Interface Science*, vol. 237, no. 1, pp. 54–61, 2001.
- [199] V. Vadillo-Rodríguez, H. J. Busscher, W. Norde, J. De Vries, R. J. B. Dijkstra, I. Stokroos, and H. C. Van Der Mei, "Comparison of atomic force microscopy interaction forces between bacteria and silicon nitride substrata for three commonly used immobilization methods.," *Applied and Environmental Microbiology*, vol. 70, no. 9, pp. 5441–5446, 2004.
- [200] M. S. Kuyukina, I. O. Korshunova, E. V. Rubtsova, and I. B. Ivshina, "Methods of microorganism immobilization for dynamic atomic-force studies (review).," *Applied Biochemistry and Microbiology*, vol. 50, no. 1, pp. 1–9, 2013.
- [201] R. D. Turner, N. H. Thomson, J. Kirkham, and D. Devine, "Improvement of the pore trapping method to immobilize vital coccoid bacteria for high-resolution AFM: a study of *Staphylococcus aureus*," *Journal of Microscopy*, vol. 238, no. 2, pp. 102–110, 2010.
- [202] A. Méndez-Vilas, A. M. Gallardo-Moreno, and M. L. González-Martín, "Atomic force microscopy of mechanically trapped bacterial cells.," *Microscopy and Microanalysis*, vol. 13, no. 1, pp. 55–64, 2007.
- [203] I. M. Helander, H. L. Alakomi, K. Latva-Kala, and P. Koski, "Polyethyleneimine is an effective permeabilizer of gram-negative bacteria.," *Microbiology*, vol. 143, pp. 3193–3199, 1997.
- [204] G. Andre, S. Kulakauskas, M.-P. Chapot-Chartier, B. Navet, M. Deghorain, E. Bernard, P. Hols, and Y. F. Dufrêne, "Imaging the nanoscale organization of peptidoglycan in living *Lactococcus lactis* cells.," *Nature Communications*, vol. 1, no. 3, pp. 1–8, 2010.
- [205] H. V. Rukke, I. K. Hegna, and F. C. Petersen, "Identification of a functional capsule locus in *Streptococcus mitis*," *Molecular Oral Microbiology*, vol. 27, no. 2, pp. 95–108, 2012.
- [206] N. Suzuki, M. Seki, Y. Nakano, Y. Kiyoura, M. Maeno, and Y. Yamashita, "Discrimination of *Streptococcus pneumoniae* from viridans group streptococci by genomic subtractive hybridization," *Journal of Clinical Microbiology*, vol. 43, no. 9, pp. 4528–4534, 2005.

- [207] S. E. Cross, J. Kreth, L. Zhu, F. Qi, A. E. Pelling, W. Shi, and J. K. Gimzewski, “Atomic force microscopy study of the structure-function relationships of the biofilm-forming bacterium *Streptococcus mutans*,” *Nanotechnology*, vol. 17, no. 4, pp. S1–S7, 2006.
- [208] R. Gupta, J. Yang, Y. Dong, E. Swiatlo, J.-R. Zhang, D. W. Metzger, and G. Bai, “Deletion of *arcD* in *Streptococcus pneumoniae* D39 impairs its capsule and attenuates virulence,” *Infection and Immunity*, vol. 81, no. 10, pp. 3903–3911, 2013.
- [209] *Pneumococcus*. <http://www.britannica.com/science/pneumococcus>, Encyclopædia Britannica Online, 2015.
- [210] J. S. Brown, S. Hammerschmidt, and C. J. Orihuela, *Streptococcus Pneumoniae: Molecular Mechanisms of Host-Pathogen Interactions*. Elsevier, 1st ed., 2015.
- [211] “Selective penicillin-binding protein imaging probes reveal substructure in bacterial cell division,” *ACS Chemical Biology*, vol. 7, no. 10, pp. 1746–1753, 2012.
- [212] S. Kasas and A. Ikai, “A method for anchoring round shaped cells for atomic force microscope imaging,” *Biophysical Journal*, vol. 68, no. 5, pp. 1678–1680, 1995.
- [213] D. A. Lamprou, J. R. Smith, T. G. Nevell, E. Barbu, C. R. Willis, and J. Tsi-bouklis, “Self-assembled structures of alkanethiols on gold-coated cantilever tips and substrates for atomic force microscopy: Molecular organisation and conditions for reproducible deposition,” *Applied Surface Science*, vol. 256, pp. 1961–1968, 2010.
- [214] A. Ptak, H. Gojzewski, M. Kappl, and H.-J. Butt, “Influence of humidity on the nanoadhesion between a hydrophobic and a hydrophilic surface,” *Chemical Physics Letters*, vol. 503, no. 1-3, pp. 66–70, 2011.
- [215] J. R. Ell, D. E. Mulder, R. Faller, T. E. Patten, and T. L. Kuhl, “Structural Determination of High Density, ATRP Grown Polystyrene Brushes by Neutron Reflectivity,” *Macromolecules*, vol. 42, no. 24, pp. 9523–9527, 2009.
- [216] P. D. Topham, J. R. Howse, C. J. Crook, A. J. Parnell, M. Geoghegan, R. A. L. Jones, and A. J. Ryan, “Controlled growth of poly(2-diethylamino ethyl methacrylate) brushes via atom transfer radical polymerisation on planar silicon surfaces,” *Polymer International*, vol. 55, no. October 2005, pp. 808–815, 2006.
- [217] P. Chapman, R. E. Ducker, C. R. Hurley, J. K. Hobbs, and G. J. Leggett, “Fabrication of two-component, brush-on-brush topographical microstructures by combination of atom-transfer radical polymerization with polymer end-functionalization and photopatterning,” *Langmuir*, vol. 31, no. 21, pp. 5935–5944, 2015.
- [218] S. K. Sinniah, A. B. Steel, C. J. Miller, and J. E. Reutt-Robey, “Solvent Exclusion and Chemical Contrast in Scanning Force Microscopy,” *Journal of the American Chemical Society*, vol. 118, no. 37, pp. 8925–8931, 1996.

- [219] A. Noy, “Chemical force microscopy of chemical and biological interactions,” *Surface and Interface Analysis*, vol. 38, no. 11, pp. 1429–1441, 2006.
- [220] A. Beaussart, C. Péchoux, P. Trieu-Cuot, P. Hols, M.-Y. Mistou, and Y. F. Dufrêne, “Molecular mapping of the cell wall polysaccharides of the human pathogen *Streptococcus agalactiae*,” *Nanoscale*, vol. 6, no. 24, pp. 14820–14827, 2014.
- [221] D. V. Vezenov, A. V. Zhuk, G. M. Whitesides, and C. M. Lieber, “Chemical force spectroscopy in heterogeneous systems: Intermolecular interactions involving epoxy polymer, mixed monolayers, and polar solvents,” *Journal of the American Chemical Society*, vol. 124, no. 35, pp. 10578–10588, 2002.
- [222] C. D. Ma, C. Wang, C. Acevedo-Vélez, S. H. Gellman, and N. L. Abbott, “Modulation of hydrophobic interactions by proximally immobilized ions,” *Nature*, vol. 517, pp. 347–350, 2015.
- [223] S. Garde, “Physical chemistry: Hydrophobic interactions in context,” *Nature*, vol. 517, pp. 277–279, 2015.
- [224] J. R. Hull, J. J. Shannon, G. S. Tamura, and D. G. Castner, “Atomic force microscopy and surface plasmon resonance investigation of fibronectin interactions with group B streptococci,” *Biointerphases*, vol. 2, no. 2, pp. 64–72, 2007.
- [225] V. Vadillo-Rodríguez, H. J. Busscher, W. Norde, J. De Vries, and H. C. Van der Mei, “On relations between microscopic and macroscopic physicochemical properties of bacterial cell surfaces: An AFM study on *Streptococcus mitis* strains,” *Langmuir*, vol. 19, no. 6, pp. 2372–2377, 2003.
- [226] N. Thewes, P. Loskill, P. Jung, H. Peisker, M. Bischoff, M. Herrmann, and K. Jacobs, “Hydrophobic interaction governs unspecific adhesion of staphylococci: a single cell force spectroscopy study,” *Beilstein Journal of Nanotechnology*, vol. 5, pp. 1501–1512, 2014.
- [227] W. H. Brown, B. L. Iverson, E. V. Anslyn, and C. J. Foote, *Organic Chemistry*. Cengage Learning, Boston, 7th ed., 2014.
- [228] V. V. Tsukruk, A. Sidorenko, and H. Yang, “Polymer nanocomposite coatings with non-linear elastic response,” *Polymer*, vol. 43, no. 5, pp. 1695–1699, 2002.
- [229] D. Garcia-Hermoso, F. Dromer, and G. Janbon, “*Cryptococcus neoformans* capsule structure evolution *in vitro* and during murine infection,” *Infection and Immunity*, vol. 72, no. 6, pp. 3359–3365, 2004.
- [230] L. J. Hathaway, S. D. Brugger, B. Morand, M. Bangert, J. U. Rotzetter, C. Hauser, W. A. Graber, S. Gore, A. Kadioglu, and K. Mühlemann, “Capsule type of *Streptococcus pneumoniae* determines growth phenotype,” *PLOS Pathogens*, vol. 8, no. 3, p. e1002574, 2012.
- [231] B. Ryall, G. Eydallin, and T. Ferenci, “Culture History and Population Heterogeneity as Determinants of Bacterial Adaptation: the Adaptomics of a Single Environmental Transition,” *Microbiology and Molecular Biology Reviews*, vol. 76, no. 3, pp. 597–625, 2012.

- [232] G. A. Burks, S. B. Velegol, E. Paramonova, B. E. Lindenmuth, J. D. Feick, and B. E. Logan, “Macroscopic and Nanoscale Measurements of the Adhesion of Bacteria with Varying Outer Layer Surface Composition,” *Langmuir*, vol. 19, no. 6, pp. 2366–2371, 2003.
- [233] S. Voss, G. Gámez, and S. Hammerschmidt, “Impact of pneumococcal microbial surface components recognizing adhesive matrix molecules on colonization,” *Molecular Oral Microbiology*, vol. 27, no. 4, pp. 246–56, 2012.
- [234] V. Vadillo-Rodríguez, M. A. Pacha-Olivenza, M. L. Gónzalez Martín, J. M. Bruque, and A. M. Gallardo-Moreno, “Adsorption behavior of human plasma fibronectin on hydrophobic and hydrophilic Ti6Al4V substrata and its influence on bacterial adhesion and detachment,” *Journal of Biomedical Materials Research - Part A*, vol. 101 A, no. 5, pp. 1397–1404, 2013.
- [235] S. Hammerschmidt and S. Wolff, “Illustration of Pneumococcal Polysaccharide Capsule during Adherence and Invasion of Epithelial Cells,” *Infection and Immunity*, vol. 73, no. 8, pp. 4653–4667, 2005.
- [236] P. D. Ready, “Leishmaniasis emergence in Europe.,” *Euro Surveillance*, vol. 15, no. 10, p. 19505, 2010.
- [237] J. P. Farrell, *World Class Parasites Volume 4: Leishmania*. Springer Science + Business Media, New York, USA., 2002.
- [238] U. Sharma and S. Singh, “Insect vectors of *Leishmania*: Distribution, physiology and their control,” *Journal of Vector Borne Diseases*, vol. 45, no. 4, pp. 255–272, 2008.
- [239] T. Ilg, R. Etgess, P. Overath, M. J. Mcconvilleq, J. Thomas-oatest, J. Thomasll, S. W. Homans, and M. A. J. Ferguson, “Structure of *Leishmania mexicana* lipophosphoglycan,” *The Journal of Biological Chemistry*, vol. 267, no. 10, pp. 6834–3840, 1992.
- [240] N. M. Novozhilova and N. V. Bovin, “Structure, functions, and biosynthesis of glycoconjugates of *Leishmania* spp. cell surface.,” *Biochemistry (Moscow)*, vol. 75, no. 6, pp. 686–694, 2010.
- [241] A. Guha-Niyogi, D. R. Sullivan, and S. J. Turco, “Glycoconjugate structures of parasitic protozoa.,” *Glycobiology*, vol. 11, no. 4, pp. 45R–59R, 2001.
- [242] D. Sacks and S. Kamhawi, “Molecular aspects of parasite-vector and vector-host interactions in Leishmaniasis,” *Annual Reviews in Microbiology*, vol. 55, pp. 453–483, 2001.
- [243] H. Kbaier-Hachemi, S. Guerbouj, L. Turki-Mannoubi, B. Kaabi, and I. Guizani, “In vitro growth kinetics, differentiation and morphological characterisation of Tunisian *Leishmania infantum* parasites,” *Transactions of the Royal Society of Tropical Medicine and Hygiene*, vol. 106, no. 1, pp. 20–25, 2012.
- [244] R. P. P. Soares, M. E. Macedo, C. Ropert, N. F. Gontijo, I. C. Almeida, R. T. Gazzinelli, P. F. P. Pimenta, and S. J. Turco, “*Leishmania chagasi*:

- Lipophosphoglycan characterization and binding to the midgut of the sand fly vector *Lutzomyia longipalpis*,” *Molecular and Biochemical Parasitology*, vol. 121, no. 2, pp. 213–224, 2002.
- [245] L. G. Evangelista and A. C. R. Leite, “Histochemical Localization of N-Acetyl-Galactosamine in the Midgut of *Lutzomyia longipalpis* (Diptera: Psychodidae),” *Journal of Medical Entomology*, vol. 39, no. 3, pp. 432–439, 2002.
- [246] N. P. Kock, H. J. Gabius, J. Schmitz, and J. Schottelius, “Receptors for carbohydrate ligands including heparin on the cell surface of *Leishmania* and other trypanosomatids,” *Tropical Medicine & International Health*, vol. 2, no. 9, pp. 863–874, 1997.
- [247] M. Svobodová, P. A. Bates, and P. Volf, “Detection of lectin activity in *Leishmania* promastigotes and amastigotes,” *Acta Tropica*, vol. 68, no. 1, pp. 23–35, 1997.
- [248] T. Lieke, S. Nylén, L. Eidsmo, W. R. McMaster, A. M. Mohammadi, A. Khamesipour, L. Berg, and H. Akuffo, “*Leishmania* surface protein gp63 binds directly to human natural killer cells and inhibits proliferation,” *Clinical and Experimental Immunology*, vol. 153, no. 2, pp. 221–230, 2008.
- [249] J. Sádlová, P. Volf, K. Victoir, J. C. Dujardin, and J. Votýpka, “Virulent and attenuated lines of *Leishmania major*: DNA karyotypes and differences in metalloproteinase GP63,” *Folia Parasitologica*, vol. 53, no. 2, pp. 81–90, 2006.
- [250] R. J. Wheeler, E. Gluenz, and K. Gull, “The cell cycle of *Leishmania*: Morphogenetic events and their implications for parasite biology,” *Molecular Microbiology*, vol. 79, no. 3, pp. 647–662, 2011.
- [251] M. H. Wakid and P. A. Bates, “Flagellar attachment of *Leishmania* promastigotes to plastic film in vitro,” *Experimental Parasitology*, vol. 106, no. 3–4, pp. 173–8, 2004.
- [252] C. Gadelha, B. Wickstead, and K. Gull, “Flagellar and ciliary beating in trypanosome motility,” *Cell Motility and the Cytoskeleton*, vol. 64, no. 8, pp. 629–643, 2007.
- [253] D. Tranchida, E. Sperotto, T. Staedler, X. Jiang, and H. Schönherr, “Nanomechanical Properties of Oligo(ethylene glycol methacrylate) Polymer Brush-Based Biointerfaces,” *Advanced Engineering Materials*, vol. 13, no. 10, pp. B369–B376, 2011.
- [254] T. Hoffmann and L. Dougan, “Single molecule force spectroscopy using polyproteins,” *Chemical Society Reviews*, vol. 41, no. 14, pp. 4781–96, 2012.
- [255] S. J. Attwood, A. M. C. Simpson, R. Stone, S. W. Hamaia, D. Roy, R. W. Farndale, M. Ouberai, and M. E. Welland, “A Simple Bioconjugate Attachment Protocol for Use in Single Molecule Force Spectroscopy Experiments Based on Mixed Self-Assembled Monolayers,” *International Journal of Molecular Sciences*, vol. 13, no. 10, pp. 13521–13541, 2012.

- [256] D. L. Sacks, G. Modi, E. Rowton, G. Späth, L. Epstein, S. J. Turco, and S. M. Beverley, “The role of phosphoglycans in *Leishmania*-sand fly interactions.,” *Proceedings of the National Academy of Sciences of the United States of America*, vol. 97, no. 1, pp. 406–411, 2000.